

Report No. CG-D-22-97, I
DOT-VNTSC-CG-97-1.1

**U.S. Coast Guard
1995 Oil Pollution Research Grants
Publications - Part I**

U.S. Department of Transportation
Research and Special Programs Administration
John A. Volpe National Transportation Systems Center
Cambridge, MA 02142-1093



FINAL REPORT
August 1997

This document is available to the U.S. public through the
National Technical Information Service, Springfield, Virginia 22161

Prepared for:

U.S. Department of Transportation
United States Coast Guard
Marine Safety and Environmental Protection, (G-M)
Washington, DC 20593-0001

and

U.S. Coast Guard
Research and Development Center
1082 Shennecossett Road
Groton, CT 06340-6096

19971016 142

DTIC QUALITY INSPECTED 2

NOTICE

This document is disseminated under the sponsorship of the Department of Transportation in the interest of information exchange. The United States Government assumes no liability for its contents or use thereof.

NOTICE

The United States Government does not endorse products or manufacturers. Trade or manufacturers' names appear herein solely because they are considered essential to the objective of this report.

1. Report No. CG-D-22-97, I		2. Government Accession No.		3. Recipient's Catalog No.	
4. Title and Subtitle U.S. Coast Guard 1995 Oil Pollution Research Grants Publications - Part I				5. Report Date August 1997	
				6. Performing Organization Code Project No: 4123	
7. Author(s)				8. Performing Organization Report No. R&DC 23/97, I	
9. Performing Organization Name and Address Research and Special Programs Administration John A. Volpe National Transportation Systems Center Cambridge, MA 02142-1093				10. Work Unit No. (TRAIS)	
				11. Contract or Grant No. DTRS57-95-G-00065	
12. Sponsoring Agency Name and Address U.S. Department of Transportation United States Coast Guard Marine Safety and Environmental Protection (G-M) Washington, DC 20593-0001 U.S. Coast Guard Research and Development Center 1082 Shennecossett Road Groton, CT 06340-6096				13. Type of Report and Period Covered Final Report	
				14. Sponsoring Agency Code Commandant (G-MOR) U.S. Coast Guard Headquarters Washington, DC 20593-0001	
15. Supplementary Notes The R&DC point of contact is Kenneth Bitting, 860-441-2733.					
16. Abstract The Oil Pollution Research Grants Program was created by the Oil Pollution Act (OPA) of 1990, P.L. 101-380 (OPA 90), 33 U.S.C. 28761(c)(8) and 2761(c)(9). The OPA established a regional research program and authorized those agencies represented on the Interagency Coordinating Committee on Oil Pollution Research, including the U.S. Coast Guard (USCG), to make grants to universities and other research institutions to perform research related to regional effects of oil pollution. The USCG established such a grant program and the John A. Volpe National Transportation Systems Center (Volpe Center), a component of the Research and Special Programs Administration of the Department of Transportation (DOT), was chosen to administer this program on behalf of the USCG. In August 1995, the Volpe Center awarded seven one-year grants. Coast Guard funds were matched by funds from the university or non-profit research institution. This report contains the final reports for research performed under these grants.					
17. Key Words oil pollution research oil pollution grants			18. Distribution Statement This document is available to the U.S. public through the National Technical Information Service, Springfield, VA 22161.		
19. Security Classif. (of this report) UNCLASSIFIED		20. SECURITY CLASSIF. (of this page) UNCLASSIFIED		21. No. of Pages	
				22. Price	

[BLANK]

PREFACE

PUBLICATIONS OF THE U.S. COAST GUARD 1995 OIL POLLUTION RESEARCH GRANTS

On March 24, 1989, the EXXON VALDEZ ran aground on Bligh Reef in Prince William Sound, Alaska producing the largest oil spill in U.S. history. Following this event, the Coast Guard reexamined its mission needs and technology to formulate an R&D effort for the 1990s. Workshops were held within the Coast Guard and with other Federal agencies and private sector organizations to identify spill response needs and R&D efforts that would support those needs. One of the workshops was a U.S. Coast Guard (USCG) sponsored Interagency Planning Workshop on oil spill research and development on September 26-27, 1989. This workshop exchanged information and initiated the development of a coordinated national plan for oil spill research and development under Title VII of the Oil Pollution Act of 1990.

The Oil Pollution Research Grant Program was created by the Oil Pollution Act of 1990, P.L. 101-380 (OPA 90), 33 U.S.C. 2761 (c)(8) and 2761 (c)(9). The OPA established a regional research program and authorized those agencies represented on the Interagency Coordinating Committee on Oil Pollution Research, including the USCG, to make grants to universities and other research institutions to perform research related to regional effects of oil pollution. The USCG established such a grant program, and the John A. Volpe National Transportation Systems Center (Volpe Center), a component of the Research and Special Programs Administration of the Department of Transportation (DOT), was chosen to administer this program on behalf of the USCG.

The Volpe Center mailed Grant Applications to about 200 universities and non-profit research institutions during the first week of January 1995. The mailing list included institutions from all the Coast Guard districts. On March 13, 1995 the Volpe Center received 25 applications from six districts. These proposals were reviewed by the Volpe Center and the Coast Guard Research and Development Center and the recommendations forwarded to the Interagency Committee on Oil Pollution Research for approval. Seven one-year Grants were awarded in June 1995. Coast Guard funds were matched by funds from the university or non-profit research institution.

In August 1994, the Volpe Center awarded ten one-year Grants. Three of these Grants were extended for a second year in June 1995 to expand the research effort.

This report contains the Final Reports for research performed under these seven 1995 Grants. The results are presented in two volumes. For further information contact Kenneth Bitting at the U.S Coast Guard Research and Development Center, Groton, Connecticut (860) 441-2733.

Additional copies of this document are available through the National Technical Information Service, Springfield, Virginia 22161.

METRIC/ENGLISH CONVERSION FACTORS	
ENGLISH TO METRIC	METRIC TO ENGLISH
LENGTH (APPROXIMATE) 1 inch (in) = 2.5 centimeters (cm) 1 foot (ft) = 30 centimeters (cm) 1 yard (yd) = 0.9 meter (m) 1 mile (mi) = 1.6 kilometers (km)	LENGTH (APPROXIMATE) 1 millimeter (mm) = 0.04 inch (in) 1 centimeter (cm) = 0.4 inch (in) 1 meter (m) = 3.3 feet (ft) 1 meter (m) = 1.1 yards (yd) 1 kilometer (km) = 0.6 mile (mi)
AREA (APPROXIMATE) 1 square inch (sq in, in ²) = 6.5 square centimeters (cm ²) 1 square foot (sq ft, ft ²) = 0.09 square meter (m ²) 1 square yard (sq yd, yd ²) = 0.8 square meter (m ²) 1 square mile (sq mi, mi ²) = 2.6 square kilometers (km ²) 1 acre = 0.4 hectare (ha) = 4,000 square meters (m ²)	AREA (APPROXIMATE) 1 square centimeter (cm ²) = 0.16 square inch (sq in, in ²) 1 square meter (m ²) = 1.2 square yards (sq yd, yd ²) 1 square kilometer (km ²) = 0.4 square mile (sq mi, mi ²) 10,000 square meters (m ²) = 1 hectare (ha) = 2.5 acres
MASS - WEIGHT (APPROXIMATE) 1 ounce (oz) = 28 grams (gm) 1 pound (lb) = .45 kilogram (kg) 1 short ton = 2,000 pounds (lb) = 0.9 tonne (t)	MASS - WEIGHT (APPROXIMATE) 1 gram (gm) = 0.036 ounce (oz) 1 kilogram (kg) = 2.2 pounds (lb) 1 tonne (t) = 1,000 kilograms (kg) = 1.1 short tons
VOLUME (APPROXIMATE) 1 teaspoon (tsp) = 5 milliliters (ml) 1 tablespoon (tbsp) = 15 milliliters (ml) 1 fluid ounce (fl oz) = 30 milliliters (ml) 1 cup (c) = 0.24 liter (l) 1 pint (pt) = 0.47 liter (l) 1 quart (qt) = 0.96 liter (l) 1 gallon (gal) = 3.8 liters (l) 1 cubic foot (cu ft, ft ³) = 0.03 cubic meter (m ³) 1 cubic yard (cu yd, yd ³) = 0.76 cubic meter (m ³)	VOLUME (APPROXIMATE) 1 milliliter (ml) = 0.03 fluid ounce (fl oz) 1 liter (l) = 2.1 pints (pt) 1 liter (l) = 1.06 quarts (qt) 1 liter (l) = 0.26 gallon (gal) 1 cubic meter (m ³) = 36 cubic feet (cu ft, ft ³) 1 cubic meter (m ³) = 1.3 cubic yards (cu yd, yd ³)
TEMPERATURE (EXACT) $^{\circ}\text{C} = 5/9(^{\circ}\text{F} - 32)$	TEMPERATURE (EXACT) $^{\circ}\text{F} = 9/5(^{\circ}\text{C}) + 32$
QUICK INCH-CENTIMETER LENGTH CONVERSION 	
QUICK FAHRENHEIT-CELSIUS TEMPERATURE CONVERSION 	
For more exact and or other conversion factors, see NIST Miscellaneous Publication 286, Units of Weights and Measures. Price \$2.50. SD Catalog No. C13 10286.	

Updated 8/1/96

TABLE OF CONTENTS

Part I

<u>Section</u>	<u>Page</u>
RUPTURE ANALYSIS OF OIL TANKERS IN A SIDE COLLISION: THEORY OF BOW CUTTING THROUGH DECKS	1
B.C. Simonsen and T. Wierzbicki, Massachusetts Institute of Technology	
1. Abstract	3
2. Introduction	4
3. Previous Work	6
4. Comparison of Formulas for Initiation Cutting	12
5. Prediction of Steady State Cutting Force	13
6. Problem Statement and Basic Idea of Model	15
7. Basic Equations for Plasticity, Fracture and Friction	20
8. Energy Dissipation in Plasticity and Fracture	24
9. Friction and Perpendicular Reaction	26
10. Total Reaction and Verification	29
11. Conclusion	32
12. Appendix A - Model Geometry	34
13. References	38
RUPTURE ANALYSIS OF OIL TANKERS IN A SIDE COLLISION: GLOBAL STRUCTURAL MODEL OF BOW INDENTATION INTO SHIP SIDE	41
T. Wierzbicki and B.C. Simonsen, Massachusetts Institute of Technology	
1. Executive Summary	43
2. Plate Strip Model with Spreading Deformation	45
3. Equivalence of Plate and Plate Strip Formulation	66
4. Plate Indentation by a Hemispherical Bow	70
5. Punch Indentation into a Deck	81
6. References	92
RUPTURE ANALYSIS OF OIL TANKERS IN A SIDE COLLISION: HARD POINT FRACTURE OF SHELL PLATING	93
F.A. McClintock and J. Atmadja, Massachusetts Institute of Technology	
1. Introduction	96
2. Finite Element Studies of Effects of Strain Hardening and of Compliance at Hardpoint Supports	97
3. Lumped Parameter Estimate of Hardpoint Necking	100
4. A Buckled Stiffener Mode of Hardpoint Fracture	105
5. Conclusions	107
6. References	109

TABLE OF CONTENTS (cont.)

Part I

<u>Section</u>	<u>Page</u>
7. Appendix 1 - Conditions for Necking in Transversely Plane Strain Plates of Power-Law Hardening Material with Prestrain	110
8. Appendix 2 - Fitting Data Using a Power-Law Stress-Strain Curve with Pre-strain	111
NUMERICAL MODELING OF OIL CONTAINMENT BY A BOOM/BARRIER SYSTEM: PHASE II	
S.T. Grilli, Z. Hu, M.L. Spaulding, and D. Liang, University of Rhode Island	
1. Introduction and Project Overview	131
2. Piecewise Constant Vortex Sheet (PCVS) Model and Applications	139
3. Periodic Continuous Vortex Sheet (CVS) Model and Applications to KH Instability	176
4. Computation of Quasi Steady-State Slick Shape	190
5. Effects of Interfacial Friction on Vorticity Updating Equations	201
6. Conclusions	207
7. Bibliography	210
DEVELOPMENT OF A RAPID CURRENT CONTAINMENT BOOM: PHASE II	
M. R. Swift, B. Celikkol, P. Coyne, R. Steen, and M. Ozyalvac, University of New Hampshire	
1. Introduction	215
2. Two-Dimensional Oil Retention Results	221
3. Three-Dimensional Design Development	228
4. Semi-Rigid System	231
5. Flexible Systems	239
6. Discussion	252
7. References	253

Part II

<u>Section</u>	<u>Page</u>
FILTRATION STUDIES FOR REMOVAL OF ORIMULSION® FROM WATER IN PORTS	
J. Englehardt and D. Meeroff, University of Miami	
	255

TABLE OF CONTENTS (cont.)

Part II

<u>Section</u>	<u>Page</u>
1. Introduction	260
2. Methods	280
3. Results	295
4. Discussion	347
5. Conclusions and Recommendations	362
6. References	366
7. Appendix A - Calibration Curve for Orimulsion® Concentration Versus Volatile Suspended Solids Concentration	374
8. Appendix B - Results of Tests of Natural Additives to Improve Handling and Filterability of Orimulsion® Suspensions	376
9. Appendix C - Results of Burette Tests to Identify Diatomite Grade	383
10. Appendix D - Ultrafiltration Pilot Test Data, Including Filtration of Orimulsion®/Clay Suspensions	398
11. Appendix E - Precoat Pilot Plant	413
12. Appendix F - Ultrafiltration Pilot Plant	418

MICRO- AND MESO-SCALE METHODS FOR PREDICTING THE BEHAVIOR OF LOW-API GRAVITY OILS (LAPIO) SPILLED ON WATER	423
S.A. Ostazeski, S.C. Macomber, L.G. Roberts, and A.D. Uhler, Batelle Ocean Sciences	

1. Introduction	428
2. Methodology	431
3. Results and Discussion of Results	439
4. Conclusions	478
5. References	480
6. Appendix A - GC/FID Chromatograms	483
7. Appendix B - Polycyclic Aromatic Hydrocarbon Distributions	503
8. Appendix C - Iatroscan Chromatograms	510

SOURCE IDENTIFICATION OF OIL SPILLS BASED ON THE ISOTOPIC COMPOSITION OF INDIVIDUAL COMPONENTS IN WEATHERED OIL SAMPLES	531
R.P. Philp, L. Mansuy, and J. Allen, University of Oklahoma	

1. Introduction	534
2. Experimental Section	536
3. Results and Discussion	538

TABLE OF CONTENTS (cont.)

Part II

<u>Section</u>	<u>Page</u>
HUMAN RELIABILITY AND ERROR PREVENTION IN TANKBARGE TRANSFER OPERATIONS	559
E. Iakovou, S.J. Czaja, C. Douligeris, J.H. Moses, University of Miami	
J. Sharit, State University of New York at Buffalo	
1. Introduction	561
2. Methodolgy	562
3. Analysis of Accident Reports and Citations	568
4. Tankerman Training and Licensing	574
5. Interviews	576
6. Observations	583
7. Anecdotal Evidence and Near Misses	584
8. Summary and Recommendations	585
9. References	590
10. Appendix A - An Example of Task Analysis of Tankbarge Oil Transfer Operations	593
11. Appendix B - A Classification of Performance Shaping Factors (from Swain and Guttman, 1983)	598
12. Appendix C - Typical MCIR Cover Pages	600
13. Appendix D - Plots Associated with MCIR Data	607
14. Appendix E - Examples of Narrative Supplements Contained within MCIR Reports	617
15. Appendix F - An Example of an Observation Form Used in This Study	629
16. Appendix G - Examples of Anecdotal Evidence	631

**RUPTURE ANALYSIS OF OIL TANKERS IN A SIDE COLLISION: THEORY OF BOW
CUTTING THROUGH DECKS**

B.C. Simonsen and T. Wierzbicki, Massachusetts Institute of Technology

1 Abstract

A closed form solution to the problem of initiation and steady state wedge cutting through a ductile metal plate is presented. The considered problem is an idealization of the cutting process of a sharp raked bow of a ship into a deck of a stricken ship. A new kinematic model is proposed for the strain and displacement fields and it is demonstrated that the analysis is greatly simplified if the strain field is assumed to be dominated by plastic shear strains and moving hinge lines. Also, it is shown that the present shear model offers the basis for a convenient extension of the presented plate model to include more structural members as for example the stiffeners attached to deck. The fracture process is discussed and the model is formulated partly on the basis of the material fracture toughness. The effect of friction and the reaction force perpendicular to the direction of motion is derived theoretically in a new consistent manner. The derived expressions are discussed and compared to previously published experimental results and formulas.

2 Introduction

One of the primary energy absorbing mechanisms in a grounding or collision event is the so-called plate cutting process. Most authors use the terms 'cutting' or 'tearing' although some of the observed failure modes are quite complex and have little resemblance to the original meaning of these words. The mechanics of the cutting process is complicated and involves plastic flow of the plate in the vicinity of the wedge tip (and, some would argue, fracture processes there), friction between wedge and plate, membrane deformation of the plate, and large-scale bending of the plate "flaps" remote from the wedge tip into various scroll motifs and other folding patterns.

In this paper, the plate cutting phenomenon is described qualitatively, some of the most significant previous work is discussed and summarized, and new theories are derived for steady state plate cutting by a wedge.

Depending on the deformation mode which develops, the plate cutting phenomena described in literature can be divided into three categories, see Figure 1:

1. Stable or clean curling cut. The plate is separated at the tip or in front of the wedge and rolls and folds to the same side during the entire process.
2. Braided cut. The plate separates at the wedge tip as in the clean curling cut but the deformed flaps fold back and forth.
3. Concertina tearing. The plate folds back and forth in front of the wedge while it is torn at remote boundaries.

The experimental and theoretical analyses of these three classes fall into two main categories;

- "Initiation or transient wedge penetration". The wedge penetration is considered from the point of initial contact between wedge tip and plate edge to the point where the mean resistance force reaches a constant level. Normally the initiation phase can be assumed to terminate when the shoulders of the wedge enter the plate, [12]. Since the maximum width of the penetrator in the plate increases with penetration, the reaction force is also an increasing function of the penetration. This process was initially considered as an idealization of a rigid ship bow penetrating into the deck-plating of another ship in a collision but recently it has also been applied to groundings. Several authors, for example [17], [5] and [18], have applied results or models for this process as an approximation to problems of 'steady state penetration' described below.
- "Steady state penetration". If the penetrator has a finite width, the plate reaction force will reach a constant mean level after a certain penetration and the process is then said to be in steady state. This process is considered an

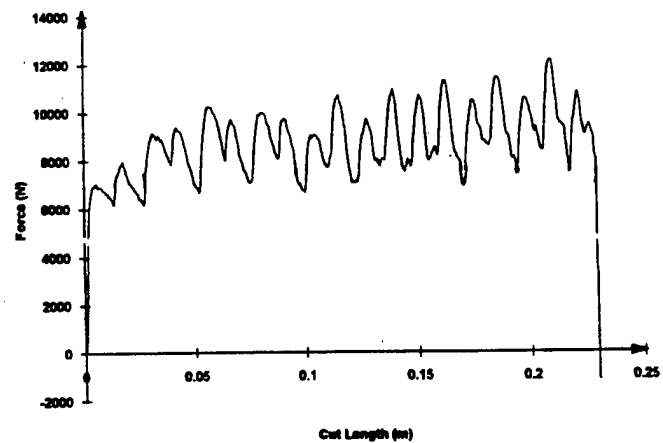
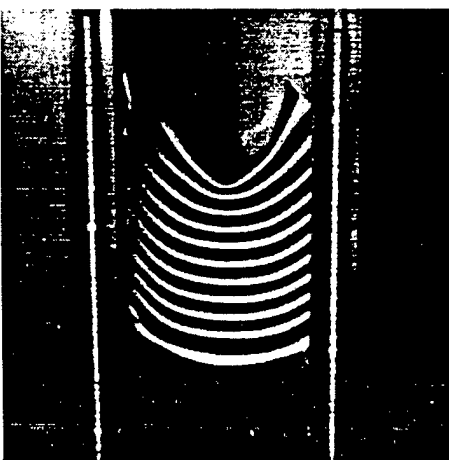
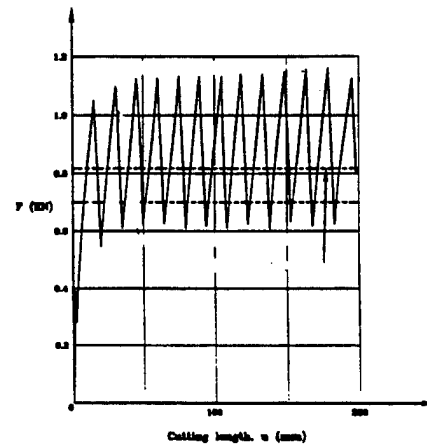
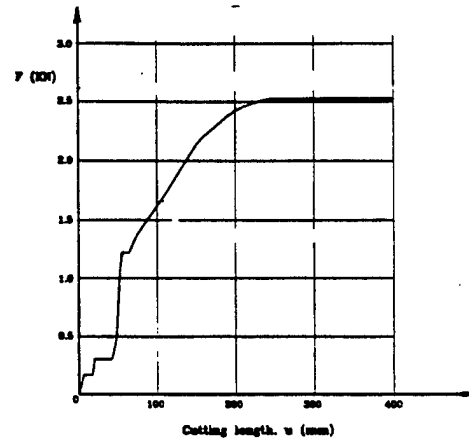
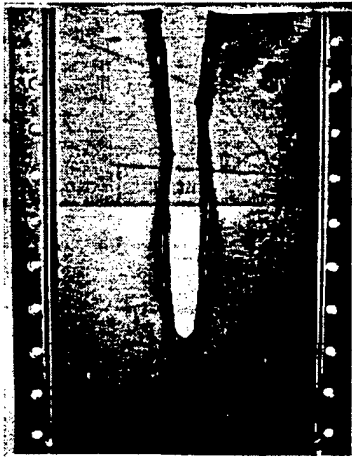


Figure 1: Photographs of three cutting modes: clean curling cut, braided cut, and concertina tearing with corresponding force-displacement diagrams

idealization of a rock pinnacle or ice reef cutting through a ship bottom in a grounding or ice collision event.

For each of the three examples shown in Figure 1, the deformation was large enough for the steady state to be reached so the figure shows the deformation and the reaction in both the initiation and the steady state phases.

The present paper is concerned with the clean curled cutting so whenever the term 'cutting' is used in the following without further explanation it refers to this specific cutting mode.

3 Previous work

A thorough literature review was presented recently (1990) by Lu and Calladine, [12], but since then the list of relevant publications has been expanded. A brief summary of literature pertinent to the field of plate cutting is given below.

The basic geometrical features of the cutting set-up used in the reported experimental work is shown in Figure 2.

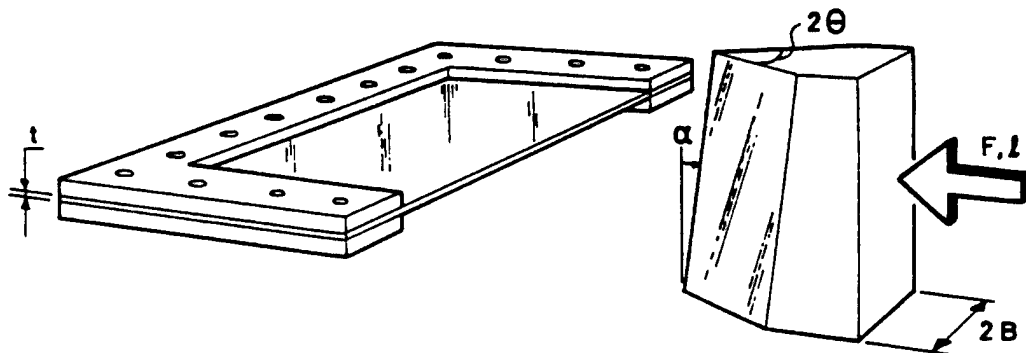


Figure 2: Cutting set-up

The definition of the inclination angle, α , varies; some perform experiments with an inclined plate and some incline the cutting edge as shown in Figure 2.

Earlier experiments were performed with drophammer tests but to eliminate dynamic effects - which are difficult to interpret - most recent work is all based on quasi-static testing.

Several authors developed simple formulas giving the energy absorption, W , as a function of the penetration, l , in the plate. The reaction force, F , is then calculated from $W(l)$ as $F(l) = \frac{dW}{dl}$ with a correction factor when needed due to the inconsistency of dimensions. In the next section the formulas are compared.

The notation used in the paper is given below.

F	Reaction force from plate on wedge (N)
W	Absorbed energy (Nm)
l	Length of penetration into plate (mm)
t	Plate thickness (mm)
δ_t	Crack tip opening displacement (mm)
$\bar{\delta}_t$	Non dimensional crack tip opening displacement, $\bar{\delta}_t = \delta_t/t$
2θ	Semi wedge angle
$2B$	Shoulder width of wedge
b	Spacing between longitudinal stiffeners
μ	Coefficient of friction
α	Angle between cutting edge and normal to plate
σ_y	Initial yield stress
σ_0	Energy equivalent flow stress

Not all of the empirical formulas listed in the following are dimensionally consistent, i.e. they are not independent of the dimensions of the involved parameters. If not defined otherwise, F is in $[N]$, W is in $[Nm(=J)]$, and l, t is in $[mm]$.

Akita and Kitamura (1972), [2] and [3], conducted tests with penetration of a rigid wedge into a steel plate. They proposed a simple conceptual model in which the plate exerts a normal compressive stress of σ_y onto the plate over the nominal contact area. Equilibrium then gives the total resistance force of the plate as

$$F = 2\sigma_y t l \tan\theta \quad (1)$$

The analysis does not take the actual deformation mode of rolling plate flaps into account and as it is shown in Figure 3 of the next section, the proposed formula, Eq. (1), overpredicts the actual plate resistance.

Vaughan (1978,80), [28], [29] used the experimental data of Akita and Kitamura, [3], together with Minorsky's formula, [16], to estimate the damage suffered by a ship bottom cut by a reef or ice. Vaughan assumed that the energy would be absorbed in two mechanisms, plastic deformation and creation of new surfaces by fracture, and thus came up with an two term empirical expression for the energy absorption:

$$W = 33.3 l t + 0.093 l^2 t \tan\theta \quad (2)$$

$$F = 33300 t + 0.19 l t \tan\theta \quad (3)$$

Vaughan subsequently performed sixty four drop-hammer experiments, [29], with both t and θ varying. Based on the same idea of two major energy absorbing mechanisms, he obtained the expression

$$W = 5.5 l t^{1.5} + 0.0044 l^2 t^2 \tan \theta \quad (4)$$

$$F = 5500 t^{1.5} + 8.8 l t^2 \tan \theta \quad (5)$$

All experiments were performed with the plate tilted an angle, $\alpha = 10^\circ$, because it was discovered that with this orientation, the cutting of the plates occurred by flaps rolling up on one side ('clean curling cut'), in contrast to the more complicated back-and-forth bending ('braided cut') which is characteristic when $\alpha = 0^\circ$.

The reaction force is seen to have a finite value at zero penetration so for small penetrations, these formulas do not correspond to actual reaction forces.

Woisin (1982), [33], performed drop-hammer tests with $\alpha = 0^\circ$ and $2\theta = 30^\circ$, 70° , and 100° . Woisin gave the following formula which is independent of wedge angle, for the cutting energy of mild steel plates:

$$W = 4.8 l t^{1.7} \quad (6)$$

$$F = 4800 t^{1.7} \quad (7)$$

Jones, Jouri, and Birch (1984-87), [9], [10], and [11], performed drop-hammer tests on mild steel plates with $\alpha = 0^\circ$, $t = 1.6 - 6.1 \text{ mm}$, and $2\theta = 15^\circ$, 30° , 45° , and 100° . A summary of the testing of eighty nine specimens is given in [10]. The energy absorbing mechanisms - cutting, bending, elasticity and friction - were identified and an attempt was made to partition the energy delivered between them. Bending and friction energy is found to amount to about 10 % each, elasticity effects are neglectable, and the remaining - i.e. the energy absorbed in cutting - is found to be given by the formulas

$$W = \begin{cases} 3.9 l t^{1.44} & \text{for } \sigma_y = 255 \text{ MPa} \\ 7.2 l t^{1.31} & \text{for } \sigma_y = 399 \text{ MPa} \end{cases} \quad (8)$$

with corresponding resisting forces

$$F = \begin{cases} 3900 t^{1.44} & \text{for } \sigma_y = 255 \text{ MPa} \\ 7200 t^{1.31} & \text{for } \sigma_y = 399 \text{ MPa} \end{cases} \quad (9)$$

It is seen that the reaction force is not a function of the penetration. This does not correspond to observations from quasi-static tests where the reaction force is a continuously increasing function of the penetration, see Figure 1.

Atkins (1988), [6], presents the scaling laws for bodies undergoing simultaneous plastic flow and crack propagation. Assuming rigid-plastic behaviour the energy scaling for prototype (p) and model (m) follows

$$\frac{W_p}{W_m} = \frac{\lambda^2(\lambda\xi + 1)}{(\xi + 1)} \quad (10)$$

where λ is the geometrical scale factor and ξ is the ratio between the rate of energy dissipation in the far field deformation and the rate of energy in the crack tip zone in model scale.

It is argued that fracture is a governing parameter for the plate cutting process, see also [8]. By analysing the results of Jones, Jouri and Birch, [10], [11], and Lu and Calladine, [12], Atkins made an attempt to separate the energy dissipating mechanisms and find the variance of ξ . Several difficulties were encountered though, and it seems that more experimental data would be needed before an approach of scaling is applicable to practical problems. It should be noted that in the work outlined below (for example Lu and Calladine, [12]) all energy is assumed to be dissipated in plastic flow so the scaling of energy, W_p/W_m , follows λ^3 corresponding to $\xi = \infty$.

Lu and Calladine (1990), [12], performed quasi-static cutting tests with 35 case hardened mild steel plates ($\alpha = 0^\circ, 10^\circ, 20^\circ$ and $2\theta = 20^\circ, 40^\circ$) and by using Buckingham's dimensional analysis they found the formula

$$W = C_{1.3} \sigma_y l^{1.3} t^{1.7} \quad \text{for } 5 < l/t < 150 \quad (11)$$

The corresponding force becomes

$$F = 1.3 C_{1.3} \sigma_y l^{0.3} t^{1.7} \quad \text{for } 5 < l/t < 150 \quad (12)$$

where $C_{1.3}$ is a purely empirical constant which depends on the cutting conditions such as wedge and tilt angles. Unlike Eqs. (2-8), the formula by Lu and Calladine is seen to be dimensionally consistent.

As it will be discussed in more detail later, Lu and Calladine made valuable contributions to the field by discussing the effect of friction, fracture and dynamics. Also, [12] presents the first attempt to investigate the effect of a finite shoulder width and thus the phase of steady state cutting.

Wierzbicki and Thomas (1993), [32], have developed an analytical model for prediction of the cutting force and derived an expression, identical in form and characteristics to the results presented by Lu and Calladine:

$$F = 3.28 \sigma_0 \mu^{0.4} l^{0.4} t^{1.6} \bar{\delta}_t^{0.2} \quad (13)$$

for a coefficient of friction, $0.1 < \mu < 0.4$ and a wedge angle, $10^\circ < \theta < 30^\circ$. It is the first publication where a coefficient of friction, μ , and a fracture parameter, $\bar{\delta}_t$, enters the expression explicitly.

Paik (1994,95), [18] and [19], has investigated the cutting response of stiffened steel plates. In [18], the analysis is based on dimensional analysis, fifty cutting experiments, and the hypothesis that longitudinal stiffeners can be included by using an area equivalent plate thickness, t_{eq} . By applying a least-square best fit to the experimental data, Paik expressed the energy absorption and cutting force as

$$W = C_{1.5} C_f \sigma_0 t_{eq}^{1.5} l^{1.5} \quad (14)$$

$$F = 1.5 C_{1.5} C_f \sigma_0 t_{eq}^{1.5} l^{0.5} \quad (15)$$

with the coefficient, $C_{1.5}$, being a function of wedge angle alone:

$$C_{1.5} = 1.112 - 1.156\theta + 3.760\theta^2 \quad (16)$$

and the dynamic correction factor, C_f , expressed as a function of the initial impact velocity, V , as

$$C_f = 1.0 - 0.042V + 0.001V^2 \quad (17)$$

In accord with Lu and Calladine, [12], Paik considers inertia effects to be negligible whereas strain rate effects tend to raise the load level and dynamic effects on friction tend to lower the load. In all, it is interesting to note that C_f is found to be a decreasing function of the impact velocity, for example $C_f = 1$ at $V = 0 \text{ m/s}$ and $C_f = 0.67$ at $V = 8 \text{ m/s}$. It should be noted that the correction factor, C_f is found from the drop hammer results of Jones and Jouri, [10]. In drop hammer tests the velocity decreases from V to zero but this change in velocity has not been taken into account in the derivation of C_f so Eq. (17) cannot necessarily be used in Eq. (15) for an instantaneous velocity.

In [19], the effect of transverse stiffeners is discussed and it is proposed that these should be included in the analysis in a discrete manner (as opposed to the continuous 'smearing' technique proposed for longitudinal members).

Wierzbicki (1994), [30], developed a closed form solution for the reaction force when a concertina tearing deformation mode (see Figure 1) develops. By assuming a kinematically admissible deformation mode and applying the principle of virtual work, the mean resistance force is found to be

$$F = 2\sqrt{3}\sigma_0 t^2 \left[\frac{2}{\sqrt{3}} \left(\frac{b}{t} \right)^{1/3} + \frac{\delta_t}{t} \right] \quad (18)$$

Astrup (1994), [5], conducted experiments ($2\theta = 60^\circ$, $\alpha = 10^\circ$, $2B = 250 \text{ mm}$, $t = 15, 20 \text{ mm}$) to investigate the cutting of thick plates with a wedge of finite width. The observed failure modes were quite complex in that both stable plate

cutting and concertina tearing modes were seen. It is noted in [5] that the measured reaction force was generally 60 - 75 % higher than that predicted by the formula of Lu and Calladine. It is argued that this difference is due to strain rate effects and frictional effects. Another reason is that the test wedge had a finite shoulder width whereas the formula of Lu and Calladine is based on the initial penetration. This means that after the wedge shoulders have entered the plate a cutting mode different to that observed in Lu and Calladine's experiments will develop. Large scours were observed on the cut specimens and it is argued that a coefficient of friction equal to 0.5 - 0.55 seems reasonable. By comparing the energy absorption in the *initial* deformation with the drop hammer tests of Jones et al, [10], it is found that there are no significant size effects in the cutting phenomenon.

Zheng and Wierzbicki (1995), [35], have developed a closed form solution for the reaction force after steady state is reached. It is assumed that the cutting process consists of three different energy absorbing mechanisms:

1. ductile fracture in a small zone in front of the wedge
2. bending of the plate in moving hinge lines
3. membrane deformation

A suitable model was postulated for the kinematics with one free parameter, the so-called plate rolling radius, R . The rate of energy dissipation in each of the three mechanisms listed above, is expressed as a function of this rolling-radius. In compliance with the idea of a least upper bound, the total resistance is found by minimizing the total resistance force with respect to the rolling radius.

The resistance force is given by

$$F = \frac{\sigma_0 t^2}{4} \left[2 \frac{B+R}{R} + 1.27 \frac{R}{t} \cos\theta + 1.28\theta^2 \frac{\cos(\theta/2)}{\cos\theta} \frac{(R+B)^2}{Rt} \right] (1 + \mu \cot\theta) \quad (19)$$

with the rolling radius,

$$R = B \sqrt{\frac{2(t/B) + 1.28\theta^2 \cos(\theta/2)/\cos\theta}{1.27\cos\theta + 1.28\theta^2 \cos(\theta/2)/\cos\theta}} \quad (20)$$

Ohtsubo and Wang (1995), [17] presents an analysis method somewhat similar to that of Wierzbicki and Thomas, [32]. A kinematic model is proposed and the energy dissipation of the plastic flow in the tip zone and in rolling hinge lines is calculated.

The expression for the cutting force becomes

$$F = 1.51 \sigma_0 t^{1.5} l^{0.5} \sin^{0.5}(\theta) \left(1 + \frac{\mu}{\tan \theta} \right) \quad (21)$$

4 Comparison of Formulas for Initiation Cutting

Figure 3 shows a comparison of the proposed formulas for the initial cutting together with the results of one of the experiments reported in [12]. The input data for the calculations are given in Table 1.

Table 1: Main data for comparison example

Plate thickness, t	0.9 mm
Wedge angle, 2θ	40°
Flow stress, $\sigma_y = \sigma_0$	255 MPa
Coefficient of friction, μ	0.3
Nondimensional crack opening displacement, $\bar{\delta}_t$	1.
Length of penetration, l	0-80 mm

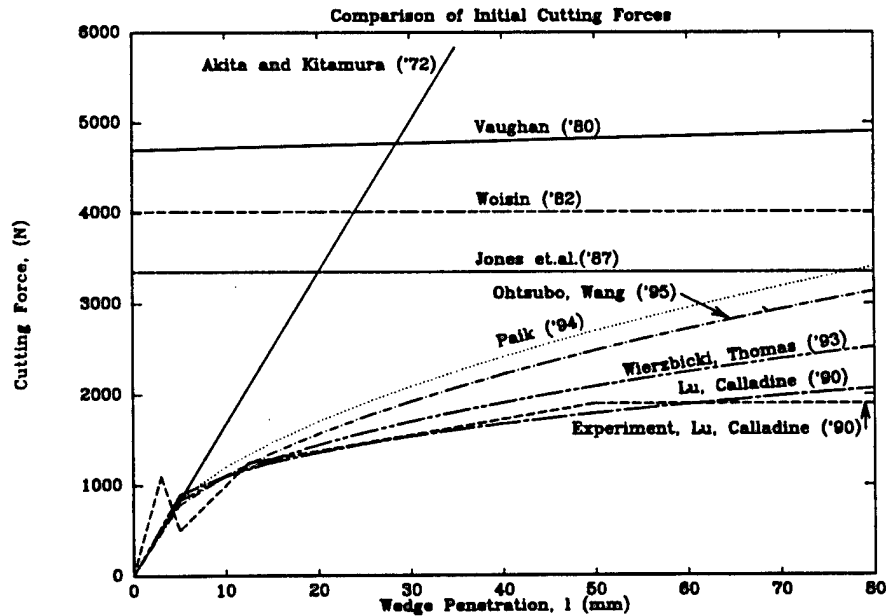


Figure 3: Comparison of several formulas proposed in the literature with the result of one of Lu and Calladine's, [12], experiments

It is seen that overall there is a significant difference between the formulas. However, the latest formulas proposed by Lu and Calladine, Wierzbicki and Thomas, Paik, and Ohtsubo and Wang show a similar trend which corresponds quite well with the experimental result.

5 Prediction of Steady State Cutting Force

Lu and Calladine, [12] and Paik and Lee, [19], Astrup, [5], Yahiaoui et.al., [34] and Zheng and Wierzbicki, [35] performed tests with wedges of finite width but the only formula in which the wedge width enters explicitly is due to Zheng and Wierzbicki, [35]. Based on the argument that the rock size in grounding is usually large, Paik and Lee omit an analysis of the effect of wedge width. Although many rocks are undoubtedly large it is even important to analyse the consequences of reef shaped rocks, for example like the one that caused the catastrophic damage to Exxon Valdez. The experimental results of Lu and Calladine, [12], Yahiaoui et.al., [34] and Astrup, [5] are summarized in Table 2. In all of the reported tests, the wedge angle was inclined an angle $\alpha = 10^\circ$ in order to obtain the clean curling cutting mode shown in Figure 1.

Lu and Calladine, [12], observed that the main features of the physical behaviour and of the resulting load-deformation curve are of the same kind as in the initiation cutting until the upper edge of the plate reaches the shoulder of the wedge whereupon the resisting force remains practically constant as the wedge penetrates further. On the other hand Thomas, [26], found that the initiation phase goes beyond the point where the shoulders enter the plate - it is rather twice as long as suggested by Lu and Calladine. Based on these observations it seems realistic to use the proposed formulas for initiation cutting up to a certain point of penetration and assume that the load level is retained from this point of penetration throughout the rest of the deformation. This penetration, l , is then

$$l = \kappa_{ini} \frac{2B}{\tan \theta} \quad (22)$$

with $\kappa_{ini} = 1 - 2$. Table 3 below presents results of this approach, i.e. the penetration, l , of Eq. (22) is used in the formulas for initiation cutting, Eqs. (12, 13, 15, 21). Corresponding to the findings of Lu and Calladine and Thomas the value of κ_{ini} is taken as respectively 1 and 2 in Table 3. Clearly, the approach is approximate because the deformation pattern shifts from a mode of cutting and curling in the initiation mode to a mode of cutting, curling and membrane deformation in the steady state phase. The particular deformation mode of the steady state phase was considered by Zheng and Wierzbicki, [35], who derived Eq. (19).

The input values to the formulas used in Table 3 (B , t etc.) are taken corresponding to the experimental results presented in Table 2. The coefficient of friction is assumed to be $\mu=0.3$.

Table 2: Experimental results for steady state cutting. In all experiments the wedge was inclined an angle, $\alpha = 10^\circ$.

Experiments by	σ_0 (<i>Mpa</i>)	θ ($^\circ$)	$2B$ (<i>mm</i>)	t (<i>mm</i>)	F (<i>kN</i>)
1. Lu & Calladine, [12]	272	10	10	1.6	6.0
2. Yahiaoui et.al., [34]	270	45	19	0.75	2.5
3. Astrup, [5]	526	30	250	20	2250

Table 3: Theoretical prediction of steady state cutting for the experimental results of Table 2. The following abbreviations are used for the formulas used: L/C: Lu and Calladine, W/T: Wierzbicki and Thomas, O/W: Ohtsubo and Wang, Z/W: Zheng and Wierzbicki.

Theoretical Prediction, $\kappa_{ini} = 1$

Experiments by	L/C Eq. (12) (<i>kN</i>)	W/T Eq. (13) (<i>kN</i>)	Paik Eq. (15) (<i>kN</i>)	O/W Eq. (21) (<i>kN</i>)	Z/W Eq. (19) (<i>kN</i>)
1. Lu & Calladine, [12]	5.81	5.88	6.37	7.05	3.81
2. Yahiaoui et.al., [34]	1.14	1.12	2.89	1.26	3.28
3. Astrup, [5]	1514	1459	2258	1588	1580

Theoretical Prediction, $\kappa_{ini} = 2$

Experiments by	L/C Eq. (12) (<i>kN</i>)	W/T Eq. (13) (<i>kN</i>)	Paik Eq. (15) (<i>kN</i>)	O/W Eq. (21) (<i>kN</i>)	
1. Lu & Calladine, [12]	7.15	7.76	9.01	9.97	
2. Yahiaoui et.al., [34]	1.41	1.48	4.08	1.78	
3. Astrup, [5]	1864	1925	3193	2246	

As in Figure 3, the difference between various theoretical predictions is seen to be quite remarkable. It is interesting to note that the formula of Paik, Eq. (15), corresponds well with all of the observed results when $\kappa_{ini} = 1$ is used. It should be noted that if the coefficient of friction is increased to $\mu = 0.55$ as proposed by Astrup, [5], the theoretical prediction for Astrup's results of Ohtsubo/Wang ($\kappa_{ini} = 1$) and Zheng/Wierzbicki rise from 1588 kN, 1580 kN to 2041 kN and 2030 kN respectively. These results are seen to correspond quite well to the experimental value of 2250 kN.

6 Problem Statement and Basic Idea of Model

The remainder of the present paper is concerned with derivation and verification of a theoretical model for analysis of steady state cutting of a metal plate by a prismatic wedge.

The ultimate goal of these studies is to be able to analyse an assembled ship bottom structure which is significantly more complex than just a bare plate. The approach taken here is to postulate the displacement and strain fields and then, by use of the principle of virtual work, find the resisting force of the plate. The advantage of this type of approach over a purely experimental one is that once the major deformation and energy dissipating mechanisms are identified, it is possible to consistently add stiffeners to the plate and find the energy dissipation and resisting force of the total assembled structure, see [22]. To derive general expressions for the resistance of such a hull bottom assembly from experimental data alone seems to be an overwhelming task. The idea of smearing longitudinal stiffeners presented by Paik, [18], is promising but for use in design of complex structures it would seem unable to capture all the effects of structural details.

The basic idea of the present approach is illustrated below. A prismatic wedge cuts through a ductile plate which is assumed to deform as shown in Figure 4. Since the process is considered to be in steady state this picture of the deformation does not change in time.

There are three energy dissipating mechanisms in the considered deformation mode:

- Moving hinge lines
- Membrane deformation of the plate
- Material separation in the crack tip zone

In reality, there is no clear distinction between these mechanisms but it has been shown in several areas of sheet metal deformation and fracture that such a separation of energy absorbing mechanisms often adequately represents the observed behaviour leading to great simplifications of the theoretical analysis, see e.g. Atkins, [6], Alexander, [4], and Wierzbicki and Abramowicz, [31].

It is worth to note that the material flows *through* the deformation zone shown in Figure 4 and 5 in contrast to many structural problems where the volume of deformation is stationary within the structure. The present deformation pattern resembles one of fluid flow around a blunt body. Similar to most of fluid flow solutions an Eulerian description of motion is used. As illustrated in Figure 4 the material flow is described in a (ξ, η) coordinate system where ξ follows the streamlines and η is in the perpendicular direction. As a material element moves along a streamline it experiences bending as it passes the OP -line followed by a continuous increasing

shear deformation as it moves towards the wedge shoulder. If the material element is close to the centerline it experiences an additional tensile deformation in the perpendicular (η -) direction as it passes the zone of plate separation in front of the wedge.

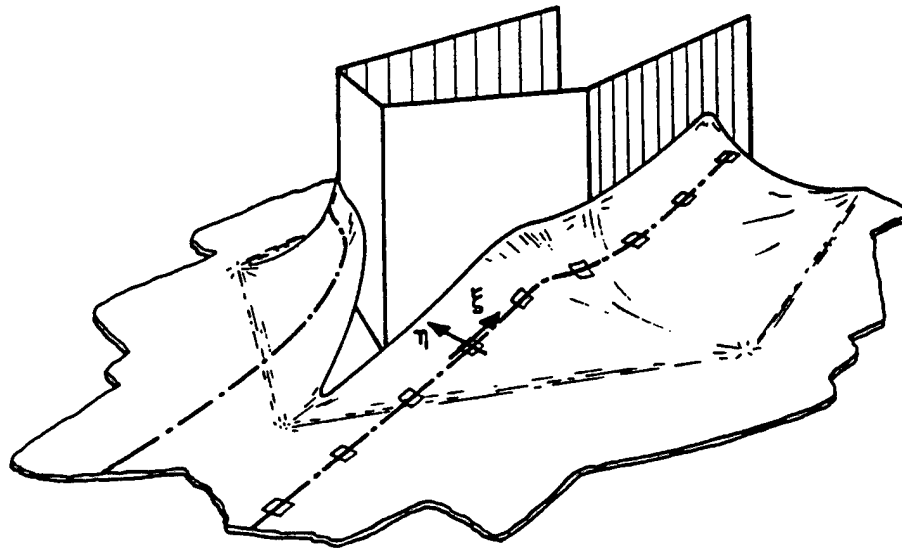


Figure 4: Assumed mode of deformation

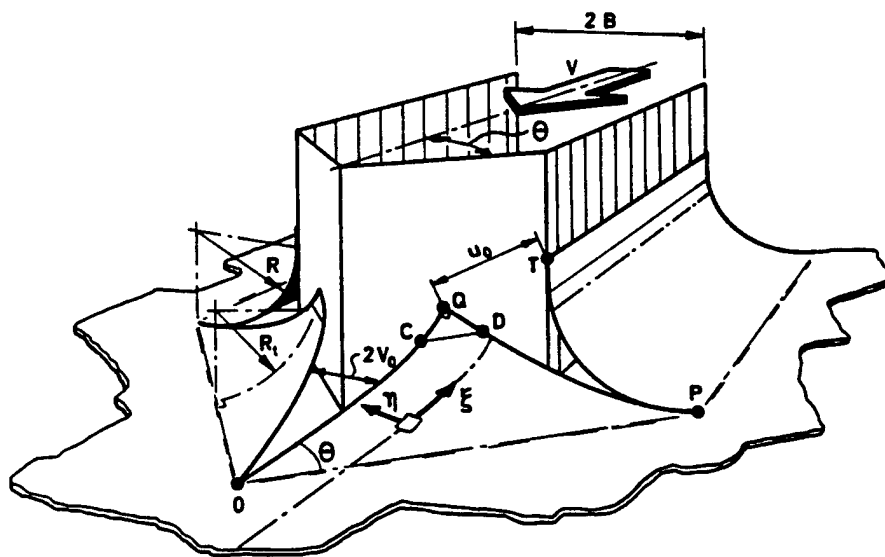


Figure 5: Necessary straining illustrated by gap width

Moving hinge lines.

The moving hinge line OP in Figure 4 changes the curvature of the undisturbed plate from 0 to $1/R_t$ and the hinge line CD reverts the curvature back to zero so that there is a straight plate flap conforming to the wedge sides. The rolling radius, R_t is kept as a variable in the formulation and taken as the value which gives the lowest rate of energy dissipation. In the wake of the wedge, the rolling radius is $R = R_t/\cos\theta$. The assumed mode of deformation with plane flaps conforming to the wedge corresponds well to the experimental observations of Astrup, [5], Yahiaoui, [34], Rodd and MacCampbell, [21], and Lu and Calladine, [12].

Membrane deformation.

Figure 5 shows the geometry that is seen if the plate was cut at the center line and along the edges PT, PQ and folded without membrane deformation of the plate (this could be done with a piece of paper and a pair of scissors). Then, the gaps between the plate edges PT and PQ are indicative of the amount of membrane straining necessary for material continuity during the cutting process. In the large scale tests of Astrup, [5], a few lateral cracks were also observed (along line PT in Figure 5) but for thin plates this is not seen.

The necessary straining can be accommodated by an infinite number of possible strain fields. The actual strain rate field is the one that minimizes the instantaneous rate of energy dissipation of material flow, fracture and friction. Little is published about the strain field in steady state cutting but useful information can be obtained from inspection of cut specimens. The cut plate will transmit direct tensile (or compressive) stresses in the ξ direction, and likewise tensile strains will develop. This can be deduced from Figure 1 for the curled cut where the deformed plate is seen to be buckled. During the cutting process, the longitudinal plate fibres are stretched in the deforming zone at the wedge front, and instead of recompressing back to the original length leaving straight flaps in the wake, the plate buckles. As mentioned, however, the plating of a ship structure has stiffeners attached to it and the presence of longitudinal stiffeners which are often quite substantial tend to prevent the development of tensile deformation in the longitudinal direction of the hull structure when the deformation is large enough for the longitudinals to be involved.

The hull plating will rather deform in a mode where longitudinal fibres are sheared with respect to each other. Such a deformation mode of predominantly shear in the (ξ, η) coordinate system (see Figure 4) was reported by Turgeon, [27], for small scale tests without fracture and by Rodd and MacCampbell, [21] for large scale grounding tests with a double bottom being deformed by a conical rock. Figure 6 shows the failure mode of the test reported by Rodd and MacCampbell. Significant shear bands are observed in the bottom plating.



Figure 6: Failure mode of ship bottom observed in NSW Test no 1, [21], (worm's eye view)

Also, in the large scale cutting tests of Astrup, [5], the deformed plate flaps were seen to be nearly plane, indicating shear rather than tensile deformation. Based on these observations, the present formulation for the membrane deformation rests on the assumption that the in-plane strains in the far field are all shear strains. It is recognized that this is not always the case but as it will be argued later this assumption greatly simplifies the analysis. Since longitudinal fibres are not stretched, the present model also provides a realistic basic deformation pattern model for the case of a longitudinally stiffened plate.

Near tip plate separation. Although the process of the near tip crack zone has been considered explicitly by several authors no-one has yet applied a theory to the problem of plate cutting which covers in detail and generality the material splitting process. Lu and Calladine, [14], argue that the cutting process can be described at a sufficient level of accuracy with the flow stress as the only material parameter. A discussion on this topic is given by Atkins and Lu and Calladine in [8] and [13].

Stronge et.al., [24], [25], performed an experimental and theoretical study on the problem of tube splitting and concluded that the relative contribution of the tearing energy to the total energy dissipation is small. This supports those of the presented analyses of Section 3 where fracture parameters are not included. Several authors leave material fracture parameters out of the analysis based on the observation that the crack tip stays right at the wedge tip so that the separation process is one of plastic flow rather than fracture. For highly ductile specimens as those thin plates of mild steel used in several of the reported model tests being cut by a sharp wedge it is true and not too surprising that the plate separates at the cutting edge. However, for less ductile specimens - for example thick hull plating, [5], or other types of material, [12] - or blunt nosed wedges, [21], [15], the crack was observed to run ahead of the wedge and a general theory should therefore cover this situation and thus consider the fracture toughness of the material.

In the large scale double bottom grounding tests reported in [21], an unstable crack was seen to unzip a part of the structure in front of the wedge. A stable crack in the outer bottom propagated with the penetration of the rock but at a certain point of penetration the crack suddenly propagated through a transverse bulkhead far into the inner hull plating. To capture this complex type of behaviour would require very detailed elasto-plastic calculations. Theoretically, the finite element method would be applicable but for practical use in design it is too labour intensive so the present approach is based on a less accurate rigid-plastic analysis.

The question of whether fracture should be included or not is handled in our mathematical model by choosing between purely plastic flow or fracture depending on which of the two alternative modes gives the lowest energy dissipation. This corresponds to normal fracture criteria for ductile materials, see for example Atkins, [7].

7 Basic Equations for Plasticity, Fracture and Friction

When external loads are applied to a deformable structure, the power of these loads must be equal to the incremental energy stored elastically or dissipated in the structure. Assuming a rigid-plastic structure, no elastic energy can be stored and the power of the external loads thus equals the rate of energy dissipated by plastic deformations, fracture and frictional effects on the structure surface. This can be expressed as;

$$F \cdot V = \dot{E}_p + \dot{E}_c + \dot{E}_f = F_{P,c} \cdot V + \int_S p \mu V_{rel} dS \quad (23)$$

where

- F is the resisting force of the structure in the direction of V
 V is the relative velocity between ship and rock
 \dot{E}_p is the rate of plastic energy dissipation.
 \dot{E}_c is the rate of energy dissipation in the crack tip zone.
 \dot{E}_f is the rate of energy dissipated by frictional forces on the surface of the structure
 $F_{P,c}$ is the so-called plastic resistance which here includes both plasticity and fracture
 μ is the Coulomb coefficient of friction
 p is the normal pressure on the rock from the plate element dS
 S denotes the contact area between rock and plate
 V_{rel} is the relative velocity between rock and plate element, dS

In the present model, the internal energy dissipation and frictional effects are considered separately without coupling. Kinematically admissible displacement fields are constructed according to Figure 5 and from the assumed deformation fields, the corresponding rates of energies, \dot{E}_p , \dot{E}_c and \dot{E}_f are calculated. The assumed kinematics of the deformation has one free parameter, the plate rolling radius R , and it is postulated that the actual deformation mode is the one that minimizes the total rate of energy dissipation.

Supporting our approach, Atkins, [6], [7], has shown that the rigid-plastic approximations to tearing problems often adequately represent observed behaviour when fracture is accompanied by, or preceded by, extensive plastic flow. Examples (other than plate cutting) which include both fracture and far field deformation are tensile tearing of a deep double-edge notched (DEN) specimens and trouser tearing. The basic idea of the methods for finding the specific work of fracture, G_c , is to perform experiments to determine all parameters but \dot{E}_c in Eq. (23). Then, from \dot{E}_c and the kinematics of the specific problem, G_c can be determined. As mentioned, the distinction between a crack tip zone and the far field presented by Atkins is also applied in the present analysis.

Plastic Energy Dissipation in Far Field

With rigid-plastic material obeying von Mises yield criterion the plane stress yield condition can be written as;

$$F = \sigma_{xx}^2 + \sigma_{yy}^2 + \sigma_{xy}^2 + 3\sigma_0^2 - \sigma_0^2 = 0 \quad (24)$$

where σ_0 is the uniaxial yield stress. For real construction materials σ_0 is a function of strain history and strain rate. Here, σ_0 is considered constant and equal to an average flow stress for the considered process. Thus, the flow stress is higher than the initial yield stress but lower than the ultimate stress, σ_u . Following Abramowicz and Wierzbicki, [1], an estimate of the energy equivalent flow stress is $\sigma_0 = 0.92 \cdot \sigma_u$.

For a deforming plate of area S , the rate of internal energy dissipation can be expressed as;

$$\dot{E}_P = \dot{E}_m + \dot{E}_b = \int_S N_{\alpha\beta} \dot{\epsilon}_{\alpha\beta} dS + \int_S M_{\alpha\beta} \dot{\kappa}_{\alpha\beta} dS \quad (25)$$

where $N_{\alpha\beta}$, $M_{\alpha\beta}$ are components of the membrane force and bending moment tensors, and $\dot{\epsilon}_{\alpha\beta}$, $\dot{\kappa}_{\alpha\beta}$ are the corresponding generalized strain and curvature rates calculated in the deformed configuration. The two terms in the above equation represent the rate of membrane and bending energy dissipation, \dot{E}_m and \dot{E}_b respectively. In general $N_{\alpha\beta}$ and $M_{\alpha\beta}$ in Eq. (25) are related by the yield condition, Eq. (24). However, this interaction between moments and membrane forces is very cumbersome to handle analytically and it is neglected in the present analysis.

It is assumed that the deformation zone consists of a series of discrete moving hinge lines and a number of deforming plate elements. Taking the rock to be stationary, the hull deformation can be thought of as a steady-state flow of hull material past the rock. Since the material moves *through* a deformation zone, it is convenient to introduce a spatial-Eulerian coordinate system (ξ, η) , where ξ is directed along the material stream lines and η is perpendicular to them, see Figure 4 and Figure 5.

The material derivative of a given quantity $[]$ is, in general, composed of two parts;

$$\frac{D[]}{Dt} = \frac{\partial[]}{\partial t} + \nabla[] \cdot \mathbf{V}_\alpha \quad (26)$$

where the components of the gradient vector, ∇ , and velocity vector, \mathbf{V}_α , are;

$$\nabla = \begin{bmatrix} \partial/\partial\xi \\ \partial/\partial\eta \end{bmatrix} \quad \mathbf{V}_\alpha = \begin{bmatrix} \frac{\partial\xi}{\partial t} \\ \frac{\partial\eta}{\partial t} \end{bmatrix} \quad (27)$$

For a steady-state process the time change of any quantity, $[]$, at a given location is zero. Therefore, the first term in Eq. (26) vanishes. Furthermore, since material points follow the stream lines with a velocity of V , $\partial\eta/\partial t = 0$ and $\partial\xi/\partial t = V$. Therefore, for steady state flow Eq. (26) reduces to

$$\frac{D[]}{Dt} = V \frac{\partial[]}{\partial\xi} \quad (28)$$

The rate of membrane energy dissipation in Eq. (25) for a plate strip of width $d\eta$ can be expressed as

$$d\dot{E}_m = t \int_{\xi_a}^{\xi_b} \sigma_{\alpha\beta} \dot{\epsilon}_{\alpha\beta} d\xi d\eta \quad (29)$$

where (ξ_a, ξ_b) are boundaries of the local plastically deforming zone. By using the yield condition, Eq. (24), and the associate flow rule, Eq. (29) can be written as

$$d\dot{E}_m = \frac{2}{\sqrt{3}} \sigma_0 t \int_{\xi_a}^{\xi_b} \sqrt{\dot{\epsilon}_{\xi\xi}^2 + \dot{\epsilon}_{\eta\eta}^2 + \dot{\epsilon}_{\xi\xi}\dot{\epsilon}_{\eta\eta} + \dot{\epsilon}_{\xi\eta}^2} d\xi d\eta \quad (30)$$

For a steady state process Eq. (28) can be used to transform the timely strain derivatives of Eq. (30) into space derivatives. Then, by assuming proportional strain paths and performing the integration over the length of the deformation zone from ξ_a to ξ_b , the expression for the rate of membrane energy dissipation becomes

$$d\dot{E}_m = \sigma_0 V t [\epsilon_{eq}] d\eta \quad (31)$$

where $[\epsilon_{eq}]$ is the change in equivalent strain of a material element from entering to leaving the deformation zone. The equivalent strain is given by

$$\epsilon_{eq} = \frac{2}{\sqrt{3}} \sqrt{\epsilon_{\xi\xi}^2 + \epsilon_{\eta\eta}^2 + \epsilon_{\xi\xi}\epsilon_{\eta\eta} + \epsilon_{\xi\eta}^2} \quad (32)$$

Using Eq. (28) it can be shown, [23], that the rate of bending energy dissipation, $d\dot{E}_b$, for a plate strip of width $d\eta$ is

$$d\dot{E}_b = V_n M_0 [\kappa_{nn}] dL = V M_0 [\kappa_{nn}] d\eta \quad (33)$$

where dL is the length of the hinge line, $[\kappa_{nn}]$ is the jump in curvature over a hinge line, V_n the normal velocity of the hinge line, and M_0 is the plane strain fully plastic bending moment per unit length;

$$M_0 = \frac{2}{\sqrt{3}} \frac{\sigma_0 t^2}{4} \quad (34)$$

Expression Eq. (33) should be integrated over all hinge lines appearing in the given problem.

Energy Dissipation in Crack Tip Zone

As mentioned in Section 6 several different views on how to treat the tip zone process theoretically have been presented.

One approach is to use the ductile fracture toughness, G_c , giving a rate of energy dissipation in the tip zone of

$$\dot{E}_c = G_c \dot{A} = G_c t V \quad (35)$$

where $\dot{A} = t V$ is the rate by which new area is generated.

One disadvantage with use of Eq. (35) is that G_c is highly dependent on the actual strain history up to the point of fracture. For mild steel Atkins, [7], reports values of G_c ranging from 200-1000 kJ/m^2 depending on the fracture mode so carefully planned experiments have to be carried out to determine the actual values of G_c .

For very ductile materials or narrow sharp wedges the plate does not separate in a true fracture mode but the material is rather forced to flow around the wedge making the use of a fracture toughness parameter questionable. The rate of energy dissipation for this alternative mode of purely plastic flow is an integral over the volume of the tip zone;

$$\dot{E}_c = \int_S \sigma_0 \dot{\epsilon}_{eq} t dS_{tip\ zone} \quad (36)$$

The choice of deformation mode in the present formulation is based on the standard fracture mechanics approach of choosing the deformation mode (Eq. (35) or Eq. (36)) that gives the lowest rate of energy dissipation.

8 Energy Dissipation in Plasticity and Fracture

The basics for the development of the expressions for the rate of energy dissipation in the tip zone and in the far field has been described in Sections 6 and 7. The final expressions are derived below. The deformation in the far field is divided into membrane deformation and bending.

Tip zone

The energy dissipation rate for this process is given by Eqs. (35) and (36). In order to evaluate the integral of Eq. (36) we assume that the strain field is dominated by tensile strains in the lateral (η) direction. This is not fully consistent with the assumption that the PT-PQ gap in Figure 5 is accomodated by shear strains alone but estimates indicate that the effect of shear in the tip zone is small. Indeed, due to symmetry, the shear must be zero at the center line.

Following Eq. (36) it is sufficient to consider the total equivalent strain of the material in the wake of the cutting edge. With $\epsilon_{\xi\xi} = \epsilon_{\xi\eta} = 0$, the final expression is found as an integral over the width of the plastic zone in the wake of the cutting edge;

$$\dot{E}_c = 2 \sigma_0 V t \int [\epsilon_{eq}] d\eta \quad (37)$$

$$= 2 \sigma_0 V t \int_{\eta_l}^{\eta_u} \left[\frac{2}{\sqrt{3}} \epsilon_{\eta\eta} \right] d\eta \quad (38)$$

$$= \frac{4}{\sqrt{3}} \sigma_0 V t v_0 \quad (39)$$

where η_l and η_u denote lower and upper boundaries for the strain field in the lateral direction on one side of the center line and v_0 is half of the maximum gap width between the plate curls in front of the wedge.

In Appendix A it is shown that

$$v_0 \approx 0.16 R \cos^2 \theta (1 + 0.55 \theta^2) \quad (40)$$

giving the final expression as

$$\dot{E}_c = \frac{0.64}{\sqrt{3}} \sigma_0 V t R \cos^2 \theta (1 + 0.55 \theta^2) \quad (41)$$

Far field, membrane deformation

As discussed in Section 6 we assume that material over the PT-PQ gap shown in Figure 5 is accommodated by shear strains; the plate deforms as a bundle of longitudinal inextensible chords.

From Eq. (31) the rate of energy dissipation is found as an integral of the equivalent strain over the width of the plastic zone in the wake of the wedge, for example along the PT-line, see Figure 5;

$$\dot{E}_m = 2 \sigma_0 V t \int_{\eta_P}^{\eta_T} \left[\frac{2}{\sqrt{3}} \varepsilon_{\xi\eta} \right] d\eta \quad (42)$$

$$= 2 \sigma_0 V t \int_{\eta_P}^{\eta_T} \left[\frac{2}{\sqrt{3}} \frac{1}{2} \left(\frac{\partial u}{\partial \eta} + \frac{\partial v}{\partial \xi} \right) \right] d\eta \quad (43)$$

$$= \frac{2}{\sqrt{3}} \sigma_0 V t [u_P - u_T] = \frac{2}{\sqrt{3}} \sigma_0 V t u_0 \quad (44)$$

where u_0 is the distance between Q and T in Figure 5. In Appendix A it is shown that $u_0 \approx B \theta$ so the final expression becomes

$$\dot{E}_m = \frac{2}{\sqrt{3}} \sigma_0 V t B \theta \quad (45)$$

Far field, bending

As illustrated by Figure 5, the steady state cutting process involves several areas of bending. The relevant bending radii are the radius at the side of the wedge, R , and the radius in front of the wedge, R_t .

For point T to be at the shoulder wedge, the relation between these radii becomes

$$R_t = R \cos \theta \quad (46)$$

The three primary bending mechanisms are;

1. Initial curling; the curvature of the undeformed plate changes from 0 to $1/R_t$ (hinge line OP).

2. Hinge lines at wedge front; the plate is straightened out so that the curvature is reverted from $1/R_t$ back to 0 for a part of the plate (hinge line CD).
3. Bending around the wedge shoulder (line PT).

The hinge lines of point 2 and 3 above are in areas of high membrane straining so if the true interaction on the yield curve (Eq. (24)) was taken into account these hinges would give very limited resistance and they are therefore neglected in the following.

Since the jump in curvature is $[\kappa_{nn}] = 1/R_t = 1/R \cos\theta$ and the total width of the hinge line perpendicular to the direction of motion is $B + R$, the final expression for the rate of energy dissipation due to bending becomes (see Eq. (33))

$$\dot{E}_b = 2 \int V M_0 [\kappa_{nn}] d\eta \quad (47)$$

$$= \frac{\sigma_0 t^2 (B + R) V}{\sqrt{3} R \cos\theta} \quad (48)$$

9 Friction and Perpendicular Reaction

Friction is an important energy dissipating mechanism. Wierzbicki and Thomas, [32], and Ohtsubo and Wang, [17], use a factor for the effect of friction on the plate resistance;

$$g = \frac{F}{F_{P,c}} = 1 + \frac{\mu}{\tan\theta} \quad (49)$$

which indicates that friction increases the resistance by 52 % for the example of $\mu = 0.3$ and $\theta = 30^\circ$. In a study of tube splitting on a flat die, Stronge et.al., [25], use a friction factor of $g = 1/(1 - \mu)$. For the case of aluminium against a steel die they measure a coefficient of friction of $\mu = 0.56$ giving a friction factor of $g = 2.27$.

As indicated by Eq. (23) we assume a Coulomb type of friction where the frictional stress at the interface between plate and wedge is proportional to the normal pressure and it is shown below that the friction factor, g , can then be consistently derived from Eq. (23) and requirement of equilibrium. Noting that the surface, S , in Eq. (23) is plane and assuming that V_{rel} is constant over this surface gives the expression

$$F \cdot V = F_{P,c} \cdot V + 2 \mu N V_{rel} \quad (50)$$

where N is the normal force one of the front wedge sides.

The relative velocity, V_{rel} between the plate and the wedge at the contact area is assumed to be inclined an angle, ζ , from the plane of the plate, Figure 7. This angle depends on the rolling of the plate curls on the wedge and it can be shown that ζ must be bound by 0 and θ , $0 \leq \zeta \leq \theta$.

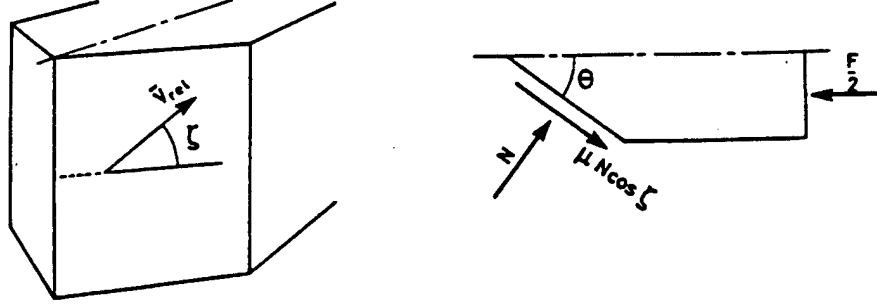


Figure 7: Definition of direction of relative velocity and free body diagram for wedge

Pippenger reports scouring traces on a $\theta = 45^\circ$ wedge to have $\zeta = 22.5^\circ$ and $\zeta = 17.9^\circ$ for experiments with $\alpha = 70^\circ$ and $\alpha = 45^\circ$ respectively. As an estimate we will thus use $\zeta = \theta/2$ which also makes sense intuitively.

The tangential friction force on the wedge is in the same direction as V_{rel} . Figure 7 shows the direction of V_{rel} and a free body diagram of the wedge.

It is seen that horizontal equilibrium can be expressed as

$$\frac{F}{2} = N \sin \theta + \mu N \cos \theta \cos \zeta \Rightarrow \quad (51)$$

$$N = \frac{F}{2(\sin \theta + \mu \cos \theta \cos \zeta)} \quad (52)$$

Inserting into Eq. (50) gives

$$F = F_{P,c} \left(1 - \frac{\mu}{\sin \theta + \mu \cos \theta \cos \zeta} \right)^{-1} \quad (53)$$

If we use consider the example of $\theta = \pi/2$ and $\zeta = \pi/2$, corresponding to the tube splitting process, the friction factor becomes $g = 1/(1 - \mu)$ which is the same expression as used by Stronge et.al., [25].

Inserting $\zeta = \theta/2$ in Eq. (52) gives the final expression for the friction factor;

$$g(\mu, \theta) = \frac{F}{F_{P,c}} = \left(1 - \frac{\mu}{\sin \theta + \mu \cos \theta \cos(\theta/2)} \right)^{-1} \quad (54)$$

It is seen that this expression is different from that used by Wierzbicki and Thomas, [32], and Ohtsubo and Wang, [17], Eq. (49). Eq. (49) gives lower values for g than our Eq. (54). At $\mu = 0.3$ and $\theta = 10^\circ, 30^\circ, 45^\circ$ the difference is 3.2 %, 9.0% and 13 % respectively.

The reaction force, F_V on the plate perpendicular to the direction of motion is the vertical component of the friction force μN :

$$\begin{aligned}
F_V &= -2\mu N \sin\zeta \\
&= F \frac{-2\mu \sin\zeta}{2(\sin\theta + \mu \cos\theta \cos\zeta)}
\end{aligned} \tag{55}$$

With $\zeta = \theta/2$ the ratio between the vertical reaction and the horizontal resistance thus becomes

$$k(\mu, \theta) = \frac{F_V}{F} = \frac{-\mu \sin(\theta/2)}{\sin\theta + \mu \cos\theta \cos(\theta/2)} \tag{56}$$

Using the approach described above, Pippenger, [20], has derived the relations corresponding to Eqs. (54, 56) for the case of a wedge which is inclined an angle, α (see Figure 2), from the direction perpendicular to the plate. Keeping the relations in their most general form but modifying Pippenger's expressions according to the assumption $V_{rel} = V$ we get;

$$\frac{F}{F_{P,c}} = g = \left(1 - \frac{\mu}{\sin\beta \sin\theta' + \mu (\cos\theta' \cos\zeta + \sin\zeta \cos\beta \sin\theta')}\right)^{-1} \tag{57}$$

$$\frac{F_V}{F} = k = \frac{\cos\beta - \mu \sin\zeta \sin\beta}{\sin\beta \sin\theta' + \mu (\cos\theta' \cos\zeta + \sin\zeta \sin\theta' \cos\beta)} \tag{58}$$

where θ' is the projected wedge angle and β is an intermediate value;

$$\theta' = \tan^{-1}(\tan\theta \cos\alpha) \tag{59}$$

$$\beta = \tan^{-1}(1/(\sin\theta' \tan\alpha)) \tag{60}$$

For $\alpha = 0$, it is seen that $\theta' = \theta$, $\beta = \pi/2$ and with $\zeta = \theta/2$ Eqs. (57, 58) reduce to Eqs. (54, 56) as expected.

Figure 8 shows the friction factor, g , as a function of wedge angle, θ , for $\mu = 0.3, 0.45, 0.6$ and $\alpha = 10^\circ$. Taking $\mu = 0.3$, $\alpha = 10^\circ$ and $\theta = 10^\circ, 30^\circ$ and 45° gives friction factors, g , of 2.8, 1.7 and 1.5, respectively indicating a very significant contribution of friction to the total plate resistance.

It should be noted that the effect of friction comes as a factor which is independent of the rolling radius, R . Likewise, the plastic/fracture resistance derived in the previous section was found to be independent of μ so the radius which minimizes the resistance force becomes independent of μ . This does probably not reflect reality¹ but at present there is not sufficient information available about this problem to improve the model in this respect.

¹For the tube splitting process, Stronge et.al., [25] use an expression for the plate rolling radius which is a strong function of μ

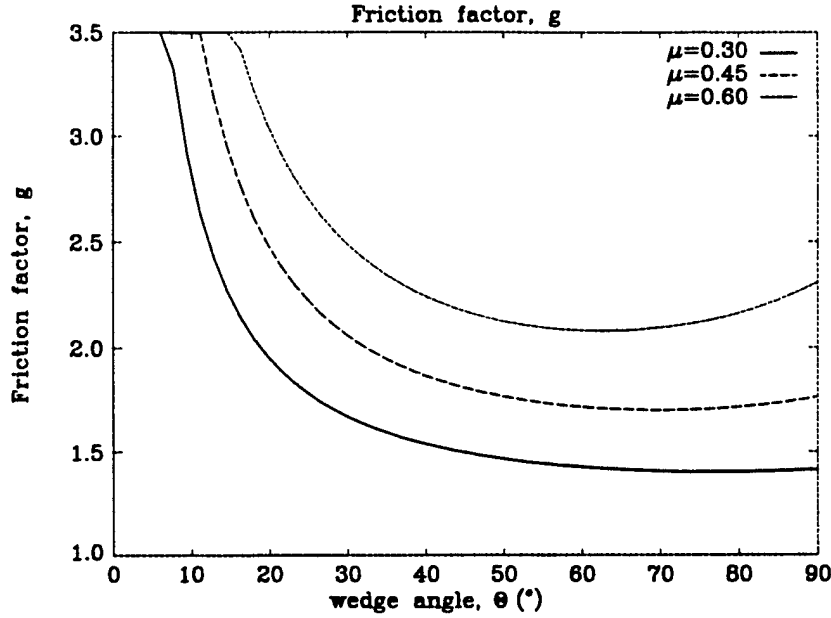


Figure 8: Friction factor, g . $\mu = 0.3, 0.45, 0.6$ and $\alpha = 10^\circ$.

Also, it should be noted that all of the contact pressure is assumed to be on the front plane sides of the wedge. However, the cornerpoint at the shoulders and the front tip might transmit some force. The effect of the shoulders will tend to increase the friction factor whereas the force on the front tip tends to lower it. For wedges with sharp edges the effect of these edge irregularities is believed to be small but for some types of idealized rocks, like for example the cone shaped rock analyzed by Rodd and MacCampbell, [21], these effects are dominating and prediction of g and k becomes a cumbersome task.

Figure 9 shows k as a function of wedge inclination angle, α , for $\theta = 45^\circ$ and $\mu = 0.3, 0.45, 0.6$. For small inclination angles, α , the vertical component of the frictional force dominates over the normal force, and the total vertical force is thus negative.

10 Total Reaction and Verification

The problem of two alternative deformation modes in the tip zone in front of the cutting edge was described in Sections 6 and 7. Below, the resistance force is derived for both alternative modes.

Combining Eqs. (23, 41, 45, 48 and 57) gives the plastic/fracture resistance force on the plate for the mode where the crack does not run ahead of the wedge;

$$F = g(\mu, \theta, \alpha) \frac{\dot{E}_c + \dot{E}_m + \dot{E}_b}{V}$$

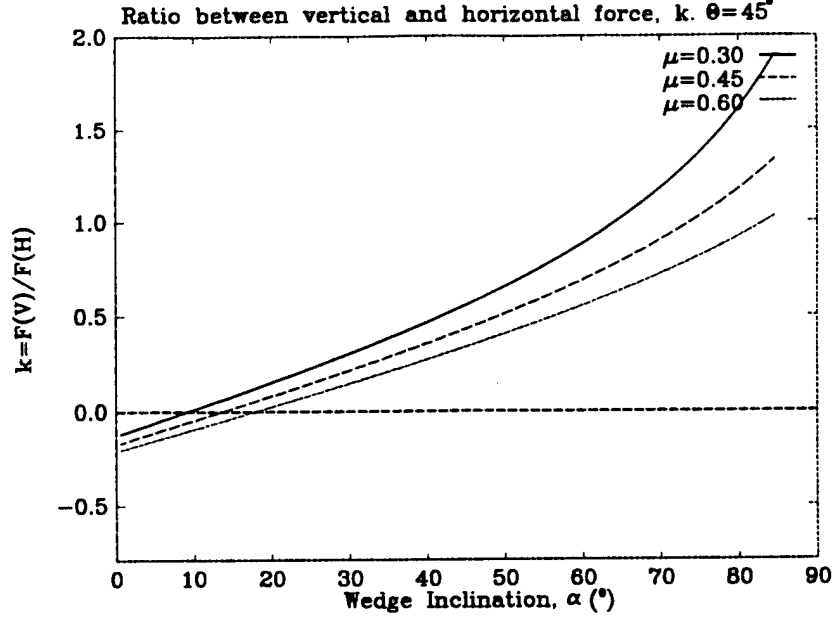


Figure 9: Ratio between vertical and horizontal force, k . $\theta = 45^\circ$ and $\mu = 0.3, 0.45, 0.6$.

$$= g(\mu, \theta, \alpha) \left\{ \frac{0.64}{\sqrt{3}} \sigma_0 t R \cos^2 \theta (1 + 0.55 \theta^2) + \right. \quad (61)$$

$$\left. \frac{2}{\sqrt{3}} \sigma_0 t B \theta + \frac{\sigma_0 t^2 (B + R)}{\sqrt{3} R \cos \theta} \right\}$$

$$R \leq B \frac{1}{\pi/2 - 1} = 1.75 B \quad (62)$$

The limit of R , Eq. (62), comes from the general kinematic requirement that the deformed plate flaps must be in contact with the wedge. The rolling radius, R , which gives the lowest resisting force becomes

$$R = \sqrt{\frac{B t}{0.64 (1 + 0.55 \theta^2) \cos^3 \theta}} \quad (63)$$

In the alternative crack tip deformation mode where the crack runs ahead of the wedge, the rate of energy dissipation in the tip zone is not a function of R and the total rate of energy dissipation does therefore not have a mathematical minimum as above; it is a monotonically decreasing function of the rolling radius. Using the maximum allowable rolling radius for kinematic consistency, Eq. (62), with Eqs. (23, 35, 45, 48 and 57) then gives the resistance force as

$$F = g(\mu, \theta, \alpha) \left\{ G_c t + \frac{2}{\sqrt{3}} \sigma_0 t B \theta + \frac{1.57 \sigma_0 t^2}{\sqrt{3} \cos \theta} \right\} \quad (64)$$

In order to verify the derived equations, the experimental results showed in Section 3 are considered again. Application of Eq. (64) imposes the difficulty that the fracture parameter, G_c is unknown. Lu et.al., [14], perform an experimental study on tearing energy in splitting metal tubes and present an expression and test results for mild steel plates which seems to be independent of plate thickness (at least for thicknesses between 0.5 mm and 1.5 mm);

$$G_c = 8.8 \text{ mm } \sigma_u \epsilon_f \quad (65)$$

Assuming that the separation process in plate cutting resembles that of tube splitting, this relation is applied below. However, as also stated by Lu et.al., the parameter, G_c , is a crude one to use in other problems than the specific one considered in the test because the tearing energy is highly dependent the detailed stress-strain state in the process. This was also noted by Atkins, [7] who reported values for G_c ranging from 200 - 1000 kJ/m^2 depending on the type of tearing process. Therefore, to apply expressions like Eqs. (64, 65) really requires further work on the detailed ductile separation process.

The friction factors, g , in the following verification examples are calculated from $\mu = 0.3$, $\alpha = 10^\circ$. The fracture strains of the three experiments are assumed to be 0.25, 0.25 and 0.15 respectively giving fracture toughnesses of 600 kJ/m^2 , 600 kJ/m^2 and 700 kJ/m^2 .

Table 4 shows a comparison between the theoretical prediction of the two presented models and the experimental results which were also presented in Table 2.

Table 4: Steady state cutting. Theoretical predictions and experimental results for three tests.

Experiments by	g from Eq. (54)	R (mm) Eq. (63)	F (kN) Eq. (61)	F (kN) Eq. (64)	F (kN) Measured
1. Lu & Calladine, [12]	2.81	3.59	5.58	5.72	6.0
2. Yahiaoui et.al., [34]	1.50	4.85	3.53	3.58	2.5
3. Astrup, [5]	1.67	72.3	2372	1722	2250

The theory, Eq. (61) with Eq. (63), over predicts the forces of the three reported tests by - 7 %, 41 % and 5 %. Thus, except for the test of Yahiaoui, [34], there is seen to be very good agreement between theory and experiments even though the scale of the problems is different by an order of magnitude. Also, it is noted that the difference between the two calculation models, Eq. (61) and Eq. (64) is small.

Table 5 shows how the energy dissipation is distributed between deformation mechanisms and friction when the plate resistance is calculated from Eq. (61).

Table 5: Partitioning of energy between deformation mechanisms and friction. Calculation model assuming purely plastic flow at wedge tip. $E_{tot} = E_c + E_b + E_m$. $\xi = E_{far\ field}/E_{tip\ zone}$

Experiments by	Friction $\frac{(g-1)}{g}$	Front tip $\frac{E_c}{E_{tot}}$	Shear $\frac{E_m}{E_{tot}}$	Bending $\frac{E_b}{E_{tot}}$	ξ $\frac{(E_m+E_b)}{E_c}$
1. Lu & Calladine, [12]	64 %	29 %	22 %	49 %	2.5
2. Yahiaoui et.al., [34]	33 %	10 %	74 %	16 %	8.7
3. Astrup, [5]	40 %	17 %	56 %	27 %	4.9

It is interesting to note how differently the energy is distributed in the three examples due to different wedge angles, plate thicknesses and wedge width, and it indicates why it is difficult to derive formulas that capture all dependencies on a purely empirical basis. The last column in Table 5 shows the importance of the tip zone process relative to the far field deformation. It is clear that the far field energy dissipation is dominant in these examples. In principle, Eq. (61) works in all scales but if we were to use the scaling formula presented by Atkins, Eq. (10), this ratio, ξ , of energy in the far field to energy in the tip zone should be used.

11 Conclusion

The paper presents a literature review and develops new formulas for calculating the resistance of a ductile plate being cut by a wedge of finite width. Analysis of previously published work shows a significant difference between proposed formulas. However, most of the results were derived for the initiation cutting rather than for the steady state cutting. The presently proposed calculational model is based on the energy dissipation rate in an assumed deformation mode consisting of a plastic tip zone, moving bending hinge lines and a membrane deformation zone. It is shown, how the analysis simplifies if the membrane deformation zone is assumed to be dominated by plastic shear strains. Attempts were made to model the tip zone both by a purely plastic flow mode and by a plastic fracture mode governed by the material fracture toughness. It is recognized, however, that more work is needed to fully understand contribution of the tip zone in cutting and tearing deformation mode. Friction was taken into account and formulas were derived both for the so called friction factor and for the vertical to horizontal force ratio. A comparison of the proposed formulas with experiments of Lu and Calladine, [12], Astrup, [5], and Yahiaoui, [34] and shows a good overall agreement.

Acknowledgment

All drawings were carefully prepared by Hugo Heinicke. The work is greatly acknowledged.

Nomenclature

$F_{P,c}$	Plastic and fracture resistance force
F	Total resistance force in the direction of motion
F_V	Reaction force perpendicular to direction of motion
\dot{E}_c	Rate of energy dissipation in tip zone
\dot{E}_m	Rate of energy dissipation for membrane deformation
\dot{E}_b	Rate of energy dissipation for bending
R	Radius of plate curls at the side of the wedge
R_t	Radius of plate curls at the front of the wedge, $R_t = R \cos \theta$
t	Plate thickness
S	Surface area of plate element
u_o	Gap opening at the wedge shoulder, Figure 5
v_o	Half gap opening at the wedge tip, Figure 5
η	Coordinate perpendicular to material streamline
ξ	Coordinate in the direction of material streamline
u	Displacement in direction of ξ
v	Displacement in direction of η
μ	Coulomb coefficient of friction
σ_y	Initial yield stress
σ_u	Ultimate stress
σ_0	Energy equivalent flow stress
ϵ_f	Strain to fracture
G_c	Material fracture toughness
α	Angle between cutting edge and normal to plate
θ	Semi wedge angle, half of total angle between front sides
g	Friction factor, $g = F/F_{P,c}$
k	Vertical to horizontal force ratio, $k = F_V/F$
<i>Others</i>	Defined where used

A Model Geometry

The objective of this section is to find the gap openings u_0 and $2v_0$ shown in Figure 5 expressed in terms of the rolling radius, $R(= R_t/\cos\theta)$, the wedge shoulder width, $2B$ and the wedge semi angle, θ .

Gap opening at wedge front

It is convenient to introduce two coordinate systems, a global system, $(X, Y, Z)_G$, and a local system, $(x, y, z)_l$, both with origin at point O . The z - and Z -axes point vertically upwards, the X_G -axis is in the symmetri line pointing towards the wedge tip and the x_l -axis is in the bending hinge line, OP . The y_l - and Y_G -axes are defined from the other axes. An arc line coordinate, s , which follows the curling edge of the plate is also introduced, see Figure 10. The s -axis also has origin at point O .

A point on the edge with the arc line coordinate, s , has the local coordinates

$$\begin{aligned} x_l &= s \cos\theta \\ y_l &= -R_t \sin\left(\frac{s \sin\theta}{R_t}\right) \\ z_l &= R_t \left(1 - \cos\left(\frac{s \sin\theta}{R_t}\right)\right) \end{aligned} \quad (66)$$

The general relation between local and global coordinates is given by the transformation

$$\begin{aligned} X_G &= x_l \cos\theta - y_l \sin\theta \\ Y_G &= x_l \sin\theta + y_l \cos\theta \\ Z_G &= z_l \end{aligned} \quad (67)$$

Inserting Eq. (66) into Eq. (67) gives the global coordinates for a point on the plate edge with coordinate s ;

$$X_G = (s \cos\theta) \cos\theta - \left(-R_t \sin\left(\frac{s \sin\theta}{R_t}\right)\right) \sin\theta \quad (68)$$

$$Y_G = (s \cos\theta) \sin\theta + \left(-R_t \sin\left(\frac{s \sin\theta}{R_t}\right)\right) \cos\theta \quad (69)$$

$$Z_G = z_l \quad (70)$$

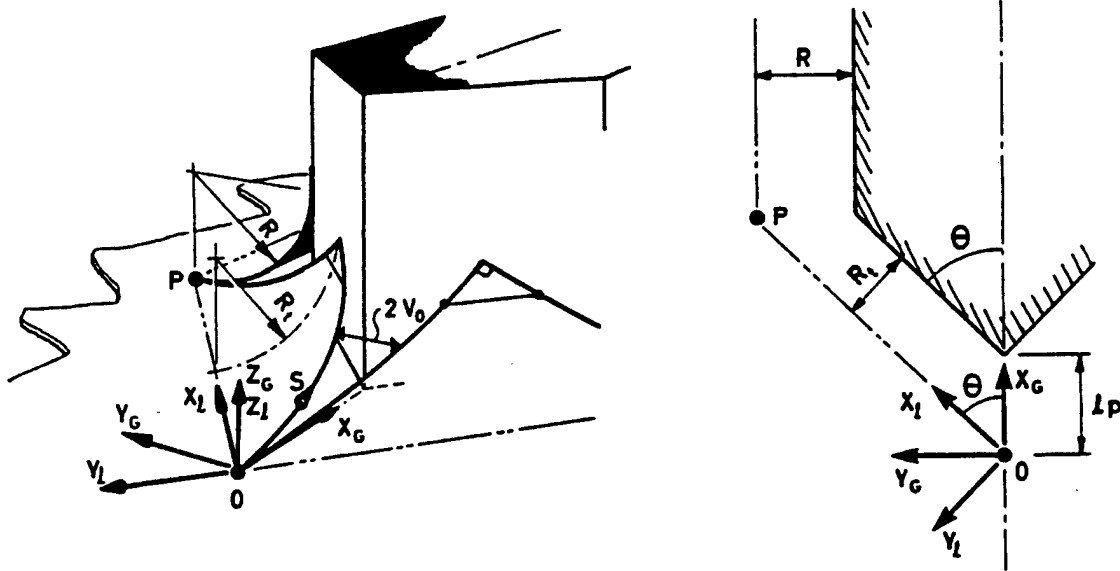


Figure 10: Definitions used for finding the gap width at the wedge tip

Since the gap opening is $2v_0 = 2Y_G$ it is now given from Eq. (69) as a function of s , R and θ ;

$$2v_0 = 2 \left(s \cos\theta \sin\theta - R \cos^2\theta \sin\left(\frac{s}{R}\tan\theta\right) \right) \quad (71)$$

The objective is to find the gap width at the cutting edge, i.e. at the point where $X_G = l_p = R/\sin\theta = R/\tan\theta$, see Figure 10. Eq. (68) is too complex to be solved in a closed form for s , otherwise this value of s should be inserted into Eq. (71) giving the final expression sought. It has to be done numerically.

As an initial guess we could calculate the gap width at $s = l_p = R/\tan\theta$. From Eq. (71) the expression becomes

$$2v_0 = 2R \cos^2\theta (1 - \sin 1) = 0.317 R \cos^2\theta \quad (72)$$

By comparing this expression to the exact solution found from numerical solution of Eqs. (68, 71) it is found that the final expression for the gap width, $2v_0$ at the cutting edge is very well approximated by the expression

$$2v_0 = 0.317 R \cos^2\theta (1 + 0.55\theta^2) \quad (73)$$

The error of Eq. (73) at 10° , 30° , 45° is respectively 0.25 %, 1.3 % and 0.18 %.

Gap opening at wedge shoulders

It is convenient to define a coordinate system, (X, Y, Z) , at the shoulder in the plane of the undeformed plate. The Z -axis points vertically upwards along the shoulder line, the Y -axis is in the plane of the undeformed plate and it is perpendicular to the Z -axis and to the wedge sides. The X -axis is defined from the Y - and Z axes, see Figure 11.

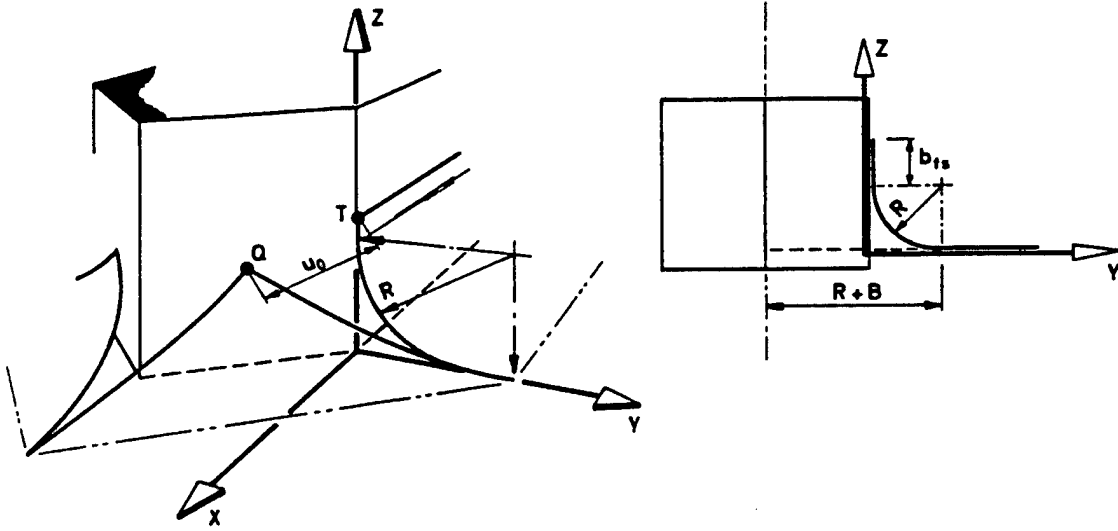


Figure 11: Definitions used for finding the gap width at the wedge sides

The total width of the deformed plate on one side of the symmetry line is $R + B$ and the length of the curved part of the flap is $\pi R/2$ so the width of the straight part of the flap at the wedge sides becomes

$$b_{fs} = (R + B) - \pi R/2 = B - R(\pi/2 - 1) \quad (74)$$

Likewise, it can be shown that the width of the straight part of the flap at the wedge front becomes

$$b_{ff} = \cos\theta (B - R(\pi/2 - 1)) \quad (75)$$

We require the tangent of the deformed plate flaps to conform to the wedge as shown in Figure 11 giving the requirement

$$b_f \geq 0 \Rightarrow \quad (76)$$

$$R \leq \frac{B}{\pi/2 - 1} \approx 1.75 B \quad (77)$$

The position of point T is

$$\begin{pmatrix} X \\ Y \\ Z \end{pmatrix}_T = \begin{pmatrix} 0 \\ 0 \\ B + R(2 - \pi/2) \end{pmatrix} \quad (78)$$

and the position of point Q is

$$\begin{pmatrix} X \\ Y \\ Z \end{pmatrix}_Q = \begin{pmatrix} B \sin \theta \cos \theta \\ -B \sin^2 \theta \\ (B + R(2 - \pi/2)) \cos \theta \end{pmatrix} \quad (79)$$

The distance between T and Q is then given by

$$\begin{aligned} u_0 &= ((X_T - X_Q)^2 + (Y_T - Y_Q)^2 + (Z_T - Z_Q)^2)^{0.5} \\ &= (B^2 \sin^2 \theta + (1 - \cos \theta)^2 (B + R(2 - \pi/2))^2)^{0.5} \end{aligned} \quad (80)$$

Figure 12 and Figure 13 show the variation of the gap width with rolling radius and wedge angle from Eq. (80).

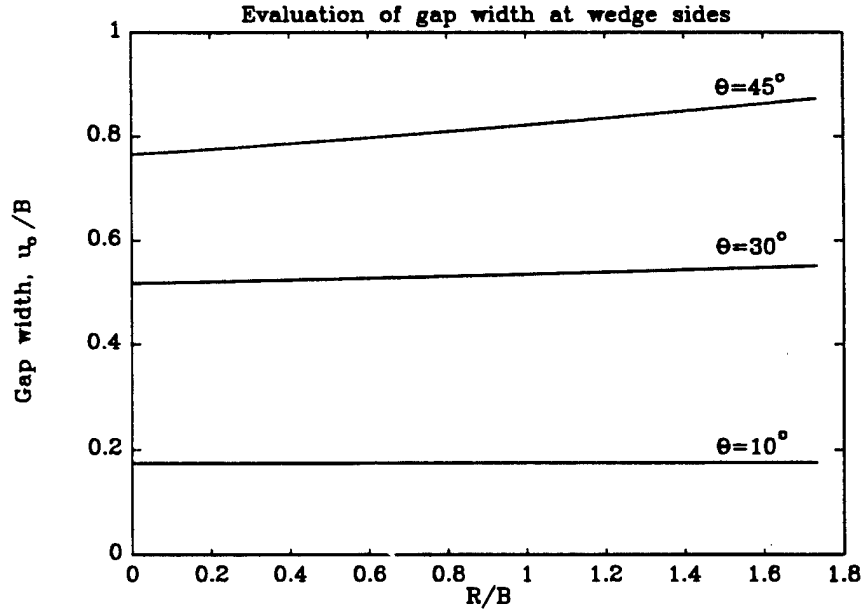


Figure 12: Variation of gap width with rolling radius

It is seen from Figure 12 that u_0/B is a very weak function of the rolling radius and Figure 13 illustrates that Eq. (80) is well approximated by the expression

$$u_0 = B \theta \quad (81)$$

for the considered ranges of θ and R .

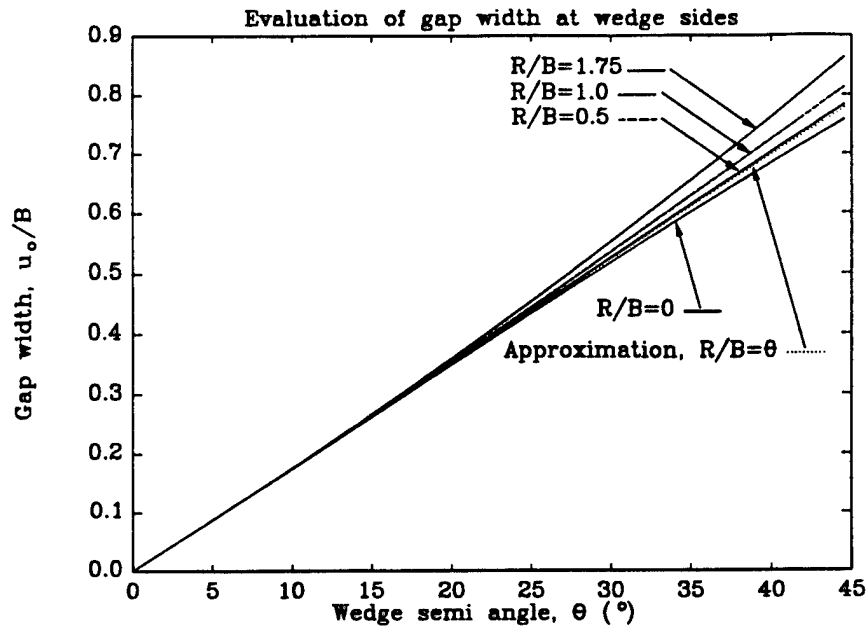


Figure 13: Variation of gap width with wedge angle

References

- [1] W. Abramowicz and T. Wierzbicki. Axial crushing of foam filled columns. *Int. J. of Mech. Sci.*, 30(3/4):263–271, 1988.
- [2] Y. Akita, N. Ando, Y. Fujita, and K. Kitamura. Studies on collision-protective structures in nuclear-powered ships. *Nucl. Engng Design*, 19(365), 1972.
- [3] Y. Akita and K. Kitamura. A study on collision by an elastic stem to a side structure of ships. *J. of the Society of Naval Architects of Japan*, 131:307–317, 1972.
- [4] J.M. Alexander. An approximate analysis of the collapse of thin cylindrical shells under axial loading. *Quart. J. Mechanics Applied Mathematics*, 13:10–15, 1969.
- [5] O. Astrup. Cutting of thick plates by a wedge. *Joint MIT-Industry Report, Tanker Safety*, 27, Jan 1994.
- [6] A.G. Atkins. Scaling in combined plastic flow and fracture. *Int. J. Mech. Sci.*, 30(173), 1988.
- [7] A.G. Atkins. Tearing of thin metal sheets. In T. Wierzbicki and N. Jones, editors, *Structural Failure*, pages 107–132. John Wiley & Sons, 1989.

- [8] A.G. Atkins. Letter to the editor. *Int. J. Mech. Sci.*, 33(1):69 – 71, 1991.
- [9] N. Jones. Scaling of inelastic structures loaded dynamically. *Structural Impact and Crashworthiness*, 1:45–74, 1984. G.A.O. Davies, Ed., Elsevier Applied Science Publishers.
- [10] N. Jones and W. S. Jouri. A study of plate tearing for ship collision and grounding damage. *J. Ship Res.*, 31(253), 1987.
- [11] N. Jones, W.S. Jouri, and R.S. Birch. On the scaling of ship collision damage. In *3rd International Congress on Marine Technology*, pages 287–294, Athens, Greece, 1984. International Maritime Association of East Mediterranean, Phivos Publishing Co.
- [12] G. Lu and C. R. Calladine. On the cutting of a plate by a wedge. *Int. J. Mech. Sci.*, 32:295–313, 1990.
- [13] G. Lu and C. R. Calladine. Author's reply. *Int. J. Mech. Sci.*, 33(1):73–74, 1991.
- [14] G. Lu et al. An experimental study on tearing energy in splitting square metal tubes. *Int. J. Mech. Sci.*, 36(12):1087–1097, 1994.
- [15] L.M. Maxwell. Effect of rock geometry on the failure modes of plates and the forces in grounding experiments. Technical Report 15, Joint MIT-Industry Program on Tanker Safety, May 1993.
- [16] V. U. Minorsky. An analysis of ship collisions with reference to protection of nuclear power plants. *Journal of Ship Research*, 3:1–4, 1959.
- [17] H. Ohtsubo and G. Wang. An upper-bound solution to the problem of plate tearing. *J Mar Sci technol*, 1(1), 1995.
- [18] J.K. Paik. Cutting of a longitudinally stiffened plate by a wedge. *J. of Ship Research*, 38(4):340–348, 1994.
- [19] J.K. Paik and T.K. Lee. Cutting tests for a stiffened plate by a wedge. In *MARIENV*, Tokyo, September 1995.
- [20] D. Pippenger. Coupled vertical and horizontal resistance of hull girder in grounding accidents. Technical Report 46, Joint MIT-Industry Program on Tanker Safety, May 1995.
- [21] J.L. Rodd and S. MacCampbell. Double hull tanker grounding experiments. In *The Advanced (unidirectional) Double-Hull Technical Symposium*, Gaithersburg, Maryland, 1994.

- [22] B.C. Simonsen and T. Wierzbicki. Grounding bottom damage and ship motion over a rock. In *Proceedings of The Sixth International Offshore and Polar Engineering Conference*, Los Angeles, USA, 1996. Submitted for Publication in Int. J. of Offshore and Polar Eng.
- [23] B.C. Simonsen, T. Wierzbicki, and S.K. Choi. Theoretical manual on grounding damage of a hull bottom structure - vol. i. Technical Report 52, Joint MIT-Industry Program on Tanker Safety, June 1995.
- [24] W.J. Stronge, T.X. Yu, and W. Johnson. *Energy dissipation by splitting and curling tubes*, volume 2, pages 576-587. Applied Science, London, 1983. (edited by J. Morton).
- [25] W.J. Stronge, T.X. Yu, and W. Johnson. Long stroke energy dissipation in splitting tubes. *Int. J. Mech. Sci.*, 25:637-647, 1984.
- [26] P.F. Thomas. Application of plate cutting mechanics to damage prediction in ship grounding. *Joint MIT-Industry Report, Tanker Safety*, 8, May 1992.
- [27] J. Turgeon. Analysis of hull damage without fracture in single-bottom transversally framed ships subjected to grounding. Technical Report 48, Joint MIT-Industry Program on Tanker Safety, May 1995.
- [28] H. Vaughan. Bending and tearing of plate with application to ship bottom damage. *The Naval Architect*, 3:97-99, May 1978.
- [29] H. Vaughan. The tearing of mild steel plate. *J. Ship Research*, 24(96), 1980.
- [30] T. Wierzbicki. Concertina tearing of metal plates - improved solution and comparison. *Joint MIT-Industry Report, Tanker Safety*, 22, 1994.
- [31] T. Wierzbicki and W. Abramowicz. On the crushing mechanics of thin-walled structures. *J. Appl. Mech.*, 5, 1983.
- [32] T. Wierzbicki and P. Thomas. Closed-form solution for wedge cutting force through thin metal sheets. *Int. J. Mech. Sci.*, 35(3), 1993.
- [33] G. Woisin. Comments on Vaughan: the tearing strength of mild steel plate. *J. Ship Res.*, 26(1):50-52, 1987.
- [34] M. Yahiaoui, M. Bracco, P. Little, and K. Trauth. Experimental studies on scale models for grounding. Technical Report 18, Joint MIT-Industry Program on Tanker Safety, Jan 1994.
- [35] Z.M. Zheng and T. Wierzbicki. Steady state wedge indentation - improved theory and validation. *Joint MIT-Industry Report, Tanker Safety*, 42, 1995.

**RUPTURE ANALYSIS OF OIL TANKERS IN A SIDE COLLISION: GLOBAL
STRUCTURAL MODEL OF BOW INDENTATION INTO SHIP SIDE**

T. Wierzbicki and B.C. Simonsen, Massachusetts Institute of Technology

1 Executive Summary

Since the pioneering work of Minorsky in 1958 the collision damage of ships has been extensively studied in literature. In the past few years there has been renewed interest in this type of problem, as exemplified by for example [4], [7]. For a complete review of the subject, the reader is referred to the work by Jones, [4], and subsequent reports of the International Ship Structure Committees. Three main approaches emerged in the literature. The empirically based methods (Minorsky, Woisin), the Finite Element Method (DYNA-3D, PAM-CRASH, ABAQUS, ADINA, DYTRAN) and the analytical approach (McDermott et.al., Hysing, Reckling etc.). The present report belongs to the latter category. The underlying philosophy of the present approach is rooted in the First Principles of Mechanics and is consistently based on the energy methods in plastic structural mechanics with finite displacements and rotations.

The objective of this report is to develop a theoretical basis for studying collision damage of the side structure of a stricken ship. It is not our intention to predict the extent of damage to any particular ship. Instead, a number of fundamental problems not previously treated in the literature were formulated and solved. The report consists of four self-contained and independent parts.

In the first part a plate strip model is developed for a longitudinally stiffened single hull ship which includes finite strength of transverse frames. It is shown that the dent size is increasing with the indentation depth. The rate of spreading of deformation to the neighbouring bays depends on the plastic strength of the supporting structure relative to the longitudinal strength of the plate strip. Another interesting result of the present solution is the effect of evening-out of strains over several bays in the case of a low longitudinal resistance of the supporting frames.

In the second part of this report two kinematically admissible solutions for a square rigid-plastic plate under a point load are compared. One is a 2-dimensional solution with all components of the strain tensor retained. The other one is a simplified solution in which the plate strength is derived from two perpendicular sets of plate strips where the shear strength is neglected. A full equivalence of both solutions was proved by taking von Mises yield condition in the plate solution and a limited interaction curve in the plate strip solution.

The third part of the present report is devoted to the derivation of an exact solution of punch indentation into a circular plate. A distinguished feature of the solution is a progressive contact (wrapping) of the plate around a hemispherical punch. It is shown that the force-deflection relationship and the critical strain to rupture depend on the radius of the plate as well as the punch radius. An approximate solution was also developed which opened a way for generalizing the circular plate solution to a rectangular plate subjected to an eccentric impact. The solution was further extended to cover orthotropic plates.

The resistance of decks/bulkheads to in-plane indentation of a rigid punch is treated in the fourth and last part of this report. The analysis is similar in spirit to the earlier solution for web crushing presented as Reports # 23 and 38 of the Phase I Tanker Safety Project. The important new contribution of the present approach is that the length of the folding wave is not assumed, as in the previous analyses, but found as a part of the solution. A simpler force-displacement relationship is obtained in the case of both symmetric and unsymmetric impact.

The solution is valid up to the point of first fracture. Beyond that point the plate will fail in the central cut mode or the concertina folding mode, depending on the geometry of the impacting bow, location of the indentation site and direction of deck stiffeners. The central cut failure mode is covered in a very comprehensive way in the Report # 1 of the Collision Project. References to the concertina tearing solutions were given earlier.

It is believed that the results of the present study (Reports # 1 and 2, together with the relevant deliverables of Phase I Tanker Safety Project) will give important background information for developing more detailed structural models of collision induced damage of a broad class of ships.

2 Plate strip model with Spreading Deformation

2.1 Model Overview, Basic Assumptions

The present study focuses on the response of the ship side of a longitudinally stiffened single skin VLCC being struck in the lateral direction by a ship. The bow of the striking ship is assumed to be rigid and the current approach for analyzing the response of the struck ship is based on dividing the structure into a series of individual members:

- beams (plate/stiffener combination)
- transverse frames
- decks

In order to predict the spreading of the deforming zone, the present report is primarily concerned with deformation of the longitudinal beams and their interaction with the connected transverse frames. Decks are covered in Report # 1 and Section 5. The derived theory of this section is based on intact structural members, i.e. rupture is not considered here.

2.2 Failure and Resistance of Transverse Members

We will consider two types of deformation of the transverse members (frames or bulk heads) depending on the location of the point or area of contact.

If the bow of the striking ship is in direct contact with the transverse member, the member will deform in a local/global mode as described in [3].

On the other hand, if the area of contact is between two transverse members and there is no direct contact between the bow and the transverse frame, the mode of deformation is different because load is transmitted through shell plating, stiffeners, or other longitudinal members. Again, the deformation mode of the transverse will be either local or global depending on the scantlings of the considered ship. An example of the so-called global deformation mode is failure of the entire transverse frame in a plastic mechanism whereas an example of the local failure mode could be failure of the weld between a transverse frame and the longitudinal. Most often - and for the specific

example considered at the end of the paper - the transverse members are so deep and sturdy that the dominating failure mode is the local one.

An example of the local failure in the transverse is illustrated in Figure 1. When the load on the longitudinal reaches a certain level, the welded connection between the longitudinal girder and the transverse fails.

An estimate of this load level is

$$F_{tr,1} = \frac{\sigma_0}{\sqrt{3}} \left(\frac{2}{3} h_{w,lng} \right) t_{tr} \quad (1)$$

where

$h_{w,lng}$ is the height of the longitudinal girder
 t_{tr} is the plate thickness of the transverse frame

This initial failure is followed by contact between the flange of the longitudinal and the transverse and subsequent concertina tearing of the plating in the transverse. The problem of concertina tearing is thoroughly described in [10] and an estimate of the initial load level is here given as

$$F_{tr,2} = \sigma_0 b_{f,lng} t_{tr} \quad (2)$$

where $b_{f,lng}$ is the flange width of the longitudinal. In the following, these load levels are assumed to be constant throughout the deformation process. The use of an energy equivalent flow stress instead of the initial yield stress is introduced to compensate for the actual variation in force with deformation. The theory is formulated so that it can take into account the actual force-deformation relationship. As an initial estimate, the load level after failure is here assumed to be

$$F_{tr} = \frac{F_{tr,1} + F_{tr,2}}{2} \quad (3)$$

2.3 Initial Failure and Deformation

Consider the example where the penetrating bow strikes between two frames, see Figure 2.

The classical method for treating this problem is to assume that the deformation is confined to the zone between the two frames closest to the

area of contact. However, it is obvious that if the longitudinal beams are very sturdy and the local strength of the transverse members is relatively low, the deformation will immediately go beyond the nearest stiffeners. This problem of initial failure is conveniently solved below by the upper bound theorem of plasticity.

Figure 2 shows three possible deformation modes on one side of the point of contact. Similar modes develop on the other side of the contact point so in the following it is sufficient to consider only one side. Assuming that we know the load level, F_{tr} , corresponding to the local failure in joints between longitudinals and transverse members discussed in section 2.2, we can calculate the load levels, P , corresponding to initial failure in the different deformation modes. Then, in compliance with the upper bound method, we choose the deformation mode which gives the smallest failure load.

The principle of virtual work states that the power of the external force, $P V_0$, equals the rate of internal energy dissipation, \dot{E}_i , in the structure:

$$P V_0 = \dot{E}_i \quad (4)$$

Using Eq. (4), the load level can be calculated for all kinematically admissible deformation modes. For the three modes shown in Figure 2 we get:

Deformation mode 1:

$$\begin{aligned} P^1 V_0 &= 2 M_0 \frac{V_0}{l_1} \Rightarrow \\ P^1 &= 2 \frac{M_0}{l_1} \end{aligned} \quad (5)$$

where M_0 is the fully plastic bending moment and l_1 is the distance from the point of contact to the nearest stiffener.

Deformation mode 2:

$$\begin{aligned} P^2 V_0 &= 2 M_0 \frac{V_0}{l_2} + \frac{l_2 - l_1}{l_2} F_{tr} V_0 \Rightarrow \\ P^2 &= 2 \frac{M_0}{l_2} + \frac{l_2 - l_1}{l_2} F_{tr} \end{aligned} \quad (6)$$

Deformation mode 3:

$$\begin{aligned} P^3 V_0 &= 2 M_0 \frac{V_0}{l_3} + \frac{l_3 - l_2}{l_3} F_{tr} V_0 + \frac{l_3 - l_1}{l_3} F_{tr} V_0 \Rightarrow \\ P^3 &= 2 \frac{M_0}{l_3} + \frac{l_3 - l_2}{l_3} F_{tr} + \frac{l_3 - l_1}{l_3} F_{tr} \end{aligned} \quad (7)$$

In general, the collision force corresponding to the i 'th deformation mode can be expressed as

$$P^i = 2 \frac{M_0}{l_i} + \frac{F_{tr}}{l_i} \sum_{j=1}^{i-1} (l_i - l_j) \quad (8)$$

where l_i is the distance from the point of contact to the i 'th stiffener outwards. The deformation mode which actually develops in the initial failure is the one corresponding to the lowest collision force:

$$P = \min(P^i), \quad i = 1, 2, 3, \dots \quad (9)$$

2.4 Sequence of Deformation

As the penetration increases, the mode of deformation changes from the initial mode described in the previous section to modes that extend further away from the point of contact.

In the present study, the model for this spreading of the deforming zone is based on equilibrium at the intersections between transverse frames and longitudinals.

From Figure 3 it is seen that equilibrium in the lateral direction at a joint between a longitudinal and a transverse can be expressed as

$$F_{tr} = T (\sin\theta_1 - \sin\theta_2) \quad (10)$$

where T is the axial force in the longitudinal and θ_1 and θ_2 denote rotation angles of the beam sections at the joint. For moderate angles the jump in rotation over a joint becomes

$$\theta_1 - \theta_2 = \frac{F_{tr}}{T} \quad (11)$$

It is noted that the axial force, T , is assumed to be the same (equal to the full plastic strength) on both sides of the transverse and the longitudinal equilibrium must therefore be neglected. For the more complex case of a strain hardening material, longitudinal equilibrium can also be obtained. This is discussed later in section 2.7.

As mentioned it is also assumed that F_{tr} is constant throughout the deformation process. The jump in angle, $\Delta\theta = \theta_1 - \theta_2$, over a longitudinal-transverse joint is therefore constant after the joint has failed. This implies that the deformation can be considered as a rotation of the beam around the outer point of the deforming zone. All other nodes in the deforming zone are rigid in the sense that no bending is taking place at these nodes. Due to the deflection and rotation, however, the beam sections are strained axially.

According to Eq. (11) with $\theta_2 = 0$, an intact joint between a transverse member and a longitudinal fails when the beam on one side has deformed to a rotation

$$\theta = \frac{F_{tr}}{T} \quad (12)$$

Figure 4 shows the sequence of deformation for the numerical example considered at the end of the paper. The following notation and numbering is used: The nodes are numbered from 0 to N starting at the point of contact. Node 1 is the joint at the boundary of the deforming zone for the initial deformation mode. Node N is at the boundary of the deforming zone for a given penetration. Initially $N = 1$ and N then increases as the deformation spreads. x_i denotes the longitudinal distance from the point of contact to node no i . The lateral velocity of the point of contact (node 0) is denoted V_0 , so the rate of rotation for the deforming beam around node N is

$$\dot{\theta}_N = \frac{V_0}{x_N - x_0} \quad (13)$$

The lateral velocity of the i 'th node point is

$$\begin{aligned} V_i &= \dot{\theta}_N (x_N - x_i) \\ &= V_0 \frac{x_N - x_i}{x_N - x_0}, \quad i = 1, 2, \dots, N \end{aligned} \quad (14)$$

2.5 Load-penetration Relationship

When applying the principle of virtual work, Eq. (4), it is necessary to express the rate of internal energy dissipation as a function of the velocity of the external force, as it was done in Section 2.3. In the present study which excludes decks there are three mechanisms that contribute to the internal energy dissipation:

1. bending of the beam at node N and at the point of contact
2. extensional deformation of the beam
3. deformation in shearing/concertina tearing at the intersections between longitudinals and transverse members.

Below, the rate of internal energy dissipation for these three mechanisms are expressed as a function of the velocity, V_0 , of the collision force, P.

1. Bending

Using the plastic moment capacity of the plating/stiffener combination, M_0 , and the rate of rotation, $\dot{\theta}_N$, from Eq. (13), the rate of internal energy dissipation for the bending hinges at node 0 and node N becomes

$$\dot{E}_{bending} = 2 \frac{M_0}{x_N - x_0} V_0 \quad (15)$$

2. Extension

The non-linear strain measure is

$$\varepsilon = \frac{du}{dx} + \frac{1}{2} \left(\frac{dw}{dx} \right)^2 \quad (16)$$

Initially we neglect the in-plane displacement, i.e. $u = 0$. This simplification is further discussed in Section 2.7. The strain rate becomes

$$\dot{\varepsilon} = \frac{dw}{dx} \frac{d\dot{w}}{dx} \quad (17)$$

where w is a lateral coordinate and x is a longitudinal coordinate. Since the beam is straight between node points, it is sufficient to consider the N beam sections. For beam section no i (i.e. the section between node $i-1$ and i , $i = 1, 2, \dots, N$), δ_i denotes the difference in lateral endpoint displacements, $\delta_i = w_{i-1} - w_i$, and $l_i = x_i - x_{i-1}$ is the length of this section. Then, the strain rate of this beam section becomes

$$\dot{\epsilon}_i = \frac{\delta_i \dot{\delta}_i}{l_i^2} \quad (18)$$

From Eq. (14) we get

$$\dot{\delta}_i = V_{i-1} - V_i = V_0 \frac{x_i - x_{i-1}}{x_N - x_0} \quad (19)$$

The total energy dissipation is the sum of the energy dissipation of the individual N beam sections. The result reduces to the relatively simple expression

$$\dot{E}_{extension} = \sum_{i=1}^N \sigma_0 A \dot{\epsilon}_i l_i = \sigma_0 A \frac{w_0 - w_N}{x_N - x_0} V_0 \quad (20)$$

where A is the cross section of the beam. It is interesting to note that we only need the positions of the boundary nodes, $i = 0$ and $i = N$, to determine the energy dissipation rate of all the intermediate beam sections.

3. Deformation of intersections between longitudinals and transverse members

As mentioned in Section 2.2, it is assumed that the force at the failed transverse frames, F_{tr} , is constant throughout the deformation process. The velocity of the deformation at frame i ($i < N$) is

$$V_i = V_0 \frac{x_N - x_i}{x_N - x_0} \quad (21)$$

so the total rate of energy dissipation at the joints is

$$\dot{E}_{trans} = V_0 \frac{F_{tr}}{x_N - x_0} \sum_i (x_N - x_i) \quad (22)$$

The summation should be carried out over the joints $i = 1, 2, \dots, N-1$ and the joints which are deformed in the initial deformation mode (since these are not included in joints $i = 1, 2, \dots, N$).

Total energy dissipation and collision force

The total rate of energy dissipation at a given instant where the deformation extends to node no N is given by Eqs. (15, 20, 22). Using Eq. (4) then gives the total load, P , corresponding to the considered deformation on one side of the point of contact:

$$\begin{aligned} P V_0 &= \dot{E}_{bending} + \dot{E}_{extension} + \dot{E}_{trans} \Rightarrow \\ P &= \frac{2M_0}{x_N - x_0} + \sigma_0 A \frac{w_0 - w_N}{x_N - x_0} + \frac{F_{tr}}{x_N - x_0} \sum_i (x_N - x_i) \end{aligned} \quad (23)$$

By selecting the origin of the (x, w) coordinate system at the initial point of contact, we get $x_0 = 0$ and $w_N = 0$, so Eq. (20) simplifies to the expression

$$P = \frac{1}{x_N} \left\{ 2M_0 + T_0 w_0 + F_{tr} \sum_i (x_N - x_i) \right\} \quad (24)$$

where $T_0 = \sigma_0 A$ is the fully plastic axial force.

2.6 Numerical Example

As an application example of the derived theory, we consider penetration into the side of a single skin VLCC with scantlings like Exxon Valdez. As in the previous sections we consider a single beam composed of a heavy longitudinal T-stiffener attached to side plating of width corresponding to vertical stiffener spacing.

2.6.1 Ship Data

Energy equivalent flow stress, σ_0 :	320 MPa
Plastic axial force, T_0 :	10.1 MN
Plastic moment capacity of plate/stiffener, M_0 :	2.27 MNm
Depth of web in longitudinal, $h_{w,lng}$:	0.711 m
Width of flange in longitudinal, $b_{f,lng}$:	0.203 m
Plate thickness of transverse, t_{tr} :	0.0175 m
Distance from point of contact to first transverse, l_1 :	2.44 m
Distance from point of contact to second transverse, l_2 :	7.32 m
Distance from point of contact to third transverse, l_3 :	12.2 m

2.6.2 Initial Failure

Inserting values into Eqs. (1, 2, 3) we get

$$\begin{aligned}F_{tr,1} &= 1.13 \text{ MN} \\F_{tr,2} &= 1.53 \text{ MN} \\F_{tr} &= \frac{(1.13 + 1.53)}{2} \text{ MN} = 1.3 \text{ MN}\end{aligned}$$

Now the initial load corresponding to the first three deformation modes can be calculated from Eqs. (5, 6, 7)

$$\begin{aligned}P^1 &= 1.86 \text{ MN} \\P^2 &= 1.49 \text{ MN} \\P^3 &= 1.93 \text{ MN}\end{aligned}$$

The initial failure will therefore be in deformation mode 2, with the force, $P = P^2 = 1.49 \text{ MN}$.

2.6.3 Load Penetration Relationship

From Eq. (11), the maximum jump in angle over a joint becomes

$$\theta_1 - \theta_2 = \frac{F_{tr}}{T} = \frac{1.3 MN}{10.1 MN} = 7.37^\circ \quad (25)$$

Using Eq. (24) the total load-deformation history can now be established. Below is calculated the load-penetration history until the deforming zone has spread to include four transverse members.

a. Initial failure, $N = 1$.

As shown in Figure 4, the initial deforming zone includes one transverse member and a beam of 7.32 m. The transverse at the boundary of the deforming zone will fail when the beam has deflected to an angle, $\theta = 7.37^\circ = 0.129 \text{ rad}$. This corresponds to a deflection at the point of contact of $w_0 = 0.129 \cdot 7.32 \text{ m} = 0.94 \text{ m}$. Phase 1 ($N = 1$) therefore lasts until the penetration is 0.94m. Using Eq. (24), the collision force at the beginning and the end of this phase is found to be

$$\begin{aligned} P &= 1.49 \text{ MN} & \text{at } w_0 &= 0 \text{ m} \\ P &= 2.78 \text{ MN} & \text{at } w_0 &= 0.94 \text{ m} \end{aligned}$$

b. Phase 2, $N = 2$.

This phase lasts until the beam section between node 1 and 2 has rotated to the angle, $\theta = 7.37^\circ = 0.129 \text{ rad}$. This corresponds to a total deflection at the point of contact of $w_0 = 0.94 \text{ m} + 0.129 \cdot 12.2 \text{ m} = 2.51 \text{ m}$.

Inserting into Eq. (24) for the penetration at the beginning of the phase gives

$$P = \frac{10^6}{12.2} (2 \cdot 2.27 + 10.1 \cdot 0.94 + 1.3(4.88 + 9.76)) N = 2.71 \cdot 10^6 N \quad (26)$$

The collision force at the beginning and the end of this phase becomes

$$\begin{aligned} P &= 2.71 \text{ MN} & \text{at } w_0 &= 0.94 \text{ m} \\ P &= 4.01 \text{ MN} & \text{at } w_0 &= 2.51 \text{ m} \end{aligned}$$

c. Phase 3, $N = 3$.

Using same procedure as above, the collision force at the beginning and the end of this phase becomes

$$\begin{array}{ll} P=3.98 \text{ MN} & \text{at } w_o=2.51 \text{ m} \\ P=5.28 \text{ MN} & \text{at } w_o=4.71 \text{ m} \end{array}$$

d. Phase 4, $N=4$.

Using same procedure as above, the collision force at the beginning and the end of this phase becomes

$$\begin{array}{ll} P=5.25 \text{ MN} & \text{at } w_o=4.71 \text{ m} \\ P=6.55 \text{ MN} & \text{at } w_o=7.54 \text{ m} \end{array}$$

The calculated load-penetration relationship is plotted in Figure 5.

2.7 Effect of In-Plane Displacement

In all previous analyses of plastic deformation of beams and plates including those in the present report, it was assumed that the material points move perpendicular to the undeformed surface of the structure. This assumption is realistic for fully clamped edge conditions. However, for a continuing beam with crushable intermediate supports which is the case with our plate strip indentation model presented above, the validity of this assumption must be checked. The present analysis is concerned with a string model. It is conducted in the following three steps

Case I Rigid-perfectly plastic model with no intermediate supports

Case II Rigid-linear strain-hardening model with no longitudinal resistance of intermediate supports

Case III Rigid-linear strain-hardening model *with* longitudinal resistance of intermediate supports

2.7.1 Case I, Rigid-perfectly Plastic Model

Consider two adjacent bays as shown in Figure 6. Only bay # 2 undergoes out-of-plane displacement. The strain and the strain rates in the bays are

$$\varepsilon_1 = \frac{u}{l} \quad (27)$$

$$\dot{\varepsilon}_1 = \frac{\dot{u}}{l} \quad (28)$$

$$\varepsilon_2 = \frac{1}{2} \left(\frac{w}{l} \right)^2 - \frac{u}{l} \quad (29)$$

$$\dot{\varepsilon}_2 = \frac{w \dot{w}}{l^2} - \frac{\dot{u}}{l} \quad (30)$$

For horizontal equilibrium we infer that there is the same tensile force in both bays;

$$N_1 = N_2 = N_0 \quad (31)$$

The global rate of energy equation, Eq. (4) becomes

$$\begin{aligned} P w &= \int_0^l N_1 \dot{\varepsilon}_1 dx + \int_0^l N_2 \dot{\varepsilon}_2 dx \\ &= N_0 \int_0^l \left(\frac{\dot{u}}{l} + \frac{w \dot{w}}{l^2} - \frac{\dot{u}}{l} \right) dx \\ &= N_0 \frac{w \dot{w}}{l} \end{aligned} \quad (32)$$

The indentation force for case I then becomes

$$P_I = N_0 \frac{w}{l} \quad (33)$$

P_I is seen to be independent of the inplane displacement, u . Furthermore, there is no way to find the magnitude of the in-plane displacement in this model # 1. As shown below, however, introduction of strain hardening makes the problem of the in-plane displacement well defined.

2.7.2 Case II, Rigid-linear Strain-hardening Model

Stress is here assumed to be related to strain by the relation

$$\sigma = \sigma_0 + E_p \varepsilon \quad (34)$$

Using Eqs. (27 - 30, 34) with the global equilibrium, Eq. (32), the collision force for Case II can then be expressed as

$$P_{II} = N_1 \frac{\dot{u}}{\dot{w}} + N_2 \left(\frac{w}{l} - \frac{\dot{u}}{\dot{w}} \right) \quad (35)$$

where

$$N_1 = t \left(\sigma_0 + E_p \frac{u}{l} \right) \quad (36)$$

$$N_2 = t \left(\sigma_0 + E_p \left(\frac{1}{2} \left(\frac{w}{l} \right)^2 - \frac{u}{l} \right) \right) \quad (37)$$

and the unknown velocity ratio, \dot{u}/\dot{w} can be found by minimizing P ;

$$\begin{aligned} \frac{dP}{d(\dot{u}/\dot{w})} &= 0 \quad \Rightarrow \\ N_1 - N_2 &= 0 \end{aligned} \quad (38)$$

which says that membrane forces in both segments should be equal. That in turn implies that strains must be equal;

$$\frac{u}{l} = \frac{1}{2} \left(\frac{w}{l} \right)^2 - \frac{u}{l} \quad (39)$$

Therefore, for the minimum to occur, the in-plane displacement must be related to the out-of-plane displacement by

$$u = \frac{1}{4} \frac{w^2}{l} \quad (40)$$

$$\dot{u} = \frac{1}{2} \frac{w \dot{w}}{l} \quad (41)$$

Substituting the above values back into Eq. (35) gives the new solution;

$$P_{II} = t \left[\sigma_0 + \frac{1}{4} E_p \left(\frac{w}{l} \right)^2 \right] \frac{w}{l} \quad (42)$$

For small values of the plastic modules, E_p , prediction of the reaction force by Eq. (33) and Eq. (42) are the same. However, strains in the hardening material model are one half of those in the rigid-perfectly plastic model so for prediction of fracture, it can be crucial to consider strain hardening effects.

2.7.3 Case III, Rigid-linear Strain-hardening Model, Intermediate Supports

Finally, in model # 3 a horizontal resistance, F_{12} , is associated with the in-plane displacement, u , at the intermediate support, see Figure 7. The additional energy dissipated is $\dot{E} = F_{12} \dot{u}$. Eq. (35) is now modified accordingly to

$$P_{III} = N_1 \frac{\dot{u}}{\dot{w}} + N_2 \left(\frac{w}{l} - \frac{\dot{u}}{\dot{w}} \right) + F_{12} \frac{\dot{u}}{\dot{w}} \quad (43)$$

From the minimum condition we obtain

$$N_1 - N_2 + F_{12} = 0 \quad (44)$$

which gives

$$\frac{u}{l} = \frac{1}{4} \left(\frac{w}{l} \right)^2 - \frac{F_{12}}{t E_p} \quad (45)$$

As a result, there is a difference between the strains in both bays equal to

$$\Delta \varepsilon = \varepsilon_2 - \varepsilon_1 = \frac{2 F_{12}}{t E_p} \quad (46)$$

It can be concluded that strains in the plate strip model attain maximum in the central bay and then diminish from bay to bay, where the jump is given by Eq. (46).

2.8 Conclusion

The present section has presented a theory which is able to predict the response of a ship side being penetrated by a rigid bow. Based on dividing the structure into longitudinal beams and transverse members, the theory calculates the collision force with due consideration to the spreading of the deforming zone as the penetration increases. As an application example, the load-penetration relationship is calculated for a single hull VLCC with scantlings like Exxon Valdez. In a study of the effect of in-plane displacements and strain-hardening it is shown that these effects are normally neglectable for calculation of the structural reaction before rupture but it may be very important for prediction of the point of fracture.

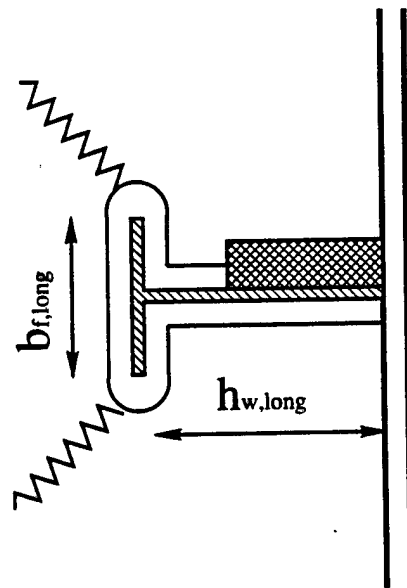
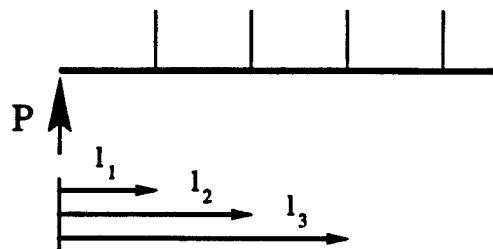
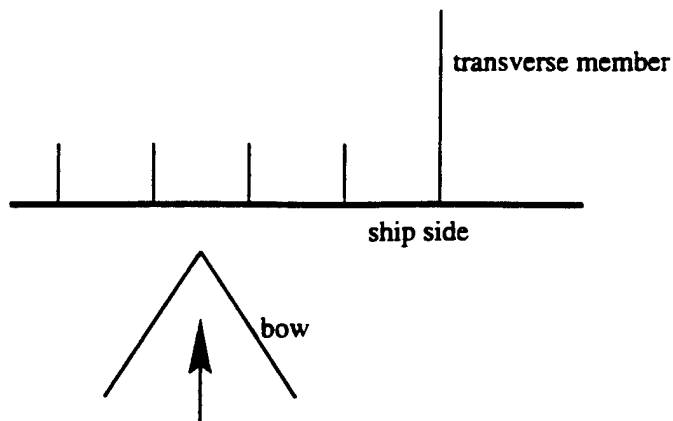
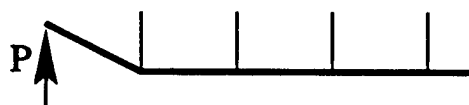


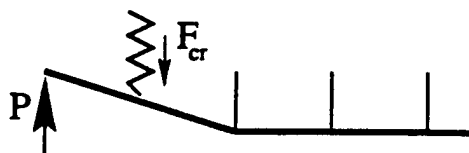
Figure 1: Local failure at intersection between longitudinal and transverse member



Def. mode 1:



Def. mode 2:



Def. mode 3:

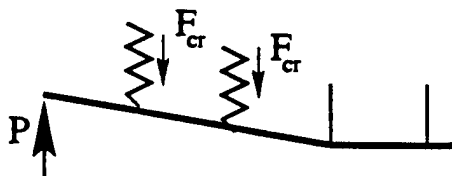


Figure 2: Initial deformation mode

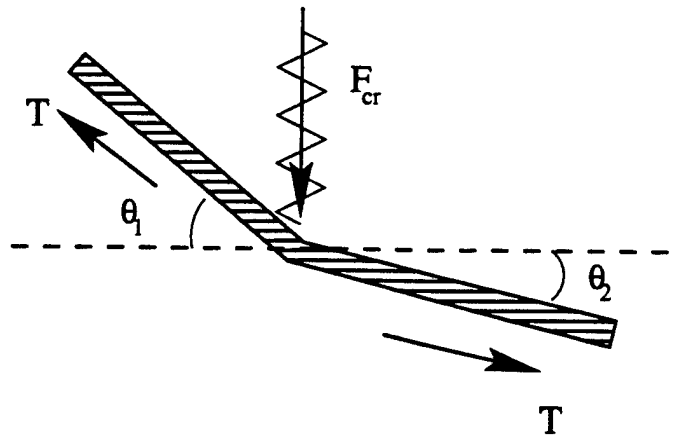


Figure 3: Lateral equilibrium at joints between longitudinals and transverse members

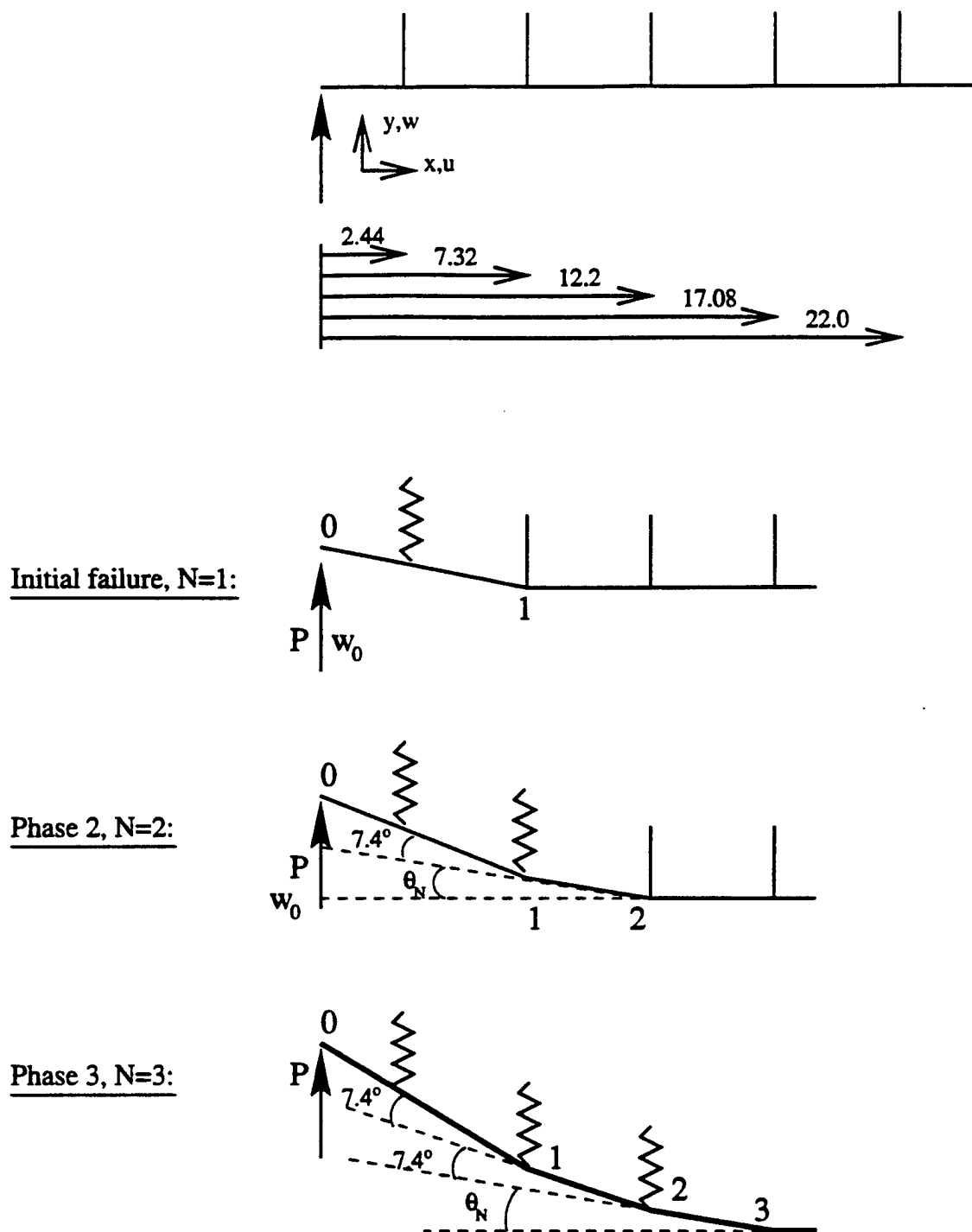


Figure 4: Sequence of deformation and notation

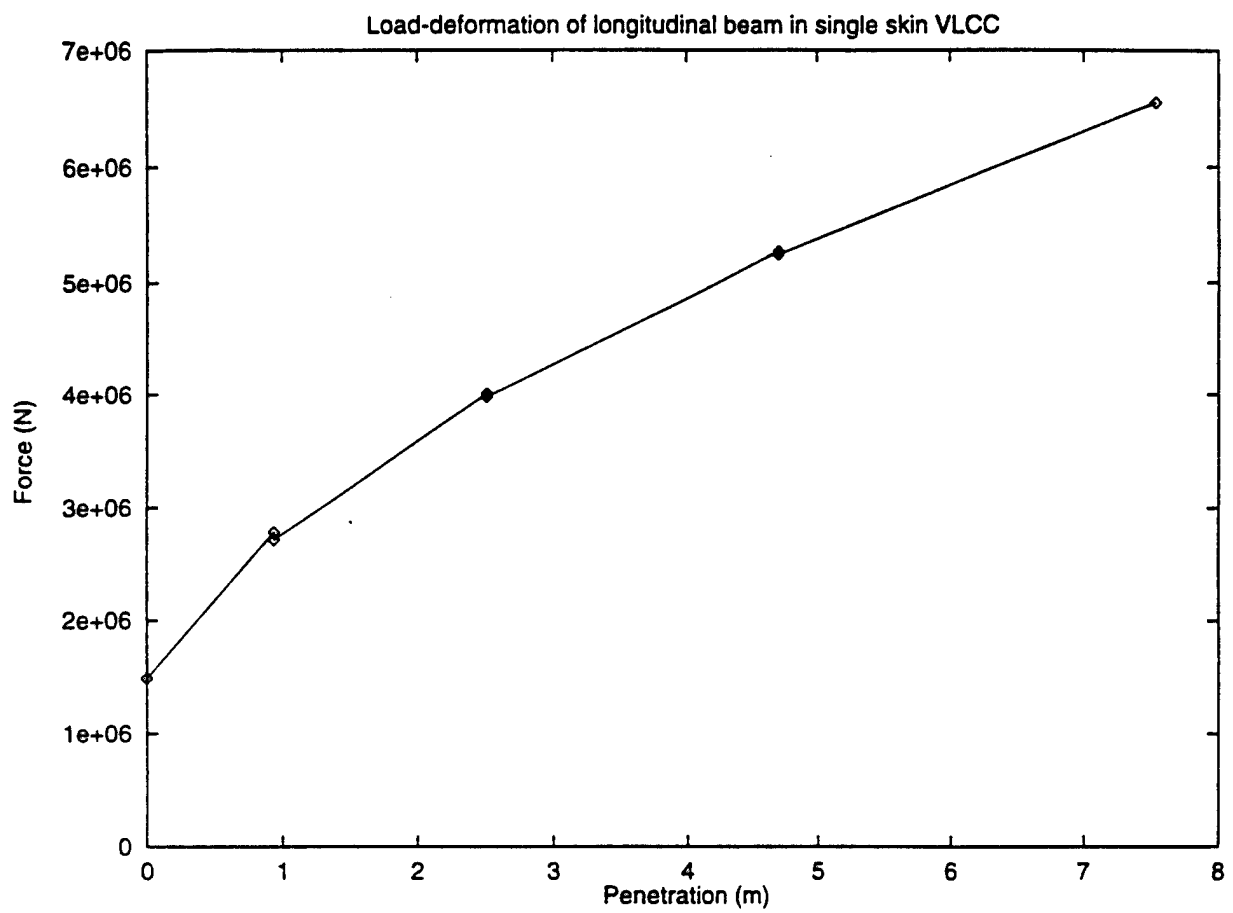


Figure 5: Load-deformation relationship

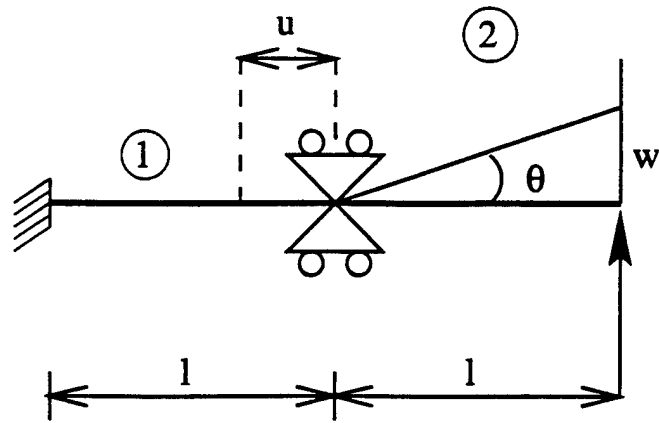


Figure 6: Model for analysis of effect of in-plane displacement, u . Cases I and II

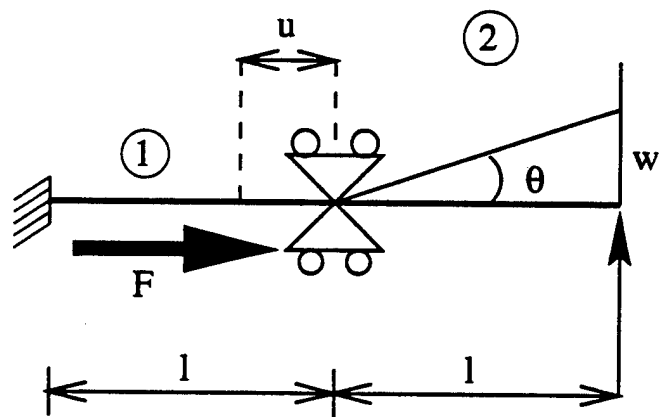


Figure 7: Model for analysis of effect of in-plane displacement, u . Case III

3 Equivalence of Plate and Plate Strip Formulation

3.1 Resistance of a Plate

Consider a rectangular plate of dimensions $2a \cdot 2b$ subjected to an increasing deflection, w_0 , at its center. Of interest is the resisting force, P , of the plate. The problem is formulated within the moderately large deflection theory of plates with $w_0 > t$ so that bending resistance can be neglected.

The Lagrangian strain tensor, $\varepsilon_{\alpha\beta}$ is defined by

$$\varepsilon_{\alpha\beta} = \frac{1}{2} (u_{\alpha,\beta} + u_{\beta,\alpha}) + \frac{1}{2} w_{,\alpha} w_{,\beta} \quad (47)$$

where u_α are components of the in-plane displacement while w denotes the out-of-plane displacements. The in-plane components are neglected for simplicity, $u_\alpha = 0$. The three components of the strain tensor are

$$\begin{aligned} \varepsilon_{xx} &= \frac{1}{2} \left(\frac{dw}{dx} \right)^2 \\ \varepsilon_{yy} &= \frac{1}{2} \left(\frac{dw}{dy} \right)^2 \\ \varepsilon_{xy} &= \frac{1}{2} \frac{dw}{dx} \frac{dw}{dy} \end{aligned} \quad (48)$$

The rate of the external loading must be equal to the rate of energy dissipation in the plate. Using the von Mises yield criterion this requirement is expressed by

$$P \dot{w}_0 = \frac{2}{\sqrt{3}} \sigma_0 t \int_S \sqrt{\dot{\varepsilon}_{xx}^2 + \dot{\varepsilon}_{yy}^2 + \dot{\varepsilon}_{xx} \dot{\varepsilon}_{yy} + \dot{\varepsilon}_{xy}^2} dS \quad (49)$$

where the integration is performed over the deforming part of the plate. The following simple but realistic deformation field is assumed for one quarter of the plate. It satisfies the clamped boundary condition.

$$w(x, y) = w_0 \frac{x}{a} \frac{y}{b} \quad (50)$$

the (x, y) -coordinate system beginning at a corner point, see Figure 8. The strain components resulting from the above displacement field are

$$\begin{aligned}\epsilon_{xx} &= \frac{1}{2} \left(\frac{w_0}{a} \right)^2 \left(\frac{y}{b} \right)^2 \\ \epsilon_{yy} &= \frac{1}{2} \left(\frac{w_0}{b} \right)^2 \left(\frac{x}{a} \right)^2 \\ \epsilon_{xy} &= \frac{1}{2} \frac{w_0^2}{ab} \frac{xy}{ab}\end{aligned}\tag{51}$$

Differentiating the above expressions with respect to time gives

$$\begin{aligned}\dot{\epsilon}_{xx} &= \frac{w_0 \dot{w}_0}{a^2} \left(\frac{y}{b} \right)^2 \\ \dot{\epsilon}_{yy} &= \frac{w_0 \dot{w}_0}{b^2} \left(\frac{x}{a} \right)^2 \\ \dot{\epsilon}_{xy} &= \frac{w_0 \dot{w}_0}{ab} \frac{xy}{ab}\end{aligned}\tag{52}$$

Substituting the above expressions into Eq. (49) and performing integration yields

$$P = \frac{2\sigma_0 t}{\sqrt{3}} \frac{4w_0}{3} \left(\frac{a}{b} + \frac{b}{a} \right)\tag{53}$$

The plate resisting force increases linearly with the central deflection and is a function of the plate aspect ratio, a/b . It is interesting to note that given the aspect ratio, the force P is independent of the dimension of the plate, which means that the deformation mode is not unique and could be local. Minimizing Eq. (53) with respect to the aspect ratio reveals that a square plate ($a = b$) offers the least resistance;

$$P_{sq} = \frac{2\sigma_0}{\sqrt{3}} \frac{8}{3} w_0 t = 3.06 \sigma_0 t w_0\tag{54}$$

In comparison, it can be recalled that a classical plate bending solution under a point load gives

$$P = 2\pi M_0 = 1.8\sigma_0 t^2\tag{55}$$

which is also independent of the size of the deforming zone.

Such a local deformation mode has been observed in experiments and was reported for example by Amdahl and Kavlie, [1].

3.2 Resistance of Plate Strip and Equivalence to Plate Formulation

In many practical applications the plate is modelled as a collection of strips which satisfy kinematic continuity but do not transmit any shear stresses, see Figure 9. For long rectangular plates strips are considered only in one direction. Plates with an aspect ratio closer to unity derive their strength from plate strips in two directions. The global equation of equilibrium takes now the form

$$P \dot{w}_0 = \frac{2}{\sqrt{3}} \sigma_0 t \int_S (\dot{\epsilon}_{xx} + \dot{\epsilon}_{yy}) dS \quad (56)$$

where the so called 'limited interaction curve' was assumed meaning that yielding of the plate in two directions is independent. It can be checked that with the same deflection field (i.e. taking $\dot{\epsilon}_{xx}$ and $\dot{\epsilon}_{yy}$ from Eq. (52)) the calculated resisting force is identical to that given by Eq. (53). This means that the neglect of shear resistance in the plate strip solution is compensated by the circumscribed yield condition over the exact von Mises yield surface.

There is however one important difference between the above two solutions. In the plate strip method, the plate is modelled as a 'bundle' of strings which must extend between two opposite clamped boundaries. Therefore, the property of 'locality' of the collapse mode is lost in this method. Although the resisting force is the same for the two approaches it is clear, however, that when it comes to prediction of strains and fracture it is important to consider the more realistic deformation mode of the plate solution.

A complete analysis of wide wedge indentation into a longitudinally or transversally stiffened plate structure with subsequent contacts and web crushing was developed by Thunes, [5].

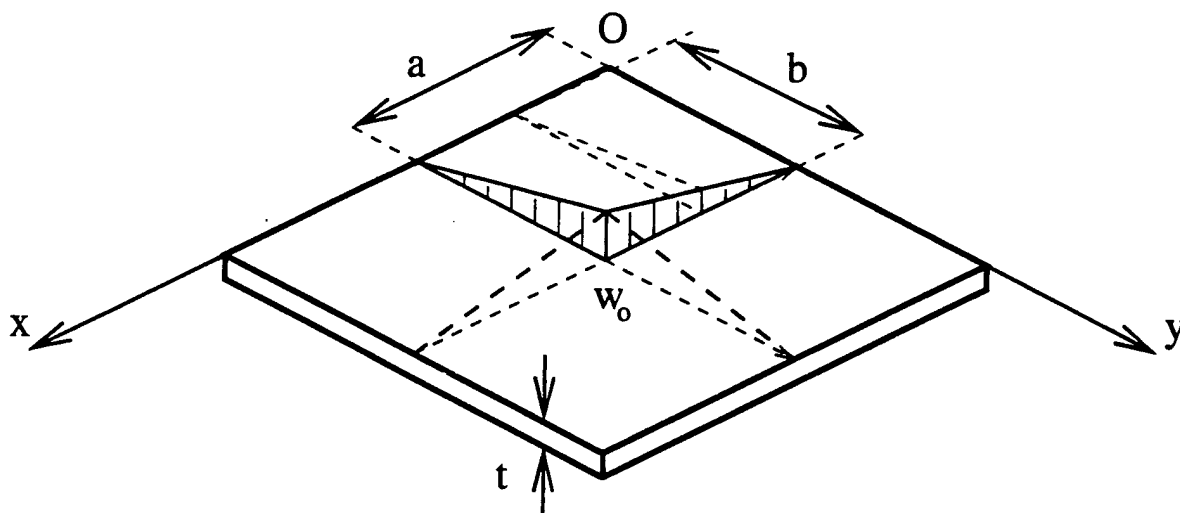


Figure 8: Assumed deformation mode for a plate

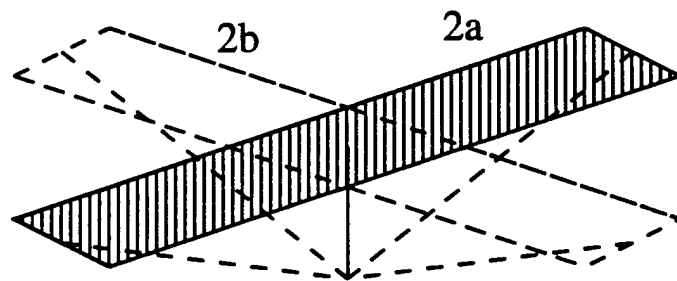


Figure 9: Plate deformation modelled by strips

4 Plate Indentation by a Hemispherical Bow

4.1 Force-Deflection Relationship

When the bow of an impacting ship penetrates into the side of the stricken ship, the side plating wraps around the bow as the local indentation process proceeds. Let us denote the radius of the hemispherical bow by R_b . In the cylindrical coordinate system (w, r, θ) , the spherical shape can be conveniently approximated by the parabolic shape

$$w(r) = \frac{r^2}{2R_b} \quad (57)$$

where the tip of the dome is taken as an origin of the coordinate system. A fully clamped circular plate of radius R is treated first. Based on this solution conclusions are drawn for square and rectangular plates.

The plate is divided into two regions. In the central rigid region, $0 < r < r_0$, the plate conforms to the shape of the bow. In the outer region, extending to the clamped boundary, $r_0 < r < R$, there is no transverse load acting on the plate. According to the theory of moderately large deflection of plates, the equation of equilibrium takes the form

$$(N_r r w')' = 0 \quad (58)$$

where prime denotes spatial differentiation (with respect to r) and N_r , the radial membrane force, is assumed to be equal to the plane strain fully plastic membrane force, $N_r = N_0 = 2\sigma_0/\sqrt{3}t$. There are two boundary conditions: one at the boundary of the plate ($r = R$) and one at the interface ($r = r_0$) between inner and outer regions:

$$w(R) = 0 \quad (59)$$

$$2\pi N_0 w' r_0 = P \quad (60)$$

Eq. (60) means that the total shear force at the interface between the rigid and deforming zone must be equal to the load exerted by the punch. Integrating Eq. (58) twice gives

$$N_0 w = C \ln r + D \quad (61)$$

where the integration constants C and D are found from boundary conditions (59, 60);

$$\frac{w}{R} = \frac{P}{2\pi R N_0} \ln \frac{r}{R} = \bar{P} \ln \frac{r}{R} \quad , r_0 < r < R \quad (62)$$

where the dimensionless plate resistance force, \bar{P} is defined as

$$\bar{P} = \frac{P}{2\pi R N_0} \quad (63)$$

The plate deflection at $r = r_0$ is

$$\frac{w_0}{R} = \bar{P} \ln \frac{r_0}{R} \quad (64)$$

The unknown radius r_0 can now be determined from the condition of slope continuity between rigid and deforming regions. Calculating the slopes respectively from Eq. (57) and (62) and equating them at $r = r_0$ one gets

$$\bar{P} \frac{R}{r_0} = \frac{r_0}{R_b} \quad (65)$$

giving an interface radius of

$$r_0 = \sqrt{\bar{P} R R_b} \quad (66)$$

With Eq. (62) and (66) the solution in the *outer* region becomes

$$\frac{w_0}{R} = \frac{1}{2} \bar{P} \ln \left(\bar{P} \frac{R_b}{R} \right) \quad (67)$$

The deflection in the *inner* region is obtained from Eq. (57) with $r = r_0$;

$$w_i = \frac{r_0^2}{2 R_b} = \frac{1}{2} \bar{P} R \quad (68)$$

With a total deflection at the center of $\delta = -w_o + w_i$, the force-deflection characteristic of the indentation process is finally given by

$$\frac{\delta}{R} = -\frac{1}{2} \bar{P} \ln \left(\bar{P} \frac{R_b}{R} \right) + \frac{1}{2} \bar{P} = \frac{1}{2} \bar{P} \left[1 - \ln \left(\bar{P} \frac{R_b}{R} \right) \right] \quad (69)$$

4.2 Determination of Strains

The Lagrangian strain in the radial direction is defined by

$$\epsilon_r = \frac{1}{2} (w')^2 \quad (70)$$

It is assumed that fracture of the plate will occur when the maximum strain reaches the critical strain to rupture, $(\epsilon_r)_{max} = \epsilon_c$. The strain is always maximum at $r = r_0$. From Eq. (57) and (66) one gets

$$\epsilon_c = \frac{1}{2} \bar{P} \frac{R}{R_b} \quad (71)$$

Eliminating the load parameter, P , in Eq. (69) the critical plate penetration to rupture becomes

$$\left(\frac{\delta}{R} \right)_c = \frac{R_b}{R} \epsilon_c \left[1 - \ln \left(2 \epsilon_c \left(\frac{R_b}{R} \right)^2 \right) \right] \quad (72)$$

Plots of Eq. (72) for several values of the plate to bow radius ratio is shown in Figure 10 as full lines. For comparison, one graph shows the solution which assumes a conical displacement field and neglects the finite radius of the bulbous bow.

$$\left(\frac{\delta}{R} \right)_c = \sqrt{2 \epsilon_c} \quad (73)$$

It is seen that the difference between the present, rigorous solution and the simplified solution is large in the entire range of parameters ϵ_c and R/R_b .

The conical displacement field for a plate corresponds to a triangular deflection profile in a plate strip. While the latter is correct in the case of a clamped beam the former is far from reality in the case of a plate under a localized punch loading. Further shortcomings of Eq. (73) is that the critical displacement to rupture does not depend on the bow radius. It should be mentioned that Eq. (73) has been frequently used in the past to predict onset of rupture of shell plating.

4.3 Approximate Solution

In order to extend the present solution to rectangular plates and unsymmetric loading it is necessary to develop a simplified analytical solution. The

following function provides a good approximation of Eq. (69) over a wide range of input parameters:

$$\left(\frac{\delta}{R}\right)_{Approx} = \frac{1}{2} \sqrt{\frac{R}{R_b}} \bar{P} \quad (74)$$

A comparison of the exact and the approximate force deflection curves for three different values of R_b/R is shown in Figure 11.

The agreement is good. On the same graph the solution based on the conical displacement field (Eq. (54)) is shown. It is seen that this solution does not really represent the physical picture of the indentation problem and gives a wrong prediction. Using Eq. (74), an approximate solution can be derived for the critical displacement to rupture. Eliminating the term $\bar{P} R/R_b$ between Eq. (71) and (74) yields

$$\left(\frac{\delta}{R}\right)_{c, Approx} = \frac{1}{2} \sqrt{2 \epsilon_c} \quad (75)$$

Two points have to be made. First, the critical penetration to rupture is only one half of that predicted by the plate strip method, Eq. (73). Second, it is seen that $(\delta/R)_{c, Approx}$ is independent on the bow radius. In order to determine the accuracy of Eq. (75) as compared with the exact solution, Eq. (72), a zoom should be made on the graph shown in Figure 10 for small values of the rupture strain, ϵ_c .

It is seen from Figure 12 that the dependence of the solution for $(\delta/R)_c$ on the ratio of radii R_b/R is rather weak. A better fit of the exact solution is obtained taking a fractional power

$$\left(\frac{\delta}{R}\right)_{c, Approx} = 1.1 \epsilon_c^{0.7} \quad (76)$$

4.4 Extension to a Rectangular Plate and an Eccentric Impact

In Section 3 of this report an equivalence was proved between the plate solution and the plate strip solution. It was shown that each set of strips in the x - and y - directions, respectively, provide one half of the resisting force for a square plate. For application of the axis-symmetric solution derived

above for the problem of deformation of a square plate, it is reasonable to assume that the length of a square plate should be taken equal to the diameter of the circular plate, $2R$.

The above hypothesis can now be extended to derive an approximate solution for an unsymmetric impact on a rectangular plate. Let us denote by R_1, R_2, R_3 and R_4 known distances from the point of impact to the four edges of the plate. The plate resistance, P , is derived from four sets of strips which are clamped respectively at four edges of the rectangular plate, as shown in Figure 13. Thus

$$P' = P'_1 + P'_2 + P'_3 + P'_4 \quad (77)$$

where

$$P'_i = \frac{P_i}{2\pi N_{0i} R_b} \quad (78)$$

is a normalized resisting force of the i -th set of strips. From Eq. (74) each fractional force, P_i , is related to the central displacement δ and distance from the edge R_i by

$$P'_i = \left(\frac{\delta}{R_i} \right)^2 \quad (79)$$

The force-displacement relationship resulting from Eqs. (77 - 79) is

$$P = 2\pi R_b N_0 \delta^2 \left[\frac{1}{R_1^2} + \frac{1}{R_2^2} + \frac{1}{R_3^2} + \frac{1}{R_4^2} \right] \quad (80)$$

In particular, for a square plate subjected to a central impact, $R_1 = R_2 = R_3 = R_4 = R$ Eq. (80) reduces to Eq. (74). In the other extreme when the impact is right on the boundary ($R_i = 0$) the resisting force blows up to infinity (for $\delta > 0$). However, if a direct contact occurs between the bow and the supporting structure, the alternative solution for decks crushing derived in a separate chapter of this report should be used. Therefore, the resisting force will always be finite.

Another way of justifying the above solution is to think of a rectangular plate as being composed of four quarters of a circular plate, see Figure 14.

4.5 Generalization to Orthotropic Plate

Conventional hull plating is reinforced by densely spaced longitudinals. Therefore, the resulting plate/beam combination forms an orthotropic plate in which the fully plastic axial force, N_{0x} in the x -direction is much larger than in the y -direction. In the case of the orthotropic plate Eq. (77) holds but one has to differentiate between the plastic membrane strengths in the x - and y -directions. Thus

$$\frac{P_1}{2\pi R_b N_{0y}} = \left(\frac{\delta}{R_1} \right)^2 \quad (81)$$

$$\frac{P_2}{2\pi R_b N_{0x}} = \left(\frac{\delta}{R_2} \right)^2 \quad (82)$$

$$\frac{P_3}{2\pi R_b N_{0y}} = \left(\frac{\delta}{R_3} \right)^2 \quad (83)$$

$$\frac{P_4}{2\pi R_b N_{0x}} = \left(\frac{\delta}{R_4} \right)^2 \quad (84)$$

The resulting force-deflection relation is still parabolic in δ but coefficients are different

$$P = 2\pi R_b \delta^2 \left[N_{0x} \left(\frac{1}{R_2^2} + \frac{1}{R_4^2} \right) + N_{0y} \left(\frac{1}{R_1^2} + \frac{1}{R_3^2} \right) \right] \quad (85)$$

The above equation reduces to Eq. (80) in the case of the isotropic plate, $N_{0x} = N_{0y} = N_0$.

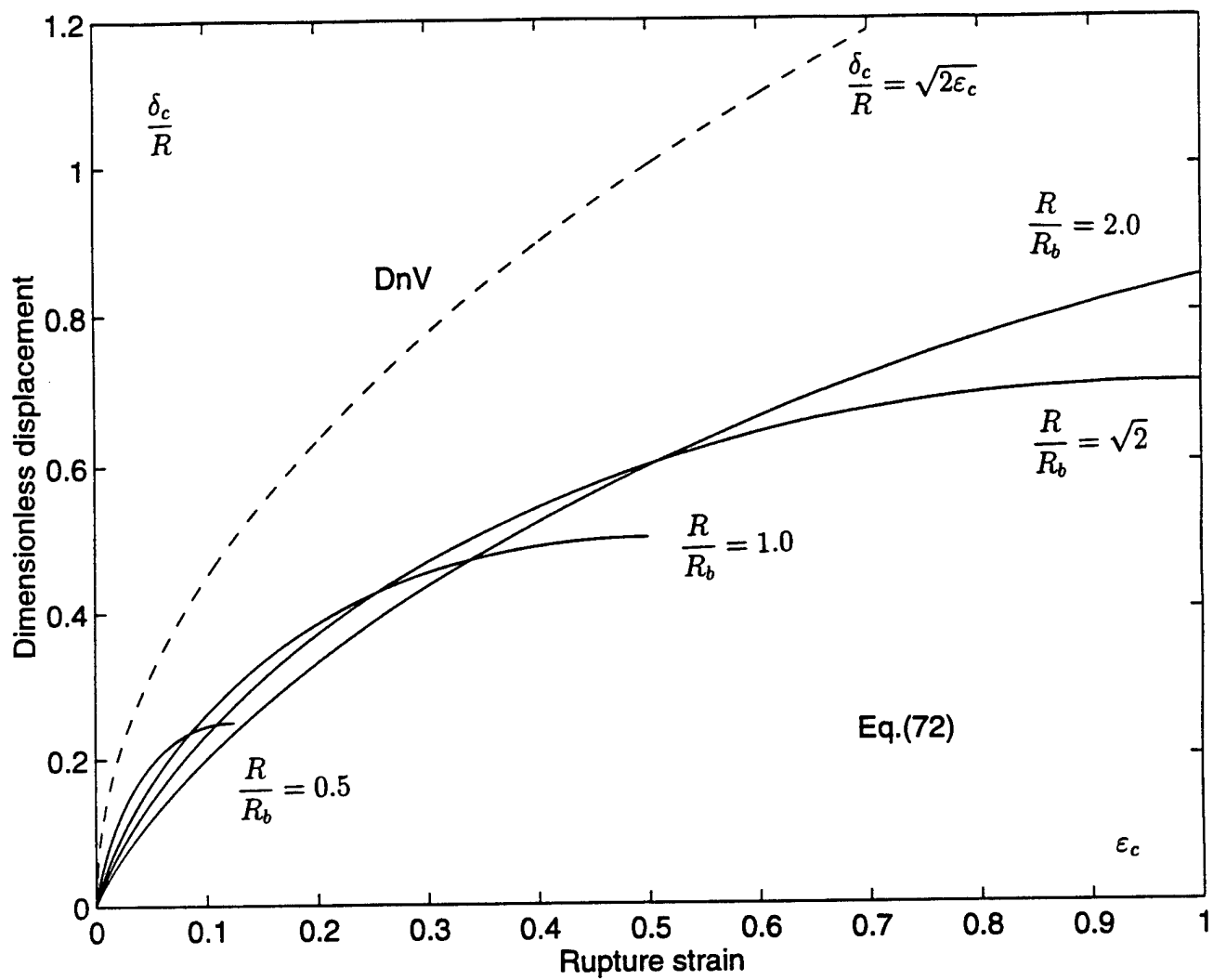


Figure 10: Critical penetration to rupture

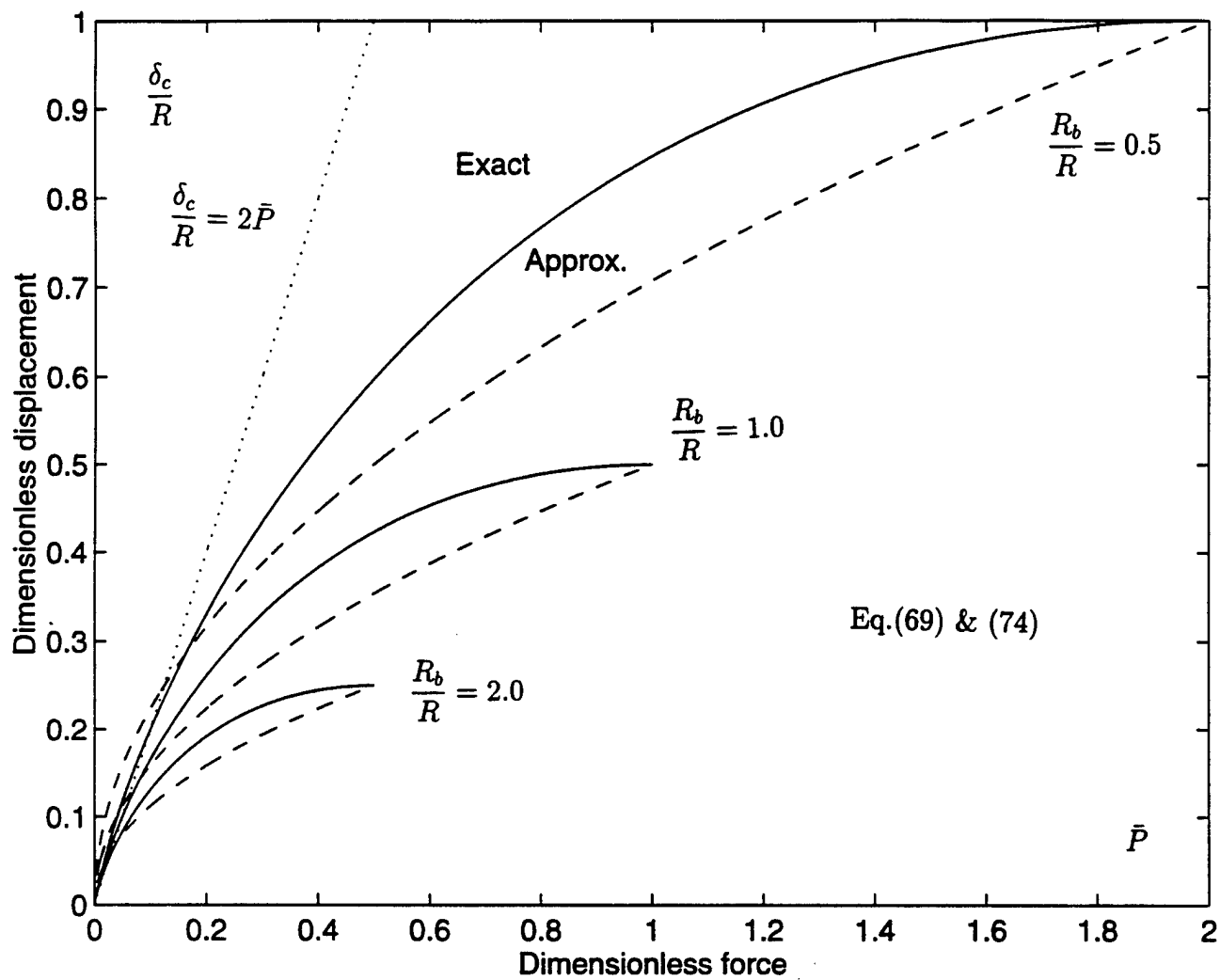


Figure 11: Load-deflection curves. Comparison between exact and approximate solutions

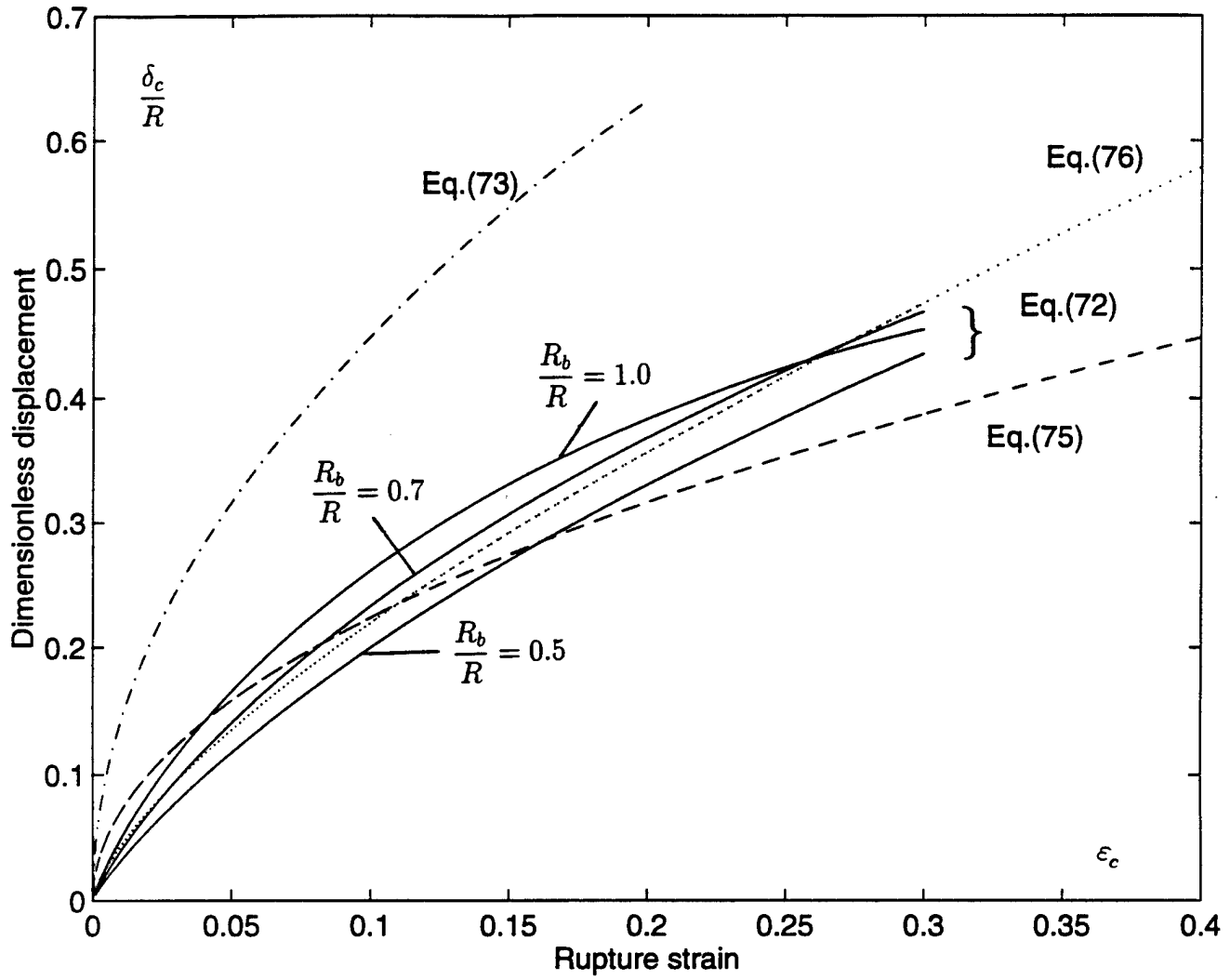


Figure 12: Critical penetration to rupture

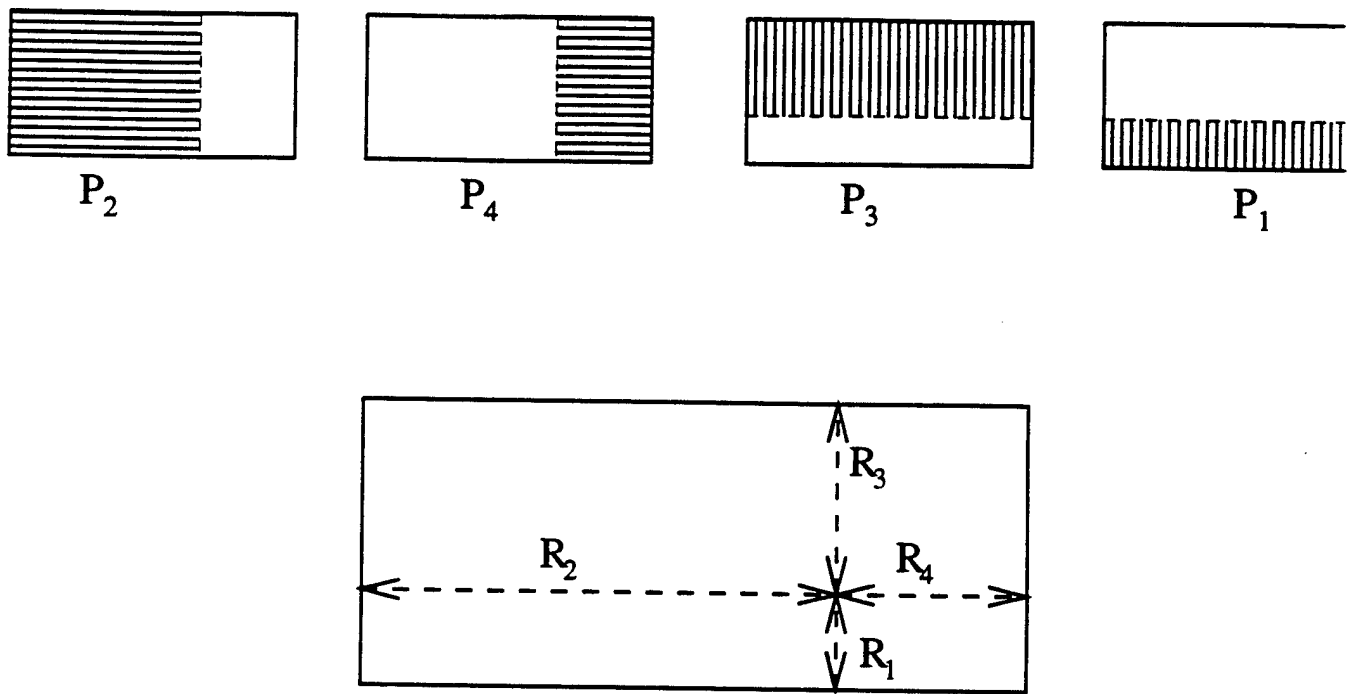


Figure 13: Eccentric impact on a rectangular plate

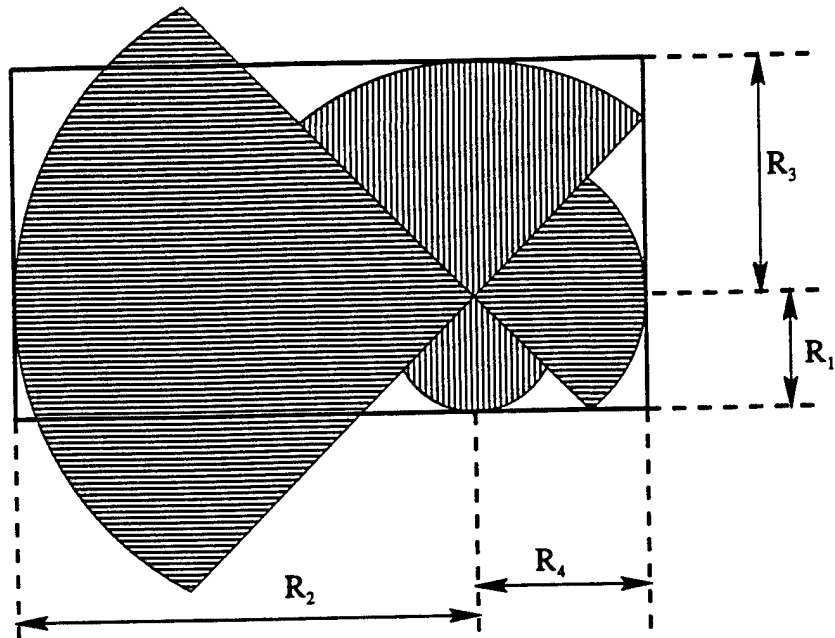


Figure 14: Application of circular plate solution to the problem of eccentric indentation into a rectangular plate

5 Punch Indentation into a Deck

5.1 Theory

Consider a portion of a deck between two transverse frames subjected to an in-plane load, P . The load is exerted for example by the bow of a colliding ship. The width of the plate is $2l$ and the height in the x -direction is long enough so that the remote boundary condition does not have any effect on the solution.

Drop wedge experiments on plates were performed among others by Vaughan, [8], [9], and Jones and Jouri, [4]. It was observed that initially the plate was folding in front of the indenter with a characteristic wavelength, H . For higher values of the impact kinetic energy fracture was initiated either at the plate symmetry line ($y = 0$) under the wedge or, more likely, at the clamped edge $y = +/ - l$. The process of wedge indentation in the so called central separation mode has been discussed in great details in the Report # 1 of the present Collision Project. At the same time fracture of the plate at the clamped boundaries give rise to the process of a concertina tearing which was studied in great details in previous publications by Wierzbicki, [10], Atkins, [2], and Trauth, [6].

The present study is concerned with the initial stage of plate indentation before onset of fracture. A solution of a similiar problem was derived by Choi et. al. [3]. However the height of the web girder b , was smaller than the length l and the wavelength H was assumed to be equal to a given fraction of b . In the present formulation H is one unknown of the problem.

Upon loading the plate buckles and folds in front of the indenter causing bending and membrane stretching of the deformed part of the plate. The global equilibrium is expressed via the balance of power

$$P \dot{\delta} = \dot{E}_m + \dot{E}_b \quad (86)$$

where \dot{E}_m and \dot{E}_b denote respectively rates of bending and membrane energies, and δ is punch displacement. A kinematically admissible displacement field is assumed consisting of four triangles, as shown in Figure 15. Bending dissipation is confined to six straight stationary hinge lines so that

$$\dot{E}_b = 8M_0 l \dot{\theta} \quad (87)$$

where

$$M_0 = \frac{2\sigma_0}{\sqrt{3}} \frac{t^2}{4} \quad (88)$$

is the fully plastic plane strain bending moment per unit length and $\dot{\theta}$ is the rotation rate at the plastic hinge. Because $H < l$ it is assumed for simplicity that the length of all hinge lines is the same and equal to l . Because decks are welded to side shell plating, it is assumed that bending energy is dissipated also by the leading edge of the plate.

From the kinematics of the problem the punch displacement δ is related to the rotation angle θ by

$$\delta = 2H(1 - \cos\theta) \quad (89)$$

Upon complete folding $\delta = 2H$ and $\theta = \pi/2$. Then the bending energy obtained by integrating Eq. (87) is

$$E_b = 4\pi M_0 l \quad (90)$$

The main contribution to the membrane energy dissipation is in-plane stretching in the y -direction. The approximate expression for the rate of membrane energy, which retains ε_{yy} but neglects the two other components of the strain rate tensor is

$$\dot{E}_m = \int_S N_0 \dot{\varepsilon}_{yy} dS \quad (91)$$

where

$$N_0 = \frac{2\sigma_0}{\sqrt{3}} t \quad (92)$$

is the fully plastic (plane strain) membrane force per unit length. In the present kinematically admissible model the strain rate is uniform in the y -direction but vary in the x -direction proportionally to the "gap" opening shown in Figure 16. However, it was shown in [3] that an average strain can be taken as the strain at $x = 0$, see Figure 17. I.e.

$$\varepsilon_{av} \approx \varepsilon_{yy}(x = 0) = \frac{1}{2} \left(\frac{\delta}{l} \right)^2 \quad (93)$$

The resulting strain rate is

$$\dot{\epsilon}_{yy} = \frac{\delta \dot{\delta}}{l^2} \quad (94)$$

and the area of the deforming region is

$$S = 4 H l \quad (95)$$

Substituting Eq. (94) and Eq. (95) into Eq. (101) one gets

$$\dot{E}_m = 4 H l N_0 \frac{\delta \dot{\delta}}{l^2} = 4 N_0 \frac{H}{l} \delta \dot{\delta} \quad (96)$$

Eq. (96) can be integrated in time to give

$$E_m = 2 N_0 \frac{H}{l} \delta^2 \quad (97)$$

The membrane energy increases with penetration depth δ and attains maximum at $\delta = 2H$:

$$(E_m)_{max} = 8 N_0 \frac{H^3}{l} \quad (98)$$

Substituting expressions for \dot{E}_b and \dot{E}_m into Eq. (86), the equation for rate of energy balance becomes

$$P \dot{\delta} = 8 M_0 l \dot{\theta} + 4 N_0 \frac{H}{l} \delta \dot{\delta} \quad (99)$$

Expanding Eq. (89) in a Taylor series and taking two term approximation gives

$$\delta = H \theta^2 \quad (100)$$

and

$$\dot{\delta} = 2 H \theta \dot{\theta} \quad (101)$$

From which

$$\dot{\theta} = \frac{\dot{\delta}}{2 \sqrt{H \delta}} \quad (102)$$

From Eqs. (99, 102) the instantaneous indentation force is found to be

$$P(\delta) = 4 M_0 \frac{l}{\sqrt{H\delta}} + 4 N_0 \frac{H\delta}{l} \quad (103)$$

where the length of the folding wave H is still to be determined. Experiments show that once hinge lines are formed, they stay fixed for the duration of the process. Therefore the magnitude of H can be found from the energy balance equation that does not involve the current indentation depth, δ ;

$$P_m 2H = E_b + E_m \quad (104)$$

where P_m is the so called mean indentation force. Using Eqs. (90, 98) yields

$$P_m = 2\pi M_0 \frac{l}{H} + 4 N_0 \frac{H^2}{l} \quad (105)$$

or

$$\frac{P_m}{M_0} = 2\pi \frac{l}{H} + 16 \frac{l}{t} \left(\frac{H}{l} \right)^2 \quad (106)$$

It is postulated that H adjusts itself so as to minimize the mean indentation force. Indeed, an analytical minimum of P_m with respect to H exists and this occurs at

$$H = \sqrt[3]{\frac{\pi}{16} l^2 t} = 0.58 \sqrt[3]{l^2 t} \quad (107)$$

Eliminating the wavelength H from Eq. (103), the final expression for the indentation force becomes

$$P = \sigma_0 t^2 \left[\frac{1.51(l/t)^{1/6}}{\sqrt{\delta/l}} + 2.68 \left(\frac{l}{t} \right)^{2/3} \frac{\delta}{l} \right] \quad (108)$$

The indentation force starts at infinity for $\delta = 0$, attains a minimum

$$P_{\min} = 3.45 \sigma_0 t^{5/3} l^{1/3} \quad (109)$$

at

$$\delta = 0.43 t^{1/3} l^{2/3} = 0.74 H \quad (110)$$

and then increases with δ . In reality there is a cut-off value at the beginning of the indentation process determined by the buckling or initial yield load, P_0 .

The present solution should be compared with the earlier concertina tearing solution, which in the present notation is

$$P_{conct} = 6.7 \sigma_0 t^{5/3} l^{1/3} \quad (111)$$

At some penetration the deformation mode will change from the denting shown in Figure 15 to the concertina tearing mode. Assuming that this transition takes place when the reaction force from Eq. (108) reaches the level of the mean concertina tearing force from Eq. (111) the penetration of transition becomes

$$\delta_{tran} = 2.11 t^{1/3} l^{2/3} \quad (112)$$

5.2 Application Example

Consider a supertanker with the following dimensions

Distance between transverse frames, $2l$:	4880 mm
Plate thickness, T :	19.1 mm
Flow stress, σ_0 :	320 Mpa

Using the theory above, at force-deflection curve can be generated:

From Eq. (111), P_{conct} =	3.94 MN
From Eq. (109), P_{min} =	2.03 MN
From Eq. (107), H =	281 mm
From Eq. (110), δ_{min} =	208 mm
From Eq. (112), δ_{tran} =	1023 mm

A plot of the force - deflection relationship is shown in Figure 18. The resisting force is seen to drop rather rapidly to its minimum value $P = 2.03 \text{ MN}$ which is reached at a relatively small indentation depth of $\delta_{min} = 0.208 \text{ m}$. Then the force is gradually increasing and at $\delta_{tran} = 1.023 \text{ m}$ it attains a value $P_{conct} = 3.94 \text{ MN}$ corresponding to a constant mean indentation force in the concertina tearing mode.

5.3 Generalization for the Unsymmetric Indentation

This problem can be easily treated using the previously derived solution and considering a sum of rate of energies and energies corresponding to the left and right portion of the plate, Figure 19.

The expression for the mean crushing force becomes

$$\frac{P_m}{M_0} = \pi \frac{l_1 + l_2}{H} + 8 \frac{H^2}{t} \left(\frac{1}{l_1} + \frac{1}{l_2} \right) \quad (113)$$

The length of the folding wave obtained by minimizing Eq. (113) with respect to H is

$$H_{1,2} = \sqrt[3]{\frac{\pi}{16} l_1 l_2 t} \quad (114)$$

which reduces to Eq. (107) if $l_1 = l_2 = l$.

On comparing Eq. (114) with its counterpart, Eq. (107), it is clear that the wavelength in an unsymmetric collision is shorter than the one in the symmetric collision.

The solution for the instantaneous indentation force, generalized to the case of an unsymmetric collision takes the form:

$$P = \sigma_0 t^2 \left\{ 0.757 \left(\frac{l_1 l_2}{\delta} \right)^{1/2} \left(\frac{\sqrt{l_1 l_2}}{t} \right)^{1/6} \left[\sqrt{\frac{l_2}{l_1}} + \sqrt{\frac{l_1}{l_2}} \right] + \dots \right. \\ \left. 1.34 \left(\frac{\sqrt{l_1 l_2}}{t} \right)^{2/3} \left[\frac{\delta}{l_1} + \frac{\delta}{l_2} \right] \right\} \quad (115)$$

The effect of the unsymmetry of the loading can be determined by dividing Eq. (115) by Eq. (108). The plate resistance is least for the symmetric collision and it increases with the amount of load eccentricity.

5.4 Second and Subsequent Folds

With the increasing indentation depth the tensile strain is getting larger and attains a maximum at $\delta = 2H$. The maximum average strain is then

$$\epsilon(\delta = 2H) = \frac{1}{2} \left(\frac{2H}{l} \right)^2 = 0.67 \left(\frac{t}{l} \right)^{2/3} \quad (116)$$

Taking values used in our numerical example this gives the strain $\epsilon_{max} = 0.027$. Although the maximum strain is larger (see Figure 17), this strain will most probably not lead to fracture for most structural steel. Therefore a second and possibly subsequent folds could be formed. It can be noted that the contribution of the bending energy (which was only 18 energy in the first field) becomes smaller and smaller and for all practical purposes it can be neglected in the process of the second fold formation.

An approximate expression for the indentation force during the formation of the second fold is

$$P = \sigma_0 t^2 2.68 \left(\frac{l}{t} \right)^{2/3} \left\{ \frac{\delta}{l} + \frac{\delta - 2H}{l} \right\} \quad (117)$$

This can be further generalized for an arbitrary number of fields, N (one field corresponds to a punch travel distance equal to $2H$).

$$P_N = \sigma_0 t^2 2.68 \left(\frac{l}{t} \right)^{2/3} \frac{1}{l} N[\delta - (N - 1)H] \quad (118)$$

For a large indentation depth N can be treated as a continuous variable

$$N = \frac{\delta}{2H} \quad (119)$$

Using Eq. (107) and Eqs. (118, 119), the indentation force can be put into the following simple form

$$P_{sym} = 1.16 \sigma_0 t l \left(\frac{\delta}{l} \right)^2 \quad (120)$$

The generalization to the unsymmetric impact is straightforward. Recalling Eq. (115) for the first fold solution and taking only the membrane resistance, the counterpart of Eq. (120) is

$$P_{unsym} = 0.58 \sigma_0 t (l_1 + l_2) \left(\frac{\delta^2}{l_1 + l_2} \right) \quad (121)$$

which reduces to Eq. (120) when $l_1 = l_2 = l$. It should be mentioned that the above solution loses its validity as $l_1 \rightarrow 0$, $l_2 \rightarrow 2l$ ($l_1 + l_2 = 2l$). Clearly, a different failure mode must be activated if the impact point is too close to

the clamped edge of the plate. A consideration of such a new mode would require a detailed analysis of hard point fracture which is beyond the scope of the present project.

5.5 Mode Transition

The present solution is valid until the first fracture occurs at the most strained fiber (strain criterion) or the force attains a level necessary to activate the concertina tearing mode (force criterion). In view of an uncertainty in deciding on the value of the critical strain to rupture, the force criterion is preferable.

The solution for the concertina tearing mode, extended to the unsymmetric loading is

$$P_{conct} = 4 \sigma_0 t^2 \left[\frac{4l_1 l_2}{t(l_1 + l_2)} \right]^{1/3} \quad (122)$$

The switching point between the initiation mode, Eq. (121), and the concertina tearing mode, Eq. (122), occurs at

$$\delta_c = 3.31 t^{1/3} \left(\frac{l_1 l_2}{l_1 + l_2} \right)^{2/3} \quad (123)$$

In particular, for a symmetric impact the critical indentation depth is

$$\delta_c = 2.08 t^{1/3} l^{2/3} \quad (124)$$

Using the values in the numerical example, Eq. (124) gives $\delta_c = 1.01 m$ which is realistic.

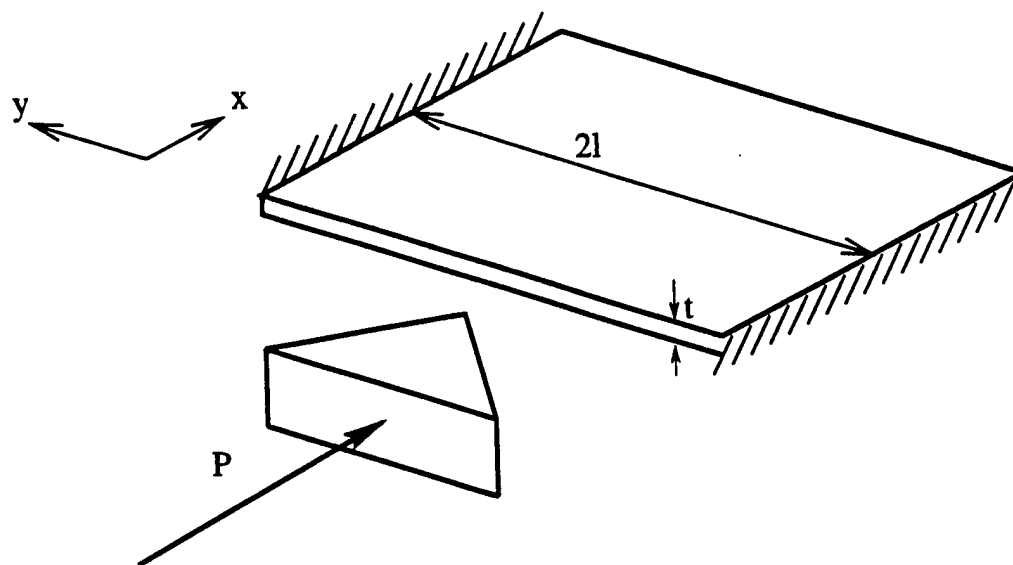


Figure 15: Problem definition sketch for punch indentation into a deck

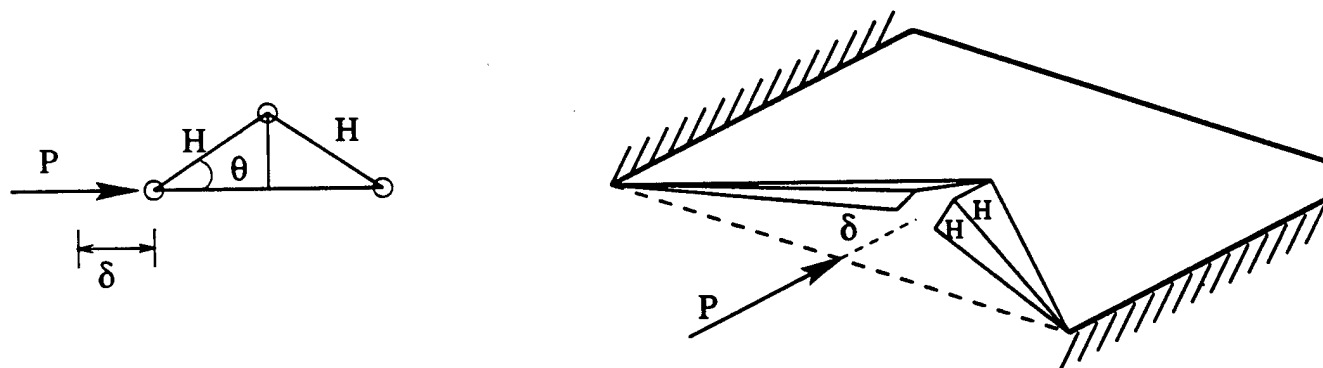


Figure 16: Assumed simplified deformation mode

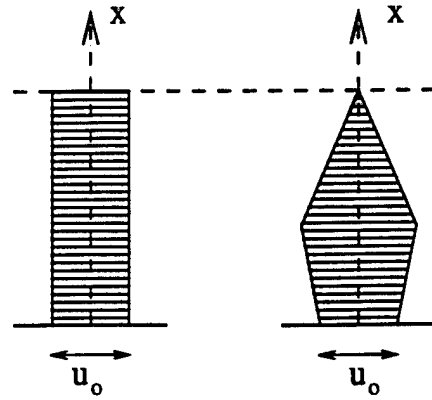


Figure 17: Assumption of average membrane strain

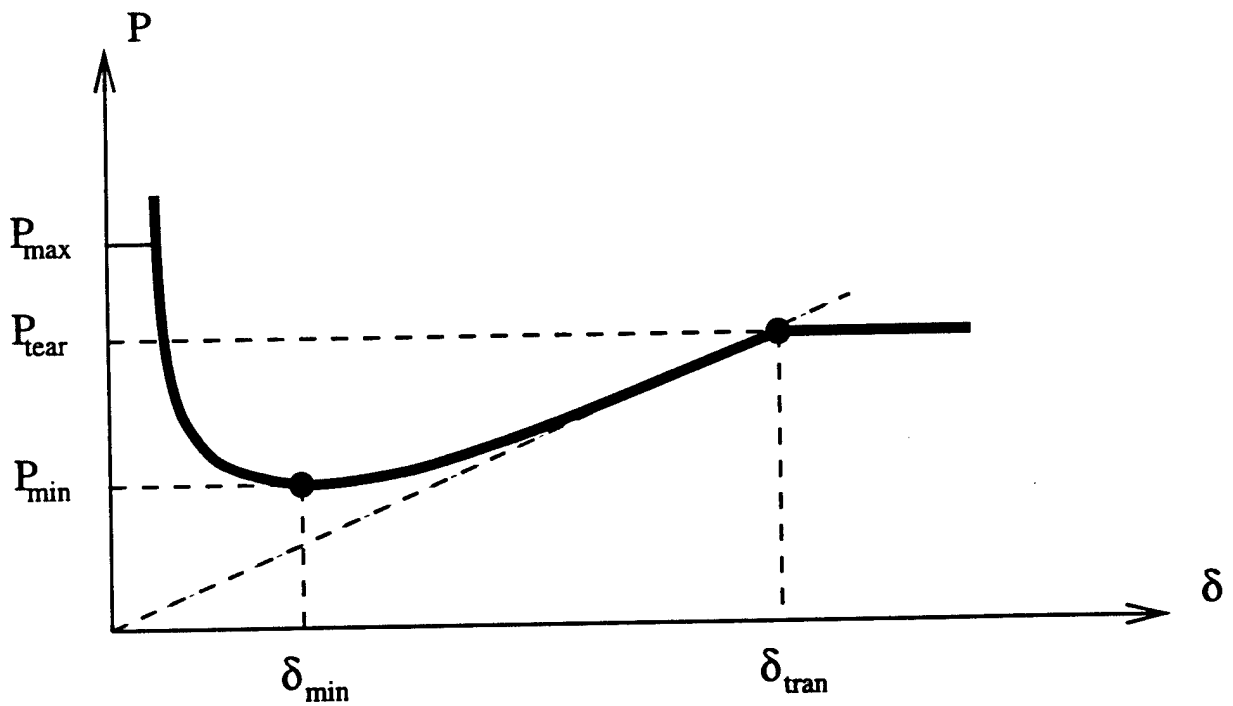


Figure 18: Sketch of force-deflection relationship for punch indentation into a deck

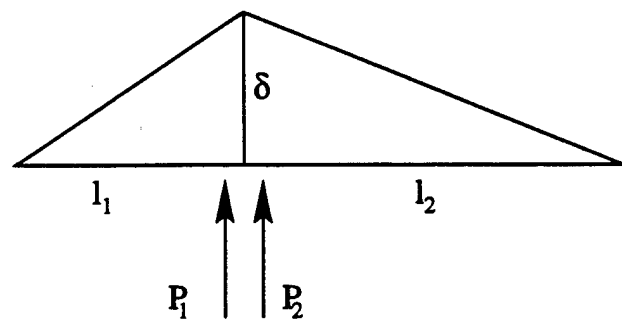


Figure 19: Unsymmetric loading

References

- [1] Jørgen Amdahl and Dag Kavlie. Experimental and numerical simulation of double hull stranding. *DNV-MIT Workshop on Mechanics of Ship Collision and Grounding*, 1, 1992. Edited by O. Astrup.
- [2] A. G. Atkins. A single curl failure of metal plates in ship grounding. Technical Report 17, Joint MIT-Industry Program on Tanker Safety, June 1993.
- [3] Sung K. Choi, T. Wierzbicki, Oystein Goksyr, and Jennifer Culbertson-Driscoll. Crushing resistance of a web girder with application to ship structures. *Joint MIT-Industry Project on Tanker Safety*, 38, 1994.
- [4] N. Jones and W. S. Jouri. A study of plate tearing for ship collision and grounding damage. *J. Ship Res.*, 31(253), 1987.
- [5] R. Thunes. Development of analytical models of wedge indentation into unidirectionally stiffened and orthogonally stiffened double hulls. Technical Report 21, Joint MIT-Industry Report, Tanker Safety, 1994.
- [6] K. A. Trauth. Validation of concertina tearing solution. Technical Report 34, Joint MIT-Industry Program on Tanker Safety, June 1994.
- [7] Pieter J. van der Weijde and Eberhart Haug. A concept of hybrid analytical-numerical method for collision and grounding simulations. *DNV-MIT Workshop on Mechanics of Ship Collision and Grounding*, 1, 1992. Edited by O. Astrup.
- [8] H. Vaughan. Bending and tearing of plate with application to ship bottom damage. *The Naval Architect*, 3:97-99, May 1978.
- [9] H. Vaughan. The tearing of mild steel plate. *J. Ship Research*, 24(96), 1980.
- [10] T. Wierzbicki. Concertina tearing of metal plates - improved solution and comparison. *Joint MIT-Industry Project on Tanker Safety*, 22, 1994.

**RUPTURE ANALYSIS OF OIL TANKERS IN A SIDE COLLISION: HARD
POINT FRACTURE OF SHELL PLATING**

F.A. McClintock and J. Atmadja, Massachusetts Institute of Technology

Abstract

Hulls of ships in groundings and collisions, and hulls of aircraft in hard landings, tend to fracture at hardpoints such as bulkheads. An analysis shows that this can happen by the buckling of stiffeners on the inside of a bend at the hardpoint, weakening that site and concentrating further deformation there. Reinforcements can reduce the effect.

For unstiffened plates, finite element analysis for power-law strain-hardening with exponent $n = 0.15$ shows a 45% loss in extension to maximum load when the hull plating is built-in to a rigid bulkhead, but only a 5% loss for a plate that is fillet-welded to a quarter-infinite, yielding bulkhead. At maximum load, the maximum local equivalent strain reaches 0.5, but even that does not seem to be enough to have initiated prior fracture in ship steels, or other steels with yield strengths less than $Y/E = 0.005$. A two-flange lumped-parameter model duplicates some, but not all aspects of the finite element results.

Appendices give the conditions for plane strain necking of a power-law hardening plate with pre-strain and procedures for fitting a power-law relation with or without pre-strain to a variety of tensile data. Fits to the tensile strength and beyond, without pre-strain, require data on the uniform strain or the fracture stress and strain, and should not be fitted to the yield strain.

1. Introduction

Resistance to fracture is important in the collisions of ships because the resisting forces will be much greater and the extent of damage much less if the structural members of the ship, and the joints between them, remain intact. This is true even though the work absorbed in tearing a member or a joint is small compared to the total work of deformation. That is, the effect of the integrity of a member or joint on the extent of damage is disproportionately large compared to the fraction of total work that goes into tearing a member or joint. Put another way, the work of deformation is not a unique indicator of the damage.

An important mechanism of hull fracture in collisions is the stretching of the side shell between relatively rigid bulkheads until the shell necks. The shell is so thin compared to its span between supports that once it necks, the further deformation to fracture is negligible. Preliminary finite element calculations by Atmadja (1995) showed that this necking occurs before expected from the stretching of a flat plate. It forms at hardpoints such as bulkheads, where the shell is rigidly attached and there is bending as well as stretching. Furthermore, these calculations showed very high strain concentrations that might lead to fracture even before necking, especially in view of the reduction in ductility under plane strain conditions (Clausing 1970). Such fracture at bulkheads has been observed in stricken ships and also in aircraft fuselages after hard landings (e.g. Fig. 1a, b). The task here is to predict the conditions that lead to such premature fracture. Once that is done, one can consider whether and how design can increase the deformation that the struck ship can withstand before necking and fracture of its plating.

Although many authors have studied the necking of sheets under combined in-plane loading, the superposition of bending is relatively rare. Swift (1948) used deformation theory plasticity (actually non-linear elasticity) to get a closed form solution for combined bending and stretching in plane strain deformation without necking. Deformation theory plasticity is a good approximation to actual flow theory plasticity only for radial loading, with the bending in proportion to the extension. Here the loading is not radial, because the bending angle at first increases linearly with the displacement normal to the plate, whereas the extension increases approximately as the square of the displacement. Hill (1950) pp. 292-294 followed Swift in assuming constant tension and

only the final state, with uniform thinning. Hill considered the non-hardening case, and reviewed Swift's results.

Giovanola et al. (1990) studied the dynamic pressure loading of plates with clamped and axially restrained ends, resulting in stretching of the plates and bending at their ends. Their finite element calculations and tests simulated the deformation and fracture of externally stiffened shells, so the tensile side of the bend, where the fractures began, had the extra strain concentration of the welds between shell and external ribs. The ratio of total span to thickness was only 14, much less than the value of 125 chosen here as typical of tankers. No analysis seemed likely; that lack, with the extra strain concentration on the tensile side of the bends due to the welds, prevents extrapolating their results to the smooth side plating of a ship.

Necking in sheets being drawn out from between clamping faces, around a fixed radius of curvature, were studied by McClintock, et al. (1993). In contrast to the ship collision problem, the tensile load was constant while the curvature increased to a limiting value. They found the bending moment reached a maximum at a strain of twice the strain-hardening exponent, rather than a strain approximately equal to the exponent, as in tension. More precisely, the strain for transverse necking in a plate of power-law hardening material ($\bar{\sigma} = \sigma_1 \bar{\epsilon}^n$) occurs at an in-plane strain of $\epsilon_x = n$ or an equivalent plastic strain of $\bar{\epsilon} = 2n/\sqrt{3}$ (e.g. McClintock and Zheng 1993).

The work here includes three parts, all under the history of increasing stretching and bending typical of a striking ship hitting half-way between bulkheads:

- a) Finite element studies of strain concentrations and necking in plates with various forms of compliance at the supports.
- b) Lumped parameter estimates of such hardpoint necking.
- c) Effects of stiffener buckling under tension-induced bending.

2. Finite element studies of effects of strain hardening and of compliance at hard point supports

Finite element method. Studies were made of the part of a shell plate running from a hardpoint out to the quarter span. At the quarter span there was assumed to be a center of 180° rotational symmetry, as shown in Fig. 2. The ratio of quarter-span to thickness was 31.7, typical of that in a VLCC. The program ADINA (1992) was used with automatic time stepping, large displacements, iterations to a tolerance of equivalent plastic strain

increment of 0.001, and 30 to 40 steps to peak load. The 9/3-mixed displacement-pressure elements satisfy infimum-supremum conditions (Bathe 1996). The material was assumed to be power-law hardening with no pre-strain ($\epsilon_0 = 0$) and exponents of $n = 0.1, 0.15$, or 0.2 . For simplicity in applying the deformation, the six elements at the quarter span were nearly rigid. The center node was translated but left free to rotate. As shown in Fig. 2, the resulting thinning is uniform along the plate except at the ends. The rigidity at the quarter span had little effect on the average strain in the plate and even less on the localization process at the built-in end.

The mesh had six elements through the thickness of the plate. The elements were square for the first six or eight elements at the ends, and then graded to six-to-one rectangles in the central 3/4 of the span, where the strain gradients essentially vanished. The lack of constraint due to element size was verified by pure plane strain stretching, in which necking occurred when expected. (With subsequent reduction of thickness by a factor of two in the neck, however, the elements became highly deformed and the loads fell more slowly than expected for a continuum. Eventually the program stopped due to excessive distortion of an element.)

Output consisted of not only the deformed mesh and the total in-plane load, but also the contours of accumulated equivalent plastic strain, as shown in Fig. 3 at the maximum in-plane load for $n = 0.2$. By hindsight, plotting principal strain rosettes would have shown any regions of compression or significant shear strain. The peak strain was calculated from the measured deformation of the corresponding element. With typical ship construction, fillet welds do not penetrate between the plating and bulkhead, leaving a gap of less than 1-2 mm. Note from Fig. 3 that the apparent absence of shear distortion along the line of the gap (an extension of the inner surface of the plate) means that omitting the gap in the finite element mesh, to simplify the input, had negligible effect on the necking or peak strain.

Finite element results. Three in-plane load-deformation curves are plotted in Fig. 4. They are the curves in the labels for the strain-hardening exponents: $n = 0.1, 0.15$, and 0.2 . (The two shorter curves will be discussed below, in connection with the lumped-parameter model of Fig. 6.) For comparison with in-plane extension of a plate, the loads are normalized in terms of the maximum load for in-plane, laterally plane strain tension, derived in App. 1. The maximum loads for bending at a hard point have been reduced from those for a straight plate by only 1% for $n = 0.2$ to 3% for $n = 0.1$.

The in-plane true (logarithmic) strain at maximum load, ϵ_x , is the strain hardening exponent n , from App. 1 for $\epsilon_0 = 0$. The corresponding elongations at maximum load are $e = (L - L_0)/L_0 = \exp(n) - 1 = 0.11, 0.16$, and 0.22 . From Fig. 4, for plates bent and stretched between hardpoints, the elongations to maximum load have been reduced from the in-plane values by factors of 2.0, 1.8, and 1.5. The corresponding bend angles,

$$\theta = \cos^{-1} \left[\frac{1}{1 + (L - L_0)/L_0} \right] = \cos^{-1} \left[\frac{1}{1 + e} \right], \quad (1)$$

are reduced less dramatically, from $\theta = 25^\circ$ to 17° for $n = 0.1$, from $\theta = 31^\circ$ to 23° for $n = 0.15$, and from $\theta = 35^\circ$ to 28° for $n = 0.2$.

The beneficial effects of plastic compliance at the hardpoint on the in-plane load-elongation curve are shown in Fig. 5 for $n = 0.2$ and summarized in Table 1 for all three exponents. As reference results, to the far right of Fig. 5 (the first column of Table 1) is the curve for plane strain tension, with no bending. Ending at the far left of Fig. 5 (the second column of Table 1) is the curve for a plate rigidly built-in at its end, which also appeared in Fig. 4.

The primary effect of plastic compliance is an increase in extension to peak load, rather than in the peak load itself. Joining the shell plate to a quarter-infinite bulkhead gives only a small increase in elongation to peak load. Including a deforming 45° fillet weld on the inside of the bend, along with a deforming bulkhead, brings the elongation nearly up to that of a free plate. The harder, unyielding fillet surprisingly gave more ductility, but the effect is too small to be of concern.

The largest effects, even with compliant hardpoints, are on the strain concentrations at the outside of the bend. These are summarized in Table 1 as maximum local equivalent strains, along with the principal load-deformation results described above. A typical ship steel, LR-EH36, with a yield strength of 398 N/mm^2 and a tensile strength of 563 N/mm^2 , had a total elongation of 0.23 . The uniform elongation would be less. Fitting a power-law curve with $\epsilon_0 = 0$ gives exponent of $n = 0.10 - 0.17$ (App. 2, Table A2.1). For these exponents, even with the ameliorating effect of a fillet weld, Table 1 indicates that the equivalent strain at the location of incipient necking would be $\bar{\epsilon} = 0.4$ to 0.5 . Would these levels of plane strain cause fracture?

Unfortunately few data on fracture strain are available. Not even the reduction of area, characterizing fracture in the uniaxial tensile test, is commonly reported for steels.

(Reporting the reduction of area, which can be obtained by hand measurements after fracture, has fallen into disuse with the advent of computer-controlled tensile testing without the simultaneous adoption of automatic optical cross-section measurement and data processing. Incera (1991) developed a successful prototype of such an instrument.) For the seven structural steels reported by Clausen (1970), the equivalent strains at fracture from uniaxial and plane strain tests are summarized in Table 2. He did not include the typical elongation over a gauge length of 4 diameters nor the elongation at the maximum load (the so-called uniform elongation), so a comparison with modern steels can be made only by the strain-hardening exponent calculated from the rather low ratio of yield to tensile strength (see App. 2, Table A2.1). Interpolating in Table 2, however, suggests an equivalent true fracture strain in plane strain, $\bar{\epsilon}_{fp}$, of at least 0.8, so fracture before necking does not appear likely in this case. For higher strength steels ($Y_{0.002}/E > 0.005$), it could become a problem, since the equivalent fracture strains in plane strain drop abruptly in the very high strength alloys used in some aircraft and in naval ships.

3. Lumped parameter estimate of hardpoint necking

For more direct physical insight than is given by finite element analysis, and possibly to develop a simpler tool for use in design, consider the lumped-parameter model of Fig. 6 for the behavior of a plate at a hardpoint, with two-flanges in a curved section that is in series with a straight plate, all of power-law hardening material.

Initially, as a hull is indented, the deformation is primarily in bending, so the inner surface of the plate at the hardpoint is in compression. As the indentation proceeds, the deformation in the plate becomes predominantly tensile, requiring a stress reversal. There is such a reversal also in the flanges representing the bend at the hard point, but it turns out to occur at such low bend angles that the prior compression can be ignored.

Boundary conditions from the straight plate. The extension in the straight plate is negligibly affected by that in the short curved flanges that represent the bending at the ends of the straight plate, for the typical ratio of total span to thickness of 127 considered here. Then the in-plane elongation in the straight part of the plate depends only on the bend angle θ , as in Eq. 1:

$$e_s = \frac{L - L_0}{L_0} = \frac{1}{\cos \theta} - 1 ; \quad \epsilon_s = \ln(1 + e_s) = \ln\left(\frac{1}{\cos \theta}\right) . \quad (2)$$

Table 1. Effects of a hardpoint, from finite element analysis

e	linear strain in central region of plate, $(L - L_0)/L_0$	ϵ_x	true axial strain in central region of plate, $\ln(L/L_0) \approx \ln(1/\cos\theta)$
P	in-plane plate load	$\bar{\epsilon}$	equivalent (Mises) strain; in plate, $\bar{\epsilon} = 2\epsilon_x/\sqrt{3}$
P_{nrm}	$wt_0TS(2/\sqrt{3})^{1+n}$	θ	bend angle of central region of plate
t_0	original plate thickness	$\bar{\sigma}$	equivalent (Mises) flow strength; in plate, $\bar{\sigma} = \sqrt{3}\sigma_x/2 \dots \bar{\sigma} = Y_1 \bar{\epsilon}^n$
TS	uniaxial tensile strength, $Y_1 n^n e^{-n}$		
w	width of plate		


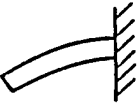



Case	Plane strain tension	Built-in support	Bulkhead	Fillet weld, $d/t = 0.45$	
				Homogen.	Unyielding
					
<u>$n = 0.1$</u>					
P_{max}/P_{nrm}	1.00	0.96		0.96	
Bending $\theta, ^\circ$	0	17.2		18.8	
$\bar{\epsilon}_{strt. plate}$	0.115	0.062		0.069	
$\bar{\epsilon}_{max}$	0.117	0.62		0.43	
<u>$n = 0.15$</u>					
P_{max}/P_{nrm}	1.00	0.97		0.98	
Bending $\theta, ^\circ$	0	22.6		25.6	
$\bar{\epsilon}_{strt. plate}$	0.173	0.11		0.13	
$\bar{\epsilon}_{max}$	0.177	0.75		0.50	
<u>$n = 0.2$</u>					
P_{max}/P_{nrm}	1.00	0.98	0.98	1.00	1.00
Bending $\theta, ^\circ$	0	27.8	28.1	32.4	33.8
$\bar{\epsilon}_{strt. plate}$	0.23	0.15	0.16	0.20	0.23
$\bar{\epsilon}_{max}$	0.23	0.87	0.85	0.67	0.71

Table 2. Round specimen and plane strain behavior of seven structural steels
From Clausen (1970).

Steel	Yield		Uniax. tens. str., TS N/mm ²	YS / TS	exponent n	Equivalent fracture strain	
	Lower yld. pt. N/mm ²	0.2% offset. N/mm ²				round ¹ $\bar{\epsilon}_{fr}$	plane strain $\bar{\epsilon}_{fp}$
ABS-C	270		429	0.629	0.1418	1.04	0.87
A302-B	371		590	0.629	0.1418	0.98	0.83
HY-80	586		690	0.850	0.0648	1.22	0.99 ²
HY130(T)		938	986	0.951	0.0289	1.06	0.62 ²
18Ni(180)		1227	1289	0.952	0.0285	1.00	0.48
10Ni-							
Cr-Mo-Co		1255	1413	0.888	0.0519	1.16	0.42
18Ni(250)		1710	1772	0.965	0.0232	0.89	0.17

¹At instability. Broken pieces showed more strain.

²Surface cracks appeared at a strain of 0.84 for HY-80, at 0.45 for HY-130(T).

The through-thickness thinning strain in the straight part of the plate, ϵ_t , is found from incompressibility and the lateral plane strain condition, $d\epsilon_z = 0$, to be the negative of the axial strain ϵ_s . Integration gives the thickness:

$$d\epsilon_s + d\epsilon_t + d\epsilon_z = 0 ; \frac{dt}{t} = d\epsilon_t = -d\epsilon_s ; t = t_0 e^{-\epsilon_s} . \quad (3)$$

Simplifications for the bend. Assume that the mean radius of curvature R of the flanges is constant from the hardpoint out to where the plate becomes straight and under pure tension. As the plate is loaded and tilted down, R will decrease and some of the material that was bent will become part of the straight plate. The effect of this residual curvature contributes to a factor F_a , introduced below in Eq. 6. Determine the active radius R from the maximum moment, at the hardpoint.

Geometrical conditions in the bend. For radii of curvature large compared to the thickness t , the usual assumptions of beam theory hold. The axial strains in the inner and outer flanges are related to the mean radius of curvature R and the thickness t , with a factor F_t to account for the effective flange spacing being less than the plate thickness:

$$\frac{F_t t}{R} = \epsilon_u - \epsilon_l \quad . \quad (4)$$

Equilibrium considerations in the bend. Denote the straight plate and the "upper" and "lower" flanges by (*s*), (*u*), and (*l*), and their initial areas by A_0 , $A_0/2$, and $A_0/2$, respectively. Then with thinning of the members as in Eq. 3, x-equilibrium requires

$$\sigma_s e^{-\epsilon_s} \cos \theta = \frac{1}{2} \sigma_u e^{-\epsilon_u} + \frac{1}{2} \sigma_l e^{-\epsilon_l} \quad . \quad (5)$$

Neglect the effects of the shear forces required for y-force equilibrium and for the steep gradients in bending moment near the bend.

For moment equilibrium, to focus on the upper flange take moments about the lower flange. Several approximations for the moment arm are shown in Fig. 7. The actual moment arm a could be greater than that given by the constant circular arc, because the radius of curvature could increase outward from the hardpoint due to decreasing moment. This effect would be reduced by the residual curvature from prior stages of loading. Alternatively, a could be less than that for constant R due to shear, as suggested by finite element studies (see Fig. 2). Allow for the net effect by introducing a factor F_a , which may be either more or less than unity. As in Eq. 4, approximate the separation of the flanges relative to the plate thickness t by a factor F_t . (For a non-hardening plate in pure bending F_t would be $1/2$; for a linearly hardening plate it would be $2/3$.) Then

$$a = F_a R (1 - \cos \theta) + (F_t t / 2) \cos \theta \quad . \quad (6)$$

Equate moments about the line of action of the lower flange at the hardpoint, taking into account the fact that the area of the flange was originally half that of the straight part of the plate and that in plane strain the thinning strain is the negative of the axial strain:

$$a \sigma_s e^{-\epsilon_s} = t F_t \left(\frac{1}{2} \right) \sigma_u e^{-\epsilon_u} \quad . \quad (7)$$

Stress-strain behavior. For simplicity assume uniaxial behavior, since the difference between it and plane strain is only a factor of the order $2/\sqrt{3}$. Assume a power-law stress-strain relation with zero pre-strain. In the straight part of the plate the loading will be

monotonic tension. In the bend, with initial elastic deformation, the contribution of the bending stresses will increase linearly with the deflection, but that of the tensile stresses will increase only quadratically, so the bending stresses will initially dominate. Calculations show that later the tensile stresses dominate. The calculations also show that the transition to tension is early enough so the compressive strains can be ignored. . The general form of the stress-strain relation that allows for either tension or compression can thus be simplified:

$$\sigma = Y_1 \varepsilon |\varepsilon|^{n-1} = Y_1 \varepsilon^n . \quad (8)$$

Method of solution. Assume a given deflection angle θ , which sets the strain ε_s in the plate according to Eq. 2. Eliminate the moment arm a by equating the values of it found from Eqs. 6 and 7. In turn eliminate $F_t t / R$ by substituting its value from Eq. 4:

$$F_a R (1 - \cos \theta) + (F_t t / 2) \cos \theta = (F_t t / 2) \sigma_u e^{-\varepsilon_u} / \sigma_s e^{-\varepsilon_s} ;$$

$$\frac{F_t t}{R} = \frac{2 F_a (1 - \cos \theta)}{\sigma_u e^{-\varepsilon_u} / \sigma_s e^{-\varepsilon_s} - \cos \theta} = \varepsilon_u - \varepsilon_l . \quad (9)$$

For a given plate deflection θ , the plate strain ε_s can be found from Eq. 2. Then with the stress-strain relation Eq. 8 and again the result that the straining in the lower flange is tensile during almost all the deformation, Eqs. 5 and 9 can be expressed as two implicit, nonlinear equations in ε_u and ε_l . Since the strain is much higher in the upper flange, these can be reduced to one implicit equation in one unknown as follows. Set to unity the factor $\exp(-\varepsilon_l)$ for the change in area of the lower flange in Eq. 5. Express σ_l in terms ε_l with the stress-strain relation Eq. 8, noting as before that the straining of the lower flange is tensile over almost all of the deformation. When that is done and Eq. 5 is solved for ε_l , it is convenient to introduce a group of variables β that ultimately depends only on ε_u and θ :

$$\varepsilon_l = [\beta(\varepsilon_u, \theta)]^{1/n} , \text{ where } \beta(\varepsilon_u, \theta) \equiv 2 \varepsilon_s^n e^{-\varepsilon_s} \cos \theta - \varepsilon_u^n e^{-\varepsilon_u} . \quad (10)$$

In Eq. 9, elimination of ϵ_l with Eq. 10 and σ_s and σ_u with the stress-strain relation Eq. 6 gives one implicit equation in the one unknown ϵ_u .

The point of major interest is whether the right hand side of Eq. 5, corrected to the in-plane plate force, will start to drop at some θ , giving necking. Replacing TS/Y_1 by $n^n e^{-n}$ from the tensile test using Eq. A2.4 with zero pre-strain ϵ_0 gives

$$\frac{P}{wt_0 TS} = \frac{1}{(n^n e^{-n}) 2 \cos \theta} \left[\epsilon_u^n e^{-\epsilon_u} + \epsilon_l |\epsilon_l|^{n-1} e^{-\epsilon_l} \right] . \quad (11)$$

$P/(wt_0 TS)$ is plotted in Fig. 4, along with the finite element results, for $n = 0.1$ and 0.2 . The curves for the line-of-action factors $F_a = 1.0, 0.5, 0.25$ (see Fig. 7) are indistinguishable from each other, except for ending at progressively higher plate elongations, as indicated by the short vertical lines.

Discussion of lumped-parameter model. The two lumped-parameter curves of Fig. 4 lie close to the finite element ones except that even for F_a as short as 0.25 they give load drops at half the elongations found from the finite element studies. A line of action of $F_a = 0.25$ corresponds to intense shear, neglected in this model but suggested by the deformed mesh of Fig. 2. Thus the lumped-parameter model gives the correct order of magnitude for the load drop, and the proper dependence on strain hardening, but is not quantitatively accurate. This is especially true for the effects of plastic compliance at the support point.

An alternative model of a linearly hardening plate under predominant bending was studied. It gave large strains, but not an estimate of a load maximum. It thus appears that finite element analysis is necessary to find the load maximum under the bending and tension history that develops in hull plating near a hardpoint, due to a collision, especially for realistically compliant hard points.

4. A buckled stiffener mode of hardpoint fracture

Qualitative description. In a collision that indents the side of a hull that has longitudinal stiffeners behind the hull plating, bending of the plating-stiffener assembly at a hardpoint will initially lead to buckling or folding of the stiffeners there, on the compression side of the bend. As the indentation of the hull increases, net in-plane loads in the assembly will become tensile. Most of the assembly, between the ends, will

remain straight and the tensile load will be carried by both the plate and the stiffener. At the hardpoint bend, the plating will stretch and the buckled stiffener will tend to straighten. Almost the entire tensile load will be carried just by the plating, so most of the extension required by indenting the hull will be concentrated at the bend until the stiffener has straightened. The displacement to straighten the stiffener will be of the order of the bend angle times the stiffener height. For bend angles of 15° this would be of the order of $\theta = \pi/12$ times the stiffener height. This displacement to straightening will be several times the plate thickness. During that extension the plate at the hardpoint bend is likely to neck and fracture while the straight assembly remains rigid.

Analysis. For a cross-sectional area of the plate A_p and tensile strength TS , necking and fracture would occur at a load of approximately $A_p TS(2/\sqrt{3})$. For simplicity and initial insight, call the deformation uniaxial, which would result in errors of the order of 15% (see Appendix 1). The straight part of the hull and stiffeners, of similar tensile strength but total cross-sectional area $A_s + A_p$, would develop this load at a strain given by

$$A_p TS = A_p Y_1 n^n e^{-(n-\epsilon_0)} = (A_p + A_s) Y_1 (\epsilon + \epsilon_0)^n e^{-\epsilon} . \quad (12)$$

Assume and verify later that the strains in the straight assembly, ϵ , are small so the last factor, $e^{-\epsilon}$, is nearly unity. Then solving for ϵ and evaluating its maximum reasonable value from a high $A_p/A_s = 2$, a high $n = 0.2$, and a low $\epsilon_0 = 0.01$ (giving a low $Y_{0.002}/TS = 0.688$) gives

$$\epsilon = \frac{n}{e} \left(\frac{A_p}{A_p + A_s} e^{\epsilon_0} \right)^{1/n} - \epsilon_0 = \frac{0.2}{2.718} \left(\frac{2}{3} e^{0.01} \right)^{1/0.2} - 0.01 = 0.00019 . \quad (13)$$

Thus this model gives virtually no strain in the plate-stiffener assembly before the tensile strength is reached in the plate over the buckled stiffener, leading to necking and fracture there.

The above model postulates local buckling at the hardpoint. Buckling might begin with a twist-buckling along the entire span. The localization of the buckling would increase as the bends tightened, and would be more the less the lateral stiffness of the stiffener. Less lateral stiffness would also increase the extension required to carry tensile

loads in the buckled stiffener. Lateral stiffness could be increased by brackets. The hat-shaped stiffeners used in aircraft would be more resistant to buckling, but would be more localized when they did buckle. The localization of tensile deformation in the plate over the buckled stiffener could be reduced by extra straps to carry the load even with the stiffener buckled. Finite element analysis would be required to quantify particular designs. .

5. Conclusions

1. For indentation of a longitudinally stiffened hull by collision, fracture in the plating is most likely at a hardpoint such as a bulkhead. Buckling of the stiffeners in the bend at the hardpoint means that the stiffeners would not contribute to the tensile load developed by further hull indentation. The limited load developed by the plate alone would not be enough to stretch the intact plate-stiffener assembly, so further extension would be concentrated in the plate over the buckled stiffeners. The concentrated extension would shortly require necking and fracture in the plate, followed by tearing of the stiffeners. This result is expressed quantitatively by Eq. 13. The effect can be modified by thicker or laterally supported stiffeners to reduce buckling, and by local hull straps to spread out the extension of the hull plating.

2. A finite element model of an unstiffened plate with a strain-hardening exponent of $n = 0.15$ indicates a 45% loss in extension compared to a straight plate (a reduction of bend angle from 31° to 23°), when a hull plate is subject to combined bending and tension at a hardpoint built in to a rigid bulkhead. When the hull plate is fillet-welded to a quarter-infinite bulkhead, all of equal hardness, the loss in extension is only about 5%.

3. Locally, an equivalent strain of the order of 0.5 develops even with this compliant hardpoint. Estimates of the equivalent plane strain at fracture indicate that such strains would not cause fracture except in very high strength alloys, with a yield strength of $Y_{0.002}/E > 0.005$.

4. A two-flange, lumped-parameter model of the behavior of an unstiffened plate at a hard-point closely followed the load-deformation behavior from the finite element analysis and gave a corresponding strain concentration, but gave a load maximum at only half of the in-plane strain of the finite element model. The lumped-parameter model does not allow predicting the effects of plastic compliance at the hard point. An alternative

bent -plate model gave large strains but failed to give a load maximum. The plate model was not included in the report.

5. Appendices are given for plane strain necking of a power-law hardening plate with pre-strain, and for fitting a power-law relation with or without pre-strain to a range of tensile data. For reasonable accuracy, two-parameter fits to the tensile strengths and beyond, without using a pre-strain, require data on the uniform strain or the fracture stress and strain, and would not fit the yield strain.

6. Future study should include off-midspan collisions, which will induce higher bend angles and plate extensions for the same hull indentation. Sliding contact along the span will cause reversals in bending near the contact point and may promote fracture there.

6. References

- ADINA (1992) Version 6.1.4 User's Manuals and Theory and Modeling Guide, Report ARD 92-4,7,8, ADINA R & D, Inc. Watertown, MA.
- Amdahl, J. and Kavlie, D. (1992) "Experimental and Numerical Simulation of Double Hull Stranding", Paper from DNV-MIT Workshop on the Mechanics of Ship Collision and Grounding", Det Norske Veritas Høvik, Oslo, Sept. 16-17 1992. Authors at Dept. of Marine Technology, The Norwegian Institute of Technology, 7034 Trondheim, Norway.
- Atmadja, J. (1995) "Weld Failures in Oil Tankers Due to Groundings - Finite Element Approach", Ocean Engineer and Master of Science Thesis in Ocean Engineering, Mass. Inst. of Tech., Cambridge. Also Tanker Safety Report (TSR) 51, 1996.
- Bathe, K.-J. (1996) "Finite Element Procedures", 2nd ed., Prentice-Hall, Englewood Cliffs, NJ, p. 276.
- Clausing, D. P. (1970) "Effect of Plastic Strain State on Ductility and Toughness", Int. J. Fracture Mech. v6, 73-85.
- Giovanola, J. H., Klopp, R. W., Simons, J. W. and Marchand, A. H. (1990) "Investigation of the Fracture Behavior of Scaled HY-130 Weldments", NAVSWC TR 90-360, Naval Surface Warfare Center, Dahlgren, VA, 22448-5000, Silver Spring, MD 20903-5000. See also Holmes, H. S., Kirkpatrick, S. W., Simons, J. W., Giovanola, J. H., and Seaman, L. (1993) "Modeling the Process of Failure in Structures", 'Structural Crashworthiness and Failure', N. Jones and T. Wierzbicki, eds., Elsevier, London, pp. 55-93.
- Hendryx, W. N. (1996) "The Angel of Flight 7529", Family Circle v109, No. 10, pp. 84-86.
- Hill, R. (1950) The Mathematical Theory of Plasticity, Clarendon Press, Oxford, reprinted.
- Il'yushin, A. A. (1946) "The Theory of Small Elastic-Plastic Deformation", Prikladnaia Matimatiki i Mekhanika, PMM v10, 347-356.
- Incera, A. F. (1991) "True Strain Measurements using Video Signals", M. S. Thesis, Dept. of Mech. Eng., Massachusetts Institute of Technology, Cambridge, MA 02139. See also a development by a company in France.
- Kardomateas, G. A. and McClintock, F. A. (1987) "Tests and Interpretation of Mixed Mode I and II Fully Plastic Fracture from Simulated Weld Defects", Int. J. Fracture v35, 103-124.
- Masubuchi, K., McClintock, F. A., and Liang, L. (1996) "Summary Report on Welding Research from the Tanker Grounding Project", Tanker Safety Report (TSR) 56, Department of Ocean Engineering, Massachusetts Institute of Technology, Cambridge, MA 02139, Chap. 4, App. A.
- McClintock, F. A. and Argon, A. S. (1966) "Mechanical Behavior of Materials", Addison Wesley, Reading MA. Reprinted 1993 by Tech Books, Fairfax, VA.
- McClintock, F. A. and Zheng, Z. M. (1993), "Ductile Fracture in Sheets under Transverse Strain Gradients", Int. J. Fracture v64, 321-337.
- McClintock, F. A., Zhou, Q., and Wierzbicki, T. (1993) "Necking in Plane Strain under Bending with Constant Tension", J. Mech. Phys. Solids v41, 1327-1343.
- Swift, H. W. (1952) "Plastic Instability under Plane Stress", J. Mech. Phys. Solids v1, 1-18.
- Swift, H. W. (1948) "Plastic Bending under Tension", Engineering v166, 333-357. See also Hill (1950), pp. 292-294.

Appendix 1 Conditions for necking in transversely plane strain plates of power-law hardening material with prestrain

Under tension with transverse plane strain, the neck forms directly across a plate (e.g. McClintock and Zheng, 1993). Consider a relation between uniaxial true stress (flow strength) and true (logarithmic) plastic strain in terms of a flow strength at unit strain Y_1 and a pre-strain ϵ_0 (see Swift, 1952):

$$Y(\epsilon) = Y_1(\epsilon + \epsilon_0)^n . \quad (\text{A1.1})$$

The constants can be found by fitting measured quantities in several ways, as discussed in App. 2.

For a plate in plane strain tension with axial strain ϵ_x , the maximum load per unit cross-sectional area of constant width w and original thickness t_0 is found by first expressing the load in terms of the true in-plane stress σ_x ; that in turn in terms of the equivalent stress $\bar{\sigma}$; that in turn in terms of the equivalent strain with $\bar{\sigma} = Y_1(\bar{\epsilon} + \epsilon_0)^n$, and then $\bar{\epsilon}$ in terms of the in-plane strain ϵ_x (e.g. Masubuchi et al. 1996, p. 4-4):

$$\frac{P_{pT}}{wt_0} = \sigma_x \frac{t}{t_0} = \frac{2}{\sqrt{3}} \bar{\sigma} e^{-\epsilon_x} = \frac{2}{\sqrt{3}} Y_1 (\bar{\epsilon} + \epsilon_0)^n e^{-\epsilon_x} = \frac{2}{\sqrt{3}} Y_1 \left(\frac{2}{\sqrt{3}} \epsilon_x + \epsilon_0 \right)^n e^{-\epsilon_x} . \quad (\text{A1.2})$$

The strain at maximum load, ϵ_{xu} , is found from $dP = 0 = d \ln P$. Aside from constants,

$$d \ln P_{pT} = 0 = d \ln \left(\frac{2}{\sqrt{3}} \epsilon_x + \epsilon_0 \right)^n + d \ln (e^{-\epsilon_x}) = n \frac{(2/\sqrt{3}) d\epsilon_x}{2\epsilon_{xu}/\sqrt{3} + \epsilon_0} - d\epsilon_x ; \quad \epsilon_{xu} = n - \frac{\sqrt{3}}{2} \epsilon_0 . \quad (\text{A1.3})$$

Normalizing Eq. A1.2 with the uniaxial tensile strength (App. 2, Eq. A2.4) gives a factor within a percent of $(2/\sqrt{3})^{1+n}$:

$$\frac{P_{pT \max}}{wt_{TS}} = \frac{2}{\sqrt{3}} \frac{\left(n(2/\sqrt{3}) \right)^n / e^{n-\epsilon_0\sqrt{3}/2}}{n^n / e^{n-\epsilon_0}} = \left(\frac{2}{\sqrt{3}} \right)^{1+n} \frac{1}{e^{\epsilon_0(1-\sqrt{3}/2)}} . \quad (\text{A1.4})$$

Appendix 2. Fitting Data using a Power-Law Stress-Strain Curve with Pre-strain

A2.1 The problem

Stress-strain curves obtained from linear extensometers are based on the original cross-sectional area and the original gauge length, giving the nominal stress P/A_0 and the nominal strain $e = (L - L_0)/L_0$. Although the strains are somewhat concentrated toward the center because of shoulder rigidity, the true strain (the integrated equivalent strain) needed for the mechanics of plasticity can be found from the length change, using $\epsilon = \int dL/L = \ln(L/L_0)$. The true stress $\sigma = P/A$ can also be found, since incompressibility and near homogeneity of area along the length make A/A_0 approximately L_0/L .

The tensile strength is the nominal stress at maximum load. Beyond the tensile strength the homogeneity of area is lost, as follows. The load drop in the weakest section unloads the rest elastically and deformation is concentrated in a neck. The current area needed for the true stress can no longer be approximated from overall length change given by the nominal strain.

For structures with strain concentrations (and for metal-working), there is still a need for true stress and strain, so there is a need to extrapolate the data obtained at the tensile strength or below to greater stresses and strains. (To be sure, the true stress-strain curve can be obtained from manually measuring the minimum diameter as the test proceeds, or from computer-processed optical data, but information from either such source is rare.) Power-law stress-strain curves are a common way of making the needed extrapolation. We show here that a good fit of the yield and tensile strengths and of the uniform elongation requires a 3-parameter, rather than the usual 2-parameter power law equation.

A2.2 Analysis of 3- and 2-parameter power law fits

Consider a 3-parameter true stress-strain curve of the form

$$\sigma = Y_1(\epsilon + \epsilon_0)^n, \quad (A2.1)$$

where Y_1 may be thought of as the flow strength (true stress) at unit strain, ϵ is the true (logarithmic) strain, $\epsilon = \ln(1 + e)$, and ϵ_0 is a pre-strain (Swift 1952 or Masubuchi et al., 1996, Eq. 4-31). Equation A2.1 can be fitted to stress-strain data in several ways.

Yield and tensile strengths are almost always available. One more datum is needed for the three constants of Eq. A2.1. The selection is made on the basis of availability and the magnitude of the strains that are to be predicted.

Yield strength. To fit Eq. A2.1 to a nominal stress-strain curve such as that of Fig. A2.1 for the ship bottom shell plate of Amdahl and Kavlie (1992), the initial flow strength (yield strength Y_S) can be regarded as the strength (stress needed for further yield) at one of several plastic strains: Y_0 at $\epsilon = 0$, $Y_{0.002}$ at the conventional offset plastic strain of $\epsilon = 0.002$, or Y_{LYP} at the end of the lower yield point (here $\epsilon_{LYP} = 0.0122$). The pre-strain ϵ_0 can be fitted or taken to be zero. (Sometimes the curve is fitted to the total, rather than to the plastic strain; the difference is negligible except near yield.) Here the analysis is fitted to the end of the lower yield point, but for generality (LYP) can be thought of as standing for (0), (0.002), or (LYP), according to context:

$$Y_{LYP} = Y_1 (\epsilon_{LYP} + \epsilon_0)^n . \quad (A2.2)$$

Tensile strength. The maximum load, defining the tensile strength, is found in terms of the true stress σ and the cross-sectional area A : $dP = d(A\sigma) = A d\sigma + \sigma dA = 0$. From incompressibility $dA/A = -d\epsilon$. Together, these give $d\sigma/d\epsilon = \sigma$. Substituting Eq. A2.1 into this gives the true (logarithmic) strain at the tensile strength, ϵ_u (the maximum uniform strain):

$$n = \epsilon_u + \epsilon_0 ; \quad \epsilon_u = n - \epsilon_0 . \quad (A2.3)$$

Since the tensile strength is based on the original area,

$$TS = Y_1 (n)^n \exp(-n + \epsilon_0) . \quad (A2.4)$$

Taking the ratio of yield to tensile strength, Eq. A2.2 to Eq. A2.4, eliminates the unknown Y_1 and gives one implicit equation for ϵ_0 and n :

$$\frac{Y_{LYP}}{TS} = \left(\frac{\epsilon_{LYP} + \epsilon_0}{n} \right)^n \frac{e^{n-\epsilon_0}}{e^{\epsilon_{LYP}}} , \quad (A2.5)$$

where e is here the base of natural logarithms.

Auxiliary data. A second needed relation between n and ϵ_0 can be found from one of the following three quantities, depending on the data available and the part of the stress-strain curve to be fitted: i) the initial slope of the stress-strain curve, ii) the true strain at the tensile strength ϵ_u (the uniform strain), or iii) the nominal stress and reduction of area at fracture, FS and RA. From incompressibility, the true strain at fracture, ϵ_f , is given in terms of the RA by

$$\epsilon_f = \ln \frac{\delta L_f}{\delta L_0} = \ln \frac{A_0}{A_f} = \ln \frac{A_0}{A_0 - (A_0 - A_f)} = \ln \frac{1}{1 - RA} \quad (A2.6)$$

With necking, the uniaxial true stress $\sigma = P/A$ is more than the equivalent flow stress $\bar{\sigma}$ that governs plastic deformation because of the hydrostatic tension in the center of the specimen caused by the radially outward stresses in the shoulders. Bridgman gave a factor for the ratio between the two in terms of ratio of cross-sectional radius to the profile radius, a/R (e.g. McClintock and Argon 1966, pp. 322-325)

$$F_B = \frac{\bar{\sigma}}{P/A} = \frac{a/2R}{(1 + a/2R) \ln(1 + a/2R)} \approx \frac{1}{(1 + a/2R) \left(1 - \frac{a/2R}{2} + \frac{(a/2R)^2}{3} - \dots \right)} \quad (A2.7)$$

where empirically, $a/2R \approx (\epsilon - \epsilon_u) / 2$.

Thus the three alternative relations to supplement Eq. A2.5 are

$$\left(\frac{Y'}{Y} \right)_{LYP} = \frac{n}{\epsilon_{LYP} + \epsilon_0} \quad , \quad n = \epsilon_u + \epsilon_0 \quad , \quad \text{or} \quad \frac{FS}{TS} = \left(\frac{\epsilon_f + \epsilon_0}{n} \right)^n \frac{e^{n - \epsilon_0}}{F_B e^{\epsilon_f}} \quad (A2.8abc)$$

Equations A2.8a,b allow explicitly eliminating n from Eq. A2.5, leaving an implicit equation for ϵ_0 which can be solved in a few iterations with a programmable calculator. Then the remaining constants can be found explicitly. Alternatively, if fits at the tensile and fracture strengths are of more concern than at yield, and reduction of area as well as a nominal stress-strain curve is available, a similar procedure can be followed with Eqs. A2.6b and c, using the same calculator program with a change of variables.

A2.3 Example of power-law fitting to ship bottom shell plating data giving nominal fracture strength but not reduction of area.

Amdahl and Kavlie (1992) gave the nominal stress-strain curve of Fig. A2.1, from which (with precision only for numerical consistency)

$$Y_0 = Y_{LYP} = 319.0 \text{ MN/mm}^2, \quad \epsilon_{LYP} = 0.0122,$$

$$(Y'/Y)_{LYP} = 11.55,$$

$$TS = 435.3 \text{ MN/mm}^2, \quad e_u = 0.1834, \quad \epsilon_u = \ln(1 + e_u) = 0.1684.$$

$$FS = 332.4 \text{ MN/mm}^2.$$

3-parameter fits. The results found by fitting the Swift equation to these data, using Eq. A2.5 with either arbitrary or actual lower yield strains, $\epsilon_{YP} = 0.002$ or 0.0122 , and the initial slope using Eq. A2.6a or the uniform elongation using Eq. A2.6b, are given in the first four columns of Table A2.1. Fits to the initial slope gave a uniform strain 10-15% high, depending on whether the fitting was to a nearly zero initial yield strain or to the end of the lower yield point. Fits to the uniform strain gave initial slopes 25 to 40% high. These differences could give problems where high strains around a crack are to be predicted from the elastic-plastic deformation of the surrounding parts of a structure. (Note that Y_1 is not *really* the true stress at unit strain unless it has been fitted there; rather, it is an empirical fitting constant.)

The fracture strain ϵ_f to reach the nominal fracture strength FS is surprisingly consistent over these fits, but the actual ϵ_f was not reported.

2-parameter, zero pre-strain fits. Since often only yield and tensile strength data are available, two-parameter fits are used. If they are made with the pre-strain ϵ_0 set to zero they take advantage of Il'yushin's (1946) proof that the stresses scale with the loads for pure power-law behavior. Then if the yield strength is taken at a plastic strain of 0.002, Eqs A2.1 - A2.6 apply with $\epsilon_0 = 0$ and $\epsilon_{LYP} = \epsilon_{YS} = 0.002$. The results are given in the last two columns of Table A2.1.

Fitting to YS/TS gives an elongation at the tensile strength of $e_u = 0.1042$, only 60% of the observed value, $e_u = 0.1834$. Conversely, fitting at ϵ_u gives YS/TS 15% high. In either case, the slopes at the yield strength are high by factors of 5 to 7, so predictions of fully plastic crack in an elastic-plastic structure would probably be poor.

The extrapolated strain to fracture is 20% low for the fit to YS/TS , but reasonable for the fit to ϵ_u . Again, the experimental value is not known.

Table A2.1 Power-law fits of Eq. 2A.1, to data for a ship bottom plate

(Amdahl and Kavlie 1992). $Y_{LYP} = 319.0$ MPa, $TS = 435.3$ MPa, $FS = 332.4$ MPa.

Data for power-law fit are full underlined;

further data for extrapolation to fracture strain are dotted underlined.

	<u>3-parameter, Eq. 2A.1, Swift (1952)</u>				<u>2-parameter</u> (no pre-strain ϵ_0)	
ϵ_0	0.0155	0.0053	0.0105	-0.0021	<u>0.</u>	<u>0.</u>
ϵ_{LYP}	<u>0.002</u>	<u>0.0122</u>	<u>0.002</u>	<u>0.0122</u>	<u>0.002</u>	<u>0.002</u>
$(Y/Y)_{LYP}$	<u>11.55</u>	<u>11.55</u>	14.31	16.47	52.09	84.20
YS/TS	<u>0.7337</u>	<u>0.7337</u>	<u>0.7337</u>	<u>0.7337</u>	<u>0.7337</u>	0.8386
ϵ_u	0.1865	0.1967	<u>0.1684</u>	<u>0.1684</u>	0.1042	<u>0.1684</u>
n	0.2020	0.2020	0.1789	0.1663	0.1042	0.1684
Y_1 , MPa	735.9	735.9	708.3	692.8	611.5	695.4
FS/TS	<u>0.7636</u>	<u>0.7636</u>	<u>0.7636</u>	<u>0.7636</u>	<u>0.7636</u>	<u>0.7636</u>
ϵ_f	0.9166	0.9268	0.86997	0.8533	0.6999	0.8561

A2.4 Example of power-law fitting to structural steel with tensile data including nominal fracture strength and true fracture strain

Kardomateas and McClintock (1987) gave data for six different structural alloys, including the uniform strain and the fracture strain and equivalent stress (with the Bridgman correction for the increase in the equivalent stress above the nominal. They did not, however, report the slope of the stress-strain curve at yield. Results for their softest steel, hot-rolled A-36, are given in Table A2.2.

The three-parameter fit is within 10%, regardless of the assumed yield strain. The two-parameter fit requires having enough data so the lower yield point strain is no longer used in fitting. Otherwise the fit is badly in error.

Table A2.2 Power-law fits of Eq. 2A.1 to hot-rolled A36 steel. (Data from Kardomateas and McClintock 1987.). $Y_{LYP} = 337$ MPa, $TS = 469$ MPa, $\bar{\sigma}_f = 880$ MPa..

Data for primary power-law fit are full underlined;
secondary data for extrapolation to other descriptors are dotted underlined.

	<u>3-parameter, Eq. 2A.1, Swift (1952)</u>				<u>2-parameter</u> (no pre-strain ϵ_0)			
ϵ_0	0.0315	0.0315	-0.0097	-0.0097	<u>0.</u>	<u>0.</u>	<u>0.</u>	<u>0.</u>
ϵ_{LYP}	<u>0.002</u>	<u>0.002</u>	<u>0.032</u>	<u>0.032</u>	<u>0.002</u>	<u>0.002</u>	0.0274	0.0248
$(Y'/Y)_{LYP}$	8.096	8.096	10.339	10.339	54.6	120.	9.124	9.677
Y_{LYP}/TS	<u>0.719</u>	<u>0.719</u>	<u>0.719</u>	<u>0.719</u>	<u>0.719</u>	0.402	<u>0.719</u>	<u>0.719</u>
ϵ_u	<u>0.24</u>	<u>0.24</u>	<u>0.24</u>	<u>0.24</u>	0.1093	<u>0.24</u>	0.250	<u>0.24</u>
n	0.2715	0.2715	0.2303	0.2303	0.1093.	0.24	0.250	0.24
Y_1 , MPa	849	843	836	857	666	853	852	853
σ_f/TS	<u>1.876</u>	1.891	<u>1.876</u>	1.834	<u>1.876</u>	1.848	<u>1.876</u>	<u>1.876</u>
ϵ_f	1.107	<u>1.14</u>	1.258	<u>1.14</u>	12.72	<u>1.14</u>	<u>1.14</u>	1.214

A2.5 Calculator program (HP-42S) for fitting 2- or 3- parameter power-law relations to tensile test data including slope at initial yield and nominal or true, Bridgman-corrected fracture strength

The program is based on inverse Lukaciewicz (Polish) notation in which numbers are entered into a stack with the most recent on the bottom. Unary operators, such as e^x , act on the bottom number in the stack and return the result there. Binary operators, such as y^x or $+$, act on the lower two numbers of the stack and return the result to the bottom of the stack. The remaining numbers are dropped one position to fill the empty space. This procedure has many analogies to pre-algebraic human thinking. It can be converted to a programmable calculator that uses algebraic notation, with parentheses, by going back to the equations being evaluated.

This program uses a subroutine for solving that allow the user to specify by a second estimated input the variable to be solved for, so the same function, here called TT, can be used for several different objectives.

Storage register and flag assignments

VA (Y'/Y)_{LYP} (if VA > 1) or ϵ_u (if VA < 1)
VB Uniform strain ϵ_u , at the tensile strength
VC Ratio to tensile strength of nominal yield strength Y_{LYP} at ϵ_{LYP} , or nominal fracture stress FS at ϵ_f (or true fracture stress σ_f if and only if Flag 00 is set), consistent with VE
VD Pre-strain ϵ_0 , or zero.
VE Strain at 0, 0.002, or ϵ_{LYP} , or at fracture, ϵ_f , consistent with VC
01 RHS of Eq. A2.5 or A2.8c. Multiplied by 1/Bridgman factor, $1/F_B = (P/A)/\bar{\sigma}$, Eq. A2.7, if FS/TS is in VC (Flag 00 is Clear) and ϵ in VE > ϵ_u
02 $(\epsilon_f - \epsilon_u)/2 = a/(2R)$ for Bridgman correction factor, Eq. A2.7
Flag 00 Clear for nominal fracture strength FS/TS or yield strength Y_{LYP}/TS in VC. True stress will be corrected for thinning and, for ϵ_f in VE > ϵ_u in VB, will be corrected for curvature.
Set for equivalent fracture strength, σ_f/TS .

Procedures for using program

To fit to yield and tensile strengths.

*FLAGS CF 00 Clear Flag 00 for nominal, not true, yield strength in VC.
(Y'/Y)_{LYP} or ϵ_u STO VA
If VA > 1, program calculates ϵ_u from (Y'/Y)_{LYP} with Eq. A2.8a before storing ϵ_u in VB.

Store two more values to a total of three knowns and one estimate:

ϵ_0 STO VD; ϵ_{LYP} STO VE; Y_{LYP}/TS STO VC

*SOLVER TT press menu key for unknown, key in slightly different estimate, press menu key for unknown twice more.

See upper and lower limits converge, or stop with R/S.

EXIT, EXIT To leave Program TT.

Scroll down 4 times to see solution, last estimate (solution), error (<E-11), 0.

Manually evaluate $n = VB + VD$, $(Y'/Y)_y = (VB + VD)/(VE + VD)$ from Eqs. A2.8a,b.

To fit to nominal fracture strengths

*FLAGS CF 00 Clear Flag 00 for nominal rather than the true, Bridgman-corrected fracture strength.

ϵ_u STO VA Program stores ϵ_u in VB.

Store two more values to a total of three knowns and one estimate:

ϵ_0 STO VD; ϵ_f STO VE; FS/TS STO VC

*SOLVER TT and continue SOLVER procedures as above for yield, tensile.

Manually evaluate $n = VB + VD$, $Y_1 = TS[e(=1 * e^x)/(VB+VD)]^{(VB+VD)}$ from Eqs. A2.8b, A2.4.

To fit to true, Bridgman-corrected fracture strengths

*FLAGS SF 00 Set Flag 00 for the true, Bridgman-corrected, rather than the nominal, fracture strength in VC.

ϵ_u STO VA Program stores ϵ_u in VB.

Store two more values to a total of three knowns and one estimate:

ϵ_0 STO VD; ϵ_f STO VE; σ_f/TS STO VC

*SOLVER TT and continue SOLVER procedures as above for yield, tensile.

Manually evaluate as above for nominal fracture strengths.

Calculator program. with comments

First prgm line no., prgm size and name, and possible unknown variables (except VA):

00 (150-Byte Pgm) LBL "TT"
02 MVAR "VA" through MVAR "VE"

Since $(Y'/Y)_{LYP}$ or ϵ_u in VA, if VA < 1 GTO 01 to put value of VA in VB:

07 1 RCL "VA" x<y? GTO 01

Else find ϵ_u from Eqs. A2.8a,b: $(Y'/Y)_{LYP}(\epsilon_{LYP} + \epsilon_0) - \epsilon_0 = \epsilon_u$.((Y'/Y)_{LYP} already in bottom of stack) and proceed:

11 RCL "VE" RCL "VD" + x RCL "VD" - STO "VB" GTO 02

From above, VA was ϵ_u , so store it in VB directly and proceed:

19 LBL 01 STO "VB"

Evaluate Eq. A2.5 or A2. 8c, with $n = \epsilon_u + \epsilon_0$ from Eq. A2.3 or A2.8b, with FS or σ_f , depending on whether Flag 00 is set or cleared. E. g. if fitting yield,

$$\left(\frac{\epsilon_{LYP} + \epsilon_0}{\epsilon_u + \epsilon_0} \right)^{\epsilon_u + \epsilon_0} \frac{1}{e^{\epsilon_{LYP} - \epsilon_u}} - \frac{Y_{LYP}}{TS} = 0 \quad . \text{ Form first factor, exponentiated:}$$

21 LBL 02 RCL "VE" RCL "VD" +
25 RCL "VB" RCL "VD" + /
29 RCL "VB" RCL "VD" + y^x

Include strain in thinning factor if Flag is Clear (i. e. unless σ_f entered):

33 RCL "VE" FC?00 GTO 03 CLx 0

Form thinning factor and divide by it to get first term. Store first term so far:.

38 LBL 03 RCL "VB" - e^x / STO 01

Skip Bridgman factor for necking correction if Flag is Set (σ_f/TS entered) or $\epsilon_u > \epsilon$:

44 FS?00 GTO 04
46 RCL "VE" RCL "VB" x>y? GTO 04

For Bridgman factor, store $(\epsilon_f - \epsilon_u)/2 = a/(2R)$ from Eq. A2.7 in Register 02:

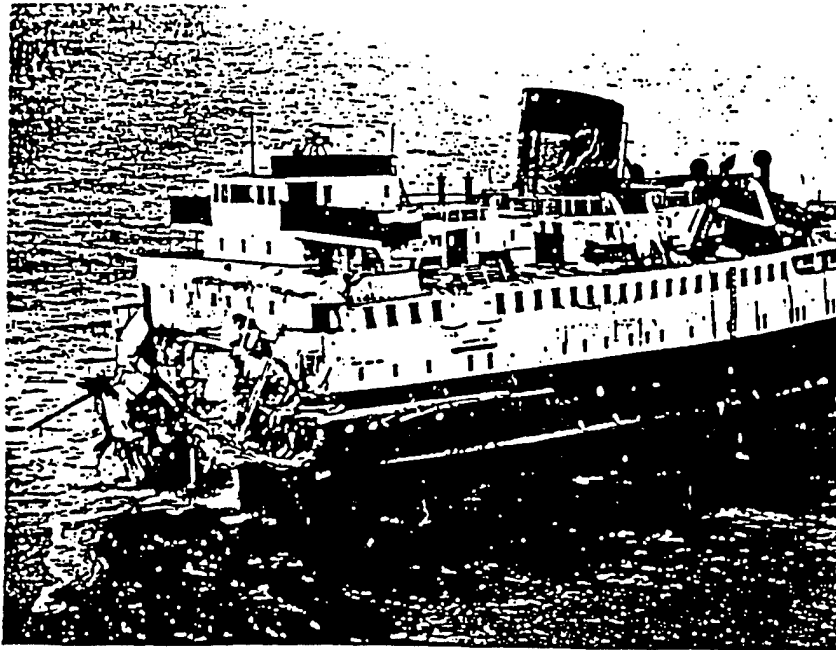
50 - 2 / STO 02

Multiply first term by reciprocal of Bridgman factor, $[1/(a/2R) + 1]\ln(a/2R + 1)$, Eq.A2.7:

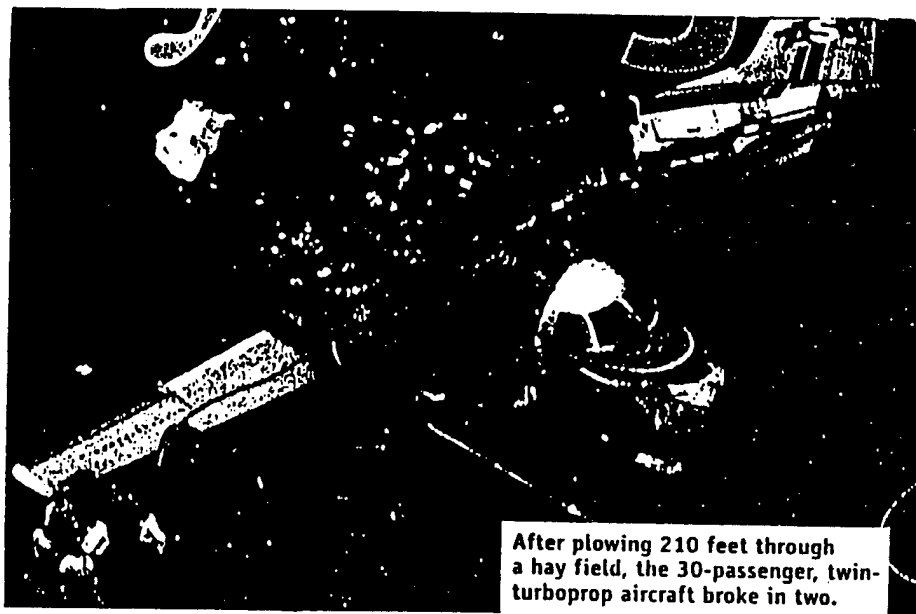
54 1/x 1 + x RCL 02 1 + ln x STO 01

Subtract Y_{LYP}/TS , FS/TS , or σ_f/TS ; SOLVER changes unknown so difference is zero:

64 LBL 04 RCL 01 RCL "VC" - END



a) The liner Duke of York, cut in half by the freighter Haiti Victory.



b) Crash-landed twin engine 30-passenger turboprop (Hendryx, 1996).

Fig. 1. Examples of hulls apparently broken at bulkheads.

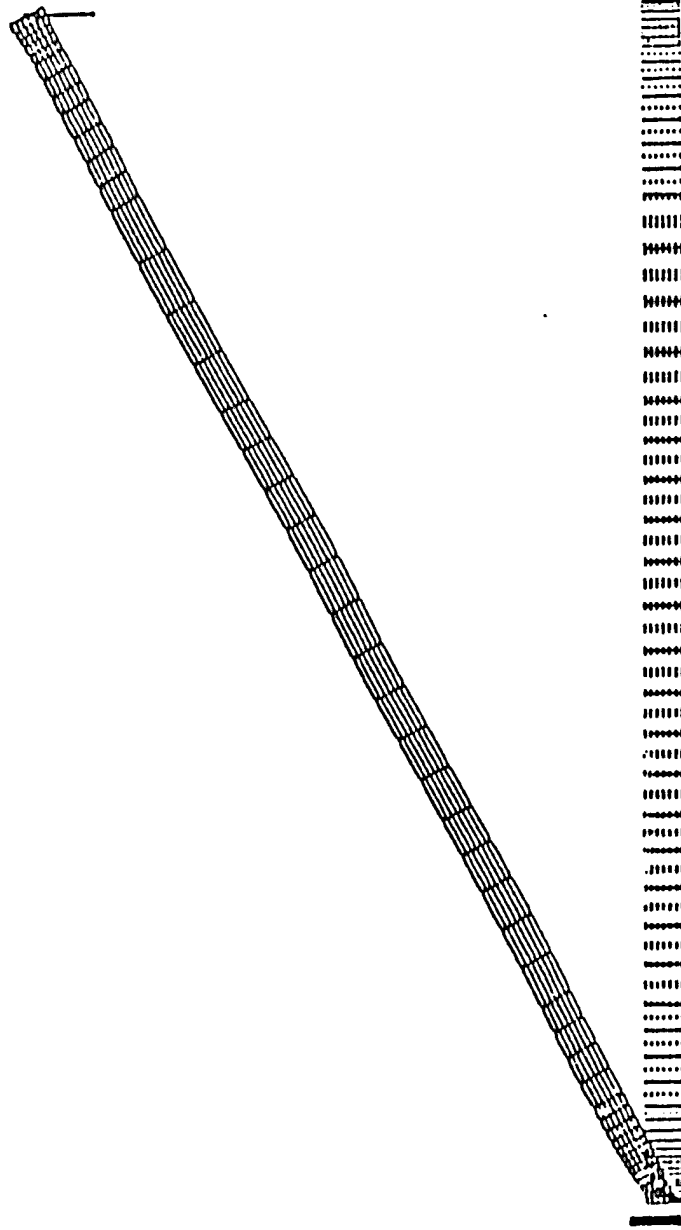


Fig. 2. Deformed mesh at maximum load for a plate built-in at the hardpoint. $n = 0.2$.

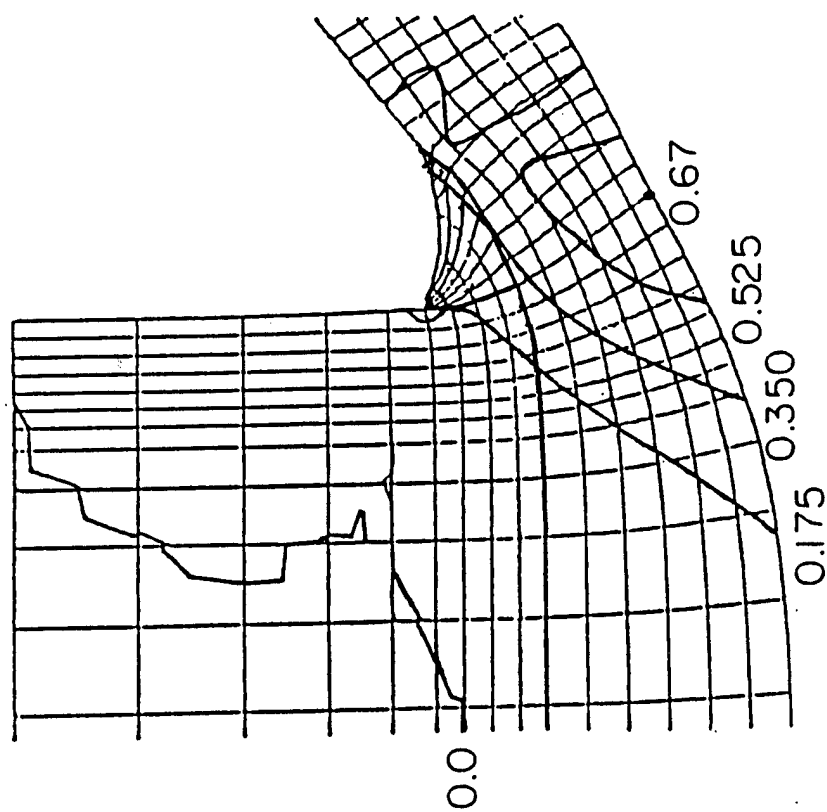


Fig. 3. Deformed mesh near a hardpoint with a homogeneous fillet weld, at maximum load. $n = 0.2$.
Contours of Mises equivalent strain $\bar{\epsilon}$.

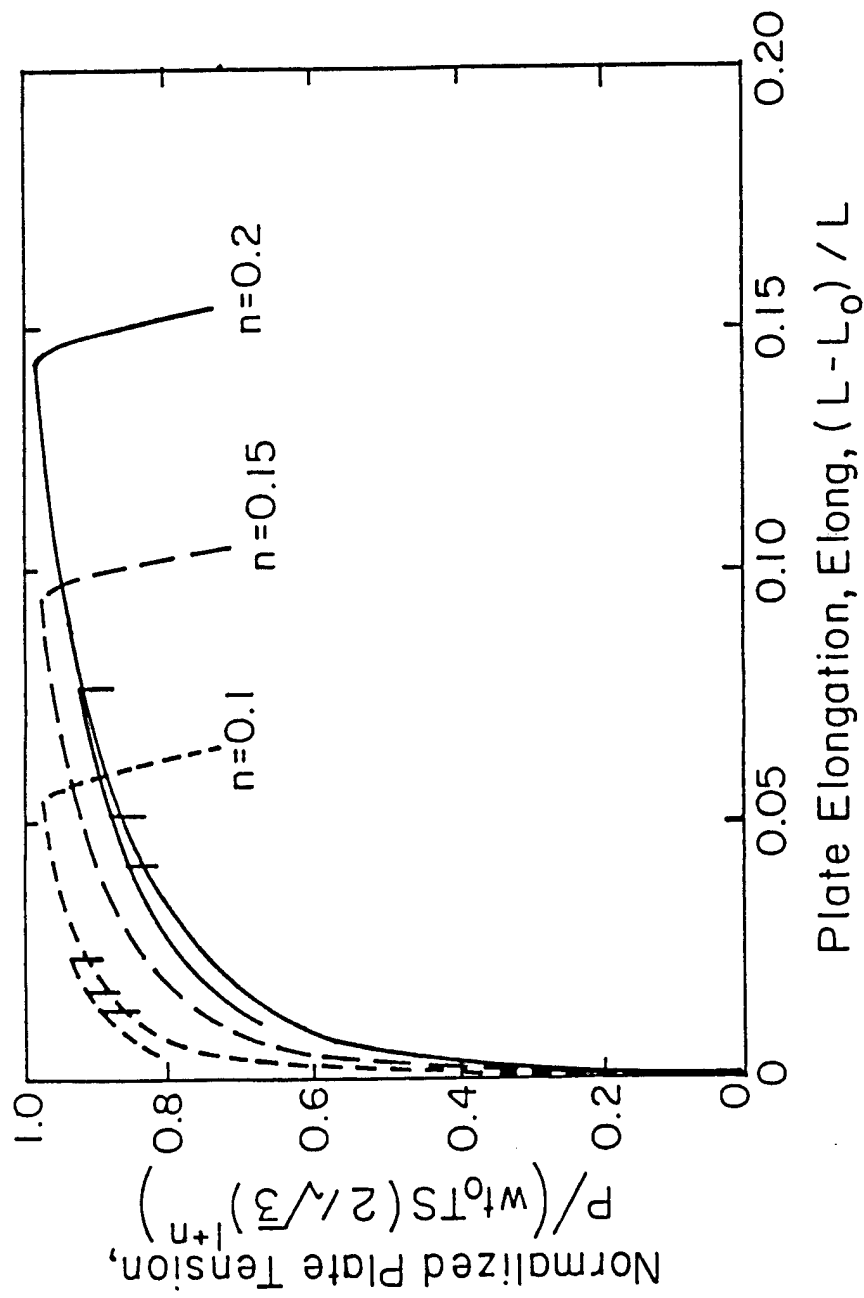


Fig. 4. Effect of strain-hardening on the in-plane load-extension plots for a plate bent and stretched between rigid supports (see Fig. 1.) Power law hardening with $\epsilon_0 = 0$. The two shorter curves with vertical load drops, for $n = 0.1$ and 0.2 , are from the lumped parameter model that gives load maxima at progressively higher extensions for the line-of-action factors $F_a = 1.0, 0.5$, and 0.25 (see Fig. 6).

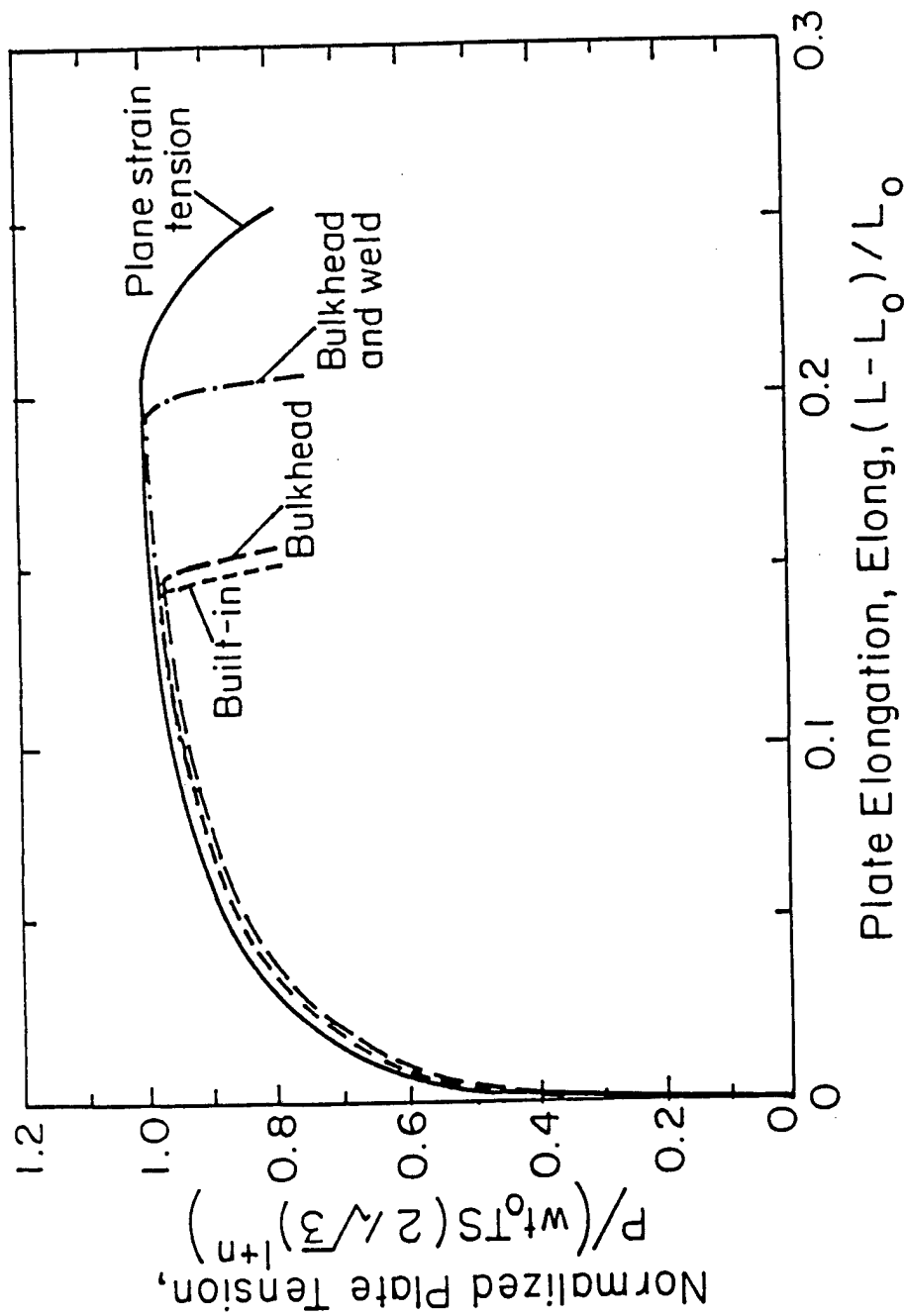


Fig. 5. Effects of support compliances on in-plane load-extension plots for plates bent and stretched between compliant supports. $n = 0.2$. "Built-in" means between rigid supports; "Bulkhead" means continuous with a large, thick bulkhead; "Bulkhead and weld" means continuous with an added fillet weld on the compression side (Fig. 2).

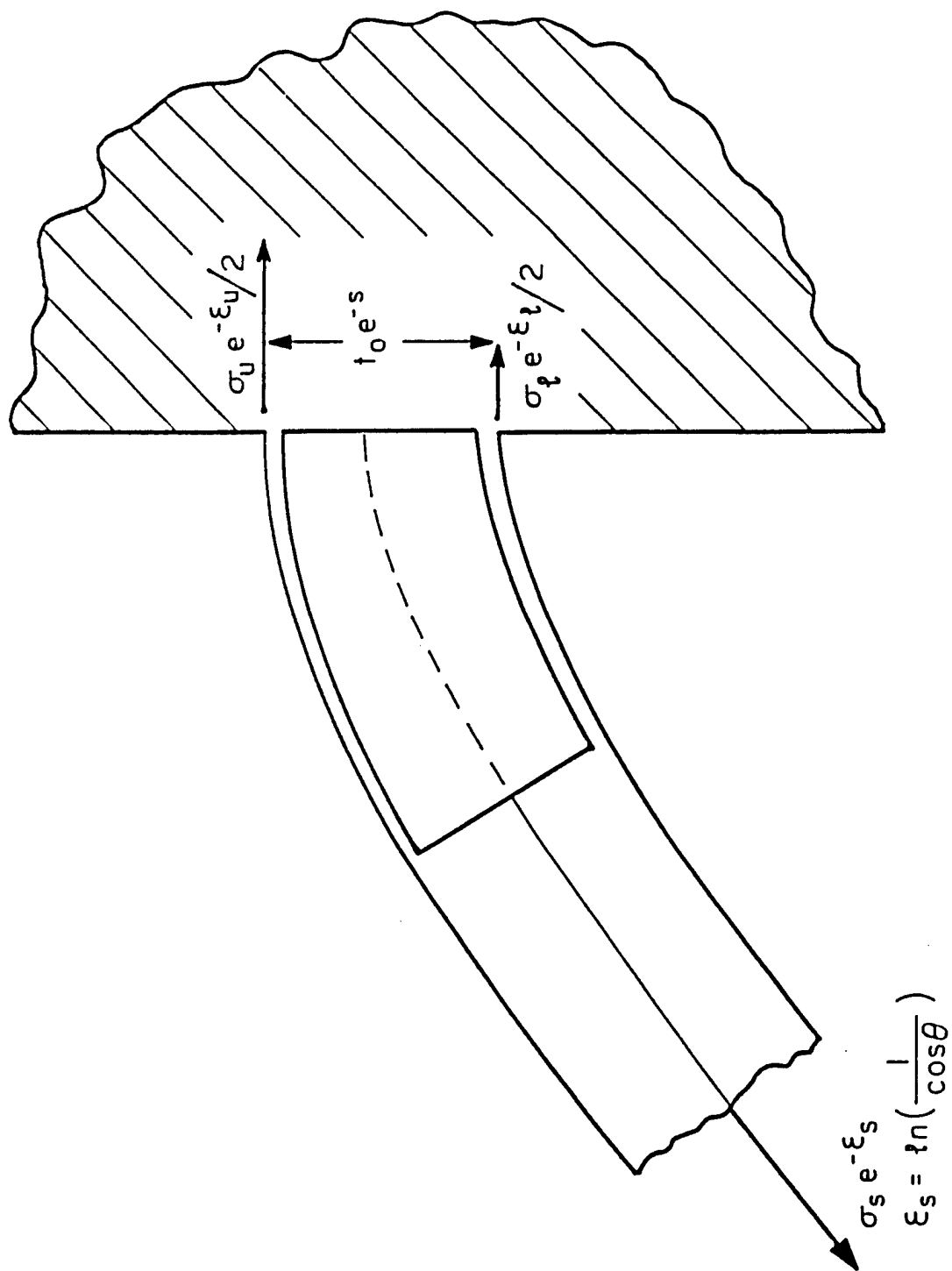


Fig. 6. Idealized flange model of a plate being bent and extended between rigid supports.

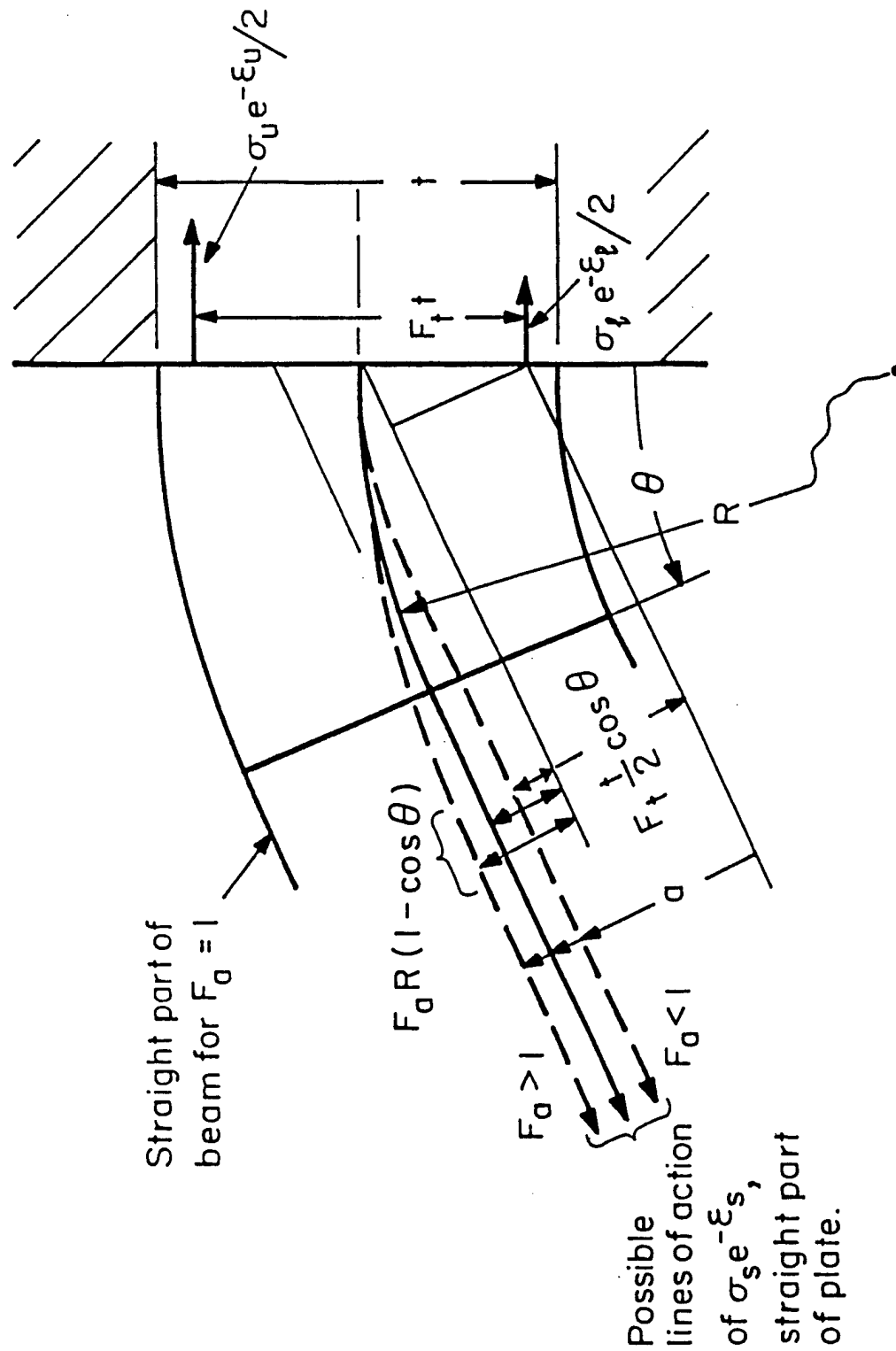


Fig. 7. Possible lines of action of the force from the straight part into the curved flanges.

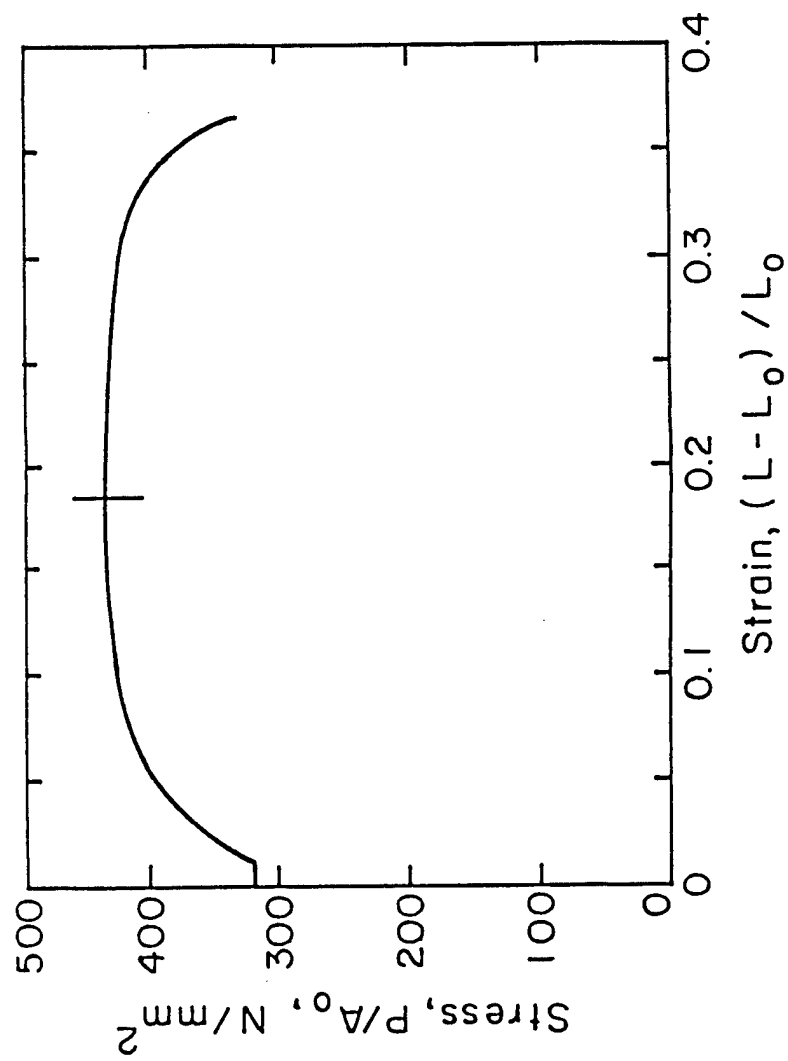


Fig. A2.1 Load-extension curve for a bottom plate of a ship. (Amdahl and Kavlie 1992).

**NUMERICAL MODELING OF OIL CONTAINMENT BY A BOOM/BARRIER SYSTEM:
PHASE II**

S.T. Grilli, Z. Hu, M.L. Spaulding, and D. Liang, University of Rhode Island

Abstract

This report presents results obtained at the University of Rhode Island, Department of Ocean Engineering, as part of a research project entitled : "Numerical Modeling of Oil Containment by a Boom/Barrier System : Phase II". This project was supported by Grant No. DTRS57-95-G-00065 of the Department of Transportation (DOT) (United States Coast Guards District (USCG) No. 1) FY 1995 Oil Pollution Research Grant Program. A 50% budget match was provided by the University of Rhode Island.

This project started on July 15, 1995, originally for a period of one year, but was subsequently extended until December 31, 1996. The Phase II project is a second year continuation of a Phase I project entitled : "A hydrodynamic model of oil containment by a boom", which was supported by DOT-USCG Grant No. DTRS-5794-G-00076 of the Department of Transportation FY 1994 Oil Pollution Research Grant Program. A third year continuation grant for Phase III of this project has been awarded as of January 1, 1997, under funding from the Minerals Management Service (MMS). The present report only covers developments and computations carried out during Phase II of the project, using a numerical model hereafter referred to as the *Phase II model*.

The long term goal of these studies is to develop computer models that will help both gain fundamental insight into oil containment failure mechanisms and outline strategies and methods for limiting the occurrence and/or the intensity of these failures, in actual field situations.

Following initial studies and model developments reported for Phase I studies (Grilli *et al.* [16]), model developments in Phase II studies have focused on three major aspects : (i) improving and complementing the models developed in Phase I, namely both periodic and non-periodic Piecewise Constant Vortex Sheet (PCVS) models; (ii) provide a better representation of hydrodynamic instabilities in the oil containment problem by developing and implementing a more accurate model based on Continuous Vortex Sheets (CVS); and (iii) both implementing and validating a numerical method for calculating the quasi-steady equilibrium shape of an oil-slick including the effects of interfacial friction, and developing a formalism to include interfacial friction effects in the Vortex Sheets (VS) time updating equations (which were ignored in Phase I model).

As a result of such model development/improvements, model applications carried out during Phase II provide more quantitative analyses and predictions than the qualitative descriptions of the oil containment behavior achieved during Phase I.

More specifically, in Chapter 1, we present an overview of the project as of the end of Phase II and, in Chapter 2, we present the PCVS models equations and applications. Looking at Figs. 2.13, 2.14, and 2.15, for instance, it can be seen that both entrainment and critical accumulation failure modes have been well qualitatively modeled using the PCVS approach. In Chapter 3, we present development and application of the new CVS model. Looking at Fig. 3.3, for instance, it can be seen that the periodic Kelvin-Helmholtz instability at an oil-water interface, and the subsequent roll-up of Vortex Sheets, have been very accurately modeled, and for a much longer time, than using the PCVS model. In

Chapter 4, we present a model and applications for calculating the quasi-steady-state initial shape of a contained oil slick. Looking at Fig. 4.3, for instance, it can be seen that the initial stable shape of an oil slick, measured by Milgram and Van Houten [29] in their laboratory experiments, was correctly recalculated using the PCVS model. Finally, in Chapter 5, we give the modified vorticity updating equations (5.20) and (5.21), including the effects of interfacial friction. These equations will be implemented and tested during Phase III studies.

Chapter 1

Introduction and project overview

1.1 Introduction

This report presents results obtained at the University of Rhode Island, Department of Ocean Engineering, as part of a research project entitled : *Numerical Modeling of Oil Containment by a Boom/Barrier System : Phase II*, which was funded by the U.S. Coast Guard (USCG) as part of the FY95 budget of the "Oil Pollution Research Grant Program" The present project is a continuation of a Phase I project : *A hydrodynamic model of oil containment by a boom : Phase I*, which was also funded by the U.S. Coast Guard (USCG), as part of the FY94 budget of the same program.

The Phase I project was aimed at developing a two-dimensional hydrodynamic model of *oil containment* by booms, to be used to investigate oil containment failure (Figs. 1.1 and 1.2). It was envisioned that this numerical model and its future improvements would help us both gain fundamental insight into oil containment failure mechanisms and outline strategies and methods for limiting the occurrence or the intensity of these failures, in actual field situations. Due to its more catastrophic nature, the failure mode referred to as *critical accumulation* was the main object of the study (Figs. 1.2, 1.3). Three main technical tasks were initially proposed : (i) numerical model selection and design; (ii) model testing and validation; and (iii) application to oil containment failure. Extensive literature review and analysis of the physical, theoretical, and numerical problems relative to oil containment were conducted as part of task (i) (Grilli *et al.* [16]). Based on this review, an initial modeling strategy was selected (hereafter referred to as the *Phase I model*). The Phase I model was implemented and validated, and used to predict oil containment failure, as part of tasks (ii) and (iii). In all cases, model results qualitatively showed the expected failure modes and the correct sensitivity to changes in physical parameters (e.g., Fig. 1.4). Details of the Phase I model development, implementation, and results can be found in Grilli *et al.* [16, 17].

The Phase II project involved various improvements of the Phase I model, hereafter referred to as the *Phase II models*, at both the level of the modeled physics (e.g., inclusion of friction effects at the oil-water interface) and the numerical methods used (e.g., higher-

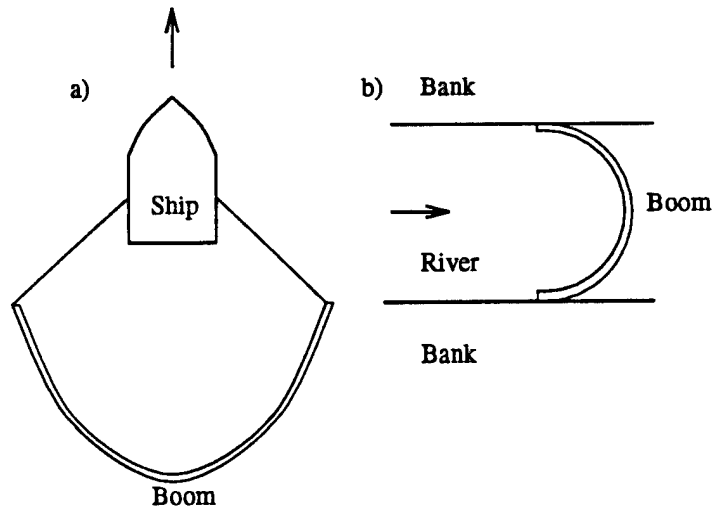


Figure 1.1: Planview of typical set-up for oil containment by : (a) a towed boom (ocean); or (b) a static boom (river). Arrows mark the direction and magnitude of the relative velocity U between boom and water.

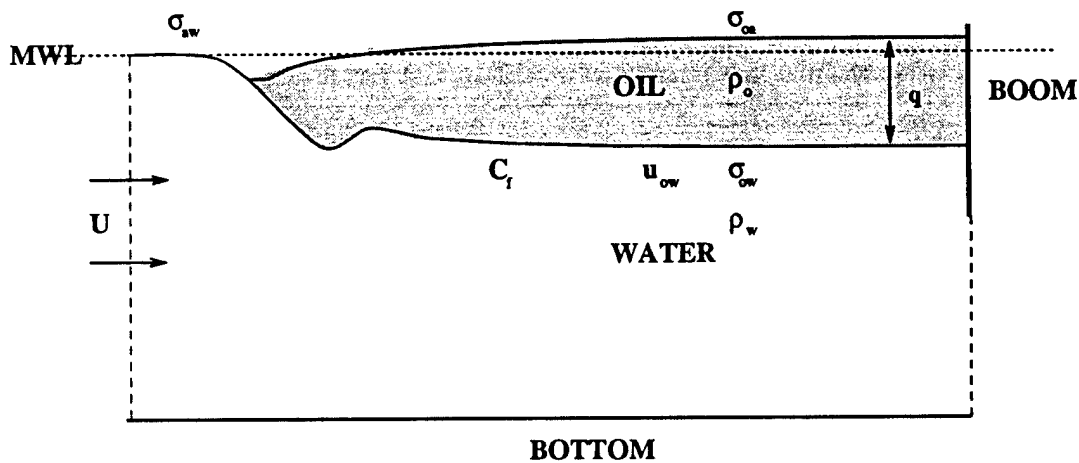


Figure 1.2: Sketch for initiation of oil containment failure by *critical accumulation*, with mention of important parameters : U , water-boom relative current velocity; u_{ow} , oil-water relative velocity; ρ_o , ρ_w , oil and water density, respectively; σ_{ow} , σ_{oa} , σ_{aw} , interfacial tension coefficients for oil-water, oil-air, and air-water, respectively; C_f , oil-water interfacial friction coefficient; q , oil slick depth; MWL, Mean Water Level.

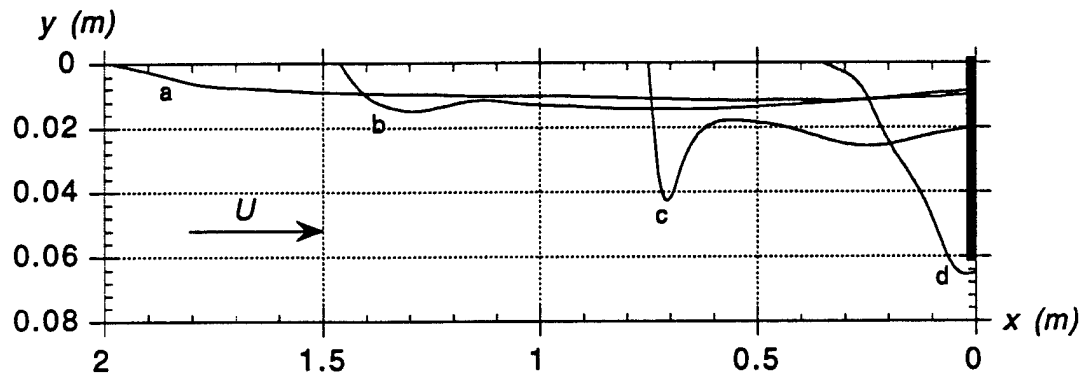


Figure 1.3: Experimental shapes of oil slicks measured in Delvigne's [9] experiments with Arabian light emulsion ($\nu_o = 2,300$ cs) for relative water-boom velocity $U = a : 0.065$; $b : 0.095$; $c : 0.128$; and $d : 0.145$ m/s. The figure shows the increase in size of the headwave and the shortening of the slick as U increases from curve a to c and, finally, the failure by *critical accumulation* with the oil slick draining under the boom in curve d.

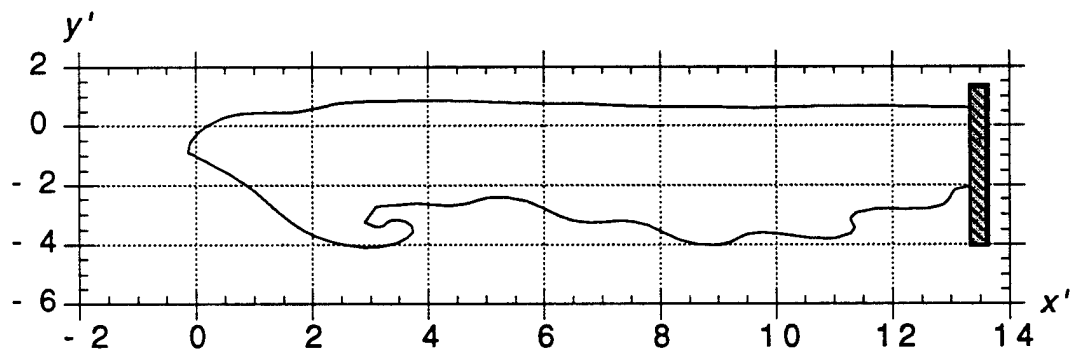


Figure 1.4: Illustration of (qualitative) computations with the Phase I model for an oil slick contained by a boom. In this case, both a headwave and interfacial instabilities develop simultaneously.

order discretization and time updating techniques). More specifically, model developments in Phase II studies focused on three major aspects :

- (i) improving the Piecewise Constant Vortex Sheet (PCVS) models, both periodic and non-periodic, developed during Phase I studies; for the non-periodic PCVS model, in particular, improvements were aimed at better addressing problems with complex boundary geometries (as needed to correctly include booms in VS models);
- (ii) developing and implementing a more accurate higher-order model, based on Continuous Vortex Sheets (CVS), which will ultimately provide a better representation of hydrodynamic instabilities in the oil containment problem; and
- (iii) both implementing and validating a numerical method for calculating the quasi-steady equilibrium shape of an oil-slick including the effects of interfacial friction, and developing a formalism to include interfacial friction effects in the Vortex Sheets (VS) time updating equations. [These were ignored in Phase I model.]

As a result of such model development/improvements, Phase II model applications presented in this report provide more quantitative predictions of the oil behavior than the qualitative description achieved during Phase I studies. In particular, using the periodic PCVS (Phase II) model, a wide parametric study of periodic interfacial instability was conducted, where values of important parameters such as oil density, surface tension, and oil-water velocity, were varied (Section 2.5.2). The modeling of oil containment by a boom using the non-periodic PCVS (Phase II) model provided more physically sound results than obtained using the Phase I model (Section 2.5.2). Application of the new periodic CVS model to the KH instability problem predicted interface VS roll-up, much further in time than in any other earlier published numerical study of this problem (Section 3.3). Finally, the calculation of the equilibrium quasi-steady shape of an oil slick showed surprisingly good agreement with experimental measurements (Section 4.6).

Despite their accuracy and relevance, the main drawbacks of the numerical models developed so far, however, are that, except for the computation of the equilibrium quasi-steady shape of a slick, there has been no comparison (and thus calibration) of the time dependent models with experimental results and that the models have assumed no surface waves. Such experimental validation and calibration will be conducted as part of the ongoing Phase III of the project, by comparing model results with experimental data obtained in the University of New Hampshire's two-dimensional flume and three-dimensional data obtained at MMS's OHMSETT flume in New Jersey.

In Chapter 1 of this report, we present key elements of the oil containment modeling problem. In Chapter 2, we present equations and results for both periodic and non-periodic improved PCVS models and, in Chapter 3, we present the same for the new CVS periodic model. In Chapter 4, we present a model and applications for calculating the quasi steady-state shape of an oil slick, including interfacial friction effects; and in Chapter 5, we give the modified vorticity updating equations including the effects of interfacial friction.

1.2 Project Overview

Booms are one of the most commonly used techniques to collect and contain oil on the sea surface, or to protect specific areas against slick spreading by containment or diversion. In the collection mode, floating boom systems are deployed on the free surface, usually in U or V configurations, and towed towards the oil slick. In the diversion mode, they are used to direct oil to the shoreline or sheltered area.

The containment of oil by a boom is illustrated by the sketches in Fig. 1.1 which correspond to both an *ocean situation* in which a boom is towed by a boat at relative speed U over the water, and a *river situation* in which a fixed boom is placed across a river flow with current U . In both cases, oil accumulates inside the boom with the maximum accumulation occurring at the boom catenary's apex, where the maximum relative water velocity also occurs. Considering the location of accumulation and the small curvature of the boom geometry around the apex point, it is often acceptable (as a first approximation) to simplify this essentially three-dimensional problem to a *two-dimensional* one in the vertical plane intersecting the boom's apex (Fig. 1.2). It is also reasonable to assume that, for both cases in Fig. 1.1, the boom does not move and the water flows under the boom at a velocity U , equal to the relative boom-water velocity.

In order to collect as much oil as possible in the shortest possible time, it is desirable to have a relative velocity as large as possible. Various hydrodynamic instabilities at the oil-water interface, however, contribute to a fairly low practical limit for the relative velocity, on the order of 0.5 m/s. In fact, for the idealized problem sketched in Fig. 1.2, laboratory observations show that interfacial waves start developing at the oil-water interface for relative current speeds, $U \simeq 0.15$ m/s. For larger speeds, these waves grow unstable and, in most cases, lead to substantial or even total loss of oil under the boom (Agrawal and Hale [1], Lau and Kirchifer [27], Wicks [39], Wilkinson [40, 41]).

In the literature, such instabilities are referred to as *boom containment failure modes* and three main types (or modes) of containment failures have thus far been identified¹:

- *drainage failure*, where an increase in relative water-boom velocity U leads to an increase in interfacial friction stresses, causing both a shortening and a thickening of the slick beyond the barrier draft d , leading to containment failure;
- *entrainment failure*, where, for high relative oil-water velocities and low viscosity oils ($\nu_o < 3,000$ cs), large interfacial stresses occur and induce shear instabilities at the oil-water interface characterized by the formation of small fast-moving interfacial waves (ripples); for sufficiently large U (on the order of 0.25 m/s), these waves may grow unstable and break, leading to subsequent entrainment of oil droplets in the underlying flow;

¹Note that, in addition to these failure modes which occur in calm weather, the effectiveness of the boom in containing oil can be severely limited by the hydrodynamic behavior of both the boom and the slick under extreme weather conditions that may create high seas. Such factors have not been considered in the Phase I and II studies.

- *critical accumulation*, where, for oils with large viscosities ($\nu_o \geq 3,000$ cs) and velocity U usually lower than for the other two modes ($U_{cr} \simeq 0.15$ m/s), the interface develops slow-moving larger scale oscillations (headwave) which eventually cause all of the oil to escape under the barrier, *independent* of barrier draft d (Fig. 1.3).

Grilli *et al.* [16] conducted an exhaustive literature review of the oil containment problem and identified the key parameters and physical phenomena governing the three failure modes listed above. They showed, in particular, that *critical accumulation* is the dominant failure mode for high viscosity oils that are found in many real slicks² (Delvigne [9], Johnston *et al.* [22]). They also clearly showed that interfacial waves occurring during entrainment and critical accumulation failure modes are both initiated and sustained by *shear instability* at the oil-water interface, usually referred to as a *Kelvin-Helmholtz (KH) instability* (Benjamin [5], Drazin [11], Jones [23], Rangel and Sirignano [33]). Based on these findings, Grilli *et al.* focused on numerical modeling of KH instability (in the context of oil containment by a boom) as the main objective for Phases I and II of this project.

KH instabilities at the oil-water interface result from the interplay of the following physical processes and parameters (Fig. 1.2),

- the relative *water-boom velocity* U , which controls the magnitude of interfacial friction forces and triggers and sustains KH instability (see Section 2.5.2);
- the fluid *density difference* $\Delta\rho_{ow} = \rho_w - \rho_o$, which affects both slick thickness and spreading forces. [In applications, this parameter is often represented by the value of the oil/water density ration $\varphi = \rho_o/\rho_w = 1 - \Delta\rho_{ow}/\rho_w$.] (see Chapter 4);
- $\Delta\rho_{ow}$ and the *surface tension* coefficient at the oil water interface, σ_{ow} , which both affect the growth of interfacial KH waves (see Section 2.5.2);
- the interfacial *friction coefficient* C_f , which controls the magnitude of interfacial friction forces (and thus affects oil slick thickness) and is dependent on interfacial shape (including irregularities due to KH waves) (see Chapter 4);
- *oil viscosity* ν_o , which damps out short interfacial waves and limits the strength of internal circulation cells within the oil slick (hence justifying a quasi-hydrostatic assumption for highly viscous oil slicks; see Chapter 4).

Other parameters of lesser importance are σ_{aw} and σ_{oa} , the air-water and oil-air surface tension, respectively.

Many experimental and theoretical studies were pursued in the 1970's to understand the physics of oil containment by a boom and to identify the conditions leading to containment failure. More recently, there has been a renewed interest in studying this problem and attempts were made to use numerical modeling tools (Zalosh [42], Bai and Kim [2], Clavelle and Rowe [7], Ertekin and Sundararaghavan [13]). Among the existing models, however,

²Due to weathering effects, oil slick viscosity increases rapidly with time for many oils.

only the work by Zalosh [42] included the key parameters, listed above, affecting interfacial instability, whereas the other models [2, 7, 13] concentrated on representing fluid behavior in the bulk of the oil and water domains in front of and/or behind the boom, and totally ignored surface tension and KH waves on the oil-water interface.

In proposing the (FY94) Phase I project, considering the high degree of complexity of physical mechanisms involved, it was anticipated that the model would only be a first step towards a more comprehensive model of oil containment that could eventually provide practically useful results. In Phase I, we thus identified three major phases in model development, corresponding to successive improvements of the level of physical phenomena modeled and, hence, also of modeling accuracy (see Grilli *et al.* [16]). The approach selected for the initial model, *the Phase I model*, was based on Zalosh's model with both improved governing equations and numerical solution (see Grilli *et al.* [16]).

Development and implementation of the Phase II models took place as part of the FY95 project and are presented in this report. We will show that the Phase II models provide significant improvements of both the level of physics modeled and the numerical accuracy, compared to the Phase I model. In particular, we will present quantitative results showing the effects of the key factors listed above, on the growth rate of interfacial KH instabilities (Section 2.5.2). We will also give results of computations for the failure of a contained slick due to instabilities in the headwave (entrainment-type failures; Section 2.5.3). Finally, we will give quantitative predictions for the equilibrium steady-state shape of a contained slick, which compare favorably with experiments.

As a summary, Fig. 1.5 gives an overall flowchart for the model development procedures followed during Phase II, with the anticipated model experimental validation/calibration tasks to be carried out in the ongoing Phase III. As indicated in the figure, the major progress in Phase II models, as compared to the Phase I model, were made in the development of new numerical algorithms for the periodic (KH instability) and non-periodic (oil-slick with a boom) Piecewise Constant Vortex Sheet (PCVS) models, and in the establishment and implementation of a higher-order model (CVS) of the same problems. Numerical/qualitative validation of the newly developed models were carried out at all stages of model developments, using both convergence tests and lower-order theoretical solutions (e.g., the linearized KH instability problem by Lamb [26]). As indicated, both the PCVS and the CVS models and related algorithms were alternately tested for the KH instability case, which contains infinite vortex sheets with periodic disturbances, and for an oil-boom containment setting, similar to Fig. 1.2, which consists of multiple discretized vortex sheets and several infinite sheets.

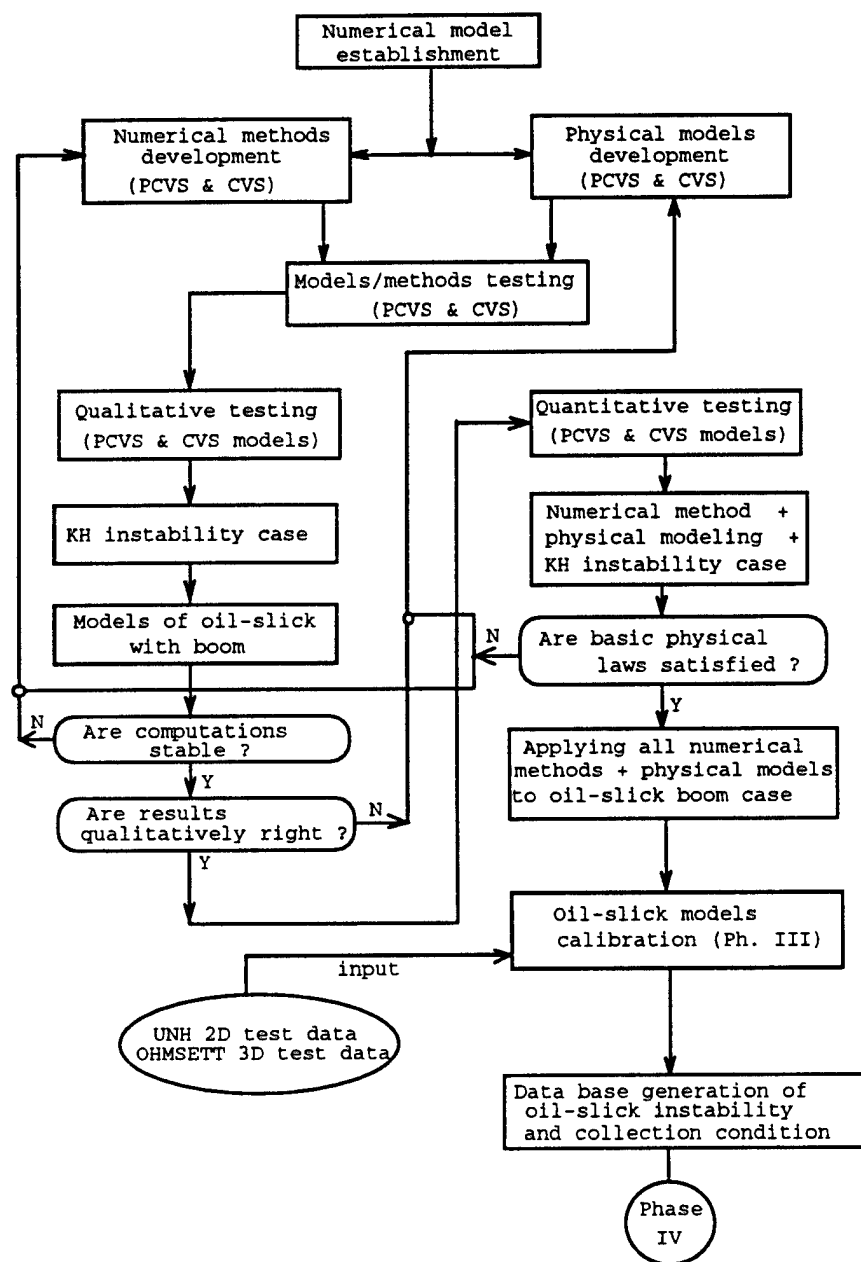


Figure 1.5: Flow chart of Phase II model development/validation procedure, with indication of Phase III validation/calibration tasks.

Chapter 2

Piecewise Constant Vortex Sheet (PCVS) model and applications

In the Phase I model developed for the containment of oil by a boom (e.g., Fig. 1.2), VS's were introduced to represent velocity discontinuity and geometry at fluid-fluid interfaces (air-water, air-oil, oil-water) and fluid-solid boundaries (boom, bottom). These VS's were discretized, along selected parts of the interfaces, using both piecewise-constant elements of vorticity (PCVS) and piecewise-polynomial geometry; semi-infinite parts of the interfaces were represented by semi-infinite VS's (Fig. 2.1).

This PCVS approach to the oil containment problem was further developed and refined during Phase II. In this Chapter, we first give a recapitulation of general VS dynamics equations (Section 2.1) and both old (Phase I) and newly developed (Phase II) improved numerical procedures (Section 2.2) used in all the models. We then review the governing equations for the periodic PCVS model (Section 2.3) and give applications of the Phase II improved numerical model (Section 2.5.2). In Section 2.4, we detail the specific improvements made during Phase II to the non-periodic PCVS model and give applications to oil containment by a boom in Section 2.5.3.

2.1 Recapitulation of VS dynamics equations

2.1.1 Velocities induced by VS's

For an inviscid fluid flow in a vertical plane (x, y) , when vorticity can be assumed to be concentrated within two-dimensional *vortex sheets* (VS), Biot-Savart's law can be used to calculate the induced velocity field, $\mathbf{u} = (u, v)$ as (Batchelor [4] p527),

$$\begin{aligned} u(x, y) &= \frac{1}{2\pi} \int \frac{y - y'}{r^2} \gamma(s) ds \\ v(x, y) &= -\frac{1}{2\pi} \int \frac{x - x'}{r^2} \gamma(s) ds \end{aligned} \quad (2.1)$$

where $\gamma(s)$ is the *clockwise* vortex sheet strength (i.e., minus the vorticity) and $s(x', y')$ is the curvilinear abscissa at points $\mathbf{x}' = (x', y')$ along the sheet.

When points $\mathbf{x} = (x, y)$ do not belong to the VS, integrals in (2.1) are non-singular. For points (x, y) on the VS, integrals in (2.1) are singular for vanishing τ and must thus be calculated in a Cauchy Principal Value (CPV) sense. In this case, (2.1) also takes the form of a Boundary Integral Equation (BIE) for $\mathbf{u}(x, y)$ on the sheet.

In the various numerical models developed in this study, discretized expressions of (2.1) are used to calculate the sheet position as a function of time, according to the Lagrangian definition of velocities, as,

$$\frac{d\mathbf{x}}{dt}(t) = \mathbf{u}(x, y) \quad (2.2)$$

where the time derivative follows the motion of the sheet.

A standard simplifying assumption in numerical models of VS dynamics is to assume that the vorticity is either *piecewise constant* or is concentrated at *point vortices* along the sheets. Despite their similarity—and sometimes their confusion in the literature—, these two representations differ in the sense that point vortices do not have a self-induced velocity contribution to Eqs. (2.1) whereas piecewise constant distributions of vortices do have self-induced velocity at the center of each interval, due to CPV integral contributions in (2.1) (Fink and Soh [14], Van de Vooren [37]).

In many studies, however, point vortices were found to only give a poor representation of continuous VS's as a function of time and often to quickly lead to inaccurate or even to unstable results. This occurs unless point vortices are continuously regridded to equal arc-length distance on the sheet (Fink and Soh [14]) and, even in this case, results cannot usually be accurately computed much beyond the initial instability and roll-up of the interface. The reason for this was discussed in Grilli *et al.* [16, 17] and various discretized equations and expressions for the CPV integrals needed for PCVS were given.

2.1.2 Rate of change of circulation on the VS's

For a vortex sheet representing the interface between two fluids moving with velocity \mathbf{u}_0 and \mathbf{u}_1 , respectively, the VS strength (i.e., vorticity density) is given by [42, 43, 37, 33],

$$\gamma(s) = \Delta u_s = u_{0s} - u_{1s} \quad (2.3)$$

in which,

$$u_{0s} = \mathbf{u}_0 \cdot \mathbf{s} \quad ; \quad u_{1s} = \mathbf{u}_1 \cdot \mathbf{s} \quad (2.4)$$

are tangential velocities on both sides of the VS, with $\mathbf{s} = [\cos \beta, \sin \beta]$, the tangential vector along the sheet and $\beta(s)$ the angle between the tangent to the sheet and the x -axis.

Using (2.3), the circulation (i.e., vorticity) associated with a small vortex element i of length Δs_i , over which constant velocity and smoothly varying geometry are assumed, is given by,

$$\Gamma(s_i) \equiv \Gamma_i = \int_{s_i - \Delta s_i/2}^{s_i + \Delta s_i/2} \gamma(s) ds \simeq (u_{0s} - u_{1s})_i \Delta s_i = \gamma_i \Delta s_i \quad (2.5)$$

For a uniform, incompressible, inviscid fluid with conservative forces, Kelvin's theorem states that the rate of change of circulation around a closed material contour moving with the fluid is zero (e.g., Batchelor [4]),

$$\frac{D\Gamma}{Dt} = 0 \quad \text{with} \quad \frac{D}{Dt} \equiv \frac{\partial}{\partial t} + \mathbf{u} \cdot \nabla \quad (2.6)$$

where D/Dt denotes the material derivative. For a vortex sheet at the interface between two regions of different velocity within the same fluid, however, Van de Vooren [37] showed that Kelvin's theorem, as stated in (2.6), is not applicable but may only be applied for a contour moving with the sheet reference velocity equal to the mean between velocities on both sides of the sheet, $\mathbf{u} = \frac{1}{2}(\mathbf{u}_0 + \mathbf{u}_1)$. This reference velocity is defined as the *sheet velocity* and will be used whenever calculating material time derivatives with respect to the sheet motion, referred to as d/dt .

For an interface between two different fluids with density ρ_0 and ρ_1 , subjected to gravity and non-zero interfacial tension σ_{01} , the fluid is non-uniform and forces are non-conservatives. Hence the rate of change of circulation around a material contour crossing the interface is non-zero and an evolution equation must be developed to predict its behavior. Zaroodny and Greenberg [45] first derived an equation for the rate of change of circulation for a continuous vortex sheet without surface tension. Zalosh [42, 43] developed a similar equation, including surface tension effects, for a sheet discretized with point vortices but made an error when he failed to consider the difference mentioned above between the time derivatives D/Dt , following fluid particles on either side of the sheet, and d/dt , following the sheet motion. This was later pointed out by Rangel and Sirignano [33] who derived the correct evolution equation, but without including gravitational effects.

Grilli *et al.* [16, 17] derived the expression for the rate of change of circulation, including gravity, density difference, and surface tension effects at the interface between two fluids. For a vortex sheet with piecewise constant vorticity elements Δs_i 's, it reads,

$$\frac{D\Gamma_i}{Dt} = 2\Delta s_i \left(\kappa \left[\frac{du_{si}}{dt} + g \sin \beta_i + \frac{1}{4} \gamma_i \frac{\partial \gamma_i}{\partial s} \right] - \frac{\sigma'_{01}}{1 + \varphi} \frac{\partial^2 \beta_i}{\partial s^2} \right) \quad (2.7)$$

where $\sigma'_{01} = \sigma_{01}/\rho_1$, $\varphi = \rho_0/\rho_1 \leq 1$, $\kappa = (1 - \varphi)/(1 + \varphi)$ is the Atwood number and, by (2.4),

$$\frac{du_{si}}{dt} = \frac{du_i}{dt} \cos \beta_i + \frac{dv_i}{dt} \sin \beta_i \quad (2.8)$$

is the tangential acceleration at point i .

In computations, a characteristic length scale is defined as λ and a characteristic time scale as $\lambda/\Delta U$, in which ΔU denotes a characteristic velocity jump at the interface. Based on these, the following nondimensional variables are introduced for coordinates of vortex element centers, their arc-length, and the time, as,

$$\xi_i = \frac{x_i}{\lambda} \quad ; \quad \eta_i = \frac{y_i}{\lambda} \quad ; \quad \Delta s_i = \frac{\Delta s_i}{\lambda} \quad ; \quad \tau = t \frac{\Delta U}{\lambda} \quad (2.9)$$

respectively, for the curvature at vortex element centers, as,

$$c_i = \lambda \frac{\partial \beta}{\partial s} \quad (2.10)$$

for velocities at vortex elements centers, as,

$$u_i = \frac{u_i}{\Delta U} \quad ; \quad v_i = \frac{v_i}{\Delta U} \quad (2.11)$$

and for the vorticity of vortex elements, as,

$$g_i = \frac{\Gamma_i}{\lambda \Delta U} \quad (2.12)$$

With these non-dimensional variables, the rate of change of vorticity of vortex elements can be expressed as,

$$\frac{dg_i}{d\tau} = 2\Delta s_i \left(\kappa \left[\frac{du_{is}}{d\tau} + \frac{g_i}{4(\Delta s_i)^2} \frac{\partial g_i}{\partial s} \right] + Fr^{-2} \sin \beta_i - We^{-1} \frac{\partial c_i}{\partial s} \right) \quad (2.13)$$

where Fr denotes the Froude number,

$$Fr = \frac{\Delta U}{\sqrt{g\kappa\lambda}} \quad (2.14)$$

and We denotes the Weber number,

$$We = \frac{\lambda(1+\varphi)(\Delta U)^2}{\sigma'_{o1}} \quad (2.15)$$

The non-dimensional tangential acceleration at the interface in (2.13) is found as ($i = 1, \dots, N$),

$$\frac{du_{is}}{d\tau} = \frac{du_i}{d\tau} \cos \beta_i + \frac{dv_i}{d\tau} \sin \beta_i \quad (2.16)$$

Details can be found in Grilli *et al.* [16].

2.1.3 Semi-infinite vortex sheets

As in Zalosh [42], horizontal semi-infinite vortex sheets will be used in the (non-periodic) computations of oil slick containment by a boom, to represent regions of the water domain with constant uniform horizontal velocity U . In Fig. 2.1, for instance, this corresponds to free surface and bottom regions both in front of the slick (e.g., from $x = -\infty$ to $x = x_\ell$) and behind the boom (e.g., from $x = x_r$ to $x = +\infty$).

Assuming no air velocity and no flow through the bottom, these semi-infinite sheets have a tangential velocity jump $\Delta u_s = \pm U$, with the negative sign being taken on the free surface and the positive sign on the bottom.

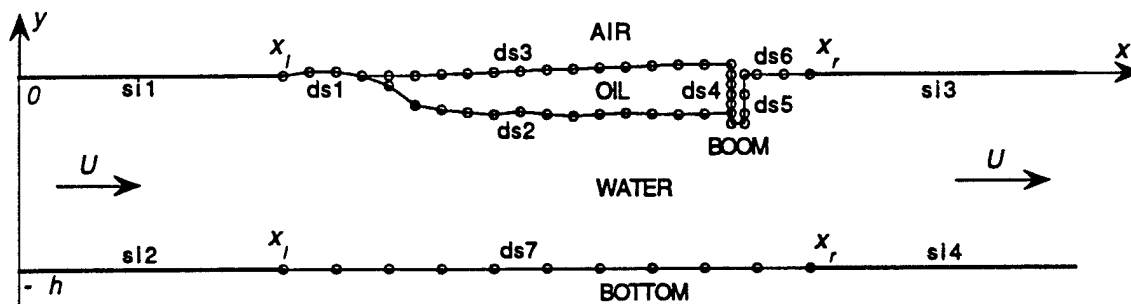


Figure 2.1: Sketch of computational domain for the oil containment by a boom, with definition of main parameters : U = flow velocity; sl1-sl4 = semi-infinite vortex sheets; ds1-ds7 = piecewise-constant discretized vortex sheets; \circ = centers of discretized vortex elements.

When parts of the fluid domain are discretized with VS elements, such semi-infinite vortex sheets provide contributions to the discretized form of Biot-Savart's Eqs. (2.1) for the sheet velocity, and also to the VS's accelerations. These contributions were calculated by Grilli *et al.* [16]. For instance, if the unperturbed free surface is at $y = 0$ and the horizontal bottom is at $y = -h$, the total contribution to the velocity of four semi-infinite vortex sheets located at $(x_l, 0)$ and $(x_r, 0)$, with strength $-U$, and at $(x_l, -h)$ and $(x_r, -h)$, with strength $+U$ is calculated as,

$$\begin{aligned}
 u_{lr} &= \frac{U}{2\pi} \left\{ 2\pi + \arctan\left(\frac{x-x_l}{y}\right) - \arctan\left(\frac{x-x_l}{y+h}\right) - \arctan\left(\frac{x-x_r}{y}\right) \right. \\
 &\quad \left. + \arctan\left(\frac{x-x_r}{y+h}\right) \right\} \\
 v_{lr} &= \frac{U}{4\pi} \log \frac{[(x-x_r)^2 + y^2][(x-x_l)^2 + (y+h)^2]}{[(x-x_l)^2 + y^2][(x-x_r)^2 + (y+h)^2]}
 \end{aligned} \tag{2.17}$$

As a verification, if we take $x_l = x_r$ in Eq. (2.17), thus assuming a uniform flow represented by two infinite vortex sheets, we see that (2.17) indeed reduces to, $u_{lr} = U$ and $v_{lr} = 0$.

For the accelerations it could be shown, similarly, that all contributions from the four sheets, as expected for a uniform flow, cancel each other and we get, $du_{lr}/dt = dv_{lr}/dt = 0$.

2.2 General numerical procedures for PCVS model

Numerical methods were developed in Phase I model for the integration of Eqs. (2.1) and (2.2). These were essentially a numerical integration of the BS equations and a time stepping procedure for the time marching. The basis of these methods have been kept in the Phase II model.

The differential equation (2.2) is solved using an explicit time stepping method in which both the geometry and the circulation on the VS's are calculated at time $\tau + \Delta\tau$, from the

known geometry and vorticity at time τ , using a truncated Taylor series as ($i = 1, \dots, N$),

$$\begin{aligned}\xi_i(\tau + \Delta\tau) &= \xi_i(\tau) + \Delta\tau u_i(\tau) + \frac{(\Delta\tau)^2}{2} \frac{du_i}{d\tau}(\tau) + \mathcal{O}[(\Delta\tau)^3] \\ \eta_i(\tau + \Delta\tau) &= \eta_i(\tau) + \Delta\tau v_i(\tau) + \frac{(\Delta\tau)^2}{2} \frac{dv_i}{d\tau}(\tau) + \mathcal{O}[(\Delta\tau)^3] \\ g_i(\tau + \Delta\tau) &= g_i(\tau) + \Delta\tau \frac{dg_i}{d\tau}(\tau) + \frac{(\Delta\tau)^2}{2} \frac{d^2g_i}{d\tau^2}(\tau) + \mathcal{O}[(\Delta\tau)^3] \quad (2.18)\end{aligned}$$

where $\Delta\tau$ denotes the nondimensional time step. Thus, starting with the VS's initial geometry and circulation, the induced velocity components u_i and v_i are calculated along the sheets using BS equations (2.1), discretized using PCVS elements. [The discretized BS equations for both periodic and non-periodic PCVS models are given in Sections 2.3.2 and 2.4.2.] Corresponding accelerations ($du_i/d\tau$, $dv_i/d\tau$) are calculated by finite backward differentiation. Time rates of change of circulation, $dg_i/d\tau$, are then calculated using Eqs. (2.13)-(2.16), and $d^2g_i/d\tau^2$ is calculated by finite backward differentiation (see Grilli *et al.* [16, 17] for details). Using these physical variables, Eq. (2.18) is used for the time updating and the whole process is repeated to calculate the solution at a later time.

Models developed during Phase I of this project, despite providing a good qualitative representation of the modeled phenomena, were not sufficiently accurate to allow good quantitative prediction. Furthermore, they were not usually stable enough to calculate interfacial evolution for a sufficiently long time. In the course of Phase II studies significant improvements were made to the models' numerical procedures to make computations both more accurate and stable. These improvements dealt with the following aspects of the computations :

- *Higher-order modeling of the geometry* : In Phase I model, higher-order sliding polynomial interpolation of the VS geometry was used. When using this method to compute interfacial evolution beyond the initial stages of instability (interfacial roll-up), however, it was observed that tangential derivatives became very irregular in regions of large curvature. This, in turn, through the effects of curvature and surface tension in the vorticity updating Eq. (2.13), caused the numerical results to rapidly become unreliable. The source of these irregularities was identified during Phase II studies as resulting from the isoparametric element mapping used in the sliding interpolation. A new interpolation/mapping method was developed that eliminated these irregularities. This method is referred to as *parity mapping* method.

To our knowledge, the origin of such irregularity problems has never been identified in earlier published studies of interfacial instabilities and may be responsible for some of the unstable results obtained by some authors, and referred to as *numerical chaos*, when using PCVS or point vortex methods to compute the roll-up of interfaces.

The parity mapping method is detailed in a following section.

- *End point periodicity and compatibility* : In the periodic KH problem (see below), the exact mathematical transformation of the infinite interface into a periodic interface

in the model both requires that the wavelength λ of periodicity be maintained closely constant and that numerical results be strictly periodic for each extremity of the discretized sheet. In the PCVS method, however, the use of the centers of constant segments as discretization points requires that both the first and last such segments be extended by half their length to represent a full wavelength. All geometrical quantities and their derivatives must also satisfy this periodicity. Although partly enforced in the Phase I model, these requirements were not all fully satisfied in the equations. Results were thus slightly less accurate for the end nodes of the interface which, through time stepping, could lead to significant errors and sometimes to the termination of computations, due to numerical sawtooth instability, before roll-up could be completed. Extended periodicity conditions have been implemented in the Phase II model for the periodic KH problem, and no irregular behavior is now observed at end nodes of the interface.

For the non-periodic oil-containment problem, VS's intersect each other at a number of locations (e.g., oil-water interface and boom, air-water interface and oil-water interface, etc...; see Fig. 2.1). At such multiple VS intersection points, components of the sheets' velocity calculated on different sheets must be compatible with each other, if the motion of the intersection point is to be uniquely defined, thus making computations stable. In the Phase I model, no particular attention was given to this problem and computations proved very unstable close to these "multiple points" which, in turn, had to be artificially maintained in their correct position. In the Phase II model, extended velocity/geometry compatibility conditions were implemented to ensure "multiple points" behaved correctly.

More details relative to "multiple points" modeling are given in a separate section.

- *Adaptive node regridding* : Regridding is a method where, through a re-interpolation of results on the interface between two fluids, nodes are redistributed according to some pre-established criterion. The simplest such redistribution (used in this model) is based on maintaining a (more or less) constant arc-length distance between nodes (i.e., segment length), throughout the computations. As the instability develops in time on the interface, VS roll-up occurs and the length of the interface increases significantly. Hence, to maintain the distance between nodes close to its original value, nodes are gradually added thereby improving the resolution of computations.

In the Phase I model, regridding was implemented but did not achieve full success. Indeed, a gradual loss of accuracy of results was observed as regridding occurred. It was understood during Phase II that this loss of accuracy resulted from small errors in the re-interpolation, of the same nature as those discussed above for modeling of the geometry. After implementing the parity mapping method for the interpolation and using it in combination with regridding procedures, it was found that these errors were mostly eliminated.

In the applications presented in Section 2.5.2, we compute the instability of a periodic

interface in both conservative and non-conservative cases. In the former case, two identical fluids are used which requires that the circulation be conserved along the interface. If no regridding occurs, this requirement is automatically satisfied in the model equations. With regridding, however, total circulation can be re-calculated at each time step and compared to the initial circulation. Doing so, it was observed that a slight change in total circulation occurred before and after regridding which could be attributed to the slightly different geometry of the interface in the two discretizations. Through time stepping, it was further observed that total circulation drifted from its initial value. Hence, a method was implemented in the model to correct the circulation of individual vortex elements and ensure that total circulation remained constant through regridding, for a given time step.

The adaptive regridding method is detailed in a following section.

2.2.1 Element parity mapping

As mentioned before, in most earlier models based on point vortices, investigators reported that, as time increased, computations became gradually unstable and, eventually, led to irregular motion of discretization points (e.g., Moore [31]; Zalosh [43]; Meiron *et al.* [30]). Such instabilities are particularly strong when surface tension effects are included (Rangel and Sirignano [33]). In most of the previously reported work, after experiencing such problems, it was concluded that numerical instabilities were likely due to improper calculation/representation of VS's motion in the models. In some work, reduction in numerical instabilities were attempted, but with little success, by improving singular integration calculations.

A detailed analysis of this problem was done during Phase II which showed that irregular motions of vortex elements are always associated with an increasingly poor accuracy of the VS geometric representation and, particularly, of tangential s -derivatives. When KH instabilities develop, intense roll-up of VS's indeed occurs (e.g., Fig. 2.3), leading to large curvature of the interface and to enhanced surface tension effects. Hence, even if a lower-order representation may be acceptable for the circulation, a higher-order representation of the geometry is needed to ensure continuity of inter-element slope and curvature. This was also concluded by Grilli and Svendsen [21], who used cubic splines, and by Grilli and Subramanya [18, 20], who introduced a fourth-order sliding polynomial interpolation of the geometry, independent of the Boundary Element (BEM) shape functions, to calculate s -derivatives in their computations of overturning surface waves.

In the Phase I model, following Grilli and Subramanya, a five-node sliding interpolation of the geometry was first tested (i.e., 4th-order isoparametric boundary element in which geometric characteristics are calculated for the middle node of the element). Slope angle and tangential derivatives were calculated by direct differentiation in the sliding element, using a BEM representation in which the geometry of each element is represented by a set of $m = 5$ locally continuous polynomial shape functions $N_j(\mu)$, analytically defined on a reference *isoparametric element* using m discretization points (nodes) (parametric mapping

in Fig. 2.2). Hence,

$$x(\mu) = \sum_{j=1}^m N_j(\mu) x_j \quad ; \quad y(\mu) = \sum_{j=1}^m N_j(\mu) y_j \quad ; \quad \gamma(\mu) = \sum_{j=1}^m N_j(\mu) \gamma_j \quad (2.19)$$

where x_j , y_j , and γ_j are coordinates and circulation for the element nodes, respectively. Derivatives with respect to the intrinsic coordinate (denoted by μ indices) are easily obtained from Eq. (2.19), using derivatives of shape functions. Key flow parameters of VS's evolution are functions of tangential s -derivatives of the interfacial slope angle β and curvature $\partial\beta/\partial s$. For each boundary element, these can be expressed as,

$$\cos \beta = \frac{x_\mu}{s_\mu} \quad ; \quad \sin \beta = \frac{y_\mu}{s_\mu} \quad ; \quad s_\mu = \{x_\mu^2 + y_\mu^2\}^{1/2} \quad (2.20)$$

$$\begin{aligned} \frac{\partial \beta}{\partial s} &= \frac{y_{\mu\mu} \cos \beta - x_{\mu\mu} \sin \beta}{s_\mu^2} \\ \frac{\partial^2 \beta}{\partial s^2} &= \frac{y_{\mu\mu\mu} \cos \beta - x_{\mu\mu\mu} \sin \beta}{s_\mu^3} - \frac{3}{2s_\mu^4} [2x_{\mu\mu}y_{\mu\mu} \cos 2\beta - (x_{\mu\mu}^2 - y_{\mu\mu}^2) \sin 2\beta] \end{aligned} \quad (2.21)$$

which can easily be calculated using derivatives of Eq. (2.19). Hence, the geometry $(x(\mu), y(\mu))$, circulation $\gamma(\mu)$, and the Jacobian s_μ^k , of each VS element k , can be calculated with Eqs. (2.19) and (2.20) and substituted into the discretized BS integrals and, similarly, these and $\partial^2\beta/\partial s^2$ calculated with Eq. (2.21) can be substituted into the vorticity updating Eqs. (2.7) or (2.13). To calculate characteristics for the next node along the VS, the sliding element was moved forward by one node. The element was kept identical for the first 3 nodes and for the last 3 nodes on the sheet.

When using this sliding element for the KH problem, however, after providing the initial trend of VS roll-up, computations rapidly failed and led to irregular motion of nodes, independent of flow conditions and physical properties. A repetition of these calculations using cubic splines did not improve results. To better identify the nature of instabilities, in Phase II, both the sliding and spline element methods were used to calculate tangential derivatives for a simple sinusoidal interface. It was found that :

- the accuracy of tangential derivatives calculated in the reference element is a function of the location of nodes on the original interface, especially if the order of derivatives is high;
- the numerical instability or irregular motion of nodes is first triggered by inaccuracies in the higher-order s -derivatives, mostly at locations where a fairly non-uniform distribution of nodes occurs within one element.

These findings explain why, for the periodic KH problem, instabilities were first observed at the extremity nodes and in roll-up regions of the interface, where the periodic boundary condition is enforced and interface node spacing is most changed, respectively.

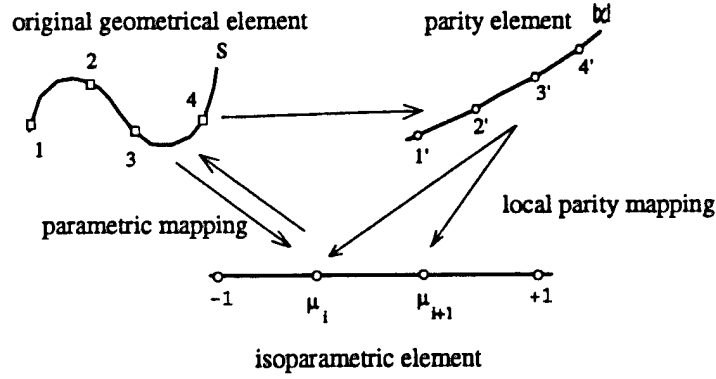


Figure 2.2: The Parity Mapping scheme for local isoparametric element

A careful analysis of these and similar results showed that the mapping of geometric elements, with irregular node spacing, to a reference element, with constant node spacing, is at the origin of small numerical inaccuracies in higher-order s -derivatives which, through time updating and enhanced surface tension effects in the roll-up regions, rapidly propagate and lead to sawtooth instabilities of the interface geometry. A new method, referred to as *parity mapping*, was thus designed to provide s -derivatives less dependent on discretization node density. Bases for this method are indicated in Fig. 2.2. In standard isoparametric element transformation, the distance between nodes in the reference element is constant. In Fig. 2.2, for instance, with a four-node element, it is equal to two-third. In the parity mapping method, a new (monotonous) mapping variable χ is defined, in between the transformation from s to μ , to create an element, with node density similar to the geometric element. The parity element is then mapped onto a reference element with intrinsic coordinate μ varying between $[-1, +1]$ and irregular node spacing. Results show that this method eliminates (or at least greatly reduces) fluctuations induced in tangential derivatives due to irregular node spacing.

The (monotonous) parity coordinate χ is defined for element nodes i such as to carry the basic geometrical information from the original node distribution, as,

$$\chi_i = \chi_{i-1} + \sqrt{|x_i| + |y_i|} \quad ; \quad i = 2, \dots, m \quad (2.22)$$

for a m -node isoparametric element ($m \geq 4$ and even), with $\chi_1 = 0$, and the middle interval in the element starting at node $m/2$. The mapping interval in the reference element is, $\Delta\mu = \mu_m - \mu_1 = 2$, and the corresponding interval for the parity mapping element is,

$$\Delta\chi = \chi_m - \chi_1 = \sum_{j=1}^{m-1} \Delta\chi_j \quad \text{with} \quad \Delta\chi_j = \chi_{j+1} - \chi_j \quad (2.23)$$

The basic relationship for the parity mapping transformation expresses a geometric similarity

between χ and μ , as,

$$\Delta\mu_i = \Delta\chi_i \frac{\Delta\mu}{\Delta\chi} \quad ; \quad i = 1, \dots, m-1 \quad (2.24)$$

For the 4-node element in Fig. 2, using Eq. (2.24), we thus have for the intermediate node coordinates ($m/2 = 2$),

$$\begin{aligned} \mu_2 &= \Delta\chi_2 \frac{2}{\Delta\chi} - 1 \\ \mu_3 &= \frac{2}{\Delta\chi}(\Delta\chi_2 + \Delta\chi_3) - 1 \end{aligned} \quad (2.25)$$

with $\Delta\chi$, $\Delta\chi_2$, and $\Delta\chi_3$ being given by Eqs. (2.22),(2.23), for the corresponding element nodal coordinates (x_i, y_i).

In the applications, the parity mapping method is used to calculate s -derivatives, based on 4-node cubic elements (as in Fig. 2.2). In this case, corresponding shape functions $N_j(\mu)$ are analytically recalculated for each element, depending on the μ_i values at intermediate nodes (i.e., here, μ_2 and μ_3 from Eq. (2.25), with $\mu_1 = -1$ and $\mu_4 = 1$ for the element extremity nodes), to satisfy the property $N_j(\mu_i) = \delta_{ij}$, as,

$$\begin{aligned} N_1(\mu) &= \frac{(\mu - \mu_2)(\mu - \mu_3)(1 - \mu)}{2(1 + \mu_2)(1 + \mu_3)} \\ N_2(\mu) &= \frac{(\mu + 1)(\mu - \mu_3)(\mu - 1)}{(1 + \mu_2)(\mu_2 - \mu_3)(\mu_2 - 1)} \\ N_3(\mu) &= \frac{(\mu + 1)(\mu - \mu_2)(\mu - 1)}{(1 + \mu_3)(\mu_3 - \mu_2)(\mu_3 - 1)} \\ N_4(\mu) &= \frac{(\mu + 1)(\mu - \mu_2)(\mu - \mu_3)}{2(1 - \mu_2)(1 - \mu_3)} \end{aligned} \quad (2.26)$$

Other geometric variables needed for the BS integrals are discretized using 4-node cubic isoparametric sliding boundary elements (i.e., with shape functions $N_j(\mu)$ given by Eq. (2.26), with $\mu_2 = -1/3$ and $\mu_3 = 1/3$), in which the middle interval only is used to interpolate between two nodes (*mid-interval interpolation*; Grilli and Subramanya [20]).

2.2.2 Adaptive regridding method

When VS's roll-up on the oil-water interface, some regions of the interface become significantly stretched, which leads to a reduced density of nodes and VS elements that may affect computational accuracy. In other regions of the interface, on the other hand, nodes will tend to concentrate which may lead to quasi-singular situations, particularly when point-vortices are used. In earlier work, node regridding methods were introduced to prevent point vortices from excessively concentrating in roll-up regions of the interface (e.g., by Rangel and Sirignano [33]) : nodes were adaptively added and regridded to equal arc-length spacing, according to the increased length of the interface with time, in order to satisfy a minimum

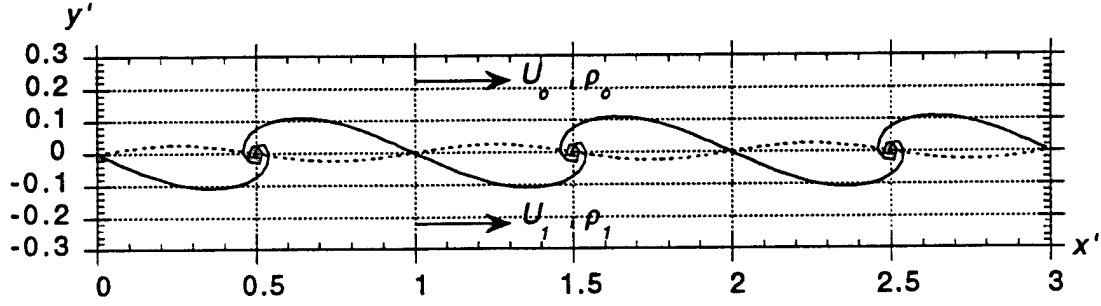


Figure 2.3: Sketch of computational set-up for periodic Kelvin-Helmholtz instability with wavelength λ (with, $x' = x/\lambda$, $y' = y/\lambda$). U_0 , U_1 are uniform velocities and ρ_0 , ρ_1 are densities, of fluid 0 and 1, respectively. Curve (---) is the initial sinusoidal perturbation on the interface between fluid 0 and 1 and (—) is the unstable interface computed at a later time.

spatial resolution requirement. In the applications of Section 2.5, for instance, nodes were added when the PCVS element average length increased or decreased by more than 1.5% over one time step.

In the present model, a similar node regridding technique is used, based on the method developed by Grilli and Subramanya [20] to study breaking surface waves. This method combines cubic spline elements and the new parity mapping interpolation method presented above. For the PCVS model, the circulation interpolation is performed at time step t^k , at the location of the regridded nodes, using the circulation densities calculated as,

$$\gamma_i^k = \frac{\Gamma_i^k}{\Delta s_i^k} \quad (2.27)$$

where i corresponds to the old node locations.

In addition, as mentioned before, a correction of the vortex elements circulation is performed in order to maintain a constant total circulation on the VS, through regridding at a given time step.

2.3 Periodic KH instability and equations for PCVS periodic model

2.3.1 KH instability problem

In this idealized problem, we consider a vertically stratified, statically stable system, made of two homogeneous immiscible inviscid fluids, of density ρ_1 (lower fluid) and $\rho_0 \leq \rho_1$ (upper fluid), interfacial tension σ_{01} , and infinite extension in the x direction, moving with uniform horizontal velocities U_1 and U_0 , respectively (Fig. 2.3). We wish to calculate the evolution of the interface between the two fluids, as a function of time, under the action

of gravity, density difference, inertial, and interfacial tension forces, when the interface is initially perturbed by a small periodic disturbance¹.

Hence, in the computations both an initial sinusoidal disturbance of wavelength λ and (small) amplitude a (i.e., $\propto a \sin 2\pi x/\lambda$), and a velocity jump, $\Delta U = |U_1 - U_o|$, are prescribed on the interface between both fluids. According to Lamb [26], the initial vorticity distribution $\gamma(x)$ corresponding to the specified geometry and velocity jump is,

$$\gamma(x) = \Delta U \left(1 + 2\pi\epsilon \left\{ \kappa \sin\left(2\pi\frac{x}{\lambda}\right) - 2\frac{\sqrt{\varphi(1-W)}}{(1+\varphi)} \cos\left(2\pi\frac{x}{\lambda}\right) \right\} \right) \quad (2.28)$$

with,

$$W = \left\{ (1-\varphi)\frac{g}{k} + \sigma_{o1}\frac{k}{\rho_1} \right\} \frac{1+\varphi}{\varphi(\Delta U)^2} \quad (2.29)$$

where $\epsilon = a/\lambda$, $k = 2\pi/\lambda$ is the wavenumber, g is the acceleration of gravity, $\varphi = \rho_o/\rho_1$ is the density ratio, and $\kappa = (1-\varphi)/(1+\varphi)$ is the Atwood number.

This problem was solved by Lamb [26] in a linear framework (see p. 373 and p. 461). He found that a periodic disturbance would always be unstable and grow exponentially with time as $\propto \exp \omega t$, if,

$$\Delta U > \Delta U_{cr} = \frac{1+\varphi}{\sqrt{\varphi}} c_o \quad (2.30)$$

with,

$$c_o = \left(\kappa \frac{g}{k} + \sigma'_{o1} \frac{k}{(1+\varphi)} \right)^{1/2} \quad (2.31)$$

the speed of propagation of interfacial waves, $\sigma'_{o1} = \sigma_{o1}/\rho_1$, and,

$$\omega = k \Delta U \frac{\sqrt{\varphi(1-W)}}{(1+\varphi)} \quad (2.32)$$

Combining Eqs. (2.29) to (2.32), one sees that the instability criterion (2.30) also corresponds to $W < 1$.

According to Eq. (2.30), the growth of the instability will be maximum for a minimum value of c_o . Hence, calculating the critical wavelength λ^{min} leading to this minimum value and replacing it in Eqs. (2.30) and (2.31), we obtain the minimum critical velocity jump causing instability (i.e., the one for which $\omega = 0$ or $W = 1$) as,

$$\Delta U_{cr}^{min} = \left(2 \frac{1+\varphi}{\varphi} \sqrt{\sigma'_{o1} g (1-\varphi)} \right)^{1/2} \quad (2.33)$$

with,

$$\lambda^{min} = 2\pi \left(\frac{\sigma'_{o1}}{g(1-\varphi)} \right)^{1/2} \quad (2.34)$$

¹When the low density fluid is above, the interface is statically stable unless the superposition of a velocity across the perturbed interface can generate inertially induced Kelvin-Helmholtz (KH) instability (Kelvin [25]).

Lamb's solution assumes that the height of interfacial waves is infinitesimal. This is only an approximation, particularly if the instability is free to develop for a long enough time. As a first approximation, however, Lamb's solution can be used both to predict the threshold velocity likely to cause initial instability of interfacial waves, and the initial stages of growth of instability in the linear regime. Moreover, despite their limitations, as we will see, Lamb's equations contain the correct physical parameters influencing interfacial instability (i.e., fluid density ratio, interfacial tension, and gravity) that will be used in the numerically exact solution presented hereafter.

2.3.2 Governing equations for PCVS periodic model

In the periodic PCVS model, full nonlinearity of geometry and flow equations is kept by representing the interface as an inviscid vortex sheet (VS) whose motion is given by the Biot-Savart integral equation (2.1) (Batchelor [4]). Hence, for the infinite interface between both fluids, the complex motion $z(s, t)$ is given by,

$$\frac{dz}{dt}(s, t) = u(s, t) - i v(s, t) = \frac{i}{2\pi} \int_{-\infty}^{+\infty} \frac{\gamma(s')}{z(s, t) - z(s', t)} ds' \quad (2.35)$$

where, $i = \sqrt{-1}$, $z = x + iy$, and s is the curvilinear coordinate along the VS. The integral in Eq. (2.35) must be understood in a Cauchy Principal Value (CPV) sense and $\gamma(s)$ is the vortex sheet strength (i.e., circulation), satisfying conservative or non-conservative evolution equations, depending on the problem treated (see next section).

Due to spatial periodicity of the KH problem, Eq. (2.35) can be transformed into (Van de Vooren, [37]),

$$\begin{aligned} u(\xi, \eta) &= \frac{d\xi}{d\tau} = \frac{1}{2} \int_0^{S(\lambda)} \frac{\sinh 2\pi(\eta - \eta')}{\cosh 2\pi(\eta - \eta') - \cos 2\pi(\xi - \xi')} dg' \\ v(\xi, \eta) &= \frac{d\eta}{d\tau} = -\frac{1}{2} \int_0^{S(\lambda)} \frac{\sin 2\pi(\xi - \xi')}{\cosh 2\pi(\eta - \eta') - \cos 2\pi(\xi - \xi')} dg' \end{aligned} \quad (2.36)$$

where dimensionless variables introduced in Eqs. (2.9)-(2.12) have been used, and dashes denote variables calculated at point s' of the VS. The VS's nondimensional velocity field (u, v) and motion (ξ, η) induced by a known vorticity distribution can thus be obtained by solving Eq. (2.36). Due to the nonlinearity in the equations, this can only be performed numerically.

When the VS representing the infinite periodic interface between two fluids is discretized using Piecewise Constant Vortex Sheets (PCVS) elements, Grilli *et al.* [16] showed that Biot-Savart equations (2.36) reduce to,

$$\begin{aligned} u_i &= \frac{1}{2} \sum_{j \neq i} g_j \frac{\sinh 2\pi(\eta_i - \eta_j)}{\cosh 2\pi(\eta_i - \eta_j) - \cos 2\pi(\xi_i - \xi_j)} + \bar{u}_i \\ v_i &= -\frac{1}{2} \sum_{j \neq i} g_j \frac{\sin 2\pi(\xi_i - \xi_j)}{\cosh 2\pi(\eta_i - \eta_j) - \cos 2\pi(\xi_i - \xi_j)} + \bar{v}_i \end{aligned} \quad (2.37)$$

for $(i, j = 1, \dots, N)$, with the indices denoting center points of PCVS elements.

In Eq. (2.37), the interface has been assumed to be discretized by N segments of length Δs_j (nondimensional length Δs_j), with piecewise-constant vorticity density γ_j or $\Gamma_j = \gamma_j \Delta s_j$ (nondimensional value g_j). Velocities \bar{u}_i and \bar{v}_i denote nondimensional velocity contributions resulting from CPV integrals due to singularities occurring when the source point (x_i, y_i) or (ξ_i, η_i) coincides with the integration point (x_j, y_j) or (ξ_j, η_j) (i.e., self-induced velocity contributions). To our knowledge, since most existing models use (less accurate) point vortices, these periodic CPV integrals have never been exactly calculated in the literature. Only Van de Vooren [37] provided a first-order approximation for these, based on a Taylor series expansion of the singularities. Full analytical expressions for \bar{u}_i and \bar{v}_i can be found in Grilli *et al.* [16] (their Eqs. 4.14 to 4.16). More accurate expressions of CPV velocities for continuous vortex sheets are given in Section 3.1.

The general numerical procedures used in the periodic PCVS model are those presented in Section 2.2.

2.4 Oil/boom containment problem and equations for the non-periodic PCVS model

2.4.1 Oil/boom containment problem

This problem physically corresponds to Figs. 1.2 to 1.4 and, for the numerical PCVS model, is illustrated by Fig. 2.1 where one can see that various interfaces between fluids and fluid or solid boundaries (air-water, oil-water, oil-boom, water-boom) are represented by semi-infinite VS's or discretized PCVS. Governing equations are the Biot-Savart Eqs. (2.1), for calculating the velocity field induced by vorticity distributions on the VS's, Eq. (2.2), for calculating the VS's movements as a function of time, and Eqs. (2.7) or (2.13), for calculating the time rate of change of vorticity along the VS's.

During Phase I studies, a simplified oil/boom containment problem was solved, following the methodology proposed by Zalosh [42], in which a semi-infinite oil slick was modeled (i.e., without a boom), and the headwave instability of the contained oil slick was calculated. Hence, to model this problem, two discretized PCVS were used, for the oil-water and the oil-air interfaces, together with three semi-infinite VS's. Computational results for this problem showed that, for sufficiently large flow velocity, the expected VS roll-up occurred in the front of the slick (see also [17] for numerical results).

During Phase II studies, the computations of instabilities in oil/boom containment systems were extended to more realistic cases including a finite slick and a solid boom. In such cases, the water-air interface in front of the slick was also discretized as a PCVS to account for the dip of the free surface observed in experiments at the slick leading edge. Doing so, 5 discretized PCVS and 3 semi-infinite or infinite VS's were used in the model (Fig. 2.4), which made it necessary to address problems of velocity and displacement compatibility at multiple intersection points between sheets.

In the following, governing equations for a PCVS multiple sheet system are first presented. Then, numerical methods specific to this problem, such as the initial conditions are presented and the treatment of multiple intersection points.

2.4.2 Governing equations for PCVS non-periodic model

For a one sheet system, discretized with N PCVS elements, Biot-Savart equations (2.1) transform into [16] (for $i = 1, \dots, N$),

$$\begin{aligned} u_i &= \frac{1}{2\pi} \sum_{j \neq i} \frac{y_i - y_j}{r_{ij}^2} \Gamma_j + \tilde{u}_i \\ v_i &= -\frac{1}{2\pi} \sum_{j \neq i} \frac{x_i - x_j}{r_{ij}^2} \Gamma_j + \tilde{v}_i \end{aligned} \quad (2.38)$$

with $\Gamma_i = \gamma_i \Delta s_i$, the vorticity attributed to each PCVS element i , r_{ij} , the distance between the centers of elements i and j of coordinates (x_i, y_i) and (x_j, y_j) , and $(\tilde{u}_i, \tilde{v}_i)$ the CPV's contributions to the velocity field (u_i, v_i) given by,

$$\begin{aligned} \tilde{u}_i &= -\frac{1}{2\pi} \frac{\Gamma_i}{\Delta s_i} \sin \beta_i \log \frac{r_{i+1/2}}{r_{i-1/2}} \\ \tilde{v}_i &= +\frac{1}{2\pi} \frac{\Gamma_i}{\Delta s_i} \cos \beta_i \log \frac{r_{i+1/2}}{r_{i-1/2}} \end{aligned} \quad (2.39)$$

where β_i is the angle between the x -axis and segment i , and $[r_{i-1/2}, r_{i+1/2}]$ denote distances from both extremities to the mid-point of element i .

When M PCVS's and some semi-infinite sheets are used (as in Fig. 2.4), using nondimensional variables (2.9) to (2.12), Eq. (2.39) is generalized as an equation for the velocity at point i of sheet l as (for $i = 1, \dots, N_l$; $l = 1, \dots, M$),

$$\begin{aligned} u_i^l &= \sum_{k=1}^M \left(\frac{1}{2\pi} \sum_{j \neq i=1}^{N_k} \frac{\eta_i^l - \eta_j^k}{(r_{ij}^{kl})^2} g_j^k + \tilde{u}_i^k \right) + u_{lr} \\ v_i^l &= \sum_{k=1}^M \left(-\frac{1}{2\pi} \sum_{j \neq i=1}^{N_k} \frac{\xi_i^l - \xi_j^k}{(r_{ij}^{kl})^2} g_j^k + \tilde{v}_i^k \right) + v_{lr} \end{aligned} \quad (2.40)$$

where indices k and l denote the PCVS number, r_{ij}^{kl} denotes the nondimensional distance between point i on sheet l and point j on sheet k (k and $l = 1, \dots, M$), calculated as,

$$r_{ij}^{kl} = \sqrt{(\xi_i^l - \xi_j^k)^2 + (\eta_i^l - \eta_j^k)^2} \quad (2.41)$$

and (u_{lr}, v_{lr}) denote nondimensional velocities induced by semi-infinite vortex sheets, calculated as in Eq. (2.17) and divided by ΔU , the reference velocity jump, and, using Eq.

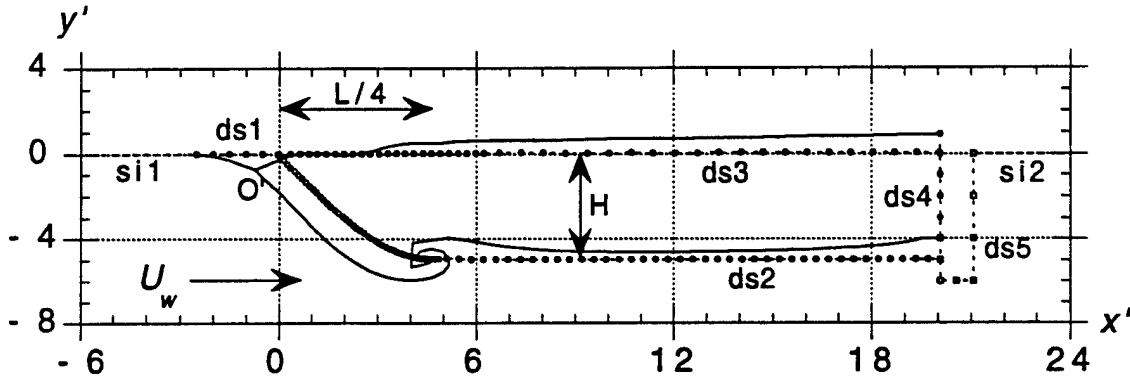


Figure 2.4: Sketch of computational domain for headwave instability of a contained oil slick, with definition of main parameters : U_w = water velocity with respect to slick ($U_o = 0$ in slick); air velocity can be set to U_a and interfacial tensions are σ_{oa} and σ_{ow} ; fluid densities are $\rho_a = 0$, ρ_o and ρ_w ; si1 and si2 = two semi-infinite vortex sheets on the air-water interface (an infinite sheet si3 (not shown) represents the bottom); ds1 to ds5 = five discretized PCVS; \circ , \bullet , and \square = centers of discretized vortex elements. (---) initial shape of the slick based on Zalosh [42] (Eqs. (2.43), (2.44)); (—) unstable shape computed at a later time.

(2.39), $(\tilde{u}_i^k, \tilde{v}_i^k)$ denote the nondimensional CPV self-induced velocity contributions given, for points i on sheet k , as,

$$\begin{aligned}\tilde{u}_i^k &= -\frac{1}{2\pi} \frac{g_i^k}{\Delta s_i^k} \sin \beta_i^k \log \frac{r_{i+1/2}^k}{r_{i-1/2}^k} \\ \tilde{v}_i^k &= +\frac{1}{2\pi} \frac{g_i^k}{\Delta s_i^k} \cos \beta_i^k \log \frac{r_{i+1/2}^k}{r_{i-1/2}^k}\end{aligned}\quad (2.42)$$

The general numerical procedures used in the non-periodic PCVS model are identical to those presented in Section 2.2. Numerical methods specific to the oil/boom problem are presented hereafter.

2.4.3 Numerical procedures specific to the oil/boom problem

Initial conditions

To solve Eq. (2.2), together with Eqs. (2.40)-(2.42) and (2.13)-(2.16), an explicit time stepping algorithm is used (as described in [16, 17]) for which initial conditions for the VS's geometry and circulation must be provided. Since several discretized VS's are included in the computational domain, the initial flow conditions on each sheet have to be estimated depending on their initial shape (Figs. 2.1, 2.4). In the present studies, however, since no frictional effects are yet included in the vorticity updating equations, the initial shape of the slick cannot yet be assumed to be the quasi-steady state shape of the slick, as calculated using the method of Section 4. This will be done during Phase III studies. Instead,

in the present case, in order to validate the non-periodic PCVS model for the oil/boom containment problem, the initial shape of the oil-water interface (ds2) was assumed to be the semi-empirical shape proposed by Zalosh [42], based on the observation of various experimental results, to represent the headwave region of a slick, i.e. (Figs. 2.1, 2.4),

$$\begin{aligned}\eta(x) &= H \sin(2\pi x/L) & \text{for } 0 \leq x \leq L/4 \\ \eta(x) &= H & \text{for } L/4 \leq x \leq L\end{aligned}\quad (2.43)$$

where H and L are the initial depth and length of the slick headwave, respectively (Fig. 2.4). Assuming flat air-water and air-oil interfaces at $y = 0$ (ds1, ds3) and quasi-hydrostatic equilibrium in the oil slick, we obtain, using Bernoulli's equation between the front and the back of the slick,

$$H = \frac{U_w^2}{2g(1 - \varphi)} \quad (2.44)$$

where U_w is the free stream water velocity. Following the work by Von Karman [38] for density intrusions along solid boundaries, Zalosh assumed a 60° value for the angle of the headwave at the leading edge. With this angle, Eq. (2.43) yields $L = 3.63H$. As pointed out by Zalosh, experimental results usually show smaller angles at the leading edge, which results in increased values of L (see, e.g., Milgram and Van Houten [29]).

According to Eq. (2.3), the initial circulation along VS's is equal to the velocity jump at the sheets. Assuming a steady-state flow and a mildly sloping oil-water interface, pending the use of the initialization method of Section 4, the initial tangential velocity along the slick is estimated as the projection of the free stream velocity in the tangential direction. Hence, according to Eqs. (2.3)-(2.5), the initial circulation of PCVS elements on the VS ds2 is given by,

$$\Gamma_i^2 = \Delta s_i^2 U_w \cos \beta_i^2 \quad (2.45)$$

The same equation is applied to estimate the initial circulation Γ_i^5 on the water-boom sheet ds5. For still air and oil, the initial circulation on the oil-water sheet ds3 is selected as zero, i.e., $\Gamma_i^3 = 0$. For the oil-boom sheet ds4, however, despite the assumption of no initial flow in the oil slick, to ensure numerical stability, it was found necessary to linearly vary the initial circulation Γ_i^4 along ds4, from the value on the last segment of sheet ds2 on the boom, to 0, when moving upward along the sheet. Otherwise, the initial circulation jump from sheet ds2 to ds4 was found to cause irregular motions of PCVS elements on the oil-water interface and, eventually, to cause numerical instability of the computations. This is because, as numerical results show, as time increases, a slow but non-zero (inviscid) flow is induced in the oil slick, as a result of the velocity jump at the oil-water interface; hence, initial conditions must account for this flow.

Multiple sheet intersection points

At *Multiple Sheet Intersection Points* (MSIP), such as O' in Fig. 2.4, the flow velocity must be continuous and the circulation must also satisfy Kelvin's theorem. Compatibility

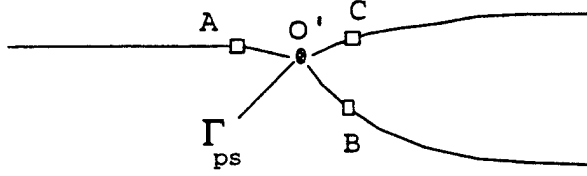


Figure 2.5: Sketch of triple (fluid) sheet intersection point at the oil slick leading edge, in the non-periodic discretized PCVS model. (□) denote last PCVS element centers on sheets ds1, ds2, and ds3.

conditions have been developed to enforce these physical requirements in the discretized PCVS model equations.

As seen in Fig. 2.4, MSIP's occur on the boom solid boundary (ds2-ds4, ds3-ds4) and at the slick leading edge O' (ds1-ds2-ds3). As an additional difficulty, point O' is a moving triple MSIP and the ds2-ds4 and ds3-ds4 MSIP's can move up and down along the boom surface. The motion of these MSIP's is not correctly predicted by the Biot-Savart equations, when discretized for PCVS elements located on separate VS's. Hence, additional compatibility equations are required to correctly describe the behavior of MSIP's.

The triple MSIP O' at the slick leading edge is sketched in Fig. 2.5 as the geometric intersection of sheets ds1-ds2-ds3. Theoretically, this intersection node is free to move in an arbitrary direction. This direction, however, must physically be related to the instantaneous motion of neighboring nodes A, B, C, on sheets ds1, ds2, ds3, respectively. For the analysis of the motion of point O', let us assume that there is a point vortex of strength Γ_{ps} located at O' (no discretization node is actually located at O' in the discretized PCVS model, since computational nodes are located at the middle of VS elements; Fig. 2.5). The assumption of a moving point vortex at O' requires that the circulation Γ_{ps} be such as to balance the average accumulation of circulation at nodes A, B, and C, i.e.,

$$\Gamma_{ps} = \frac{\alpha_{ps}}{m} \sum_{k=1}^m \Gamma_l^k \quad (2.46)$$

where α_{ps} is a constant to be numerically determined in the [0,1] range, m is the number of connecting sheets at point O' (i.e., $m = 3$ for the slick leading edge), and index l denotes the last PCVS element on sheet k (i.e., points A, B, and C in Fig. 2.5). Computations would normally begin with $\alpha_{ps} = 1.0$ and the additional contribution of the circulation Γ_{ps} to the computation of the (nondimensional) velocity field, at point i on sheet l , using Eq. (2.40), is given by,

$$\begin{aligned} u_{i,ps}^l &= \frac{g_{ps}(\eta_i^l - \eta_{o'})}{2\pi (r_{i,o'}^l)^2} [1 - \exp(-\frac{(r_{i,o'}^l)^2}{R_c^2})] \\ v_{i,ps}^l &= -\frac{g_{ps}(\xi_i^l - \xi_{o'})}{2\pi (r_{i,o'}^l)^2} [1 - \exp(-\frac{(r_{i,o'}^l)^2}{R_c^2})] \end{aligned} \quad (2.47)$$

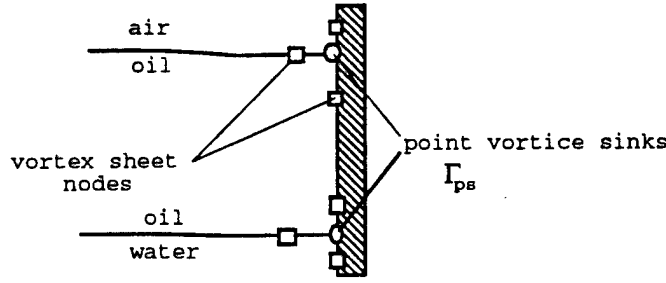


Figure 2.6: Sketch of double (fluid-solid) sheet intersection points along the boom, in the non-periodic discretized PCVS model.

with,

$$r_{i,o'}^l = \sqrt{(\xi_i^l - \xi_{o'})^2 + (\eta_i^l - \eta_{o'})^2} \quad (2.48)$$

where $(\xi_{o'}, \eta_{o'})$ denote dimensionless coordinates of the MSIP O' , and R_c is the nondimensional radius ($R_c < 1.0$) of a fictitious viscous core surrounding the point vortex Γ_{ps} . This viscous core method, introduced earlier by Zalosh [42], locally damps high frequency geometrical oscillations on the VS's and was found necessary in the present case to ensure the smooth behavior of numerical results at point O' . Finally, the motion of the triple MSIP O' is calculated in the model by assuming that the point moves with the average velocity of the adjacent nodes on the 3 intersecting sheets (i.e., A, B, C).

The other two MSIP's along the boom are intersections points ds2-ds4 and ds3-ds4 shown in Fig. 2.6. To satisfy the no-flow condition on the boom solid boundary, these two nodes are only allowed to move in the tangential direction at the boom surface (i.e., here, in the vertical direction). The numerical treatment of these nodes is similar to node O' . The circulation Γ_{ps} is first estimated ($t = 0$) at fictitious point vortices located at the geometric intersections of the VS's (Fig. 2.6), using Eq. (2.46) for $m = 2$, as the average value of the initial circulation at the extremity nodes of the intersecting sheets. As time progresses, however, small numerical errors occur at the boom which, in some cases, may make PCVS elements slightly penetrate the boom surface. In such cases, penetrated VS's sections are cut off from the discretized PCVS's, which results in a small loss/gain of circulation, say $\Delta\Gamma_{ps}$, at a given time t . To ensure that circulation is conserved, $\Delta\Gamma_{ps}$ is added to Γ_{ps} at each time step. As before, the contribution of Γ_{ps} to the induced velocity field is calculated with Eqs. (2.47) and (2.48).

2.5 Applications of PCVS models

2.5.1 Study of PCVS model convergence and stability

The numerical accuracy of the PCVS model solution depends on both the selected spatial discretization, i.e. number of *discretization nodes*, and temporal discretization, i.e. *time*

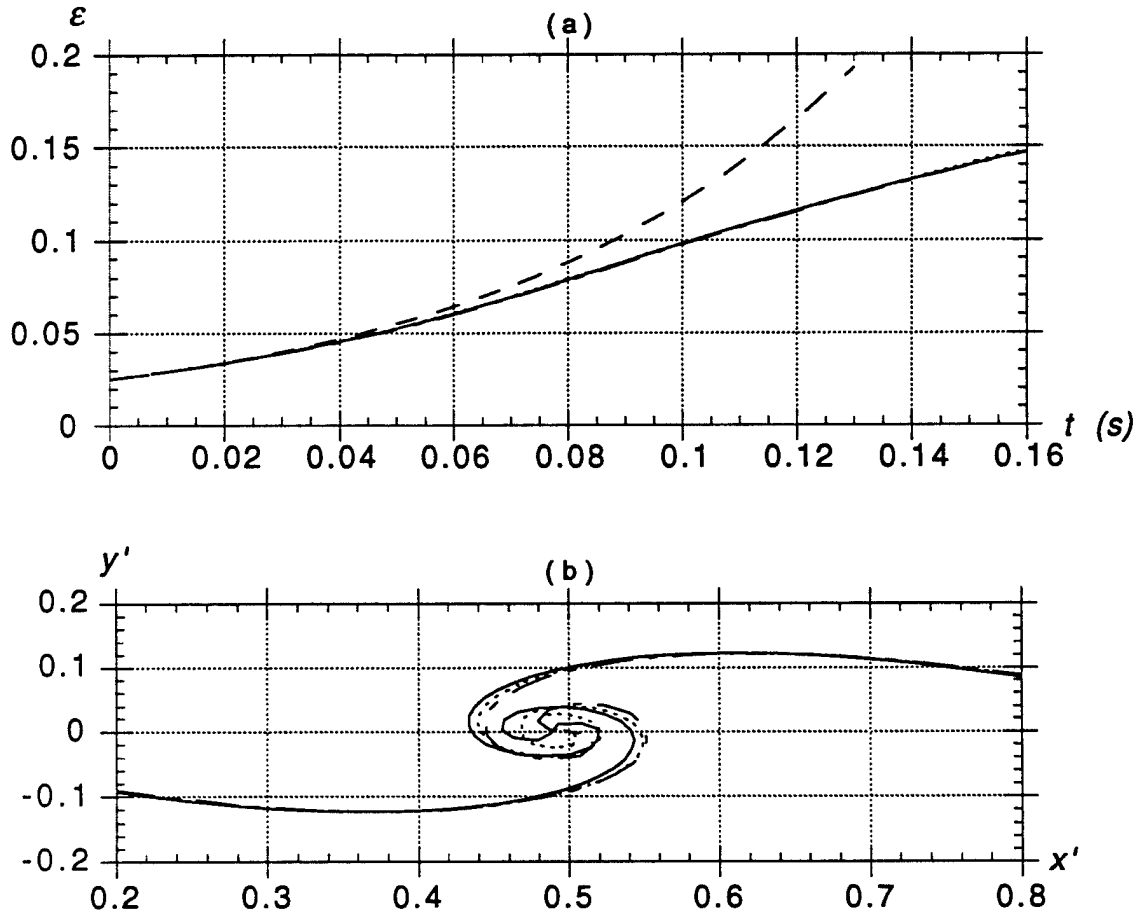


Figure 2.7: *Convergence with refinement of spatial discretization.* Computations of KH instability in a set-up similar to Fig. 2.3 with $\Delta U = 0.50$ m/s, $\varphi = 1$ (same fluid), $\lambda = 0.1$ m, and no gravity and surface tension. The time step is $\Delta\tau = 0.0001$ and the initial perturbation is a sinusoidal wave with amplitude $\varepsilon = 0.025$ and vorticity distribution according to Eq. (2.28). Initial numbers of PCVS elements $N =$ (— - —) 45, (—) 60, (- - - -) 75. (a) Maximum amplitude of interfacial disturbance compared to (— —) the linear growth rate (Lamb [26]). (b) Interfacial shape at $t = 0.128$ s.

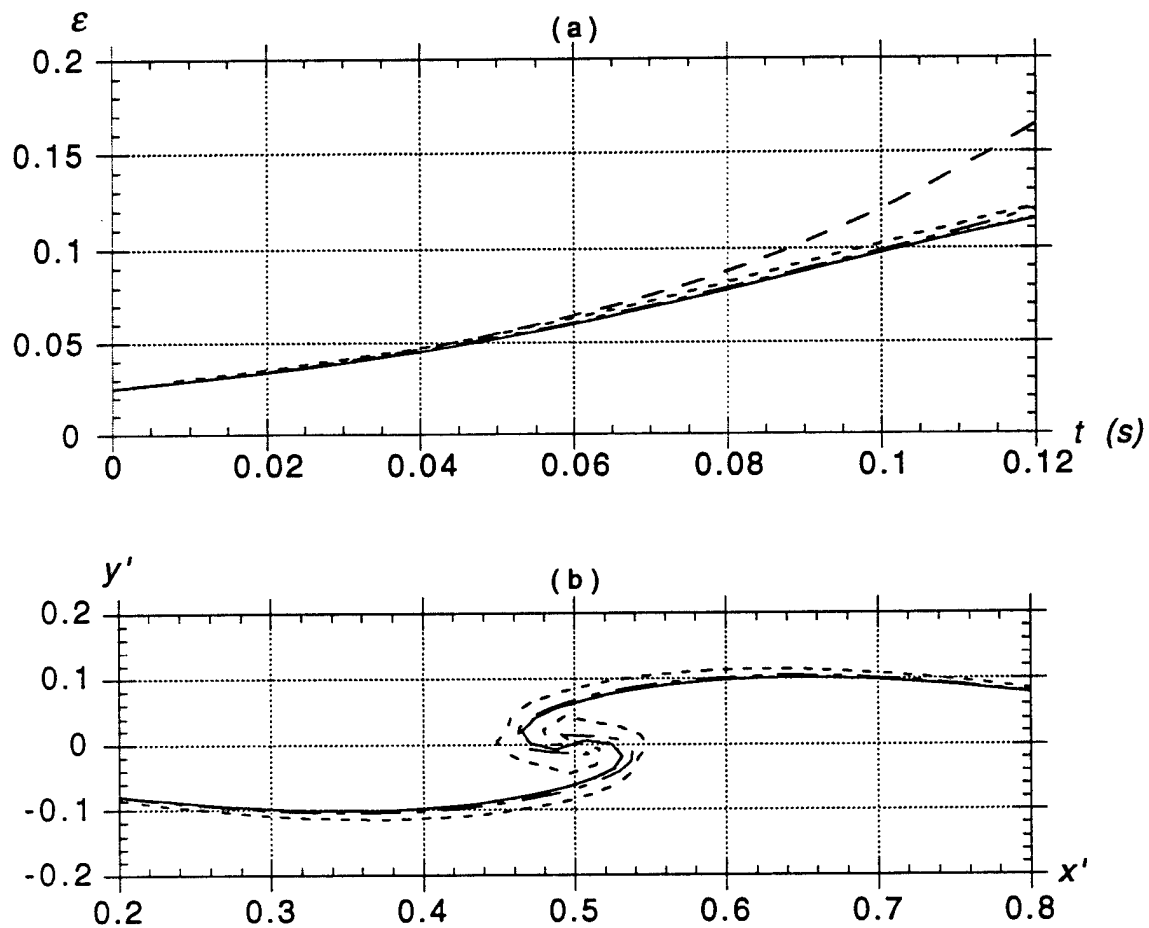


Figure 2.8: *Stability with increasing time step.* Same physical case as in Fig. 2.7 with $N = 45$ and time steps $\Delta\tau =$ (—) 0.0001, (----) 0.001, (— · —) 0.01, (---) 0.04. (a) Maximum amplitude of interfacial disturbance compared to (—) the linear growth rate (Lamb [26]). (b) Interfacial shape at $t = 0.108$ s.

step size. Although no absolute measure of accuracy is available for an arbitrary non-conservative case, the convergence of the solution with the discretization must be achieved if the model is to be recognized as stable and accurate. Hence, in this first application, the numerical convergence of the PCVS model numerical algorithms is tested by varying both the time step size and the number of discretized PCVS elements, within certain ranges. Since almost identical numerical methods are used for both the periodic and non-periodic PCVS models, convergence and stability are studied using the simpler periodic PCVS model and studying a case of KH instability on a periodic interface, as illustrated in Fig. 2.3.

For simplicity, the case solved with the periodic PCVS model is a pure shear instability case, with two identical fluids of unit density ($\varphi = \rho_0/\rho_1 = 1$) and hence no gravity, surface tension, and density difference effects. For such a case, circulation is conservative ($DT_i/Dt = 0$ in Eq. (2.7)) and, since there are no stabilizing effects, the linear analysis shows unconditional instability for $|\Delta U| > 0$, with a growth rate, $\propto \exp(\pi \Delta U t / \lambda)$ (Lamb [26]).

The physical parameters selected for this case are $\Delta U = 0.5$ m/s and $\lambda = 0.1$ m. The initial disturbance on the free surface is sinusoidal with nondimensional amplitude $\epsilon = 0.025$ and the initial circulation distribution is specified according to Eq. (2.28). A very small non-dimensional time step $\Delta\tau = 0.0001$ was first used and the initial number of PCVS elements on the interface was set to $N = 45, 60$, and 75 , in three successive computations. Regridding was used throughout the computations, to maintain a more or less constant node density along the interface as time progresses (maximum accepted PCVS element length variation over one time step was 1.5 %). Thus, in the three present cases, the number of PCVS elements at $t = 0.128$ s (Fig. 2.7b) reached 77, 106, and 128, respectively. The predicted evolutions of maximum nondimensional interfacial amplitudes are compared in Fig. 2.7a, and one can see differences between computations with different node resolution are very small. Also, note the initial agreement for $t < 0.04$ s and the subsequent differences shown in the figure between the amplitude growth rates obtained with the present nonlinear model and the rate predicted by linear theory. Clearly, for sufficiently large time, nonlinearity increases due to larger amplitudes on the interface and the instability grows slower in the nonlinear model than predicted by linear theory. This confirms earlier findings [43, 33] that nonlinearity provides stabilizing effects for the KH instability. In Fig. 2.7b, free surface shapes are compared for $t = 0.128$ s, at a time where strong roll-up of the interface has occurred. Again, differences between the three cases are not significant, except in the small roll-up region where jet resolution is more dependent on the number of PCVS elements.

Computations were then performed for the same physical case, initially discretized with $N = 45$, using four constant time step sizes varying between $\Delta\tau = 0.0001$ and 0.04 . [Due to regridding, at $t = 0.108$ s, the number of nodes increased to 61 and 75, for the first two and last two time steps, respectively.] Results for the maximum amplitude evolution and for the free surface shape at $t = 0.108$ s are given as a function of the time step size, in Figs. 2.8a and b. Amplitude growth rates and free surface shape slightly change as the time step increases but differences are not very significant until $\Delta\tau > 0.01$. For $\Delta\tau = 0.04$, computations rapidly become divergent for $t > 0.12$ s.

These two applications of the periodic PCVS model, hence, first show the good convergence of results with refined discretization (a feat rarely achieved in earlier published models, likely due to inadequate CPV integrations) and the stability of model results over a wide range of nondimensional time step size covering two orders of magnitude, from 0.0001 to 0.01.

2.5.2 Application of the periodic PCVS model to KH instability

After assessing the convergence and stability of the PCVS model numerical algorithms, the periodic model is now used to study the KH instability itself as a function of the physical factors known from the literature to influence the growth rate of instability, namely the interfacial velocity jump ΔU , the presence of gravity g (i.e., whether the two-dimensional instability occurs in a horizontal plane (no gravity), or in a vertical plane), the fluid density difference or ratio $\varphi = \rho_o/\rho_1$, the interfacial tension σ_{o1} .

Based on the literature review and the physical analysis of the linear KH problem presented earlier, for velocity jump values beyond the critical value, we expect an increase in ΔU to intensify the growth rate of instability and gravity to provide a stabilizing effect, we expect a decrease in φ to reduce the instability, and an increase in σ_{o1} to also reduce the instability. Numerical tests are carried out in the following, with the periodic PCVS model, to both confirm and quantify these expected behaviors.

Influence of velocity jump on growth rate of instability

In a linear sense [26], according to Eq. (2.30), when the velocity jump at the interface is greater than the critical value, $\Delta U > \Delta U_c$, the interface amplitude ε will grow exponentially with time, as $\varepsilon(t) \propto \exp \omega t$ and, all other factors being equal (i.e., k , φ , and σ_{o1}), the growth rate ω will increase with ΔU (see Eqs. (2.29) and (2.32)). For sufficiently large interfacial amplitude, however, due to increased nonlinearity, one should expect the linear solution to fail to predict the actual growth rate. In fact, nonlinearity should provide additional stabilizing effects reducing the growth rate.

The following numerical experiments were carried out with the periodic PCVS model to assess the effects of the velocity jump on the growth rate of KH instability. In all cases, the maximum interfacial wave amplitude ε was calculated as a function of time and compared to Lamb's [26] linear solution for the same parameter values.

Physical parameter values selected for this case were : a density ratio corresponding to a case with water and an average oil, $\varphi = 0.9$ (with $\rho_1 = 1000 \text{ kg/m}^3$), a standard surface tension coefficient for a water-oil interface, $\sigma_{o1} = 0.0237 \text{ N/m}$, and gravity $g = 9.8 \text{ m/s}^2$. In the numerical model, $N = 45$ PCVS elements were specified on the initial free surface and more were added through adaptive regridding, up to $t = 0.168 \text{ s}$. The time step interval was set to $\Delta \tau = 0.0001$. The initial sinusoidal disturbance on the free surface had an initial amplitude $\varepsilon = 0.025$ and the initial circulation distribution was specified according to Eq. (2.28).

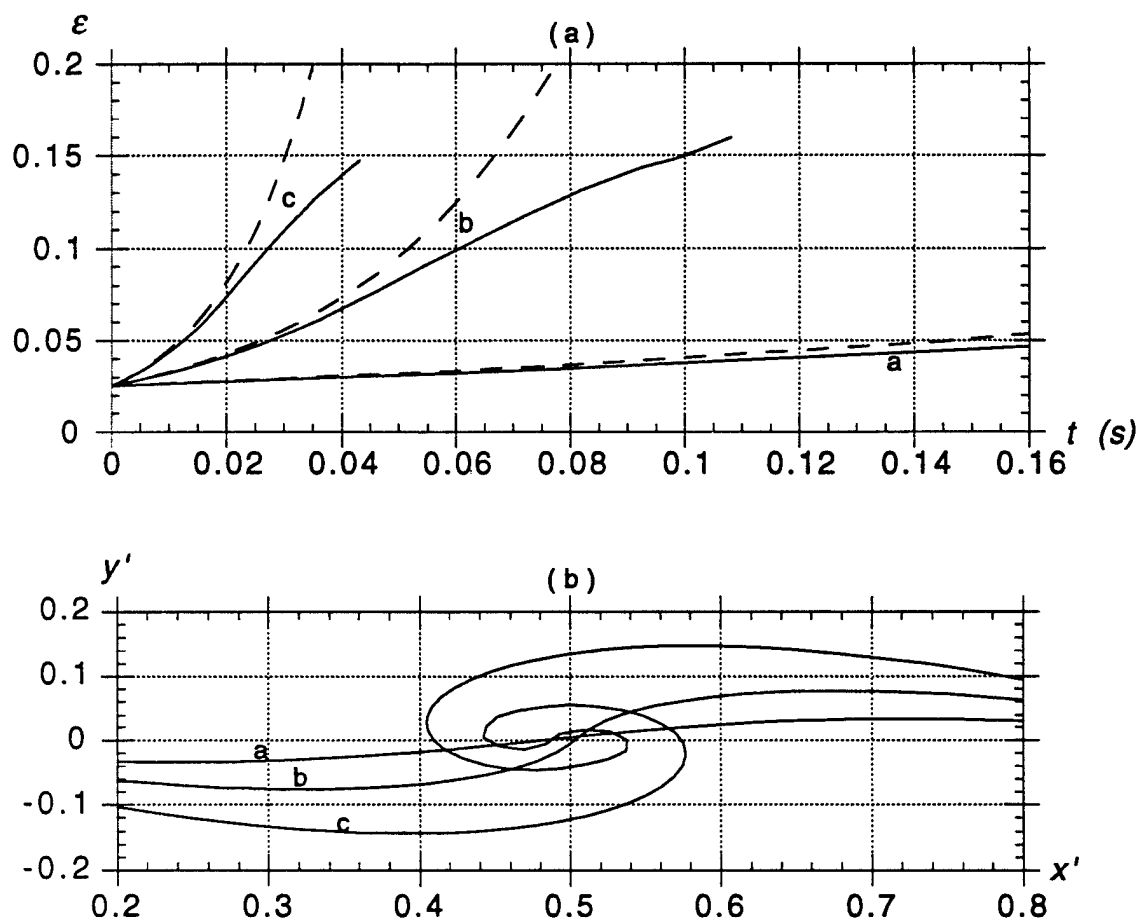


Figure 2.9: *Influence of velocity jump.* Computations of KH instability in a set-up similar to Fig. 2.3 with $\Delta U = a : 0.15$; $b : 0.30$; and $c : 0.60$ m/s, $\lambda = 0.0309$ m, $\varphi = 0.9$, $\sigma_{o1} = 0.0237$ N/m, $N = 45$, time step $\Delta\tau = 0.0001$, and $g = 9.8$ m/s². The initial perturbation is a sinusoidal wave with amplitude $\varepsilon = 0.025$ and vorticity distribution according to Eq. (2.28). (a) Maximum amplitude of interfacial disturbance compared to (— —) the linear growth rate (Lamb [26]). (b) Interfacial shape at $t = 0.045$ s.

According to Eq. (2.34), the interfacial wavelength leading to maximum growth rate of instability for this case is, $\lambda^{\min} = 0.0309$ m (i.e., $k = 203.34$ m⁻¹); hence this minimum wavelength is in the ripple wave range. This wavelength will be used in the present computations and, hence, $\lambda = \lambda^{\min}$. According to Eq. (2.33), the corresponding linear critical velocity jump for the parameters selected in this case is, $\Delta U_{cr} = \Delta U_{cr}^{\min} = 0.143$ m/s. Hence, in the following experiments, the velocity jump ΔU will be set to successive values larger than ΔU_{cr}^{\min} , equal to 0.15, 0.30, and 0.60 m/s. [Due to regridding, at time $t = 0.045$ s, the number of nodes has increased to 46, 54, and 108, for each case, respectively.]

Results are given in Fig. 2.9. Fig. 2.9a confirms the expected result that the growth rate of instability increases with ΔU (i.e., the slope of curves a, b, and c increases with ΔU), in both the linear and nonlinear cases (PCVS model). In all cases, the linear and nonlinear growth rates are nearly identical for small time, confirming the good behavior of model equations. In the first case (a), the velocity jump is only slightly larger than the critical value and the initial instability is very slow to develop. Hence, the nonlinear growth rate is just slightly lower than the linear one up to $t = 0.16$ s. When computing this case for a longer time, however, one would see that nonlinearity eventually stabilizes the interface shape and that the amplitude stops growing for $t \geq 0.35$ s, and then starts decreasing, whereas the linear instability keeps developing. Therefore, in the nonlinear regime, case a is physically stable, although the amplitude will be seen to oscillate (i.e., beat) between a maximum and minimum value as time increases. In the other two cases (b and c), the velocity jump is more than twice and four times the linear critical value, which makes the interfacial amplitude grow much faster than in case a (where $\Delta U = 1.05\Delta U_{cr}$) and quickly leads to larger nonlinear effects. As a result, nonlinear PCVS results rapidly deviate from the linear prediction and, as expected, show significantly smaller growth rates than linear results; hence, case b and c, although unstable, correspond to physically more stable cases than predicted by linear theory. In Fig. 2.9b, one further sees that interfacial shapes at $t = 0.045$ s (a time for which intense VS roll-up has already occurred for case c) are very different for the three cases : almost no change in shape has occurred for case a whereas, for cases b and c, the interface has grown steeper and has even rolled up for case c.

Influence of gravity on growth rate of instability

Rangel and Sirignano [33] studied the KH instability problem without including gravity effects. They also used a numerical point vortex method that was likely less accurate than the present method (both due to lack of CPV integrals in BS equations and a cruder geometric representation of the interface). The following numerical experiments were carried out for a case similar to one of the cases solved in [33], to assess the effects of gravity on the growth rate of KH instability represented by the maximum interfacial wave amplitude ε as a function of time. Physical parameter values for this case were : a velocity jump $\Delta U = 0.5$ m/s, $\lambda = 0.1$ m, a density ratio $\varphi = 0.9$ (as for a case with water and an average oil of density 0.9), a surface tension coefficient $\sigma_{o1} = 0.0237$ N/m (water-oil standard value). Numerical

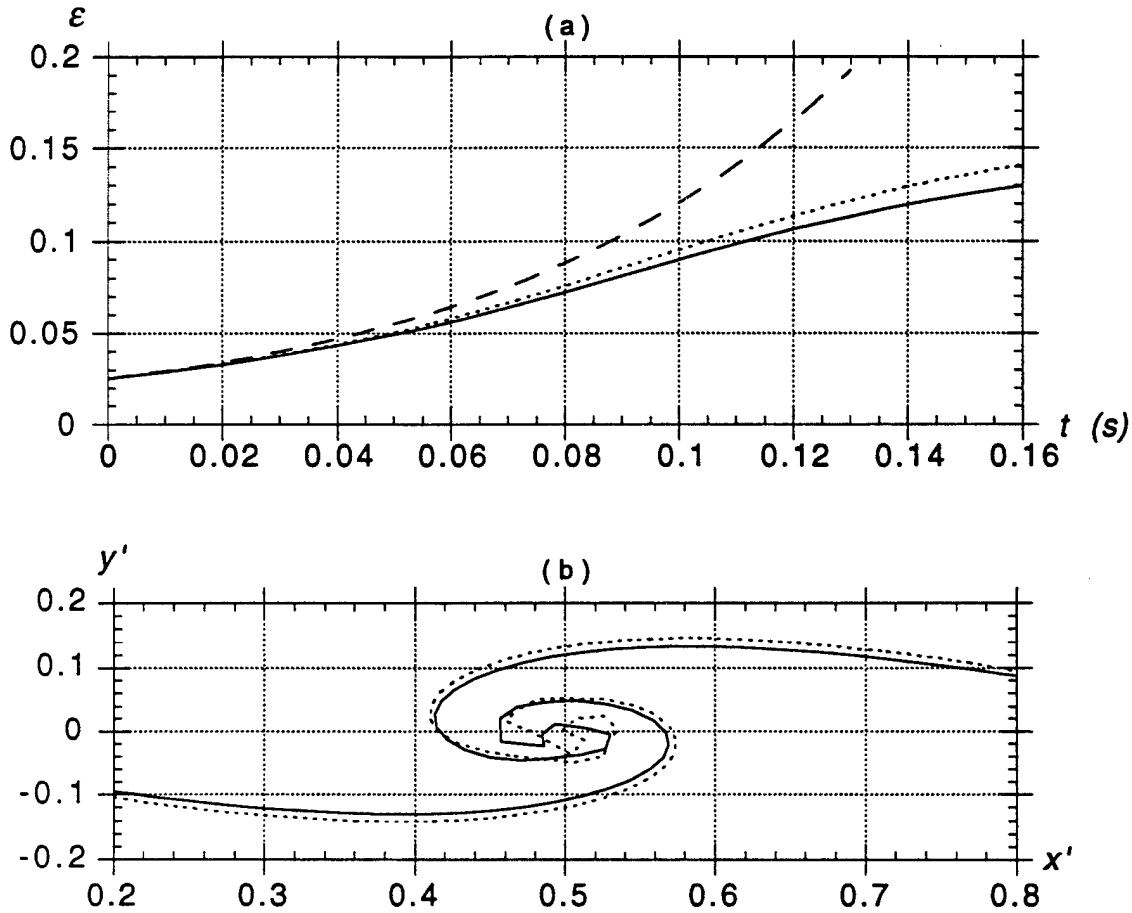


Figure 2.10: *Influence of gravity.* Computations of KH instability in a set-up similar to Fig. 2.3 with $\Delta U = 0.50 \text{ m/s}$, $\lambda = 0.1 \text{ m}$, $\varphi = 0.9$, $\sigma_{o1} = 0.0237 \text{ N/m}$, $N = 45$, time step $\Delta\tau = 0.0001$, and $g = (\text{—}) 9.8 \text{ m/s}^2$, $(\text{---}) 0 \text{ m/s}^2$. The initial perturbation is a sinusoidal wave with amplitude $\varepsilon = 0.025$ and vorticity distribution according to Eq. (2.28). (a) Maximum amplitude of interfacial disturbance compared to (—) the linear growth rate (Lamb [26]). (b) Interfacial shape at $t = 0.168 \text{ s}$.

parameters are the same as for the cases in the previous section. [Due to regridding, at time $t = 0.168$ s, the number of nodes has increased to 87 and 88, with and without gravity, respectively.]

For the above data, the linear critical velocity is $\Delta U_{cr} = 0.19$ m/s. Hence the present case is strongly unstable.

When including gravity effects in the model, the interface evolution is affected by additional inertial forces. Hence, the momentum of particles on the interface must slightly change to balance the vertical accelerations resulting from gravity effects. Thus, less momentum is available for further deforming the interface, which should lead the growth rate of instability to be smaller with gravity than without gravity. Numerical results reported in Fig. 2.10a confirm this analysis. Moreover, whether gravity is included or not, one can also see that, as compared to the linear growth rate, as expected, nonlinear PCVS results are more stable. In Fig. 2.10b, one further sees that interfacial shapes at $t = 0.168$ s (a time for which intense VS roll-up has occurred) are different, with and without gravity. In addition to reducing the maximum amplitude, gravity also slows down the roll-up process.

Influence of fluid density difference on growth rate of instability

The influence of the fluid density ratio $\varphi = \rho_o/\rho_1$ is tested next. In practice, for initially statically stable cases (i.e., those for which the lighter fluid lies above the heavier fluid), φ can vary within the whole range $[0,1]$. For instance, the first case corresponds to ocean surface waves for which the upper fluid is air and thus $\varphi \simeq 0$, and the second case corresponds to a stratified system with two nearly identical fluids moving at different velocities, as in the case of a stratified ocean.

The physical cases solved here with the numerical PCVS model have parameter values similar to the oil-water cases solved in the previous sections, with gravity $g = 9.8$ m/s² and density ratios first corresponding to a water-water case (1.00), and then to cases with increasingly lighter oils of successive density 0.95, 0.90, and 0.85. The numerical parameter values are identical to those used before. [Due to regridding, at time $t = 0.168$ s, the number of nodes has increased to 97, 86, 87 and 79, for each of the four cases, respectively.] For the parameter values of the last three cases, the linear critical velocity jumps are, $\Delta U_{cr} = 0.14$, 0.19, and 0.23 m/s, respectively. Hence, all three cases are expected to be strongly unstable for $\Delta U = 0.5$ m/s, the selected velocity jump in these experiments.

The effects of the density ratio on the KH instability are also related to inertial effects of momentum transfer from one fluid to the other, through the interface. From the linear theory predictions, it is expected that, as the density ratio φ decreases (i.e. as the density difference between both fluids increases), the interfacial instability growth rate should be reduced. For the nonlinear problems solved with the PCVS model, growth rates are also expected to be lower than for the corresponding linear cases. Knowing the exact magnitudes of growth rates as oil density changes is of interest in the larger context of studying the failure of oil containment by a boom as KH instability growth is closely related to the growth of the headwave region in front of the slick.

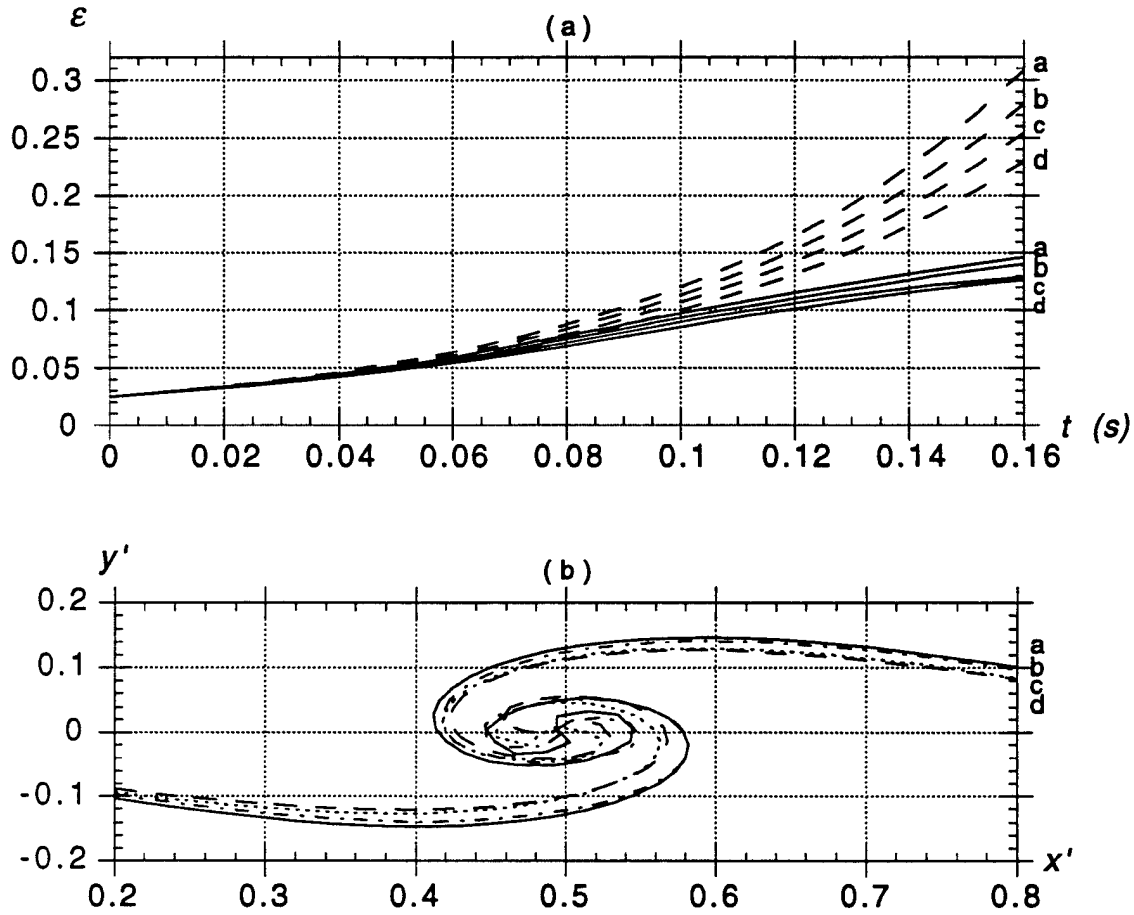


Figure 2.11: *Influence of density difference.* Computations of KH instability in a set-up similar to Fig. 2.3 with $\Delta U = 0.50$ m/s, $\lambda = 0.1$ m, $\sigma_{o1} = 0.0237$ N/m, $N = 45$, time step $\Delta \tau = 0.0001$, $g = 9.8$ m/s², and $\varphi =$ a (—) 1.0; b (---) 0.95; c (----) 0.90; d (- - - -) 0.85. The initial perturbation is a sinusoidal wave with amplitude $\varepsilon = 0.025$ and vorticity distribution according to Eq. (2.28). (a) Maximum amplitude of interfacial disturbance compared to (—) the linear growth rate (Lamb [26]). (b) Interfacial shape at $t = 0.168$ s.

Fig. 2.11 shows the numerical results. As expected, all model results in Fig. 2.11a show growth rates lower than predicted by linear theory. Further, as expected, the growth rate decreases for decreasing density ratios. In Fig. 2.11b, which compares free surface profiles at $t = 0.168$ s, one also sees that, in addition to the amplitude difference, the VS roll-up gradually slows as φ decreases.

Influence of interfacial tension on growth rate of instability

For an interface between two fluids, two boundary conditions have to be simultaneously satisfied. The first is that material fluid particles on both sides of the interface must stay in contact, and the second is that pressure on both sides of the interface must be identical. The former condition is kinematic and is automatically satisfied by the PCVS model governing equations. The second equation is dynamic and is also implicitly included in governing equations such as the vorticity updating Eq. (2.7). If surface tension effects are included in the computations, however, the pressure equilibrium equation is changed, as compared to a case with no surface tension. These effects indeed result in an additional term representing an equivalent pressure jump across the interface, expressed by, $\Delta p(s) = -\sigma_{o1}/R(s)$, where R denotes the radius of curvature along the interface, described by parameter s .

From this relation, it is seen that when the interface shape is concave upward (i.e. with a positive curvature), the pressure jump across the interface is negative, while for a concave downward interface, the pressure jump is positive. Hence, theoretically, surface tension is expected to flatten out fluctuations on the interface and thus to reduce the growth rate of KH instability. In the computational model, as soon as the interface starts rolling-up, the local interface curvature rapidly increases, which results in dramatic variations of local circulation, through surface tension effects in the vorticity updating Eq. (2.7). These variations, in turn, tend to limit the growth of interfacial waves. The computational tests in this section confirm these theoretical predictions.

As in the previous sections, the selected physical cases have parameter values corresponding to a realistic case with water and, in this case, a heavy oil of density 0.95, with the exception of successive values of the interfacial tension set to, $\sigma_{o1} = 0.0237$ N/m (standard oil-water value), 0.237 N/m (10 times this value), and 1.185 N/m (50 times this value). The numerical parameter values are identical to those used before. [Due to regridding, at time $t = 0.168$ s, the number of nodes has increased to 92, 78 and 64, for each of the three cases, respectively.] The numerical parameter values are identical to those used before. The numerical parameter values are identical to those used before. For the parameter values of the three cases tested, the linear critical velocity jumps are, $\Delta U_{cr} = 0.14, 0.21$, and 0.41 m/s, respectively. Hence, all three cases are expected to be unstable for the specified velocity jump, $\Delta U = 0.5$ m/s, although the third case with the largest interfacial tension, for which $\Delta U = 1.22\Delta U_{cr}$ should only have a fairly slow growth rate, particularly in the nonlinear regime.

Results in Fig. 2.12a confirm the expected dramatic effects of a large increase in interfacial tension on the growth rate of the instability. When surface tension is increased

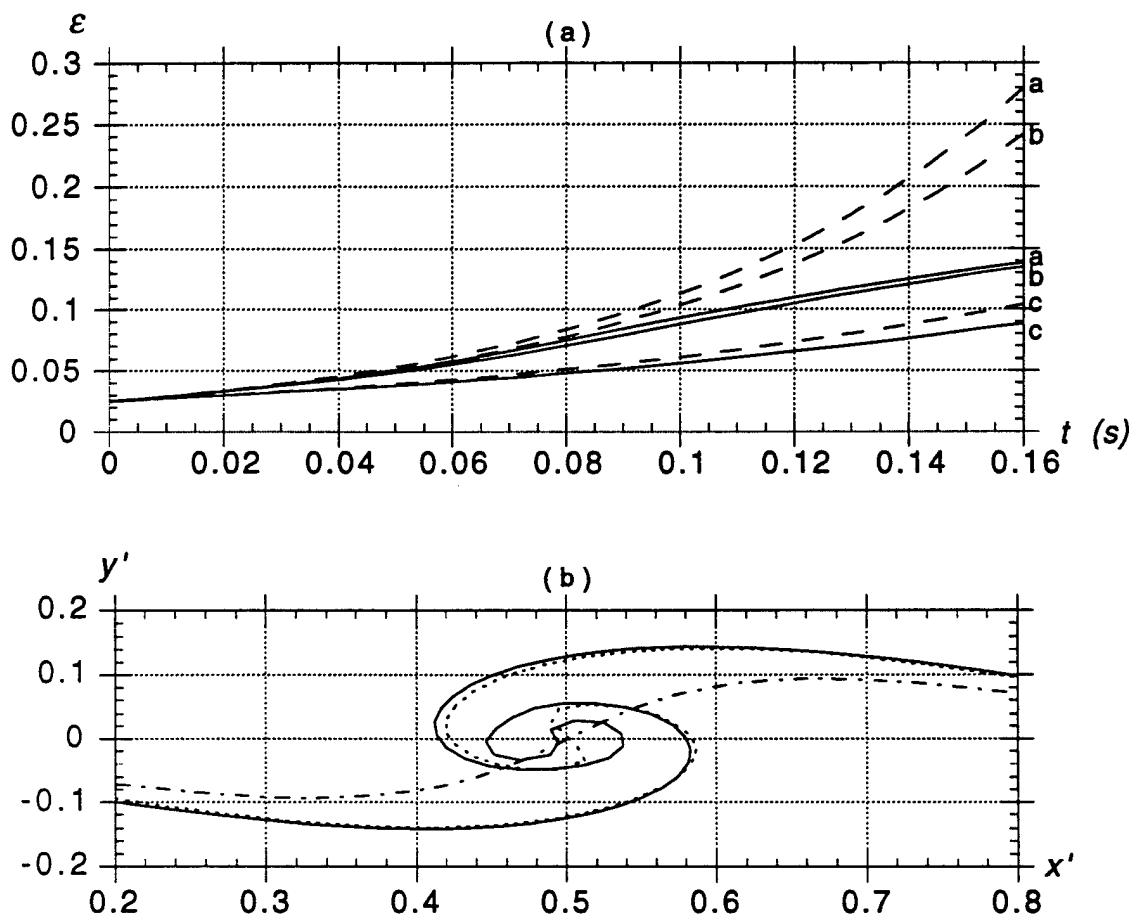


Figure 2.12: *Influence of interfacial tension.* Computations of KH instability in a set-up similar to Fig. 2.3 with $\Delta U = 0.50$ m/s, $\lambda = 0.1$ m, $\varphi = 0.95$, $N = 45$, time step $\Delta\tau = 0.0001$, $g = 9.8$ m/s², and $\sigma_{o1} =$ a (—) 0.0237 N/m; b (----) 0.237 N/m; c (— · —) 1.185 N/m. The initial perturbation is a sinusoidal wave with amplitude $\varepsilon = 0.025$ and vorticity distribution according to Eq. (2.28). (a) Maximum amplitude of interfacial disturbance compared to (— · —) the linear growth rate (Lamb [26]). (b) Interfacial shape at $t = 0.168$ s.

by a factor 50 (case c), the growth rate is almost reduced by half. Fig. 2.12b also shows the significant influence of surface tension on interfacial shape as calculated at time $t = 0.168$ s. An increase in surface tension, in addition to reducing the amplitude, strongly delays the development of KH instabilities.

It should be pointed out that, due to an insufficiently accurate geometric representation of the interface, such computations could not be performed with the Phase I model. In the present Phase II model, curvature and its derivatives are much more accurately calculated and the numerical instabilities experienced with Phase I model are thus eliminated.

Conclusions of KH instability studies

The preceding computations of interface evolution during KH instability clearly demonstrated and quantified how the interface amplitude growth depends on fluid properties and flow conditions. Throughout these computations, the improved Phase II periodic PCVS model performed very well and was thus validated as a tool for predicting interfacial behavior during KH instability. More specifically, using the PCVS model, it was found,

- (i) in the presence of gravity, the interface is subjected to stabilizing effects from buoyancy forces and the disturbance growth is slowed as compared to an identical case when gravity effects are not included;
- (ii) an increase in fluid density difference across the interface will result in reducing and slowing down the disturbance growth on the interface; the most unstable case is thus a case with two identical fluids ($\varphi = 1$) or, in the present case, the heavier oil;
- (iii) and an increase in surface tension at the interface also results in reducing and slowing down the disturbance growth on the interface; this is because surface tension, to some extent, balances the circulation accumulation in the highly curved regions of the interface.

Based on the result in (ii), one can thus postulate that, for an oil slick contained by a boom, the headwave instability growth rate will be smaller and the instability will be delayed when using a lighter oil, compared to the case of a heavier (or weathered) oil. In laboratory experiments with oil/boom systems, it is observed that the oil-water interface, at first, rolls-up in the headwave region before pieces of the interface are torn off (e.g., Delvigne [9]). Therefore, based on the results in (iii), it is theoretically expected that, if surface tension is naturally (e.g., through weathering) or artificially (e.g., through chemicals) increased, the disturbance growth on the interface will be reduced and the interface break up and resulting containment failure will be accordingly delayed (or eliminated), hence, providing additional time for collecting oil at a given (unstable) relative velocity.

In the light of the above results, in subsequent studies, particularly during Phase III, the quantitative influence of density difference and surface tension on the oil-water interface evolution, will be studied for complete oil-boom systems.

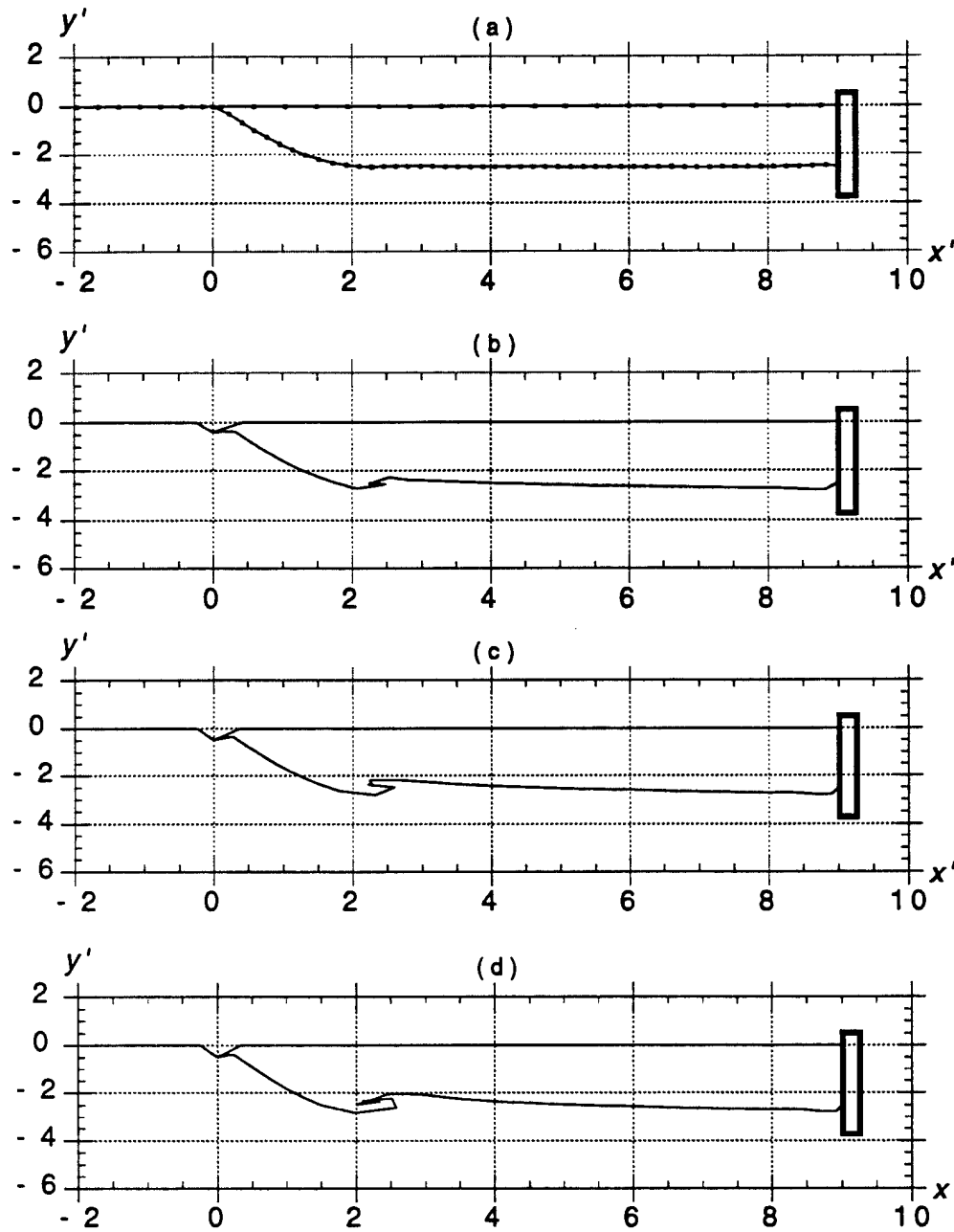


Figure 2.13: Computational results for oil/boom containment failure due to *headwave instability*, in a set-up similar to Fig. 2.4, with $U_w = 0.14$ m/s, $\varphi = 0.8$, $\lambda = 0.002$ m, and $\sigma_{ow} = 0.0237$ N/m (water-oil). Initial slick shape is computed using Eq. (2.43) and (2.44) : $H' = 2.5$, $L' = 9.08$. Three semi-infinite sheets and five PCVS's were used in the numerical model, with $N_1 = 10$, $N_2 = 50$, $N_3 = 20$, $N_4 = 21$, and $N_5 = 18$ vortex elements on each sheet, respectively. Shape of the slick at $\tau =$: (a) 0.18 ; (b) 0.67; (c) 0.75; and (d) 0.77; corresponding to 1, 61, 91, and 136 varying computational time steps, respectively. Boom draft is $d' = 1.5H'$.

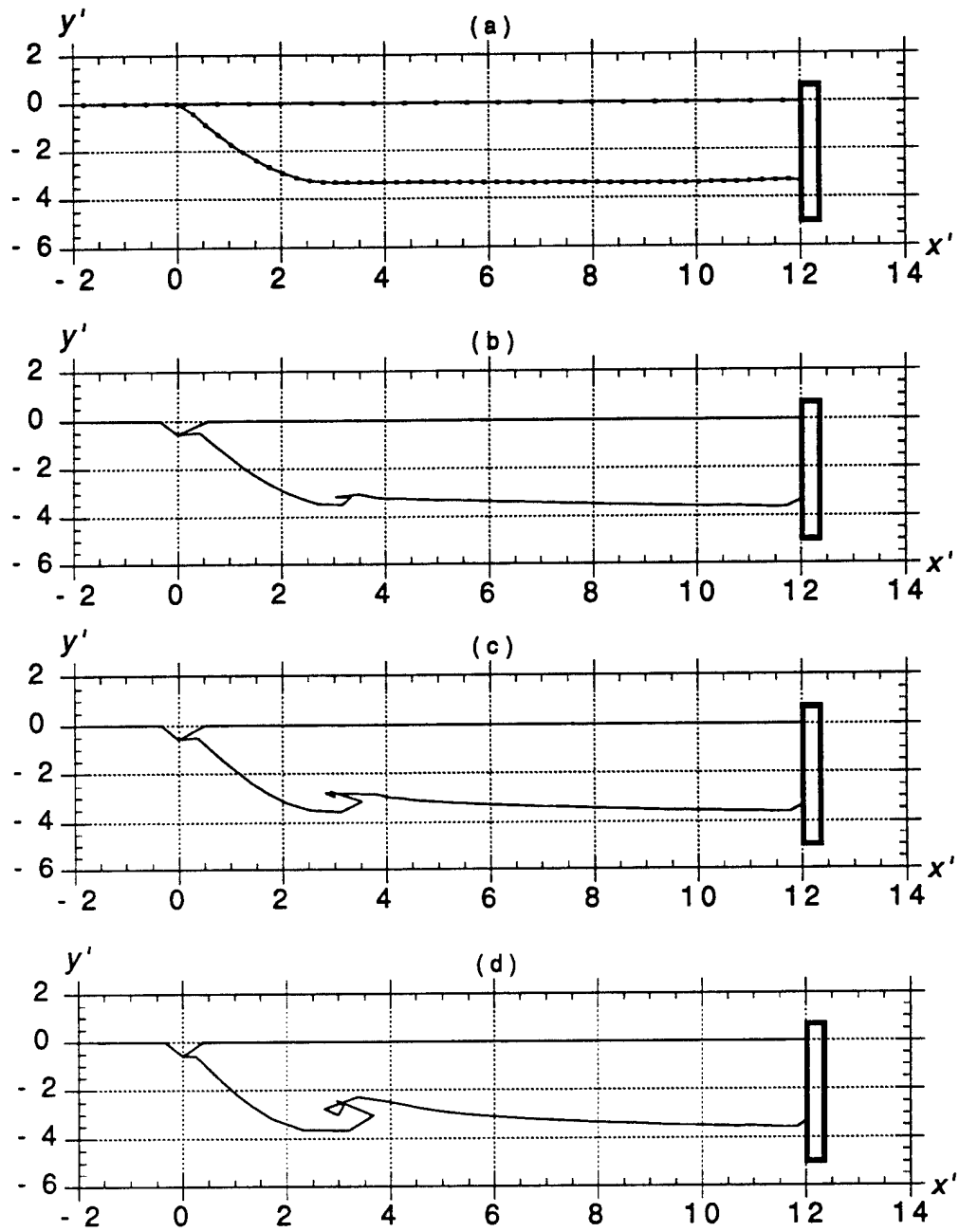


Figure 2.14: Same computations as in Fig. 2.13, with $\varphi = 0.85$, $H' = 3.33$, $L' = 12.1$. Shape of the slick at $\tau =$: (a) 0.24 ; (b) 0.87; (c) 0.92; and (d) 0.98; corresponding to 1, 46, 76, and 136 varying computational time steps, respectively.

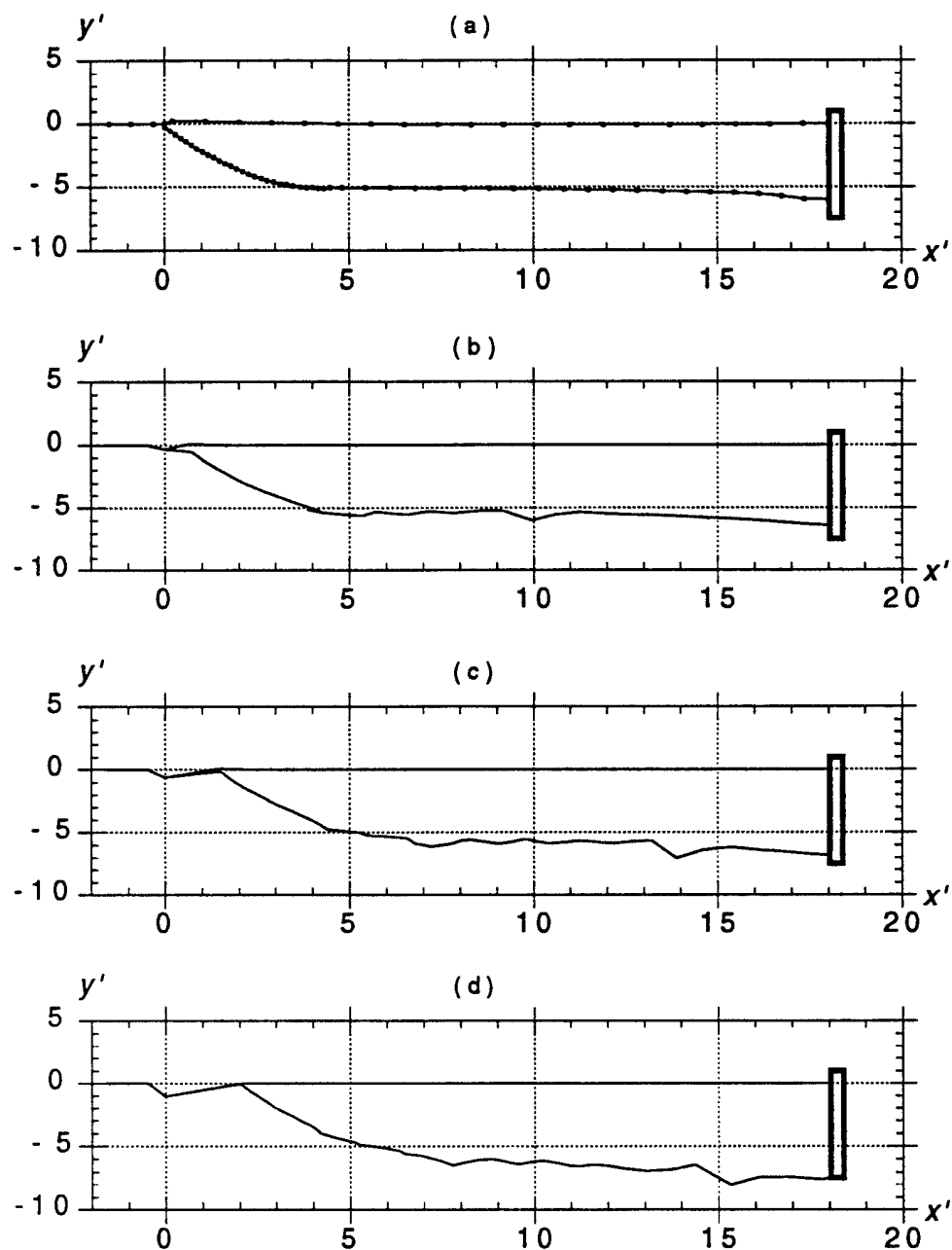


Figure 2.15: Unstable contained slick, with $\varphi = 0.90$, $U_w = 0.25$ m/s, $H' = 5.00$, and $L' = 18.2$. Shape of the slick at $\tau =$: (a) 0.36 ; (b) 2.12; (c) 3.35; and (d) 4.44; corresponding to 1, 226, 376, and 501 varying computational time steps, respectively. Numerical data are similar to cases in Figs. 2.13 and 2.14.

2.5.3 Application of the non-periodic PCVS model to oil containment by a boom

This case corresponds to the problem illustrated in Fig. 2.4. Two cases were first solved, for $\varphi = 0.8$ and 0.85 , and $U_w = 0.14$ m/s, which gave a length scale $\lambda = U_w^2/g = 0.002$ m. The surface tension coefficient was specified to the oil-water value, $\sigma_{ow} = 0.0237$ N/m. The initial shape of the slick was calculated using Eqs. (2.43) and (2.44), which gave : $H' = 2.5, 3.33$, the slick thickness; and $L' = 9.08, 12.1$, the slick length, for each case, respectively (dashes denote nondimensional variables). The boom draft was set to $d' = 1.5H'$. The circulation at the oil-water interface was initialized using Eq. (2.45).

In the model, three semi-infinite sheets and five PCVS's were used, with $N_1 = 10$, $N_2 = 50$, $N_3 = 20$, $N_4 = 21$, and $N_5 = 18$ vortex elements on each discretized sheet, respectively (see Figs. 2.13a and 2.14a for a sketch of the initial discretizations and slick shape after one time step, for each case). No node regridding was used in these calculations. The initial time step was selected based on a mesh Courant number $C_o = 0.5$. The time step was subsequently adjusted according to the relationship,

$$\Delta t = C_o \frac{\text{Min } |\Delta s_i|}{\text{Max } |\Delta u_i|} \quad (2.49)$$

where $\text{Min } |\Delta s_i|$ denotes the minimum length and $\text{Max } |\Delta u_i|$ denotes the maximum velocity, of PCVS's on the oil-water interface. After experimenting with the model, it was found that, in order to preserve the stability of numerical results when headwave instability occurred on the oil-water interface, the Courant number had to be gradually reduced to 0.06.

Figs. 2.13 and 2.14 show, for both cases, the calculated shapes of the slick at various times, the first one corresponding to one time step (Figs. 2.13a, 2.14a). The specified velocity, for both cases, is slightly smaller than the linear critical velocity of KH instability, $\Delta U_{cr}^{min} = 0.17$ and 0.16 m/s, respectively. In both cases, as time increases, an instability develops in the front of the slick, and propagates downstream as a headwave which overturns and rolls-up on itself, in a way similar to KH instability waves calculated in Section 2.5.2. The slight trough observed in experiments at the front of the slick is well reproduced in the computations (e.g., Milgram and Van Houten [29]). As expected from the KH instability studies, the second case (Fig. 2.14) which has a heavier oil shows a more intense, larger relative size, headwave instability than the first case which has a lighter oil (Fig. 2.13). Both of these cases would physically correspond to containment failure by *oil entrainment*. Indeed, as the headwave rolls up, pieces of oil can be detached and entrained in the flow under the boom. This mechanism and the rate of oil entrainment was studied by Zalosh [42], on a semi-empirical basis, for a semi-infinite slick.

A third case is calculated in Fig. 2.15, for $\varphi = 0.9$ and a relative velocity $U = 0.25$ m/s, much larger than the linear critical velocity for the KH problem, $\Delta U_{cr}^{min} = 0.14$ m/s. In this case with a higher-speed relative velocity, the instability at the oil-slick interface starts just behind the front part of the slick, as a series of small scale waves (Fig. 2.15b) which propagate downstream towards the boom. In these waves, the leading oscillation

is somewhat larger and grows even larger as it approaches the boom (Fig. 2.15c). As time increases and interfacial waves grow, the slick length decreases and the slick thickness increases. Eventually, at the end of the computations reported in the figure (Fig. 2.15d), the slick thickness at the boom is equal to the boom draft and oil is about to be entrained/drained under the boom. To calculate further than this stage with the model, the separation of vortex sheets from the boom leading edge should be implemented. This has not been done at the present stage. The results in Fig. 2.15, in which KH instabilities at the interface combined to the blockage effect at the boom lead to the unstable shortening and thickening of the slick, are typical of the oil containment failure mode referred to as *critical accumulation*.

These results show the ability of the PCVS model to predict the unstable shape of a contained oil slick. Although they appear to be qualitatively correct, they still use the empirical method by Zalosh [42] to estimate the *initial shape* of the slick, and also do not include *interfacial friction* effects which have an important influence on slick geometry and thickness. After integrating in this model the initialization of the slick shape, presented in Chapter 4, and the inclusion of frictional effects in the vorticity updating equation, presented in Chapter 5, more quantitatively realistic similar computations will be performed during Phase III, using the more accurate CVS model, presented in Chapter 3 for the velocity calculations. Model parameters will then be calibrated based on newly obtained experimental data.

Chapter 3

Periodic Continuous Vortex Sheet (CVS) model and applications to KH instability

In this chapter, a new more accurate model is proposed to compute the time evolution of the interface between two inviscid fluids moving with uniform velocity, subjected to instabilities of the Kelvin-Helmholtz (KH) type. In this model, the interface is represented by a Continuous Vortex Sheet (CVS), which both preserves the full nonlinearity of interfacial boundary conditions and provides a higher-order representation of the geometry and field variables than in the previously proposed models, like the PCVS models developed in Phase I and refined in Phase II, as presented in Chapter 2.

As in the PCVS models, time updating of CVS's geometry and circulation is calculated as a function of gravity, interfacial surface tension, and fluid density difference. To deal with the *hyper-singularities* occurring in Biot-Savart integrals Eqs. (2.1), describing CVS's velocity, when the observation point belongs to the vortex sheet, a new *intrinsic variable expansion* technique is proposed, which leads to an exact representation of CPV contributions to the BS equations.

The CVS model is applied to predicting the nonlinear growth of periodic KH instabilities in a two-fluid stratified system. Results demonstrate that the periodic CVS model provides both higher numerical accuracy and stability and gives a more accurate physical picture of the disturbance evolution than obtained when using the less accurate PCVS periodic model.

Based on these promising results, in future work to be conducted in Phase III, the CVS modeling approach will be applied to the oil/boom containment problem described in Section 2.4. As discussed in Chapter 1, however, to obtain a correct model of oil/boom containment, it will be necessary to first initialize the problem using the correct steady state slick shape, including friction effects (see Chapter 4), and using a vorticity updating equation that also includes interfacial friction effects in the CVS model (i.e., an additional term representing these effects will be added to Eq. (2.7) or (2.13); see Chapter 5).

In the following, Section 3.1 first gives an introduction to the numerical modeling of the KH problem, justifying the need for a more accurate and stable approach. Section 3.2 gives governing equations and Section 3.3 summarizes numerical procedures for the

periodic CVS model. Finally, Section 3.4 gives numerical results for model validation and applications to the KH problem.

3.1 Introduction

Over the past few decades, many attempts were made to model the velocity of continuous VS's using Biot-Savart (BS) integral equations (2.1). In such studies, one conventional approximation has often been to discretize continuous VS's by a finite number of point vortices (e.g., Rosenhead [35]). Moore [31] thus developed a point-vortex method and successfully calculated roll-up of VS's. For stratified flows, Zalosh [43] similarly studied interfacial instabilities with a method that included effects of buoyancy and surface tension. Using a similar method, Rangel and Serignano [33] predicted the evolution of initially small periodic disturbances at the interface between two fluids of different density and velocity, including surface tension, but not gravity, effects.

Despite some success, such calculations usually resulted, after a large number of time steps, in non-physical chaotic motion of point vortices. Regridding methods, introduced for instance in [33], could reduce but not totally eliminate such instabilities. Problems experienced by point-vortex approximations of VS's can be categorized as follows :

- (i) the numerical evaluation of singular CPV terms in BS integrals (2.1) is not properly handled by standard (regular) numerical integration techniques;
- (ii) the VS evolution is improperly modeled at extremity points of the computational domain, defining either periodic boundaries or the intersection between the computational domain and infinite VS's or solid boundaries;
- (iii) the geometric representation of VS's and of higher-order interfacial tangential derivatives, based on discretized points, is not sufficiently accurate as time develops;
- (iv) results converge poorly or even diverge when the VS discretization is refined and/or when non-uniform point-vortex distributions are used.

All of the above problems are numerical, not physical, in nature and are related to specific aspects of discretization methods and calculation of BS integrals. Moore [31], in fact, showed that point vortex, and even PCVS approximations methods such as presented in Chapter 2, rapidly cause roundoff and truncation errors to amplify and lead to the reported chaotic motion which ruins practical calculations¹.

By a careful analysis of work published to date, Fink and Soh [14] showed that a point vortex representation implicitly neglects logarithmic terms representing local contributions (i.e., vortex self-induced velocity) to the BS integrals. Moore [32] further showed that a weak singularity does form, after a critical time, on the discretized VS. Accordingly,

¹Note that both of these approximations have identical physical assumptions except that, in the latter, singular terms in the integrals are calculated for local constant VS elements.

the point-vortex approximation only converges up to this critical time. In agreement with Moore, Meiron *et al.* [30], solving a pure shear flow problem, found a curvature singularity of the VS. Krasny [24], using discrete Fourier analysis, proved that numerical perturbations due to roundoff errors are responsible for the observed irregular motion of point vortices. Baker and Shelley [3] examined the behavior of layered VS's, with regard to local sheet circulation induced by density and thickness changes, and showed that, beyond the critical time, the behavior of VS layers becomes irregular.

Due to the problems experienced by classical point-vortex approaches, many researchers pointed out the need for using higher-order VS representations that would reduce numerical errors and allow to better identify the physical mechanisms governing VS evolution.

In Phase I and II of this project, we addressed the four problems (i)-(iv) mentioned above, within the realm of a PCVS approximation (Chapter 2) and were able to successfully solve KH instability problems, for a wide range of parameter values (Section 2.5.2). To do so : (i) we accounted for the CPV integral contributions in Eq. (2.1); (ii) we both improved and extended periodicity conditions; (iii) we introduced a new stable and accurate higher-order representation of the geometry and tangential derivatives on the interface (parity mapping method); and (iv) we controlled model resolution by using an adaptive node regridding method, in combination with the parity mapping method. Despite the success of computations with both the periodic and non-periodic PCVS models, however, the piecewise constant approximation of vorticity that was made over VS elements in the model was shown to clearly limit both the accuracy and the time extension of computations, particularly in the most interesting case of oil containment by a boom (Section 2.5.3). This motivated the development and implementation of a more accurate model in which both the geometry and the circulation of VS are approximated by higher-order continuous polynomials. This model is hereafter referred to as the Continuous Vortex Sheet (CVS) model and its preliminary development and validation are presented in this chapter, by calculating periodic KH instabilities of a vertically stratified two-fluid system (as done in Section 2.5.2 for the periodic PCVS model).

3.2 Governing equation for the periodic CVS model

General equations governing the dynamic and rate of change of vorticity of VS's, due to gravity, surface tension, and density difference effects, were presented in Section 2.2. These equations are still applicable and will be used in the CVS model. General equations relative to the periodic KH instability problem presented in Section 2.3.1 are also applicable to the periodic CVS model. The governing BS integral equation for the velocity field and the time updating in the CVS model is given by Eqs. (2.35) and (2.36). In the present case, however, Eq. (2.36) will be integrated assuming a *higher-order spatial discretization* of both the VS geometry and circulation, based on isoparametric boundary elements (BEM; Brebbia, [6]).

As in the PCVS model, the CVS geometry over one wavelength λ is divided into M locally continuous elements, defined using a set of N discretization points. To optimize

computations, each of these elements is mapped onto a single reference element, with intrinsic coordinate μ varying between -1 and 1. Summing up element contributions, the velocity induced at time τ , for points $i = 1, \dots, N$ of coordinates (ξ_i, η_i) , is obtained from Eq. (2.36) as (nondimensional variables (2.9)-(2.12) have been used),

$$\begin{aligned} u(\xi_i, \eta_i) &= \frac{1}{2} \sum_{k=1}^M \int_{-1}^{+1} \frac{\gamma(s'(\mu)) \sinh 2\pi(\eta_i - \eta'(\mu))}{\cosh 2\pi(\eta_i - \eta'(\mu)) - \cos 2\pi(\xi_i - \xi'(\mu))} \frac{ds^k}{d\mu}(\mu) d\mu \\ v(\xi_i, \eta_i) &= -\frac{1}{2} \sum_{k=1}^M \int_{-1}^{+1} \frac{\gamma(s'(\mu)) \sin 2\pi(\xi_i - \xi'(\mu))}{\cosh 2\pi(\eta_i - \eta'(\mu)) - \cos 2\pi(\xi_i - \xi'(\mu))} \frac{ds^k}{d\mu}(\mu) d\mu \end{aligned} \quad (3.1)$$

where γ , here, denotes the nondimensional circulation (with $dg = \gamma ds$), $ds^k/d\mu$ is the (nondimensional) Jacobian of the transformation from element k to the reference element, and the time variable τ has been omitted for simplicity. Integrals in (3.1) will be calculated by numerical integration (see next Section).

3.3 Numerical methods for the periodic CVS model

In the present applications of the periodic CVS model, a cubic representation of both the geometry and circulation is used. At a given time t , BS Eqs. (3.1) are numerically integrated to calculate velocities along CVS's, using standard Gauss quadrature for the regular integrals (i.e., when point i does not belong to element k), and an intrinsic variable expansion technique is used to deal with the strong CPV singularities occurring in these integrals, as a result of self-induced velocity terms (i.e., when point i belongs to element k).

An explicit time stepping method, based on 2nd-order Lagrangian Taylor series expansions similar to those presented in Chapter 2 for the PCVS model (Eq. (2.18)), is used to calculate CVS's time evolution using velocities, accelerations, and rate of change of circulations calculated in the CVS model (the latter two being calculated as for the PCVS model).

General numerical procedures used in the periodic CVS model are identical to those given in Section 2.2 for the geometric modeling using the parity mapping method, the specification of end-point periodicity conditions, and the adaptive regridding in the PCVS models. The treatment of singular integrations in the BS Eqs. (3.1) is detailed in the following.

Singular integrations

The kernel of BS integrals (3.1) becomes strongly singular, for each element, when the observation node i coincides with one node of the integrated element k . The CPV of this integral must thus be properly evaluated. For a two-dimensional problem, as indicated by Eq. (2.1) or (2.35), the singularity is $\mathcal{O}(1/r_i)$, where r_i denotes the distance to point i .

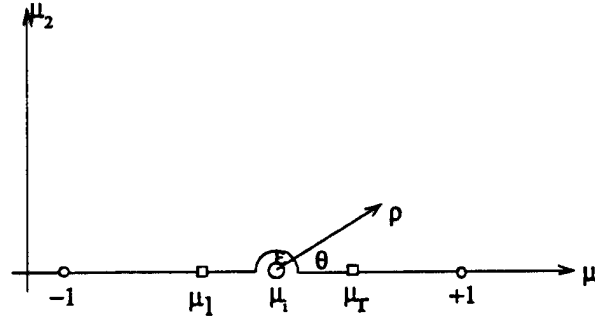


Figure 3.1: Sketch for the singular integration at point i of the reference element.

The integrand of BS Eqs. (3.1) can be defined as, $F(\mu) = N_j(\mu)J^k(\mu)f_i^{u,v}(\mu)$, where $f_i^{u,v}$ denotes one or the other kernels of the BS integral for u or v , $N_j(\mu)$ denotes shape functions (2.26) used to discretize the geometry and the circulation $\gamma = N_j\gamma_j$ on element k , and $J^k = s_\mu^k(\mu)$, the Jacobian. For each element, the strong singularity in the integrand can be represented by means of a Laurent series expansion around the singular point (x_i, y_i) , of the form (Guiggiani *et al.* [15]),

$$F(\rho, \theta) = \frac{F_{-1}(\theta)}{\rho} + F_0(\theta) \quad (3.2)$$

where (ρ, θ) denote polar coordinates centered at point i in the reference element (Fig. 3.1), and $F_0(\theta)$ and $F_{-1}(\theta)$ are $\mathcal{O}(1)$ functions of the VS geometry around point i . The integrals in Eq. (3.1) for element k can now be expressed as (Fig. 3.1),

$$\begin{aligned} I^k &= \int_{-1}^{\mu_l} F(\rho(\mu), \theta(\mu)) d\mu + \int_{\mu_l}^{\mu_r} F(\rho(\mu), \theta(\mu)) d\mu + \int_{\mu_r}^{+1} F(\rho(\mu), \theta(\mu)) d\mu \\ &= I_1^k + I_2^k + I_3^k \end{aligned} \quad (3.3)$$

where (μ_l, μ_r) denotes an interval containing the singular point, located at μ_i . With this definition, only the middle integral, I_2^k is singular in Eq. (3.3). The first and last integral can thus be calculated using regular Gauss quadrature rule, after transformation of their respective intervals into $[-1, +1]$.

When using the polar coordinates (ρ, θ) , I_2^k can be divided into three parts, by defining a semi-circular boundary of vanishing radius ϵ centered on the singular point, as,

$$\begin{aligned} I_2^k &= \lim_{\epsilon \rightarrow 0} \left\{ - \int_{\mu_i - \mu_l}^{\epsilon} \left[\frac{F_{-1}(\pi)}{\rho} + F_0(\pi) \right] d\rho - \int_{\pi}^0 \left[\frac{F_{-1}(\theta)}{\epsilon} + F_0(\theta) \right] \epsilon \sin \theta d\theta \right. \\ &\quad \left. + \int_{\epsilon}^{-\mu_i + \mu_r} \left[\frac{F_{-1}(0)}{\rho} + F_0(0) \right] d\rho \right\} \\ &= F_{-1}(0) \ln \frac{\mu_r - \mu_i}{\mu_i - \mu_l} + \int_0^{\pi} F_{-1}(\theta) \sin \theta d\theta + (\mu_i - \mu_l)F_0(\pi) + (\mu_r - \mu_i)F_0(0) \end{aligned} \quad (3.4)$$

where, by definition of the geometry on the intrinsic element, $\mu = \mu_i + \rho \cos \theta$, and the property, $F_{-1}(\theta) = -F_{-1}(\theta + \pi)$ (which is a consequence of the residue theorem) has been used to combine the first (singular) terms in the first and last integrals [15]. If μ_l and μ_r are selected symmetrically around point i , we further have,

$$\mu_i - \mu_l = \mu_r - \mu_i = \frac{\Delta\mu}{2} \quad (3.5)$$

with $\Delta\mu = \mu_r - \mu_l$, and, in this case, Eq. (3.4) simplifies into,

$$I_2^k = \int_0^\pi F_{-1}(\theta) \sin \theta d\theta + \frac{\Delta\mu}{2} [F_0(\pi) + F_0(0)] \quad (3.6)$$

The calculation of $F_0(\theta)$, $F_{-1}(\theta)$ in Eq. (3.6) first requires defining a local intrinsic coordinate expansion for, $\mathbf{x} - \mathbf{x}_i$, in the neighborhood of the singular point \mathbf{x}_i (i.e., for small ρ), where \mathbf{x} denotes another point of element k . Using the same polar coordinates system as above, we get,

$$\mathbf{x}(\mu) - \mathbf{x}_i(\mu) = \rho(\mu)\mathbf{A}(\theta(\mu)) + \rho^2(\mu)\mathbf{B}(\theta(\mu)) + \mathcal{O}(\rho^3) \quad (3.7)$$

with,

$$\mathbf{A}(\theta) = \frac{\partial \mathbf{x}}{\partial \mu}(\mu_i) C(\theta) \quad \text{with} \quad C(\theta) = \cos \theta - \tan \theta \sin \theta + \frac{\tan^2 \theta}{2} \left[\frac{d\rho}{d\mu} - \frac{1}{\cos \theta} \right] \quad (3.8)$$

and,

$$\mathbf{B}(\theta) = \frac{\partial^2 \mathbf{x}}{\partial \mu^2}(\mu_i) \left[\frac{\cos^2 \theta}{2} + \sin^2 \theta \left(\frac{\tan^2 \theta}{2} - 1 \right) \right] \quad (3.9)$$

where the first and second components of $\mathbf{A}(\theta)$ and $\mathbf{B}(\theta)$ refer to x and y coordinates, respectively.

Using Eqs. (3.7)-(3.9), we can express various parts of the kernel $F(\mu)$ of BS Eqs. (3.1) and put them in the form of expansion (3.2). After calculations, we get,

$$F_0^{u,v}(\theta) = a_0 S_0^{u,v}(\theta) + a_1(\theta) S_{-1}^{u,v}(\theta) \quad ; \quad F_{-1}^{u,v}(\theta) = a_0 S_{-1}^{u,v}(\theta) \quad (3.10)$$

where subscripts u and v indicate which of the two BS integrals (3.1) is being considered, and,

$$S_{-1}^{u,v}(\theta) = \frac{A_{2,1}(\theta)}{\pi(A_1^2(\theta) + A_2^2(\theta))} \quad ; \quad S_0^{u,v}(\theta) = \frac{B_{2,1}(\theta) - D(\theta)A_{2,1}(\theta)}{\pi(A_1^2(\theta) + A_2^2(\theta))} \quad (3.11)$$

where A_1 , A_2 , B_1 and B_2 are given by Eqs. (3.8) and (3.9), and

$$D(\theta) = 2 \frac{A_1(\theta)B_1(\theta) + A_2(\theta)B_2(\theta)}{A_1(\theta)^2 + A_2(\theta)^2} \quad (3.12)$$

and,

$$a_o = s_\mu^k(\mu_i) N_j(\mu_i) \ ; \ a_1(\theta) = C(\theta) \{ s_\mu^k(\mu_i) N_j'(\mu_i) + s_{\mu\mu}^k(\mu_i) N_j(\mu_i) \} \quad (3.13)$$

where μ indices and dashes indicate derivatives.

Accounting for relationships between odd and even functions of θ at 0 and π , the second term in Eq. (3.6) can now be calculated, using Eqs. (3.8)-(3.13) as,

$$\frac{\Delta\mu}{2} [F_0^{u,v}(\pi) + F_0^{u,v}(0)] = \Delta\mu [a_o S_0^{u,v}(0) + a_1(0) S_{-1}^{u,v}(0)] \quad (3.14)$$

with $A(0) = x_\mu$, $B(0) = \frac{x_{\mu\mu}}{2}$, $C(0) = 1$, and,

$$D(0) = \frac{x_\mu x_{\mu\mu} + y_\mu y_{\mu\mu}}{(s_\mu^k)^2} \quad (3.15)$$

and, hence,

$$S_0^{u,v}(0) = \frac{(y, x)_{\mu\mu} (s_\mu^k)^2 - 2(y, x)_\mu (x_\mu x_{\mu\mu} + y_\mu y_{\mu\mu})}{2\pi (s_\mu^k)^4} \ ; \ S_{-1}^{u,v}(0) = \frac{(y, x)_\mu}{\pi (s_\mu^k)^2} \quad (3.16)$$

Using Eqs. (3.10), (3.13) and (3.16), one can analytically calculate the integral in Eq. (3.6) and see that it vanishes. Using Eqs. (3.6) and (3.14), together with Eq. (3.16), one can then, after some transformations, calculate the singular part of Eq. (3.3) as,

$$I_2^k = \frac{1}{2\pi s_\mu^k(\mu_i)} [N_j(\mu_i) (y(\mu_i), x(\mu_i))_{\mu\mu} + 2N_j'(\mu_i) (y(\mu_i), x(\mu_i))_\mu] \quad (3.17)$$

for the first and the second BS integrals, respectively.

Finally, all terms are expressed as a function of element shape functions and nodal values, using Eqs. (2.19)-(2.21).

3.4 Applications of the periodic CVS model

3.4.1 Validation with a uniform flow

To validate the new integration methods developed for the CVS model, a steady-state case was first solved, with a simple uniform flow U between two impermeable boundaries separated by a distance h (Fig. 3.2). Two CVS's with zero amplitude ($\varepsilon = 0$) were discretized over a length equal to $\alpha = 10, 100$, or 1000 times their spacing, $\lambda = \alpha h$. Since this problem was solved with the periodic model, no semi-infinite sheets were needed at the CVS's extremities. The number of nodes on the sheets was kept constant equal to 45. To model a uniform velocity U , circulation was set to $\pm U$ on each CVS, respectively. Twenty Gauss integration points per element were used in the CVS model. Velocity was calculated with the model, using BS Eqs. (3.1), first on the VS's nodes themselves, then for 30 equally

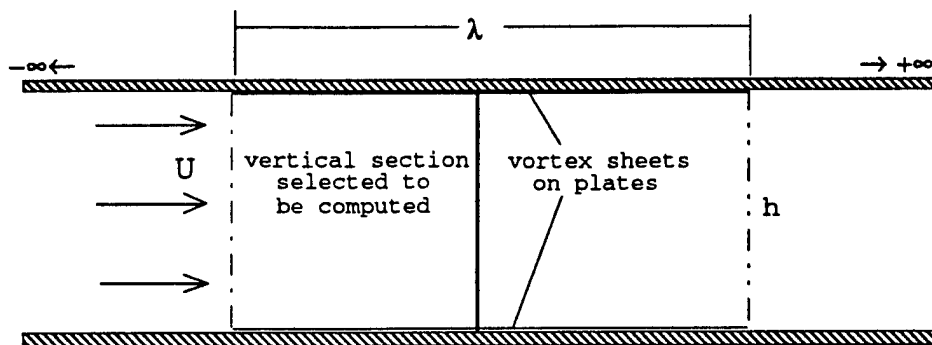


Figure 3.2: Sketch of computational domain for uniform flow between two plates

spaced points in between the VS's (Fig. 3.2). For comparison, similar computations were also performed using the PCVS periodic model described in Chapter 2.

On the VS's themselves, using the CVS model, the velocity was recalculated to within 4, 6.8, and $52.6 \cdot 10^{-6}\%$ of the exact value U , for $\alpha = 10, 100$, and 1000 , respectively. Using the PCVS method, maximum errors were $3.8 \cdot 10^{-4}$, 12.6, and 612 %, respectively. In all cases, maximum errors occurred at the VS's extremities. The very accurate results obtained with the CVS model validate the singular numerical integration procedures developed for this model. In between the sheets, errors were significantly larger, with a maximum for the points closer to the VS's. For the CVS method, maximum errors reached $1.4 \cdot 10^{-6}$, $3.6 \cdot 10^{-2}$, and 6.3 % of the exact value U , for $\alpha = 10, 100$, and 1000 , respectively. As for calculating the velocity on the sheets, in these calculations, (regular) integrations over vortex sheet elements were performed using 20 Gauss points. As internal points get increasingly closer to the VS's, however, BS integrals (3.1), though still regular, become almost singular (i.e., *quasi-singular integrals*, Grilli and Subramanya [19]). When increasing the number of Gauss points in these integrals, by subdividing the elements, as in [19], an accuracy similar to the first case ($\alpha = 10$) could be reached for the last two cases with the larger aspect ratio α . By contrast, using the PCVS method, accuracy stayed very poor in all cases, with errors of 32, 665, and 7448 %, respectively.

These results show the need for the more accurate CVS model when computational nodes get very close to each other and/or aspect ratios are large. As this will be the case for contained oil slicks, it is expected that more accurate and stable results will be obtained when using the CVS method, as compared to the PCVS method.

As a further validation of the CVS method, in the next section, an unsteady KH instability case is presented.

3.4.2 Periodic KH instability

The periodic KH instability of a two fluid vertically stratified system will be solved with the CVS model, in a set up similar to Fig. 2.3. A sinusoidal perturbation with small

nondimensional amplitude ε is prescribed on the interface, and the initial circulation $\gamma(x)$ is specified using Eq. (2.28).

A (very unstable) pure shear flow problem is first considered, with a velocity jump $\Delta U = 0.5$ m/s applied between two layers of an identical inviscid fluid of uniform density ρ (whose absolute value has no influence in the present case), i.e., $\varphi = 1$. The amplitude of perturbation is $a = 0.0025$ m and the wavelength is selected to $\lambda = 0.1$ m, corresponding to an instability at the ripple scale; the wavelength however does not matter in this problem and results would be self-similar for another wavelength. Thus, with these data, $\varepsilon = a/\lambda = 0.025$ (as for the PCVS applications in Section 2.5.2). For, $W = \kappa = \sigma_{o1} = 0$, Eq. (2.32) shows that the linear growth rate of instability for this case is $\omega = k\Delta U/2$ and, in Eq. (2.7), we see that $d\gamma/dt = 0$. Hence, as expected for this case, the CVS system is conservative.

The initial discretization in the computations has $N = 45$ equally spaced nodes per wavelength and nodes are added and regridded at each time step, in order to maintain the node resolution constant to within 1.5%, as the CVS length increases when the instability develops. In order to ensure high accuracy in these very unstable computations, the initial time step is selected as a small value, $\Delta\tau = 0.001$ (note, in this case, $\tau = \Delta t \Delta U/\lambda = 5t$), which corresponds to a mesh Courant number of 0.023. Since the spatial resolution is maintained constant through regridding, the time step also stays constant throughout computations. Model results for the time evolution of the interface for 3,000 time steps are given in Fig. 3.3. At the end of computations, the number of nodes has increased to $N = 328$ (Fig. 3.3.g, curve h).

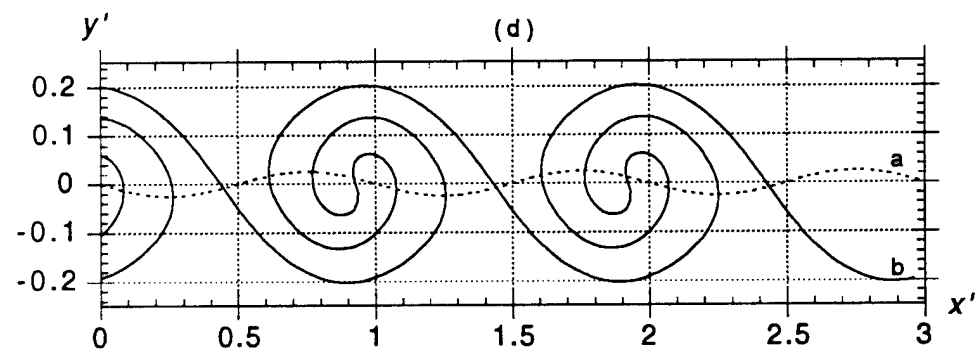
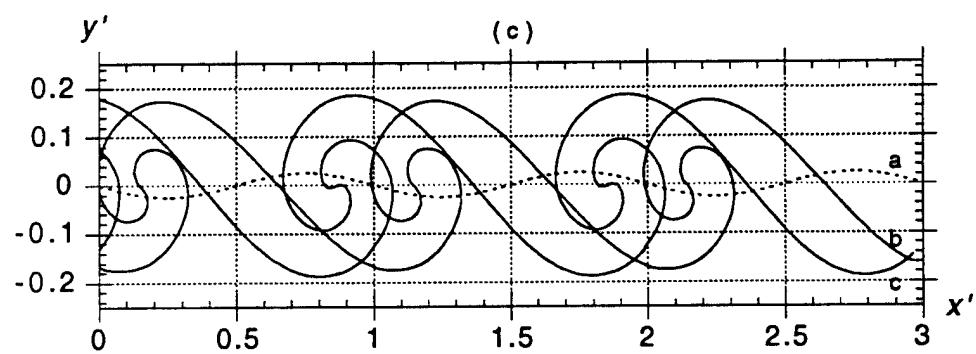
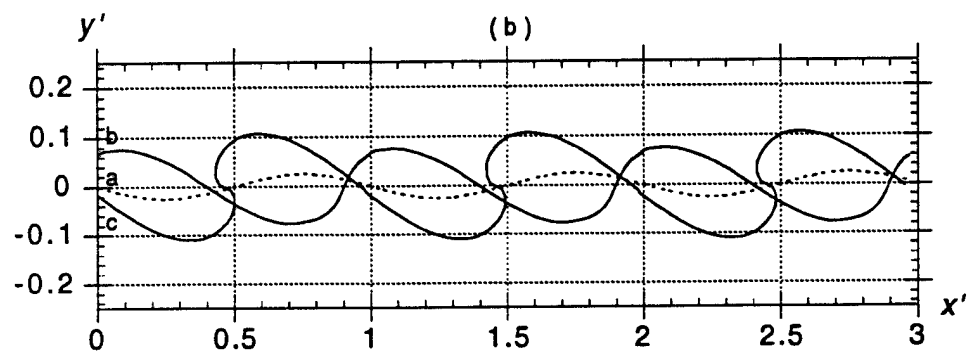
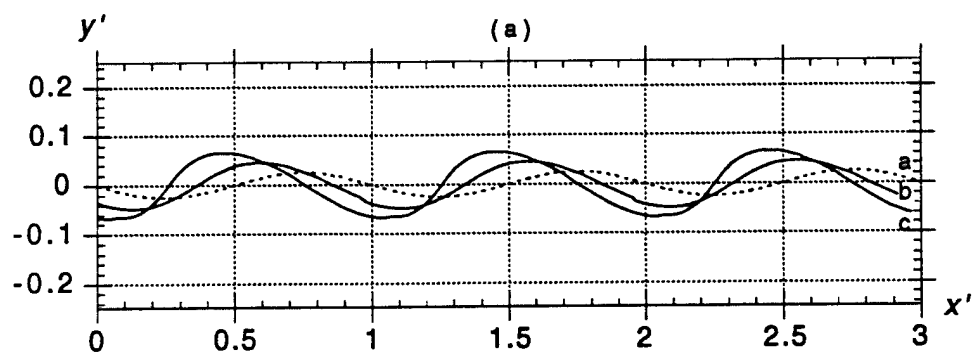
Overall, results show reasonable predictions of VS evolution. Fig. 3.3a shows that, for small time, the interface perturbation slowly grows up while more or less preserving its initial shape; hence, this is referred to as a *quasi-linear* regime. At the same time, a relative motion of crests is observed; this phenomenon, which is not observed in point-vortex or PCVS models (e.g., Rangel and Serignano [33]; Section 2.5.2), indicates that, as the instability develops, interfacial waves travel at a modified phase velocity. In Fig. 3.3b it is seen that, after the quasi-linear initial growth, the larger nonlinearity in the flow field leads to both increased wave amplitude and skewness and, eventually, to a crest overturning similar to surface wave breaking; this is referred to as the *nonlinear* regime. Comparing Figs. 3.3a and 3.3b, it is apparent that, for the same time interval of 0.6, the amplitude growth is much larger in the nonlinear regime than in the quasi-linear one. In Fig. 3.3c, the similarity of results with surface waves disappears as the interface VS starts *rolling-up*. In Figs. 3.3d-f, as time further increases, the interface roll-up becomes more pronounced. It is worth pointing out that PCVS computations such as those presented in Section 2.5.2 usually fail around the stage of Fig. 3.3d, whereas the more accurate CVS model provides very stable results for the full stages of development of VS roll-up.

After reaching a maximum value in Fig. 3.3f, Figs. 3.3g and 3.3h show that the amplitude of disturbance starts gradually decreasing, as the “roll-up cells” become more elongated. At this stage, however, it should be pointed out that different fluid regions in the roll-up cells are quite close to each other. Although not creating actual singularities in the flow, such situations lead to highly varying kernels in the BS integrals that standard Gauss

quadrature rules fail to properly integrate unless a prohibitive number of integration points is used. Such integrals, referred to as *quasi-singular*, thus require more accurate integration methods, usually, as the distance between an observation node i and an element k becomes smaller than, say, 10% of the element length (Grilli and Subramanya [19]). Quasi-singular integration methods have not yet been implemented in our model but will be implemented as part of Phase III studies. Hence, although no particular instability is observed, one might start questioning model accuracy at and beyond the stage of Fig. 3.3h.

A second application was carried out for a case with two fluids of different density, $\rho_1 = 0.9$ and $\rho_2 = 1.0$, with surface tension coefficient equal to $\sigma_{o1} = 0.0237$ N/m (the value for water and oil). The gravitational acceleration was $g = 9.81$ m/s². Other parameters, both physical and numerical, remained as before. Fig. 3.4 shows that the disturbance amplitude, ϵ , grows as a function of time, for both applications, compared to predictions of linear theory from Eq. (2.32). For both cases, as also observed in earlier studies, linear theory greatly overpredicts the growth rate of the instability. As expected from PCVS computations in Section 2.5.2, an increase in interfacial surface tension and a decrease in the upper layer density both reduce the growth rate of nonlinear instabilities. In Fig. 3.4, one can also see that, for $\varphi = 0.9$, the interface amplitude eventually stops growing and oscillates around a more or less stable shape of amplitude $\epsilon \simeq 0.05$. Hence, this case is not unstable in long term computations.

A comparison of the CVS growth rates with those predicted by the PCVS model for the same case (Fig. 2.11 curves a and c) show that the CVS model predicts smaller growth rates than the PCVS model. Fig. 3.5 in fact shows a comparison of interface shapes obtained in the PCVS and in the CVS model for the same case as in Fig. 3.3, and $t = 0.21$ s. [Beyond this time, PCVS results in Section 2.5.2 became unstable.] It is seen that the PCVS model predicts a faster growth of instability than the CVS model. Reasons for the observed differences reside in both a more accurate computation of BS integrals and a better geometric representation in the CVS model. A more detailed understanding of these results, however, still needs to be achieved.



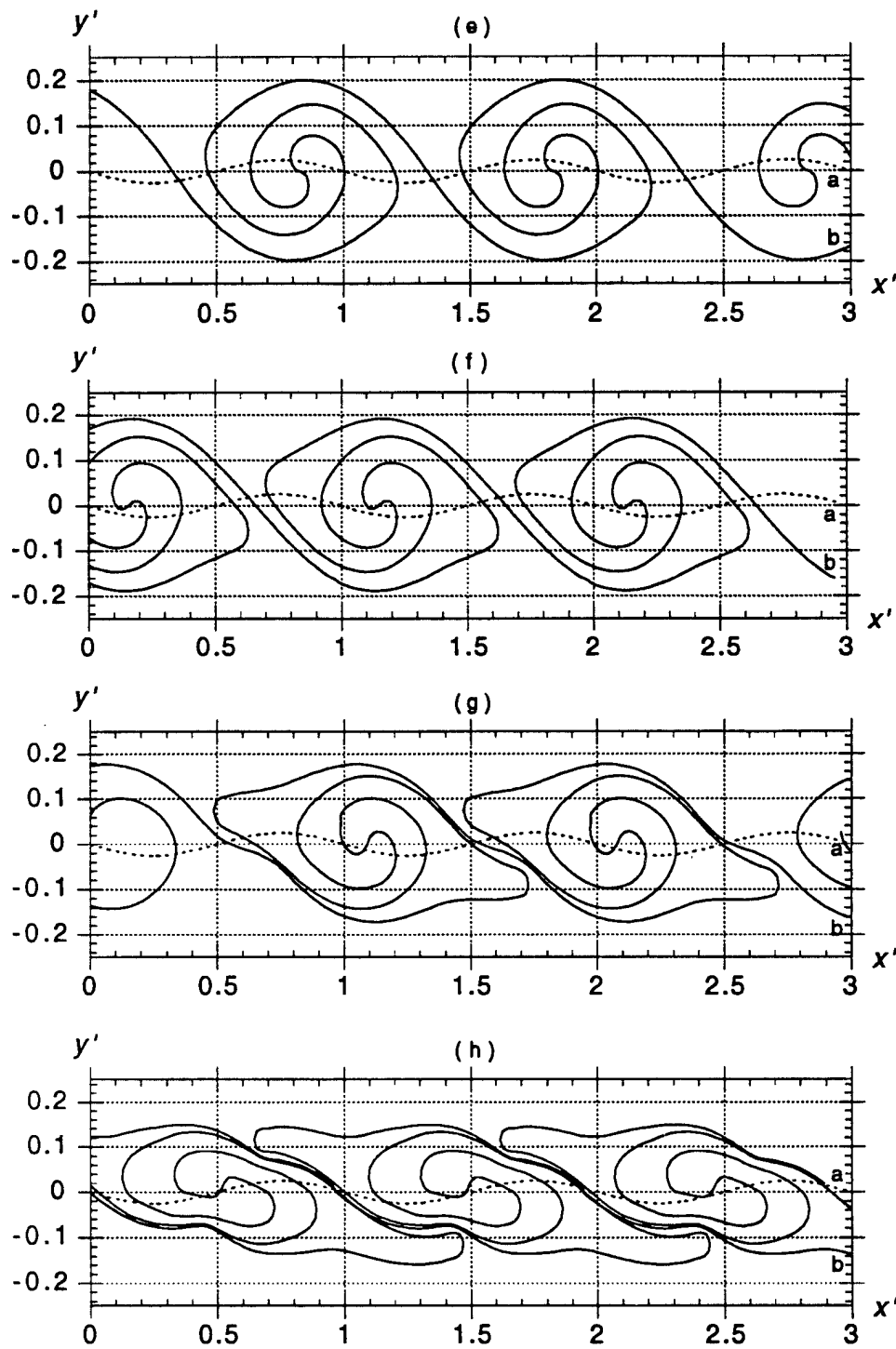


Figure 3.3: Results for periodic KH instability with wavelength $\lambda = 0.1\text{m}$, $|\Delta U| = 0.5\text{m/s}$, $\varphi = 1$, and $\sigma_{o1} = 0$. curves show interfacial shape at time t (s) = (a) a : 0.0002, b : 0.060, c : 0.120; (b) a : 0.0002, b : 0.150, c : 0.240; (c) a : 0.0002, b : 0.330, c : 0.390; (d) a : 0.0002, b : 0.480; (e) a : 0.0002, b : 0.510; (f) a : 0.0002, b : 0.540; (g) a : 0.0002, b : 0.570; (h) a : 0.0002, b : 0.600.

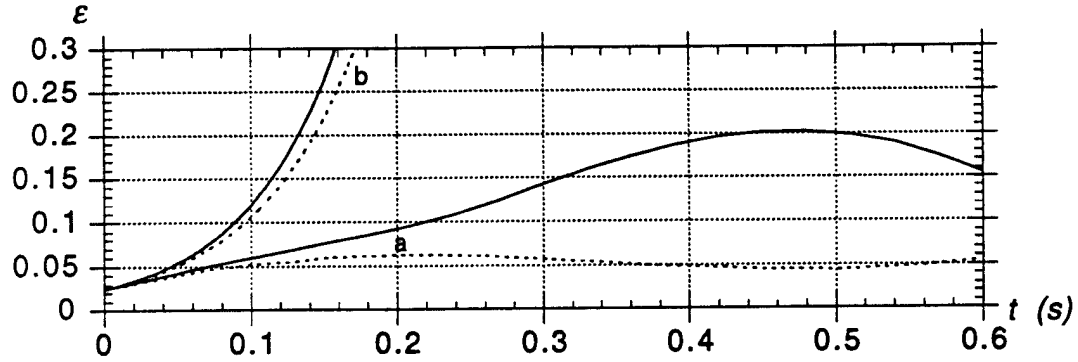


Figure 3.4: Periodic KH instability with wavelength $\lambda = 0.1\text{m}$ and $|\Delta U| = 0.5\text{m/s}$: (—) $\varphi = 1, \sigma_{o1} = 0$; (---) $\varphi = 0.9, \sigma_{o1} = 0.0237\text{ N/m}$. Curves show the maximum dimensionless amplitude of the interface ε as a function of time t for : (a) CVS model; and (b) linear theory (Lamb, 1932).

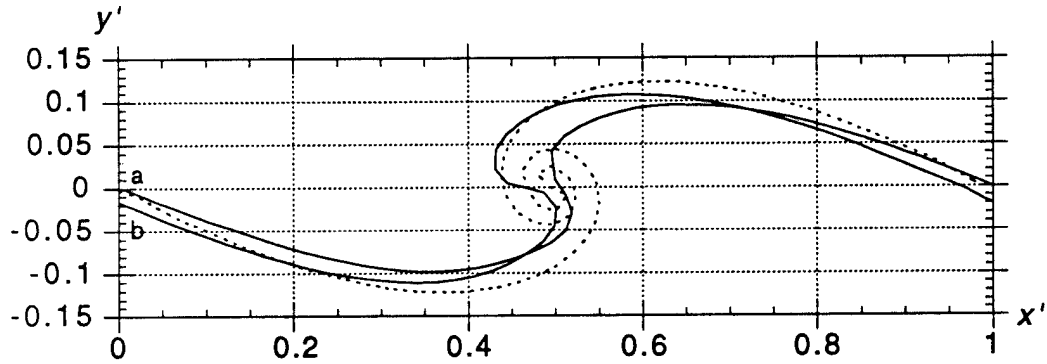


Figure 3.5: Same case as Fig. 3.3 : (—) CVS results for (a) $t = 0.210\text{ s}$, (b) $t = 0.240\text{ s}$; (---) PCVS results for $t = 0.210\text{ s}$.

3.5 Conclusions of CVS computations

A continuous CVS model was proposed for calculating the nonlinear motion of the interface between two inviscid stratified fluids. A BEM methodology was followed to develop higher-order representations of the discretized geometry and circulation in the CVS, which were used to calculate BS integrals for the velocity field. To optimize computations, local integrations of CVS elements were performed in a single reference element. The parity mapping transformation of Section 2.2.1 was used to more accurately calculate tangential derivatives in roll-up regions of the CVS. Hypersingular integrations were performed in the reference element, through a newly developed Laurent series expansion method. After testing the model for a simple uniform flow, the classical periodic Kelvin-Helmholtz instability problem was calculated to validate the new CVS model. Numerical results indicate that : (i) the CVS approximation provides a more accurate and stable numerical solution of the interface time evolution than when using the PCVS model; (ii) the CVS model eliminates the chaotic motion of interface points observed in classical point vortex or piecewise constant VS models, when computations are pushed beyond a critical time. We believe that such chaotic motions may be caused by both inaccuracies in the calculation of BS integrals and improper modeling of VS roll-up when using point vortices; (iii) the time evolution of CVS's significantly differs from the one calculated with point vortices or PCVS's. Besides a different growth rate of instability, disturbance waves in the CVS move with a specific phase velocity, larger than the VS's average velocity. Hence these waves are traveling rather than standing waves, with respect to the VS. The importance of both of these differences depends on fluid physical properties, velocity, and density difference; (iv) computations of the later stages of CVS evolution indicate that the KH disturbance growth levels up and then decreases. This is likely due to larger deformations in the roll-up regions of the VS, which start tightly spiraling and tilting to the downstream direction, implying that, after this stage, nonlinearity begins to play a more dominant role and prevents further disturbance growth. Instead, energy exchange and redistribution will occur by splitting or reuniting of roll-up sections, inside the VS itself.

During Phase III studies, the CVS model will be applied to the non-periodic oil/boom containment problem.

Chapter 4

Computation of quasi steady-state slick shape

4.1 Introduction

In the few computations of headwave instability published earlier, the initial shape of the oil slick was selected rather arbitrarily. Zalosh [42] for instance used part of a sine function to define the initial slick shape in his computations. This was also the method used in our Phase I model to initialize the shape of the oil slick (see Grilli *et al.* [16] for detail).

Based on the analysis of the oil containment problem done during Phase I of these studies, we concluded that such an arbitrary choice of initial slick shape (and dynamics) in the numerical model could induce non-physical (numerical) instabilities of the slick. An arbitrary (initial) geometry selected to represent the interface between oil and water, indeed, is not likely to satisfy both the kinematic and dynamic boundary conditions along the interface. Such a violation of the kinematic and dynamic equilibrium conditions is similar to creating an initial perturbation on the interface which, when introduced in a time dependent dynamic model, readily tries to adjust its shape to satisfy the equilibrium conditions. It is likely that such adjustments do not match actual instabilities occurring along an initially stable interface, for which the underlying current velocity is increased beyond the instability threshold U_{cr} .

In the Phase I studies, only simple cases were solved in order to qualitatively validate model equations and numerical procedures (i.e., Kelvin-Helmholtz and headwave instabilities). In those computations, the initial shape of interfaces was quite arbitrarily selected the same as in Zalosh's studies.

In the more sophisticated applications of the model to oil containment by a boom that we started to perform in Phase II of this study and for those currently taking place in Phase III, before interfacial instability can be studied in the VS model, it is necessary to calculate an initially stable shape of the oil slick interface. This shape must correspond to a small underlying current velocity, below the instability threshold $U < U_{cr}$. After this initialization stage, current velocity will then be increased beyond the instability threshold

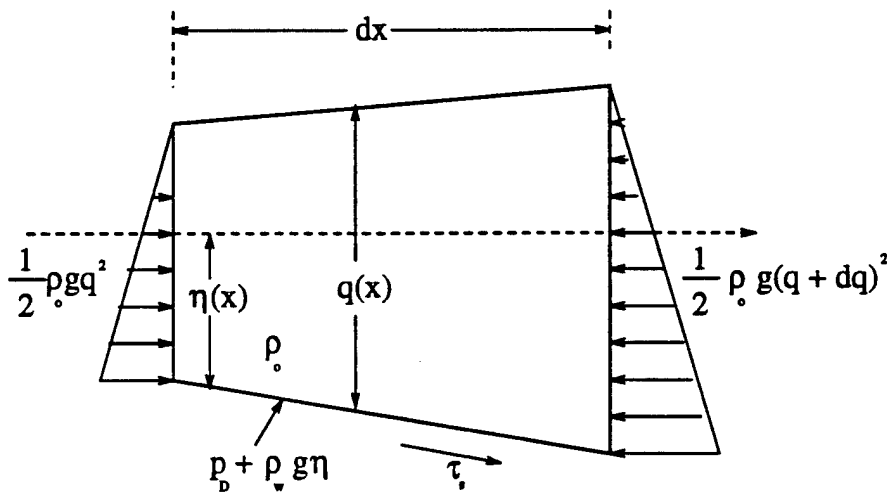


Figure 4.1: Sketch of forces acting on a differential element of length dx of the oil slick as in Milgram and Van Houten's [29] quasi-hydrostatic model.

and development of interfacial waves will be calculated as a function of time using the numerical VS model.

Initialization thus consists in finding the initial quasi-static shape of the slick interface $\eta(x)$ (measured from still water level; Fig. 4.1) that satisfies both the dynamic and kinematic conditions on the interface. In Phase I studies, Grilli *et al.* [16], following Milgram and Van Houten [29], proposed to use a quasi-hydrostatic approach within the slick to express equations for the initialization of the slick. This led to a numerical procedure to iteratively calculate the initial slick shape. No model, however, was developed at that time and no numerical results were presented.

During Phase II, the equations and numerical procedures proposed during Phase I to calculate the initial slick shape were further developed and implemented as a numerical Boundary Element Model (BEM) coupled to a finite difference iterative solver. These developments, as well as numerical applications of the BEM model, are presented in the following.

No integration of this model with the VS model, however, has been done during Phase II. Indeed, to fully integrate both BEM and VS models, it is necessary to first include interfacial friction effects in the VS time updating equations. Friction effects were theoretically worked out during Phase II (see Chapter 5), but will only be implemented as part of the calibration studies being carried out during Phase III. Integration of both models will then take place (see Fig. 1.5).

4.2 Principle of slick shape initialization

The basic quasi-hydrostatic equations for the slick shape initialization are first summarized.

Following [29], the oil slick is assumed not to significantly move and, hence, to be in quasi-hydrostatic equilibrium. Accordingly, a Bernoulli equation can be expressed between the front of the slick and any point on the slick interface, which provides the dynamic pressure p_D as (Fig. 4.1),

$$p_D = \frac{1}{2} \rho_w (U^2 - U_{ws}^2) \quad (4.1)$$

where ρ_w denotes the water density and U_{ws} is the water tangential velocity along the slick interface.

Expressing the horizontal force equilibrium along the interface we get, limiting terms to first-order,

$$(p_D + \rho_w g \eta) \frac{\partial \eta}{\partial x} + \tau_s = \rho_o g q \frac{\partial q}{\partial x} \quad (4.2)$$

where τ_s is the shear stress along the slick, q is the the total slick thickness (i.e., η plus the part above still water level; see Fig. 4.1). Expressing the vertical force equilibrium along the interface, we also get, limiting terms to first-order,

$$p_D + \rho_w g \eta = \rho_o g q \quad (4.3)$$

The shear stress along the slick is classically represented using a simple drag formula as (e.g., Batchelor, 1967),

$$\tau_s = \frac{1}{2} \rho_w C_f U_{ws}^2 \quad (4.4)$$

where C_f is a global non-dimensional friction coefficient, and a function of flow characteristics in the water and roughness along the interface.

In Milgram and Van Houten's study, the interface shape $\eta(x)$ and slick thickness $q(x)$ were experimentally measured and the tangential velocity of the underlying flow was calculated using ideal flow theory, assuming a uniform velocity U for the incident flow ahead of the slick. The friction coefficient (the only "unknown" left in the equations) was then calculated along the interface using Eqs. (4.1)-(4.4).

During Phase II of the studies, we developed a model based on the above equations and used it in reverse mode, i.e. : the friction coefficient C_f was calculated along the interface using boundary layer semi-empirical theories and the quasi-steady slick shape was then predicted. Since C_f is a function of *a priori* unknown flow characteristics (e.g., Reynolds number), an iterative method was used :

- (i) an initial slick shape was assumed following Zalosh's [42] approximation;
- (ii) the tangential velocity along the interface was calculated for the external water flow, based on ideal flow theory;
- (iii) the friction coefficient was calculated for this external flow; and
- (iv) a corrected slick shape was estimated using the quasi-hydrostatic equilibrium equations.

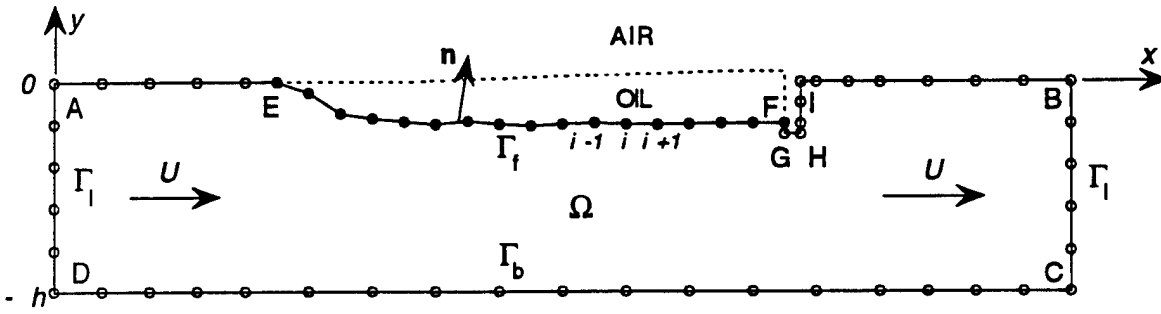


Figure 4.2: Sketch of computational domain Ω and boundaries Γ_f , Γ_l and Γ_b for the external water flow computation using streamfunction theory and the BEM model. Boundaries Γ_f and Γ_b are rigid no-flow boundaries and a uniform flow U is specified on Γ_l boundary. Discretization nodes (o) and (•) are used in the BEM solution of the water flow and locations of nodes (•) on the slick interface are iteratively calculated to satisfy equilibrium equations. Nodes A-I are double nodes in the BEM computations. Nodes marked as $i-1, i, i+1$, illustrate the finite difference iterative method.

These steps were repeated until convergence was reached on the slick geometry.

More details are provided in the following Sections for stages (ii) to (iv) of the iterative method. Results from this iterative method are presented in the last section and compared to experimental results [29].

4.3 External flow calculation

In the slick quasi-hydrostatic equilibrium equations presented above, the effect of the underlying water flow is transmitted through both the dynamic pressure and the shear stress at the interface. Both of these, essentially, depend on the water flow velocity at the interface represented by the tangential velocity U_{ws} , and on the interface geometry.

Since the slick is assumed not to move, the water flow is considered as an external flow past an obstacle having the slick/boom geometry. Hence, the free surface in front of the slick and behind the boom, together with the water/slick interface and the boom, are assumed to be rigid walls (i.e. streamlines) (Fig. 4.2). Due to the slenderness of the slick geometry, an ideal flow approximation, implying no flow separation, is made for the water flow. This will create some errors downstream of the boom where flow separation occurs but should not influence the slick shape too much, particularly in the headwave region.

Hence, using a streamfunction representation in the water domain Ω (e.g., Batchelor, 1967), continuity equation reads (Fig. 4.2),

$$\nabla^2 \psi = 0 \quad ; \text{ in } \Omega \quad (4.5)$$

where ψ is the streamfunction defined such that,

$$u_w = -\frac{\partial \psi}{\partial y} \quad ; \quad v_w = \frac{\partial \psi}{\partial x} \quad ; \quad U_{ws} = -\frac{\partial \psi}{\partial n} \quad (4.6)$$

where (u_w, v_w) are velocity components in the water and \mathbf{n} denotes the normal direction along the slick interface pointing outwards from the water (Fig. 4.2). Eq. (4.5) is solved using a Boundary Integral Equation representation (BIE),

$$\alpha(\mathbf{x}_l)\psi(\mathbf{x}_l) = \int_{\Gamma(\mathbf{x})} \left[\frac{\partial \psi}{\partial n} G(\mathbf{x}, \mathbf{x}_l) - \psi \frac{\partial G(\mathbf{x}, \mathbf{x}_l)}{\partial n} \right] d\Gamma(\mathbf{x}) \quad (4.7)$$

in which,

$$G(\mathbf{x}, \mathbf{x}_l) = -(1/2\pi) \log |\mathbf{x} - \mathbf{x}_l| \quad (4.8)$$

is the free space Green's function, $\mathbf{x} = (x, y)$ and $\mathbf{x}_l = (x_l, y_l)$ represent position vectors for points on the boundary Γ , and $\alpha(\mathbf{x}_l)$ is a geometric coefficient.

The BIE (4.7) is solved using a higher-order Boundary Element Method (BEM) (Grilli and Subramanya 1995, 1996), together with boundary conditions expressing no-flow on the bottom boundary Γ_b and on the free surface, slick interface and boom Γ_f ; and uniform incoming and outgoing flows on lateral boundaries Γ_l (see, Fig. 4.2). Note that, the present method was developed for (and thus requires) domains with boundaries located at finite distance. Hence, a bottom boundary is always needed to make sure Γ is a closed boundary. If one wishes to solve for the flow under a slick in very deep water, one just has to locate the bottom boundary far enough below the slick for this boundary not to influence the flow close to the slick interface. In practical computations, we found that, when the bottom boundary was located at least ten times deeper than the boom draft, no significant influence of the bottom boundary could be found on the tangential velocity at the slick interface.

In a streamfunction representation, no-flow conditions correspond to specifying streamlines with $\bar{\psi} = \text{constant}$. In the present case, we set $\bar{\psi} = 0$ on Γ_b and $\bar{\psi} = hU$ on Γ_f and uniform flow conditions correspond are specified as $\bar{\psi}_n = 0$ on Γ_l , where indices n indicates partial n -derivative.

A linearly varying streamfunction in the vertical direction should be obtained on Γ_l as the solution of Eq. (4.7), i.e., $\psi = |y| U$, provided no significant influence of the slick and boom occurs for the uniform flow. The solution on Γ_f directly provides, $U_{ws} = -\psi_n$, along the slick interface, to be used in Eqs. (4.1)-(4.4). Hence, the ideal flow solution allows one to calculate the dynamic pressure and the shear stress (provided C_f variation is known) along the slick, for any assumed slick shape.

Practical numerical solution of Eq. (4.7), with relevant boundary conditions, is done using a higher-order BEM method in which discretization nodes are specified on boundary $\Gamma = \Gamma_b + \Gamma_f + \Gamma_l$ and quadratic isoparametric elements are used to interpolate in between discretization nodes. Both regular and singular integrals in Eq. (4.7) are performed numerically, using Gauss quadrature methods for the regular integrals, and a similar method for the singular integral, well-suited to logarithmic singularities. An algebraic system of equations is thus assembled and solved for the unknowns at the discretization nodes, i.e., ψ or ψ_n , whichever is not set by boundary conditions. Details of the BEM method and numerical integrations can be found in Grilli *et al.* [18, 20, 21].

Additional difficulties arise in the numerical solution of the present problem in relation to the proper representation of BIE's for corners located at the intersection between boundaries

having different types of boundary conditions and normal directions (points A, B, C, D in Fig. 4.2). To address corner problems in the BEM algorithm, double-node representations and corner compatibility equations are used (Grilli and Svendsen [21]). Within boundary Γ_f , there are also points with discontinuities in the tangential direction for which, physically, the velocity must be zero. These are the corners points E,F,G,H,I. Due to the two normal directions, double-nodes are also used to represent these points but care must be taken to ensure that the numerical solution satisfies the physical requirement of zero velocity on both sides of these points.

4.4 Iterative calculation of slick shape using a finite difference method

Non-dimensional variables are introduced in Eqs. (4.1)-(4.4), based on a length scale U^2/g , a velocity scale U , and a stress scale $\rho_w U^2$ (note that for the oil-water interface, since the oil does not move, $U = \Delta U$). We thus get,

$$x' = \frac{gx}{U^2} \quad ; \quad q' = \frac{gq}{U^2} \quad ; \quad \eta' = \frac{g\eta}{U^2} \quad (4.9)$$

$$p'_D = \frac{p_D}{\rho_w U^2} \quad ; \quad \tau'_s = \frac{\tau_s}{\frac{1}{2}\rho_w U^2} \quad ; \quad C'_f = C_f \frac{U_{ws}^2}{U^2} \quad (4.10)$$

where primes denote non-dimensional variables.

Using definitions (4.9),(4.10), Eqs. (4.1)-(4.4) transform into,

$$p'_D = \frac{1}{2}(1 - U_{ws}'^2) \quad (4.11)$$

where $U_{ws}' = U_{ws}/U$.

$$(p'_D + \eta')\eta_{x'} + \frac{1}{2}\tau'_s = \varphi q' q'_{x'} \quad (4.12)$$

where x' indices denote derivatives with respect to x' , and $\varphi = \rho_o/\rho_w$.

$$p'_D + \eta' = \varphi q' \quad (4.13)$$

$$\tau'_s = C'_f \quad (4.14)$$

Combining Eqs. (4.12) to (4.14), we further get,

$$(p'_D + \eta') \left((1 - \varphi)\eta_{x'} + p'_{Dx'} \right) = \frac{\varphi}{2} C'_f \quad (4.15)$$

The set of differential equations (4.11)-(4.15) will now be transformed into Finite Difference Equations (FDE) expressed for N_{ow} nodes i along the slick interface (segment E-F in Fig. 4.2). Equation (4.15) is first developed into,

$$\eta' \eta_{x'} + p'_D \eta_{x'} + \frac{\eta' p'_{Dx'}}{1 - \varphi} + \frac{p'_D p'_{Dx'}}{1 - \varphi} = \frac{\varphi}{2(1 - \varphi)} C'_f \quad (4.16)$$

To derive a FDE representation of Eq. (4.16), we will integrate the equation between a fictitious intermediate location defined in between points $(i-1)$ and i (i.e., point $(i-1/2)$; *central difference method*), and we will assume that values of all calculated functions, η' , p'_D , and C'_f (hereafter denoted by \mathcal{F}) will be calculated at $(i-1/2)$ as,

$$\mathcal{F}_{i-1/2} = \frac{1}{2} [\mathcal{F}_{i-1} + \mathcal{F}_i] \quad (4.17)$$

We will also assume that, for the second and third terms in the left-hand-side and for the right-hand-side of Eq. (4.16), η' , p'_D , and C'_f , respectively, are approximated by their values at point i (*upwind scheme*). Doing so, Eq. (4.16) can be transformed into,

$$\begin{aligned} & \frac{1}{2} \left(\eta_i'^2 - \frac{(\eta_i' + \eta_{i-1}')^2}{4} \right) + p'_{D_i} \left(\eta_i' - \frac{\eta_i' + \eta_{i-1}'}{2} \right) + \frac{\eta_i'}{1-\varphi} \left(p'_{D_i} - \frac{p'_{D_i} + p'_{D_{i-1}}}{2} \right) \\ & + \frac{1}{2(1-\varphi)} \left(p_{D_i}^2 - \frac{(p'_{D_i} + p'_{D_{i-1}})^2}{4} \right) = \frac{\varphi}{4(1-\varphi)} C'_{f_i} (x'_i - x'_{i-1}) \end{aligned} \quad (4.18)$$

Rearranging terms in Eq. (4.18), we get,

$$\begin{aligned} & \frac{3}{4} \eta_i'^2 + \eta_i' \left(\frac{(2-\varphi)p'_{D_i} - p'_{D_{i-1}}}{1-\varphi} - \frac{\eta_{i-1}'}{2} \right) = p'_{D_i} \eta_{i-1}' \\ & - \frac{3p_{D_i}^2 - 2p'_{D_i} p'_{D_{i-1}} - p_{D_{i-1}}^2}{4(1-\varphi)} + \frac{\eta_{i-1}^2}{4} + \frac{\varphi}{2(1-\varphi)} C'_{f_i} (x'_i - x'_{i-1}) \end{aligned} \quad (4.19)$$

Eq. (4.19) is a quadratic equation for predicting η'_i , i.e., the slick elevation at point i , based on values of the slick elevation at point $(i-1)$, the dynamic pressure at points i and $(i-1)$ and the friction coefficient at point i . The dynamic pressure is calculated as a function of the tangential velocity of the external flow, using Eq. (4.11), and the friction coefficient similarly depends on the flow in the boundary layer close to the slick interface (see next Section for details). Thus, assuming an approximate initial shape for the slick, say $\eta_i'^o = \eta'^o(x'_i)$ (e.g. as in Zalosh [42]), a first BEM solution can be calculated for the underlying flow, as explained in the previous Section, providing $\psi_{n_i}^{'o} = -U_{ws_i}^{'o}$ along the slick interface.

At stage k of the iterations, the dynamic pressure is thus found, for $(i = 1, \dots, N_{ow})$ as,

$$p_{D_i}^{ik} = \frac{1}{2} (1 - \psi_{n_{oi}}^{ik2}) \quad (4.20)$$

and an improved slick shape η_i^{ik+1} can be obtained by solving Eq. (4.19) for successive points $(i = 1, \dots, N_{ow})$. A new underlying flow is then computed for the new slick interface, providing $\psi_{n_i}^{ik+1}$, and the whole process can then be repeated until convergence is reached on the slick shape between two given stages k and $k+1$, according to the criterion,

$$\text{MAX}_{(i=1, \dots, N_{ow})} \left| \frac{\eta_i^{ik+1} - \eta_i^{ik}}{\eta_i^{ik}} \right| \leq \epsilon \quad (4.21)$$

where ϵ is an *a priori* selected small number.

To eliminate sawtooth oscillations of the slick shape during the iterative process, it was found necessary to further transform Eq. (4.19) by replacing $\eta_i'^2$ in the left-hand-side by $\eta_i'^{k+1}\eta_i'^k$, i.e., combining the new updated values of η' at iteration $k + 1$ with the old calculated values at iteration k . Furthermore, to accelerate the convergence, as soon as recalculated, $\eta_i'^k$ values are replaced by $\eta_i'^{k+1}$ values. The final equation used for the FDE iterative calculation of slick shape thus reads, for ($i = 1, \dots, N_{ow}$),

$$\eta_i'^{k+1} = \frac{4(1-\varphi)p_{D_i}^k\eta_{i-1}^k - 3p_{D_i}^{k2} + 2p_{D_i}^kp_{D_{i-1}}^k + p_{D_{i-1}}^{k2} + (1-\varphi)\eta_{i-1}^{k2} + 2\varphi C_{f_i}^k(x'_i - x'_{i-1})}{3(1-\varphi)\eta_i'^k + 4(2-\varphi)p_{D_i}^k - 4p_{D_{i-1}}^k - 2(1-\varphi)\eta_{i-1}^k} \quad (4.22)$$

4.5 Friction coefficient calculation

According to the classical laminar Boundary Layer (BL) theory (e.g., Batchelor, 1967) applicable to smooth slender bodies like plates, the friction coefficient is a simple function of a Reynolds number Re based on the tangential velocity and the (arclength) distance s from the leading edge of the flow,

$$\text{Re} = \frac{U_{ws} s}{\nu_w} \quad (4.23)$$

where ν_w denotes the water kinematic viscosity. We have,

$$C_f = \frac{0.73}{\sqrt{\text{Re}}} = \epsilon (U_{ws}(s) s)^{-1/2} \quad \text{with } \epsilon = 0.73\sqrt{\nu_w} \simeq 0.00073 \quad (4.24)$$

For turbulent BL's, the literature gives the following forms for C_f ,

$$C_f = 0.0592 \text{Re}^{-1/2} \quad \text{or} \quad C_f = 0.027 \text{Re}^{-1/4} \quad (4.25)$$

Note that the latter equations do not exhibit a functional variation significantly different from Eq. (4.24).

First, assuming a very thin slick (hence $U_{ws} \simeq U$) and a small current velocity U , one can neglect dynamic effects along the slick (i.e., $U'_{ws} = 1$ and by Eq. (4.11), $p'_D = 0$). Hence, the slick shape due to pure friction can simply be found by integrating Eq. (4.16) as,

$$\eta'(x') = \left\{ \frac{\varphi}{1-\varphi} \int_0^{x'} C'_f(\xi) d\xi \right\}^{1/2} \quad (4.26)$$

Assuming $s \simeq x$ in Eq. (4.24), we further get,

$$\eta'(x') = \frac{\varphi}{1-\varphi} \sqrt{2\epsilon} x'^{1/4} \quad \text{and} \quad \eta'_{x'}(x') = \frac{\varphi}{1-\varphi} \sqrt{\frac{\epsilon}{8}} x'^{-3/4} \quad (4.27)$$

Eq. (4.27) predicts a slick shape which is both unbounded for large x' and has a vertical tangent at the leading edge ($x' = 0$).

Such results for the slick shape, however, are not realistic when compared to experiments. Furthermore, comparing the general variation of C_f given by Eq. (4.24), when $U'_{ws} = 1$, i.e. $C_f \propto s^{-1/2}$, to results calculated by Milgram and Van Houten [29] based on experiments, one can see that the true variation of C_f is much more complex along the slick, particularly in the headwave region, than predicted by this simplified (purely frictional) equation. In particular, in the experiments, C_f shows a sharp increase in front of the headwave, followed by a gradual decrease in the back of the headwave. Therefore, as concluded in [29], dynamic pressure does play an important role in determining slick shape in the headwave region. As will be shown from the computational results, U_{ws} exhibits significant variations in the headwave region and, hence, so does p'_D . This justifies using the complete iterative procedure Eqs. (4.20) -(4.22) to calculate the initial slick shape in the model, together with a representation of C_f better suited to the actual slick problem.

A more accurate prediction of C_f could be obtained by introducing a physical representation of the BL along the slick, including both laminar and turbulent regimes. This, however, would require a detailed solution of the Navier-Stokes equations in the BL, down to the scale of small geometric perturbations along the slick, together with some turbulent closure model. Due to the difficulties and uncertainties of such computations, however, at the end, one would not be guaranteed that the final values of C_f be closer to experimental values than the prediction of simple equations such as (4.24) or (4.25). Another approach is to define a semi-empirical representation of C_f along the slick, together with coefficients estimated based on experiments. The variation $C_f \propto x^{-1/2}$ obtained from above indicates that C_f should decrease from a large initial value, as x increases, and asymptotically tend to zero. This result, however, corresponds to a smooth flat boundary (like a plate), and one should expect, for a rough boundary, C_f to eventually reach a small but non-zero value, say C_{fo} , at the back of the slick. At the front of the slick, experiments show that C_f values are bounded and drop to zero at the slick leading edge. Combining these observations, the following equation is proposed for representing the variation of C_f along the slick,

$$\text{For } x \leq x_o: \quad C_f = \alpha x \exp(-\beta x^\gamma) \quad ; \quad \text{For } x \geq x_o: \quad C_f = C_{fo} \quad (4.28)$$

where coefficients α , β , γ , and C'_{fo} should be estimated based on experiments.

In Phase II, the only experiments giving details of the slick shape that could be found were those by Milgram and Van Houten [29]. Hence, these experiments were used to estimate values of the coefficients in Eq. (4.28) leading, after iterative computations, to a final slick shape $\eta(x)$ close to the experimentally measured shape. One such case is presented in the next section. In Phase III, however, new laboratory experiments will be carried out and will be used to better calibrate the present model. A deeper physical analysis of the functional variation of C_f along the slick will also be carried out to relate the coefficients in Eq. (4.28) to flow and slick geometry characteristics.

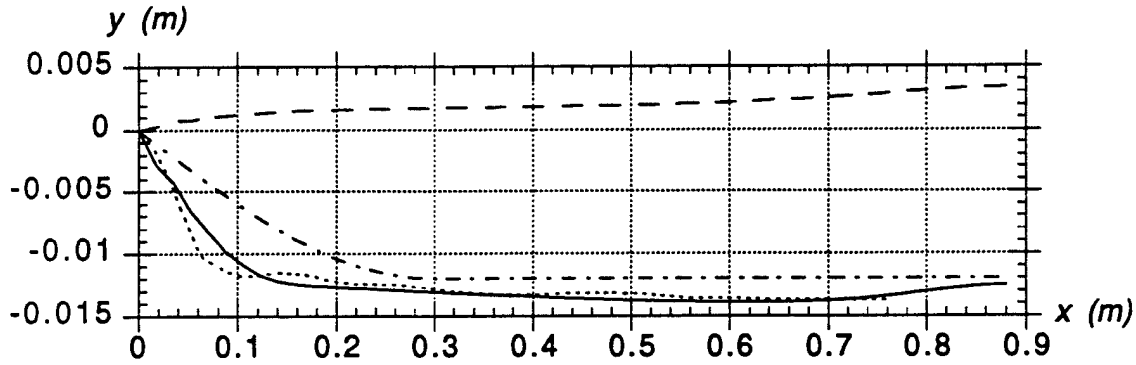


Figure 4.3: Computation of the quasi-steady shape of an oil slick with the BEM/FDE iterative method. The water density is $\rho_1 = 1000 \text{ kg/m}^3$, the oil density ratio is $\varphi = 0.88$ and the current upstream velocity is $U = 0.17 \text{ m/s}$. The friction coefficient is empirically modeled by Eq. (4.28), with $\alpha = 1.259$, $\beta = 250.0$, $\gamma = 2.5$, and $C_{fo} = 0.005$, for $x_o \simeq 0.18 \text{ m}$. The boom draft is $d = 0.175 \text{ m}$, the boom width is $w = 0.03 \text{ m}$, the water depth is $h = 0.53 \text{ m}$ and the slick length is $l = 0.88 \text{ m}$. The slick interface E-F was discretized in both the BEM and the FDE using $N_{ow} = 51$ nodes with initial uniform density. Convergence was reached after 150 iterations for $\epsilon = 10^{-8}$. Results show the interface $\eta(x)$: (---) initial shape based on Zalosh [42]; (—) final calculated shape; and (- - - -) experimental shape measured by Milgram and Van Houten [29]. Results also show the free surface shape (- . . . -) $q(x) - \eta(x)$.

4.6 Numerical results

Milgram and Van Houten [29] reported laboratory experiments for the geometry of slick contained by booms subjected to water currents of different intensity U (Fig. 4.2). Measuring the slick shape and using equations (4.1)-(4.4), they calculated the variation of the friction coefficient $C_f(x)$ along the slick.

In the present application, in order to validate the BEM/FDE procedure developed for iteratively calculating the initial quasi-steady shape of contained a oil slick, we selected a case in Milgram and Van Houten's experiments for which the current velocity was just slightly super-critical and the slick interface geometry was quite smooth. Unfortunately, no result for lower velocities were reported in their study. Using Eq. (4.28) together with the iterative procedure Eqs. (4.20)-(4.22), we then estimated the best values of coefficients α , β , γ , and C_{fo} , that led to a slick shape close to the measured one.

Physical parameters for the selected case were : the water density $\rho_1 = 1000 \text{ kg/m}^3$, the oil density ratio $\varphi = 0.88$, and the current upstream velocity is $U = 0.17 \text{ m/s}$. For these values, using the standard value of the interfacial tension, the linear analysis reported above (Eqs. (2.33) and (2.34)) leads to a critical wavelength of instability $\lambda^{min} = 0.028 \text{ m}$ and a corresponding critical velocity $U_{cr}^{min} = 0.15 \text{ m/s}$. Hence, in this case, the KH instability on the slick interface should start developing at a very slow growth rate. The laboratory experiments were conducted with a boom draft $d = 0.175 \text{ m}$, a boom width $w = 0.03 \text{ m}$, a

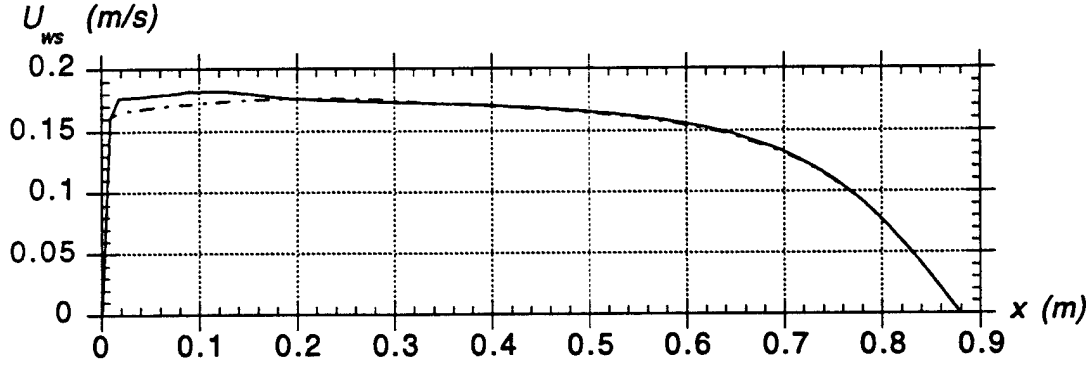


Figure 4.4: Same computations as in Fig. 4.3. Results show the interface tangential velocity $U_{ws}(x)$ computed with the BEM method for : (— - —) the initial shape based on Zalosh [42]; (——) the final calculated shape.

water depth $h = 0.53$ m, and a slick length $l \simeq 0.88$ m.

These dimensions and the above physical parameters were closely reproduced in the present computations. In the BEM/FDE procedure, $N_{ow} = 51$ nodes with initial uniform density were defined along the slick interface E-F (Fig. 4.2). In the BEM calculations, more nodes were used along the rest of the boundary and quadratic isoparametric elements were used for the interpolation. The initial slick shape $\eta^o(x)$ was selected following a method similar to Zalosh's and is given in Fig. 4.3.

Many different computations were performed in order to calculate the best values of the coefficients in Eq. (4.28). The final values found for these coefficients were : $\alpha = 1.259$, $\beta = 250.0$, $\gamma = 2.5$, and $C_{fo} = 0.005$. [Note that the location x_o was simply selected such that C_f take the value C_{fo} in the first part of Eq. (4.28); this led to $x_o \simeq 0.18$ m.] For an accuracy $\epsilon = 10^{-8}$, the final BEM/FDE run converged after 150 iterations. The converged slick shape is given in Fig. 4.3, as compared to the experiments. With the selected coefficients, the overall agreement between experiments and computations is quite good, although the experimental slick shape exhibits small fluctuations, particularly in the headwave region, likely indicating the initiation of an instability. Note the low value $C_f = C_{fo}$ in the back of the slick, indicating that friction is quite small and thus confirming that the interface shape is very smooth in this region. Experimental results were not available close to the boom. In the computations, however, due to the stagnation point for the flow at the boom, leading to a zero tangential velocity, friction along the interface gradually drops to zero and the dynamic pressure increases, which leads to a reduction of the slick thickness at the boom. As a further indication of this, Fig. 4.4 gives the variation of the tangential velocity computed along the slick and one can see that the largest differences between velocities calculated for the first and last iterations occur in the headwave region, for $x < x_o$. Finally, as a result of the quasi-hydrostatic force balance within the slick, the free surface location $[q(x) - \eta(x)]$, calculated by Eqs. (4.3) or (4.13), gradually raises up from the slick leading edge to the boom (see Fig. 4.3).

Chapter 5

Effects of interfacial friction on vorticity updating equation

5.1 Introduction

In the inviscid VS models presented in Chapters 2 and 3 (i.e., PCVS and CVS models), the interface between two fluids of density (ρ_o, ρ_1) and velocity (u_o, u_1) was treated as a continuous thin layer separating two potential flows, and the entire vorticity originated from the velocity jump $|u_o - u_1|$ across this interface was concentrated within the thin region in vortex sheet (Fig. 5.1).

In the models, the equations used to derive the vorticity updating Eq. (2.7), assumed that the interface itself satisfied both kinematic and dynamic conditions, the former representing the compatibility of motions of the sheet with respect to each fluid and the latter expressed as a pressure equilibrium on both sides of the interface/VS (i.e., in each ideal fluid), with correction for the interfacial tension induced pressure jump. Thus, all external forces and flow parameters, such as velocity, buoyancy, density difference, and surface tension, were expressed in terms of circulation change on the right-hand side of Eq. (2.7).

Experimental observations, however, show that interfacial friction plays a key role in determining the quasi-static geometry of the interface and its time evolution (e.g., Milgram and Van Houten [29]), especially in the headwave region. In Chapter 4, we presented a method to calculate the initial quasi-steady state shape of a contained oil slick, that includes friction effects. To correctly study the time evolution of such an interface, it is thus necessary to also include friction effects in the vorticity updating Eq. (2.7).

In the present Chapter, we show how this can be done. Actual implementation, test, and use of the new equation, however, will take place during Phase III studies.

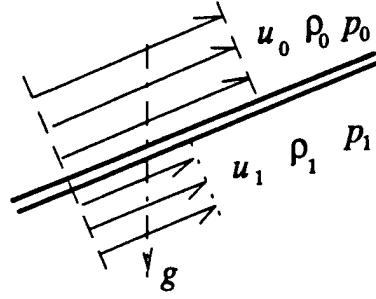


Figure 5.1: Sketch of inviscid interface/VS equilibrium

5.2 Governing equations

Friction will affect the balance of forces at the interface/VS. In our model, friction effects will be represented by equivalent tangential interfacial shear stresses (τ_o, τ_1), acting in the fluids on either side of the interface. Combined to pressures (p_o, p_1), these stresses will have to satisfy the dynamic equilibrium equation at the interface.

Following classical Boundary Layer (BL) theory, friction will be assumed to be important only in two small regions (i.e. BL's), on either side of the interface, in which viscosity dominates and velocity profiles have smooth tapered transitions. Outside of these BL regions, the fluids will still be assumed to behave as inviscid irrotational fluids. This is sketched in Fig. 5.2, where the velocity diagrams have been tapered in (thicker) BL regions on both sides of the thin interface. In these two BL's vorticity diffusion is assumed to occur in the normal direction across the interface and vorticity convection to occur in the tangential direction, both contributing to the equivalent shear stresses (τ_o, τ_1) acting on each side of the interface.

Note that friction becomes an external force acting on the interface only when a velocity jump still occurs at the interface, as sketched in Fig. 5.2, and the potential flows in fluids 0 and 1 are kept slightly away from the interface by the BL's thickness. Taking control volume elements on both sides of the interface (Zalosh [43], Rottman and Olfe [36], Grilli *et al.* [16, 17]), the rate of change of circulation on the VS can be derived under the combined action of gravity, surface tension, and friction effects at the interface between two fluids. This will first be done for a vortex sheet represented by piecewise constant vorticity elements.

Taking the material time derivative of equation (2.5), in which circulation is defined as a function of the tangential velocity jump at the VS, we get, for a VS element of length Δs_i over which velocity is assumed constant and the geometry to be smoothly varying,

$$\frac{D \Gamma}{D t}(s_i) \equiv \frac{D \Gamma_i}{D t} = \int_{s_i - \Delta s_i/2}^{s_i + \Delta s_i/2} \left(\frac{D u_{os}}{D t} - \frac{D u_{1s}}{D t} \right) ds \simeq \left(\frac{D u_{os}}{D t} - \frac{D u_{1s}}{D t} \right)_i \Delta s_i \quad (5.1)$$

For Newtonian fluids, tangential accelerations in (5.1) can be expressed, for both fluids

0 and 1, using Navier-Stokes' equations as,

$$\frac{D \mathbf{u}_{o,1}}{Dt} = -\frac{1}{\rho_{o,1}} \nabla p_{o,1} - g \nabla y + \frac{1}{\rho_{o,1}} \nabla \cdot (\mu_{o,1} \nabla \mathbf{u}_{o,1}) \quad (5.2)$$

in which p is the fluid pressure (discontinuous across the interface due to surface tension), g is the acceleration of gravity (vertical pointing in the downward y direction), and μ denotes the dynamic molecular velocity, with the last term in parenthesis representing the fluid stress tensor.

Taking the dot product of Eq. (5.2) with the tangential vector \mathbf{s} (defined as in Eq. (2.4)), we get,

$$\frac{D u_{os,1s}}{Dt} = -\frac{1}{\rho_{o,1}} \frac{\partial p_{o,1}}{\partial s} - g \sin \beta + \frac{1}{\rho_{o,1}} \nabla \cdot (\mu \nabla u_{os,1s}) \quad (5.3)$$

Now, in the BL's on both sides of the VS (sketched in Fig. 5.2), we assume velocity changes in the normal direction to be dominant over changes in the tangential direction. Hence, defining the Newtonian interfacial shear stresses as,

$$\tau_{os,1s} = -\mu_{o,1} \frac{\partial u_{os,1s}}{\partial n} \quad (5.4)$$

with n denoting the normal direction at the interface pointing outside of each fluid region, we get,

$$\frac{D u_{os,1s}}{Dt} \simeq -\frac{1}{\rho_{o,1}} \frac{\partial p_{o,1}}{\partial s} - g \sin \beta - \frac{1}{\rho_{o,1}} \frac{\partial \tau_{os,1s}}{\partial n} \quad (5.5)$$

The normal gradients of shear stresses at the interface in Eq. (5.5) will be approximated using equivalent interfacial shear stresses defined, within each BL region, with opposite directions on each side of the interface (Fig. 5.2) as,

$$\tau_{o,1} = \mp h_{o,1} \frac{\partial \tau_{os,1s}}{\partial n} \quad (5.6)$$

where h_o and h_1 denote vorticity diffusion thicknesses. [Note that this corresponds to assuming shear stresses go to zero at distances $h_{o,1}$ on either side of the interface.] We thus get,

$$\frac{D u_{os,1s}}{Dt} \simeq -\frac{1}{\rho_{o,1}} \frac{\partial p_{o,1}}{\partial s} - g \sin \beta \pm \frac{\tau_{o,1}}{\rho_{o,1} h_{o,1}} \quad (5.7)$$

Replacing tangential accelerations from Eq. (5.7) into Eq. (5.1), we get,

$$\frac{D \Gamma_i}{Dt} = \left(\frac{1}{\rho_1} \frac{\partial p_1}{\partial s} - \frac{1}{\rho_o} \frac{\partial p_o}{\partial s} + \frac{\tau_o}{\rho_o h_o} + \frac{\tau_1}{\rho_1 h_1} \right)_i \Delta s_i \quad (5.8)$$

From the definition of the *sheet velocity*, \mathbf{u} , the tangential acceleration following the vortex sheet motion is obtained as,

$$\frac{du_{si}}{dt} = \frac{1}{2} \left(\frac{du_{os}}{dt} + \frac{du_{1s}}{dt} \right)_i \quad (5.9)$$

with, according to the definitions of different material derivatives,

$$\frac{d}{dt} = \frac{D}{Dt} \pm \frac{1}{2}(\mathbf{u}_o - \mathbf{u}_1) \cdot \nabla \quad (5.10)$$

with the plus sign being taken in fluid 1 and the minus sign in fluid 0. Replacing Eq. (5.10) in (5.9), we get,

$$\frac{du_{si}}{dt} = \frac{1}{2} \left(\frac{D u_{os}}{Dt} + \frac{D u_{1s}}{Dt} \right)_i - \frac{1}{4} (u_{os} - u_{1s})_i \left(\frac{\partial u_{os}}{\partial s} - \frac{\partial u_{1s}}{\partial s} \right)_i \quad (5.11)$$

Using Navier-Stokes equations (5.7) to express tangential velocities and Eq. (2.3) to express the vortex sheet strength, we get,

$$\frac{du_{si}}{dt} = -\frac{1}{2} \left(\frac{1}{\rho_o} \frac{\partial p_o}{\partial s} + \frac{1}{\rho_1} \frac{\partial p_1}{\partial s} + 2g \sin \beta + \frac{\tau_1}{\rho_1 h_1} - \frac{\tau_o}{\rho_o h_o} \right)_i - \frac{1}{4} \gamma_i \frac{\partial \gamma_i}{\partial s} \quad (5.12)$$

From the expression of surface tension effects at the interface between two fluids (Batchelor, 1967), the pressure jump across the vortex sheet is given by,

$$p_o - p_1 = \sigma_{o1} \frac{1}{\mathcal{R}} \quad (5.13)$$

in which $1/\mathcal{R}(s)$ is the sheet curvature. In curvilinear coordinates, it can easily be shown that the curvature is identical to, $\partial \beta / \partial s$. Hence, taking the tangential derivative of (5.13), we get,

$$\frac{\partial p_o}{\partial s} - \frac{\partial p_1}{\partial s} = \sigma_{o1} \frac{\partial^2 \beta}{\partial s^2} \quad (5.14)$$

Eliminating the pressure between equations (5.8), (5.12), and (5.14), we finally get the rate of change of circulation at point s_i of the sheet as,

$$\begin{aligned} \frac{D \Gamma_i}{Dt} &= 2 \Delta s_i \left(\kappa \left[\frac{du_{si}}{dt} + g \sin \beta_i + \frac{1}{4} \gamma_i \frac{\partial \gamma_i}{\partial s} + \frac{1}{\rho_1(1-\varphi)} \left(\frac{\tau_{oi}}{h_o} + \frac{\tau_{1i}}{h_1} \right) \right] \right. \\ &\quad \left. - \frac{\sigma'_{o1}}{1+\varphi} \frac{\partial^2 \beta_i}{\partial s^2} \right) \end{aligned} \quad (5.15)$$

where $\sigma'_{o1} = \sigma_{o1}/\rho_1$, $\varphi = \rho_o/\rho_1 \leq 1$, $\kappa = (1-\varphi)/(1+\varphi)$ is the Atwood number and, by (2.4),

$$\frac{du_{si}}{dt} = \frac{du_i}{dt} \cos \beta_i + \frac{dv_i}{dt} \sin \beta_i \quad (5.16)$$

is the tangential acceleration at point i .

Various approaches can be pursued to model the interfacial shear stresses in Eq. (5.15) as a function of the flow kinematics and, ultimately, of the circulation on the VS. Laminar or turbulent BL theories, for instance, can provide a representation of shear stresses based on a combination of diffusion and convection in the BL's. The simplest global approach,

however, consists in representing the turbulent shear stresses using a semi-empirical friction coefficient, on a way similar to Eq. (4.4). In the present case, this method would give,

$$\tau_{o,1} = \frac{1}{2} \rho_{o,1} C_{fo,f1} (u_{os,1s} - u_s) |u_{os,1s} - u_s| \quad (5.17)$$

in which the relative velocity between the tangential flow velocity in each fluid $u_{os,1s}$ and the VS's tangential velocity u_s has been used. Using the definition of the VS's velocity u_s and Eq. (2.3), Eq. (5.17), for vortex element i , transforms into,

$$\tau_{oi,1i} = \pm \frac{1}{2} \rho_{o,1} C_{fo,f1} \gamma_i^2 \quad (5.18)$$

Now, with the above definition, the *effect of interfacial friction* on the rate of change of vorticity in Eq. (5.15) reads,

$$\frac{1}{\rho_1(1-\varphi)} \left(\frac{\tau_{1i}}{h_1} + \frac{\tau_{oi}}{h_o} \right) = \frac{1}{8(1-\varphi)} \gamma_i^2 \left(\varphi \frac{C_{fo}}{h_o} - \frac{C_{f1}}{h_1} \right) \quad (5.19)$$

Hence, the final equation for the rate of change of vorticity reads,

$$\begin{aligned} \frac{D \Gamma_i}{D t} = & 2 \Delta s_i \left(\kappa \left[\frac{du_{si}}{dt} + g \sin \beta_i + \frac{1}{4} \gamma_i \frac{\partial \gamma_i}{\partial s} + C_f \gamma_i^2 \right] \right. \\ & \left. - \frac{\sigma'_{o1}}{1+\varphi} \frac{\partial^2 \beta_i}{\partial s^2} \right) \end{aligned} \quad (5.20)$$

in which we have defined as,

$$C_f = \frac{1}{8(1-\varphi)} \left(\varphi \frac{C_{fo}}{h_o} - \frac{C_{f1}}{h_1} \right) \quad (5.21)$$

the global friction coefficient between fluid 0 and 1 at the VS interface.

During Phase III studies, this and other models of representation of friction at the oil-water interface will be developed, validated, and tested. In particular, using newly obtained experimental data, computations with the model will be calibrated to represent experimental measurements at best, for the geometry of a contained oil-slick as a function of time. Such calibrations will take place through the semi-empirical representation of the friction coefficient C_f along the oil-water interface (see also Chapter 4 for more discussions on this subject).

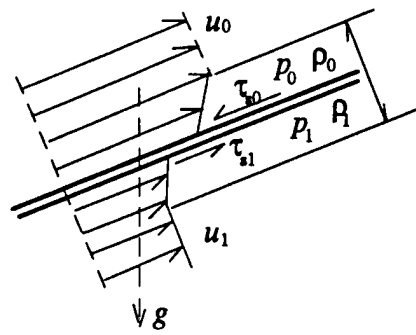


Figure 5.2: Sketch of interface/VS equilibrium including friction effects

Chapter 6

Conclusions

Following initial studies and model developments reported for Phase I studies (Grilli *et al.* [16]), model developments in Phase II studies have focused on three major aspects : (i) improving and complementing the models developed in Phase I, namely both periodic and non-periodic Piecewise Constant Vortex Sheet (PCVS) models (Chapter 2); (ii) provide a better representation of hydrodynamic instabilities in the oil containment problem by developing and implementing a more accurate model based on Continuous Vortex Sheets (CVS) (Chapter 3); and (iii) both implementing and validating a numerical method for calculating the quasi-steady equilibrium shape of an oil-slick including the effects of interfacial friction (Chapter 4), and developing a formalism to include interfacial friction effects in the Vortex Sheets (VS) time updating equations (which were ignored in Phase I model) (Chapter 5).

As a result of such model development/improvements, model applications carried out during Phase II provided more quantitative analyses and predictions than the qualitative descriptions of the oil containment behavior achieved during Phase I.

More specifically, in Chapter 2, we presented the development/improvements of PCVS periodic and non-periodic models and their application to *periodic KH instability* and *oil containment by a boom*, respectively. Figs. 2.9-2.12, for instance, show the quantitative influence of interfacial velocity jump ΔU , gravity g , fluid density ratio φ , and surface tension coefficient σ_{o1} , on the growth rate of *KH interfacial instability*, as computed with the periodic PCVS model. Throughout these computations, the improved Phase II periodic PCVS model performed very well and was thus validated as a tool for predicting interfacial behavior during KH instability. More specifically, using the PCVS model, it was found,

- (i) in the presence of gravity, the interface is subjected to stabilizing effects from buoyancy forces and the disturbance growth is slowed as compared to an identical case when gravity effects are not included;
- (ii) an increase in fluid density difference across the interface will result in reducing and slowing down the disturbance growth on the interface; the most unstable case is thus a case with two identical fluids ($\varphi = 1$) or, in the present case, the heavier oil;
- (iii) and an increase in surface tension at the interface also results in reducing and slowing

down the disturbance growth on the interface; this is because surface tension, to some extent, balances the circulation accumulation in the highly curved regions of the interface.

Based on the result in (ii), one can thus postulate that, for an oil slick contained by a boom, the headwave instability growth rate will be smaller and the instability will be delayed when using a lighter oil, compared to the case of a heavier (or weathered) oil. In laboratory experiments with oil/boom systems, it is observed that the oil-water interface, at first, rolls-up in the headwave region before pieces of the interface are torn off (e.g., Delvigne [9]). Therefore, based on the results in (iii), it is theoretically expected that, if surface tension is naturally (e.g., through weathering) or artificially (e.g., through chemicals) increased, the disturbance growth on the interface will be reduced and the interface break up and resulting containment failure will be accordingly delayed (or eliminated), hence, providing additional time for collecting oil at a given (unstable) relative velocity.

In the light of the above results, in subsequent studies, particularly during Phase III, the quantitative influence of density difference and surface tension on the oil-water interface evolution, will be studied for complete oil-boom systems. Along this line, Figs. 2.13, 2.14, and 2.15, for instance, showed computational results of the non-periodic PCVS model for the *entrainment and critical accumulation* failure modes of contained oil slicks. Despite their realism, at this stage, however, such results only show the ability of the PCVS model to capture the underlying physics and predict the unstable shape of a contained oil slick. Indeed, these results still use the empirical method by Zalosh [42] to estimate the *initial shape* of the slick, and also do not include *interfacial friction* effects which have an important influence on slick geometry and thickness. After integrating in this model the initialization of the slick shape, presented in Chapter 4, and the inclusion of frictional effects in the vorticity updating equation, presented in Chapter 5, more quantitatively realistic similar computations will be performed during Phase III, using the more accurate CVS model, presented in Chapter 3 for the velocity calculations. Model parameters will then be calibrated based on newly obtained experimental data.

In Chapter 3, we presented the development, validation, and application of a *new CVS model*. By contrast with the PCVS model, in order to achieve better accuracy and stability, this model uses higher-order spatial discretizations (cubic) for both the geometry and the computational fields along the oil-water interface. As a result, integrals in Biot-Savart equations (2.1) must be calculated numerically. This required the development of accurate integration methods for hypersingular integrals. Looking at Fig. 3.3, for instance, it can be seen that, with the CVS model, the periodic Kelvin-Helmholtz instability at an oil-water interface and the subsequent roll-up of Vortex Sheets were very accurately modeled, and for a much longer time, than when using the PCVS model. Validation cases for a simple uniform flow also showed that the CVS model provides much more accurate results for the velocities than the PCVS model, particularly for domain geometries with very high aspect ratio (as in containment of oil by a boom). This, hence, justifies the development of the CVS model. This model will be more extensively used during Phase III studies.

In Chapter 4, we presented a model and applications for calculating the *quasi-steady-*

state initial shape of a contained oil slick. Quasi-hydrostatic equilibrium was assumed in the oil slick and the external water flow velocity was computed for a specified geometry of the oil-water interface. An iterative method was used to calculate the interface shape satisfying interfacial equilibrium equations. The interfacial friction coefficient C_f was semi-empirically modeled. Looking at Fig. 4.3, for instance, it can be seen that the initial stable shape of an oil slick, measured by Milgram and Van Houten [29] in their laboratory experiments, was correctly recalculated using the PCVS model. This model will be used during Phase III studies to calculate the initial stable shape of contained oil slicks, for low tow velocities, which will then be used to initialize the VS model(s) calculating the interfacial instabilities and slick containment failures occurring for larger tow velocities.

Finally, in Chapter 5, we developed modified vorticity updating equations (5.20) and (5.21), including the effects of interfacial friction. These equations will be implemented and tested during Phase III studies in order to more accurately and quantitatively calculate the containment failure of an oil slick, whose shape will have been initialized using the model developed in Chapter 4.

Bibliography

- [1] Agrawal, R.K. and Hale, L.A. 'A new criteria for predicting head wave instability of an oil slick by a barrier', *Proc. Offshore Tech. Conf.*, Dallas, Texas, pps. 461-466, 1974.
- [2] Bai, K.J. and Kim, J.W. 'A computational model for flow around an oil boom', *Proc. Workshop on Tidal and Oil Spill Modeling*, 5-17, 1993.
- [3] Baker, G.R. and M.J., Shelley 'On the connection between thin vortex layers and vortex sheets.' *J. Fluid Mech.*, **215**, 161-194, 1990.
- [4] Batchelor, G. K., *An introduction to fluid dynamics* Cambridge University Press, 1967.
- [5] Benjamin, T.B. 'Gravity currents and related phenomena', *J. Fluid Mech.*, **31** (2), 209-248, 1968.
- [6] Brebbia, C.A., *The Boundary Elements for Engineers* John Wiley and Sons, 1978.
- [7] Clavelle, E.J. and Rowe, R.D. 'Numerical simulation of oil-boom failure by critical accumulation', *Arctic Marine Oil Spill Prog. Tech. Seminar*, 409-418, 1993.
- [8] Cross, R.H. and Hoult, D.P. 'Oil booms in tidal currents', *J. Waterways, Port. Coastal Ocean Engng.*, **98**, 1745-1758, 1972.
- [9] Delvigne, G.A.L. 'Barrier failure by critical accumulation of viscous oil', *Proc. Oil Spill Conf.*, USEPA, USCG, and Amer. Petrol. Inst., pps. 143-148, 1989.
- [10] Di Pietro, N. D. and Cox, R. G. 'The containment of an oil slick by a boom placed across a uniform stream', *J. Fluid Mech.*, **96**, 613-640, 1980.
- [11] Drazin, P.G. 'Kelvin-Helmholtz instability of finite amplitude', *J. Fluid Mech.*, **42**, 321-335, 1970.
- [12] Drazin, P.G. and Howard, L.N. 'Hydrodynamic stability of parallel flow of inviscid fluid', *Advanc. Applied Mech.*, **9**, 1, 1966.
- [13] Ertekin, R.C. and Sundararaghavan, H. 'The calculation of the instability criterion for a uniform viscous flow past a boom', *J. Offshore Mech. Artic Engng.*, **117**, 24-29, 1995.
- [14] Fink, P.T. and Soh, W.K. 'Calculation of vortex sheets in unsteady flow and application in ship hydrodynamics', *Proc. 10th Symp. on Naval Hydrodynamics*, Office of Naval Res., Washington, D.C., 463-491, 1974.
- [15] Guiggiani, M., Krishnasamy, G., Rudolph, T.J., and F.J. Rizzo 'A general algorithm for the numerical solution of hypersingular boundary integral equations.' *Trans. ASME*, **59**, 604-614, 1992.
- [16] Grilli, S.T., Hu, Z., and Spaulding, M.L. 'A hydrodynamic model of oil containment by a boom : Phase I', *Final Technical Report for DOT Grant No. DTRS57-94-G-00076*, Dept. Ocean Engng., Univ. of Rhode Island, 70pps, 1996.

- [17] Grilli, S.T., Hu, Z., and Spaulding, M.L. 'Numerical modeling of oil containment by a boom', *Proc. 19th Arctic and Marine Oilspill Program Technical Seminar (AMOP)*, 6/96, Calgary, Alberta, Canada, pps. 343-376. Environment Canada, 1996.
- [18] Grilli, S.T. and Subramanya, R. 'Recent advances in the BEM modelling of nonlinear water waves'. Chapter 4 in *Boundary Element Applications in Fluid Mechanics* (ed. H. Power), pps. 91-122. Advances in Fluid Mechanics Series. Computational Mechanics Publication, Southampton, UK, 1995.
- [19] Grilli, S.T. and Subramanya, R. 'Quasi-singular Integrations in the Modelling of Nonlinear Water Waves.' *Engng. Analys. with Boundary Elements*, 13(2), 181-191, 1994.
- [20] Grilli, S.T. and Subramanya, R. 'Numerical modeling of wave breaking induced by fixed or moving boundaries.' *Computational Mechanics* 17(6), 374-391, 1996.
- [21] Grilli, S.T. and I.A., Svendsen 'Corner Problems and Global Accuracy in the Boundary Element Solution of Nonlinear Wave Flows.' *Engng. Analys. with Boundary Elements*, 7(4), 178-195, 1990.
- [22] Johnston, A.J., Fitzmaurice, M.R. and Watt, R.G. 'Oil spill containment : viscous oils', *Proc. Oil Spill Conf. (USEPA, USCG)*, Amer. Petrol. Inst., pps. 89-94, 1993.
- [23] Jones, W. T. 'Instability at an interface between oil and flowing water', *J. of Basic Engng.*, 94, 874-878, 1972.
- [24] Krasny, R. 'A study of singularity formation in a vortex sheet by the point-vortex approximation.' *J. Fluid Mech.*, 167, 65-93, 1986.
- [25] Kelvin, Lord *Mathematical and Physical Papers* 4 76-100, Cambridge University Press, 6th edition, 1910.
- [26] Lamb, H. *Hydrodynamics* Cambridge University Press, 6th edition, 1932.
- [27] Lau, Y.L. and Kirchfer, S.A. 'A review of the dynamics of contained oil slicks in flowing water', *J. Hydraulics Div.*, 1974.
- [28] Leibovich, S. 'Oil slick instability and the entrainment failure of oil containment booms', *J. Fluids Engng.*, 98, 98-105, 1976.
- [29] Milgram, J.H. and Van Houten, R.J. 'Mechanics of a restrained layer of floating oil above a water current', *J. Hydronautics*, 12 (3), 93-108, 1978.
- [30] Meiron, D.I., Baker, G.R., and S.A. Orszag 'Analytic structure of vortex sheet dynamics. Part 1. Kelvin-Helmholtz Instability.' *J. Fluid Mech.*, 114, 283-298, 1982.
- [31] Moore, D.W. 'A numerical study of the roll-up of a finite vortex sheet.' *J. Fluid Mech.*, 63(2), 225-235, 1974.
- [32] Moore, D.W. 'The spontaneous appearance of a singularity in the shape of an evolving vortex sheet.' *Proc. Roy. Soc. London*, A365, 105, 1979.
- [33] Rangel, R.H. and Sirignano, W.A. 'Nonlinear growth of Kelvin-Helmholtz instability : Effect of surface tension and density ratio', *Phys. of Fluids*, 31 (7), 1845-1855, 1988.
- [34] Rangel, R.H. and Sirignano, W.A. 'The linear and nonlinear shear instability of a fluid sheet', *Phys. of Fluids*. A3 (10), 2392-2400, 1991.
- [35] Rosenhead, L. 'The formation of vortices from a surface of discontinuity.' *Proc. Roy. Soc. London*, A134, 170-192, 1931.
- [36] Rottman, J. W. and Olfe, D.B. 'Comment on "discretized simulation of vortex sheet evolution with buoyancy and surface tension effects" ', *J. AIAA* 15, 1214-1215, 1977.

- [37] Van de Vooren, A.I. 'Numerical investigation of the rolling-up of vortex sheets', *Proc. R. Soc. Lond.*, A 373, 67-91, 1980.
- [38] Von Karman T., 'The engineer grapples in the nonlinear problems', *Bull. Am. Math. Soc.* 46, 615-586, 1940.
- [39] Wicks, M. 'Fluid dynamics of floating oil containment by mechanical barriers in the presence of water currents', *Proc. API-FWPCA Joint Conf. on Prevention and Control of Oil Spills*, New York, Dec 15-17, Amer. Petrol. Inst., pps. 55-106, 1969.
- [40] Wilkinson, D. L. 'Dynamics of contained oil slicks', *J. Hydraulics Div.*, 98, 1013-1031, 1972.
- [41] Wilkinson, D. L. 'Limitations to length of contained oil slicks', *J. Hydraulic Div.*, 99, 701-713, 1973.
- [42] Zalosh, R.G. 'A numerical model of droplet entrainment from a contained oil slick', *Report No. CG-D-65-75*, DOT/USCG, 1974.
- [43] Zalosh, R.G. 'Discretized simulation of vortex sheet evolution with buoyancy and surface tension effects', *J. AIAA*, 14, 1517-1523, 1976.
- [44] Zalosh, R.G. and Jensen, D.S. 'A numerical model of droplet entrainment from a contained oil slick', *Proc. Fluid Mech. in Petrol. Indus.*, ASME, 17-27, 1975.
- [45] Zaroodny, S.J. and Greenberg, M.D. 'On a vortex sheet approach to the numerical calculation of water waves', *J. Comp. Phys.*, 11, 440-446, 1973.

DEVELOPMENT OF A RAPID CURRENT CONTAINMENT BOOM: PHASE II

M.R. Swift, B. Celikkol, P. Coyne, R. Steen, and M. Ozyalvac, University of New Hampshire

I. INTRODUCTION

CONTAINMENT PROBLEM

Conventional oil booms have been an essential tool in major oil spill recovery operations, but they are limited by currents. When the perpendicular component of relative current speed exceeds a critical value, oil entrainment occurs at the head of the restrained oil pool, and the boom fails due to leakage. The critical velocity, for the perpendicular component of current, normally has been found to be 0.6 - 1.0 knots depending on the oil properties.

This limitation poses a serious problem since tidal currents can exceed critical values in the approaches and/or harbors of major ports in the Northeast such as Portland, Portsmouth, Boston and New York. Currents in western rivers pose similar problems. Besides difficulty using fixed conventional booms, boom leakage also compromises the use of oil booms in oil boom/skimming operations. The sweeping speed of towed booms used to funnel oil to a skimmer is considerably restricted by leakage.

One approach to circumventing the problem is to angle the boom to the current thus reducing the perpendicular component. The oil is not contained in a pocket, but is instead deflected to a recovery point. This diversion boom approach has been developed for use in the Piscataqua River/Great Bay system, as described by Swift et al. (1990, 1991, 1992). Diversion boom experiments have been conducted at the five petroleum product terminals along the NH side of the Piscataqua - a tidal river having peak currents over 5 knots. The logistical problems which arise in deploying long lengths of angled boom, however, become severely limiting. As a practical solution, new oil boom design concepts need to be developed that at least double the critical velocity.

The purpose of the study described here is to develop oil slick barriers for rapid current operation. This report covers the second year effort (Phase II) in investigating the use of submergence plane concepts for the design and construction of floating containment systems. Laboratory studies involving 2-dimensional physical models (initiated in Phase I) were completed, and the results were applied to the development of 3-dimensional physical models and full scale systems.

PREVIOUS WORK

When floating oil is restrained by a conventional oil boom in the presence of relative current, a "headwave" forms near the leading edge of the slick as described, for example, by Wicks (1969), Agrawal and Hale (1974) and Milgram and van Houton (1978). Though the fluid dynamic processes are still the subject of research, it is known that instabilities and/or turbulence will entrain oil droplets from the headwave thus

initiating boom leakage. More recently, Delvigne (1989) has described an unstable reduction of the restrained slick termed "failure by critical accumulation". He has also summarized known laboratory studies which all indicate that boom failure occurs at less than 1 knot.

The current-induced failure mechanisms are avoided by the barrier configuration shown in Fig. 1. In this concept, the oil is not restrained by a single barrier as a pool exposed to the incident current. Instead, the oil moves down the inclined submergence plane and is trapped in a protected containment region. Research by Bianchi and Henry (1973) indicates that the concept will retain oil at relative velocities above 2 knots. This concept has been further developed by JBF Scientific, Inc. and (independently) by LPI Corp. for the purpose of designing oil skimmers. The overall goal of the research program discussed here, on the other hand, was to return to the fundamental idea in order to develop an oil barrier system capable of superior fast current performance.

The concept is consistent with and closely related to observations by Delvigne (1984) and Johnston et al. (1993) regarding closely spaced double booming (two booms deployed parallel to each other with a small separation distance). They noted that oil becomes trapped between the booms (in a slowly rotating back eddy) at incident current speeds that would normally cause leakage. In addition, a similar trapping process can happen when oil flows under ice as described by Cox et al. (1980).

FIRST YEAR DEVELOPMENT

The first year (Phase I) University of New Hampshire (UNH) study consisted primarily of developing the Fig. 1 concept in a well-ordered sequence of laboratory experiments. Tests were conducted using 2-dimensional physical models in a 40 foot recirculating flume. The system employs two variable speed impellers to drive the flow through the test section which has one side made of clear plastic allowing visual observation, photography and optical fluid velocity measurement. This "dirty water" facility is dedicated to oil spill research at UNH.

Two-dimensional shapes of trial cross-sections were used to minimize scaling effects. With the 2-dimensional approach, the cross-section configurations are about the size of the expected harbor/estuary design. Retention tests were done using oils and oil substitutes, and results were interpreted in terms of both direct observations and appropriate non-dimensional parameters.

The first set of experiments were carried out to evaluate design parameter changes in the initial Fig. 1 configuration. Tests were done using 1/16 inch beads, having specific gravities ranging from 0.89 - 0.96, to represent the "slick". These exploratory experiments were done for comparison purposes only. Results showed the best retention was obtained when the submergence plane is at a very shallow angle and the second barrier is spaced far enough to minimize flow interaction. Retention was

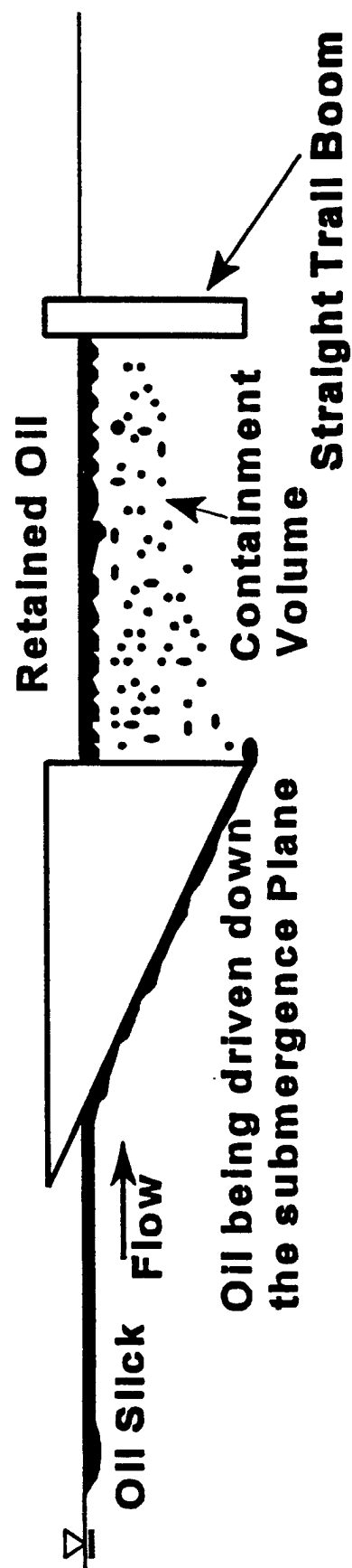


Fig. 1 Initial submergence plane/containment volume concept.

also found to be very sensitive to specific gravity. Next, flow control devices, such as baffles and scoops were tried to enhance flow of the "slick" into the quiescent containment region and to prevent washing out of the trapped oil by the current beneath the containment region. It was found that a horizontal baffle below the containment region was effective.

The subsequent series of experiments made use of vegetable, synthetic and petroleum oils. Tests showed that the modified configuration shown in Fig. 2 has the most potential for development into an effective 3-dimensional barrier. This configuration was subject to a comprehensive set of retention experiments using different oils having properties which span the range of those likely to be spilled. Tests were done at a flume speed of 1 ½ knots which is approximately 3 times the critical failure velocity for a simple single, vertical barrier under the same flume conditions. Results for oil retention were very good (above 80%) to excellent (above 90%) in all cases. The potential for this cross-section configuration to hold oil was amply demonstrated. Because some of this work overlapped into the second year study and because of its significance, the 2-dimensional retention tests are summarized in Chapter II of this report. Details of the experimental program have been provided by Swift et al. (1995), Coyne (1995) and Swift et al. (1996).

The fluid velocity distribution throughout the configuration was carefully measured using an electro-magnetic sensor and a laser doppler velocimeter (LDV). The LDV was especially effective since it is noninvasive, has a small measurement volume and can detect turbulence. Fluid velocity results are mapped in Swift et al. (1995), Coyne (1995) and Swift et al. (1996). Flow down the submergence plane was observed to be uniform at a speed slightly higher than the incident speed. A strong jet forms inside the entrance gap and extends to the surface of the containment region. The exit flow tends to favor the aft portions of the exit area through the horizontal baffle. These observations were consistent with processes contributing to the breakup of the oil slick into droplets and the droplet trajectories.

OBJECTIVES

The overall goal is to develop an operational oil barrier system, based on the Fig. 2 cross-section, which is capable of superior fast current performance. Specific objectives covered in this second year (Phase II) report include:

1. Completing 2-dimensional flume experiments and processing data for design interpretation.
2. Designing, analyzing and fabricating 3-dimensional physical models using flexible and rigid materials, and testing for shape retention.

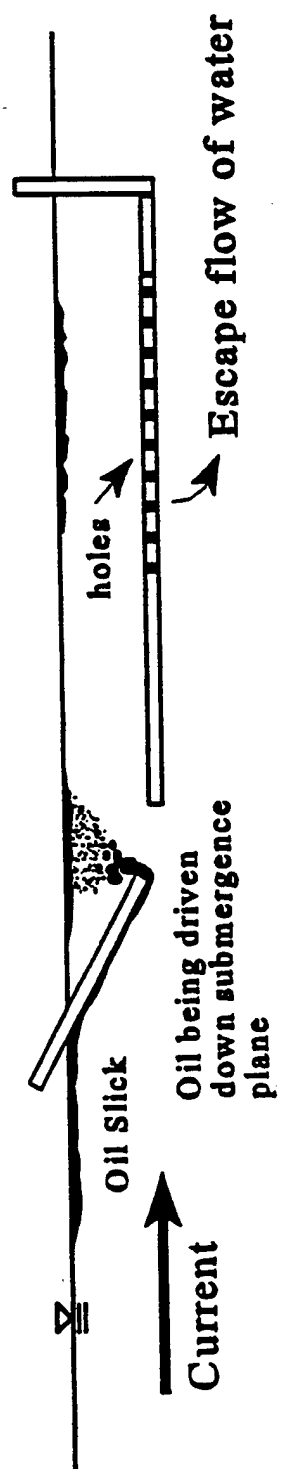


Fig. 2 Optimized barrier configuration.

3. Designing, analyzing and constructing full scale, 3-dimensional prototypes and testing for shape retention and practical aspects.

APPROACH

The first task was to complete the 2-dimensional flume tests for retention, fluid dynamics and design parameter optimization. These experiments were the primary focus of the first year study, but are summarized here for completeness and because contracts for Phase I and Phase II overlapped.

The main goal of Phase II was to develop 3-dimensional, free-floating systems that duplicate the successful 2-dimensional cross-section shown in Fig. 2. Physical models and full scale prototypes were designed, analyzed mathematically, constructed and tested in the flume, a 120 ft x 12 ft x 10 ft tow tank, a 40 ft x 30 ft x 20 ft engineering tank and in an estuarine channel subject to tidal currents. Shape retention was the major concern since the oil retention capability of the cross-section had been previously demonstrated.

Two distinct design concepts emerged - segmented barrier systems consisting of connected semi-rigid modules and continuous, flexible barriers. Development was, therefore, along two main tracks with each culminating in a full scale prototype. The intended ultimate use of these systems is as extended, long barriers to replace oil boom in critical, high current situations.

II. TWO-DIMENSIONAL OIL RETENTION RESULTS

RETENTION TEST METHODS

Oil retention tests conducted using 2-dimensional models in the flume mostly during Phase I are summarized here because of their importance to the Phase II 3-dimensional design development. In addition, contracts for Phase I and Phase II overlapped, so this experimental program and data processing extended into the second year effort. Tests were carried out using the specific cross-section dimensioned in Fig. 3. This cross-section was the result of a series of design optimization experiments as described by Swift et al. (1995, 1996) and Coyne (1995).

The developed barrier configuration shown in Fig. 3 was evaluated by conducting oil retention experiments using a variety of oils. The oils, both non-petroleum and petroleum products, were selected to encompass the range of oil properties likely to be encountered in a spill situation. The 2-dimensional configuration was duplicated using marine plywood, sheet aluminum and sheet acrylic plastic. The model spanned the full width of the tank. The model is a large scale representation and is approximately full size for a small estuarine prototype.

Before oil release, the flume was brought up to an incident flow speed of 1 ½ knots. This speed is approximately 3 times the critical velocity for oil loss using a single vertical barrier of the same draft under the same flume conditions. Oil was then released from a reservoir and spread using a manifold/splash plate system. The system then operated under steady state conditions until the experiment was terminated by stopping the oil supply and the flume flow. This was done in time to prevent the possible recycling of oil escaping past the barrier and encountering the system a second time.

All experiments were video taped, and measurements were made of oil retention. Oil and oil/water mixtures were independently recovered from within the containment region, in front of and in back of the barrier system. Each volume was allowed to separate, and the amount of oil in each volume was quantified. These measurements, as well as data on the amount released, enabled the percent of encountered oil retained by the barrier system to be calculated. The retention was computed as the amount retained in the containment region divided by the amount passing the submergence plane. This definition is actually somewhat conservative in that additional oil was stopped in front of the submergence plane and some was trapped in back of the end vertical plane. (These amounts were not counted because their ultimate fate under field conditions is uncertain.) The redundancy in oil measurements was used to make internal checks and to minimize measurement uncertainty.

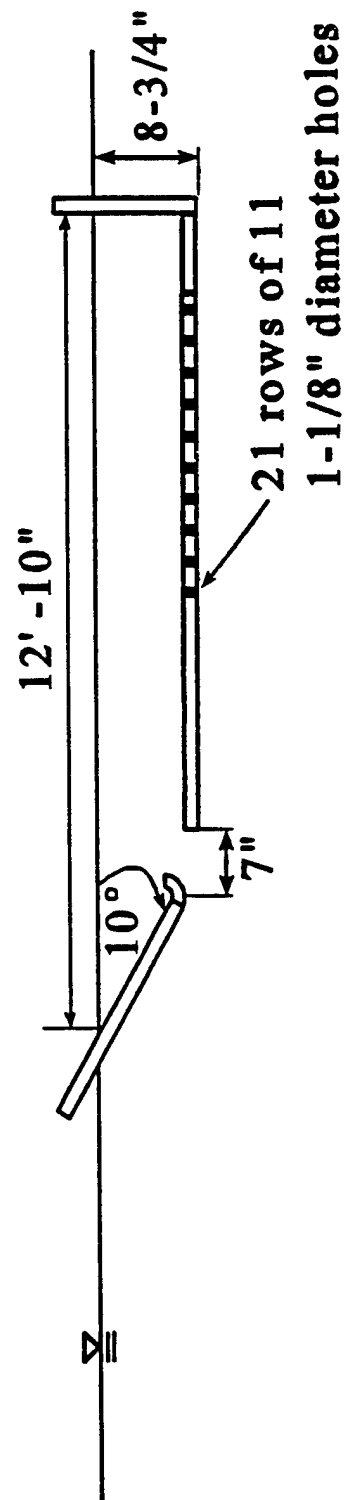


Fig. 3 Two-dimensional cross-section design dimensions.

Information on oil properties was obtained from the literature and from direct measurement. Published values by other researchers and by the product suppliers were collected and used for initial guidance. Actual oil properties for the oils used in this series of experiments were measured directly in the UNH Chemical Engineering Lab. Standard protocols were used to obtain surface tension, interfacial tension, specific gravity and viscosity.

RESULTS AND OBSERVATIONS

Results for retention rates of the oils tested and their corresponding oil properties are summarized in Table 1. It is seen that retention is generally very good (above 80%) to excellent (above 90%) in all cases. The results also indicate that performance is somewhat dependent on oil viscosity and specific gravity.

Visual and video observations were also helpful in understanding how the system works and providing insights into the critical fluid dynamic processes. The slick encountered by the submergence plane was not floating placidly in a layer at the surface but was at least partially mixed in a near surface band. The agitation was due mostly to the inherent turbulence level in the flume and, to a lesser extent, the method of introducing the oil. Because turbulent fluctuations are part of all natural flows, especially in estuaries and rivers, the test program was regarded as being a realistic representation of field conditions.

The mixed layer was concentrated while moving down the submergence plane and most entered the containment region at the entrance gap. One evident loss mechanism, however, was mixing of oil filaments so deep in the water column that the entrance was missed. Oil and water entering the containment region formed a small jet which contributed to further mixing. Most of the oil then separated into surface slicks just above the submergence plane and towards the aft surface of the containment region. These were areas of quiescent fluid, the oil simply rose to the surface and was trapped. A second loss mechanism, however, was the entrainment of small droplets in the exit flow through bottom baffle holes.

Though losses were very small in comparison to the oil retained, attention was focused on the processes of oil escape in order to build a knowledge base for future design development. The two loss mechanisms were strongly influenced by droplet size and specific gravity. Large droplets with low specific gravity have a high rise velocity. Large droplets, therefore, formed a concentrated band going down the submergence plane which favored entering the device. Once inside, large, low density droplets rose quickly and were less influenced by the exit water flow.

In general, it was observed that high viscosity oils formed large droplets, while low viscosity oils were more susceptible to turbulent breakdown into small droplets. Both the incident flow turbulence and turbulence in the entrance jet played a role.

Table 1 Retention rates and oil properties.

Oils	Density (^{lb} /ft ³)	SG	Surface tension (Dynes/cm)	Interfacial tension FW (Dynes/cm)	Viscosity (centistoke)	Retention Percentage
#2 Oil	51.66	0.8309	30.0	6.7	7.55	88
#4 Oil	54.57	0.8778	30.4	23.9	62.89	85
#5 Oil	58.49	0.9407	34.7	20.9	221.5	80
#6 Oil	62.80	1.010	37.6	17.4	4050.0	Non-floating
Silicone 1,000 cSt	60.35	0.9708	24.6	22.6	993.1	84
Silicone 10,000cSt	60.35	0.9707	25.0	23.0	10,655.0	89
Lube oil 600	55.48	0.8924	36.5	13.0	629.9	86
Lube oil 2000	57.01	0.917	36.2	27.9	2011.0	98
Lube oil 3000	57.23	0.921	28.2	31.5	3280.0	95

Density measurements taken at 30°C with a DA-3000 Density Meter.

Kinematic viscosity measurements taken at 25°C with a Brookfield synchro-electric viscometer

Surface tension and interfacial tension made with a DuNouy Ring Tensiometer

These visual observations are consistent with the Table 1 results that retention is enhanced at high viscosities and low specific gravities.

Since the role of viscosity is characterized by the Reynolds number, retention rates are expected to increase with decreasing Reynolds number. In this context, the Reynolds number (Vd/ν) can be computed using incident velocity for V , oil kinematic velocity for ν , and draft for d . The effects of buoyancy on droplet rise velocity are characterized by the internal Froude number ($V/(\frac{\Delta\rho}{\rho}gd)^{1/2}$) in which $1-\Delta\rho/\rho$ is equivalent to specific gravity. Retention is expected to improve at low internal Froude numbers which correspond to higher droplet rise velocities (as well as lower incident velocities.) Since both non-dimensional parameters are relevant, retention is plotted in Fig. 4 as a function of Reynolds number for groupings of data points having similar Froude numbers. In Fig. 5, retention is plotted as a function of internal Froude number for data points having similar Reynolds numbers. The expected trends are evident.

Overall, retention rates for the improved design configuration are very good to excellent. Visual observations of physical processes provide physical insights which enhance understanding and will contribute during the next phase of design improvements.

ADDITIONAL DESIGN CONSIDERATIONS

Other work described by Swift et al. (1995, 1996) and Coyne (1995) include fluid velocity measurements and theoretical considerations. One important conclusion was that exit area should be large compared to gap area to minimize exit flow speed and thereby reduce exit flow entrainment. Thus any increase in gap opening to capture dispersed oil requires changes also in openings through the horizontal baffle.

Another design aspect concerned turbulent mixing processes within the containment region. Turbulent dissipation associated with the jet is a necessary result of the difference in mechanical kinetic energy flowing into the system from that flowing out. The turbulence is undesirable since it tends to break down the slick into smaller droplets with greater tendency towards exit entrainment. Designs must, therefore, have sufficient separation between the gap jet and exit area. This provides the droplet rise time necessary for movement towards the surface away from the region dominated by exit flow.

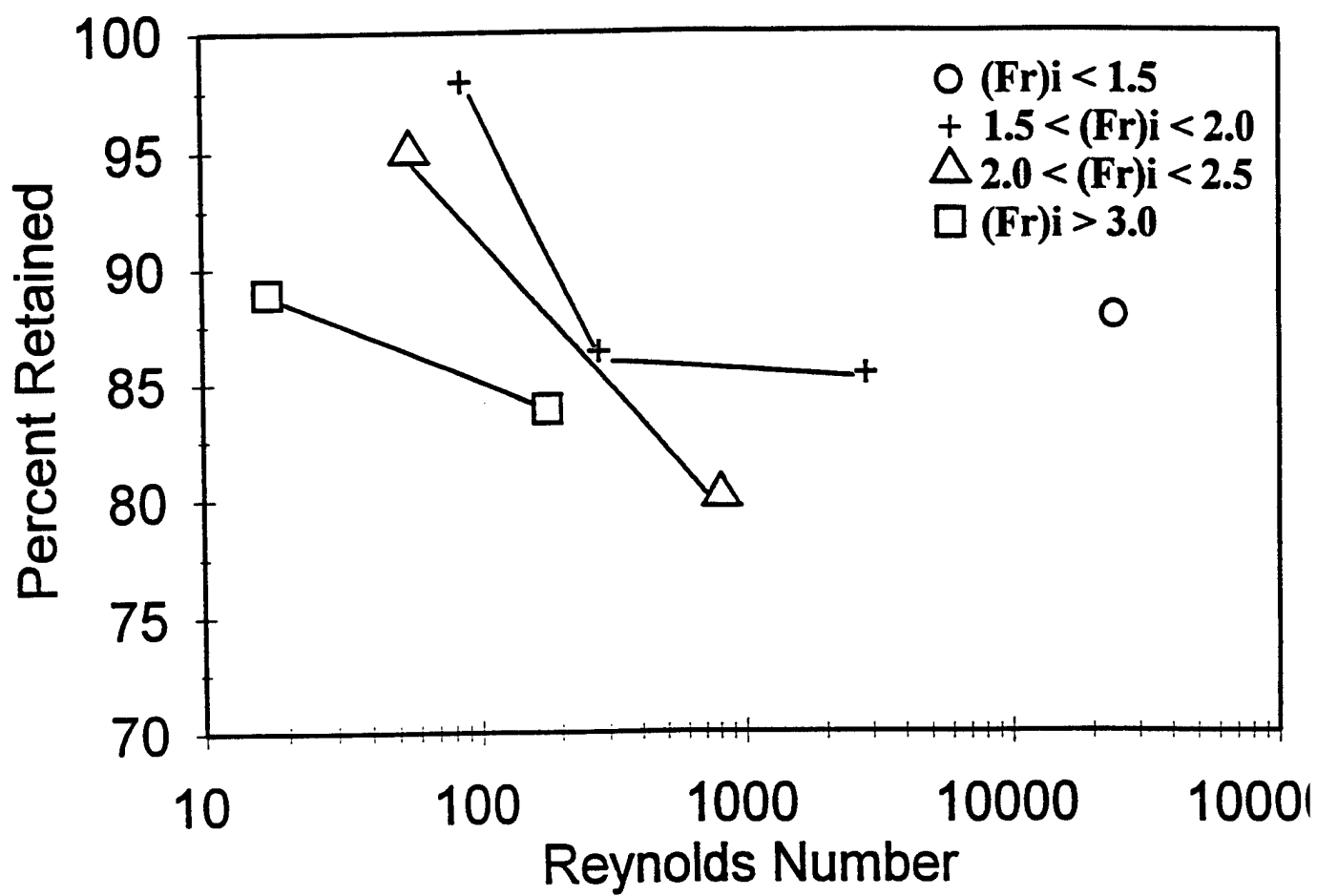


Fig. 4 Oil retention as a function of Reynolds number.

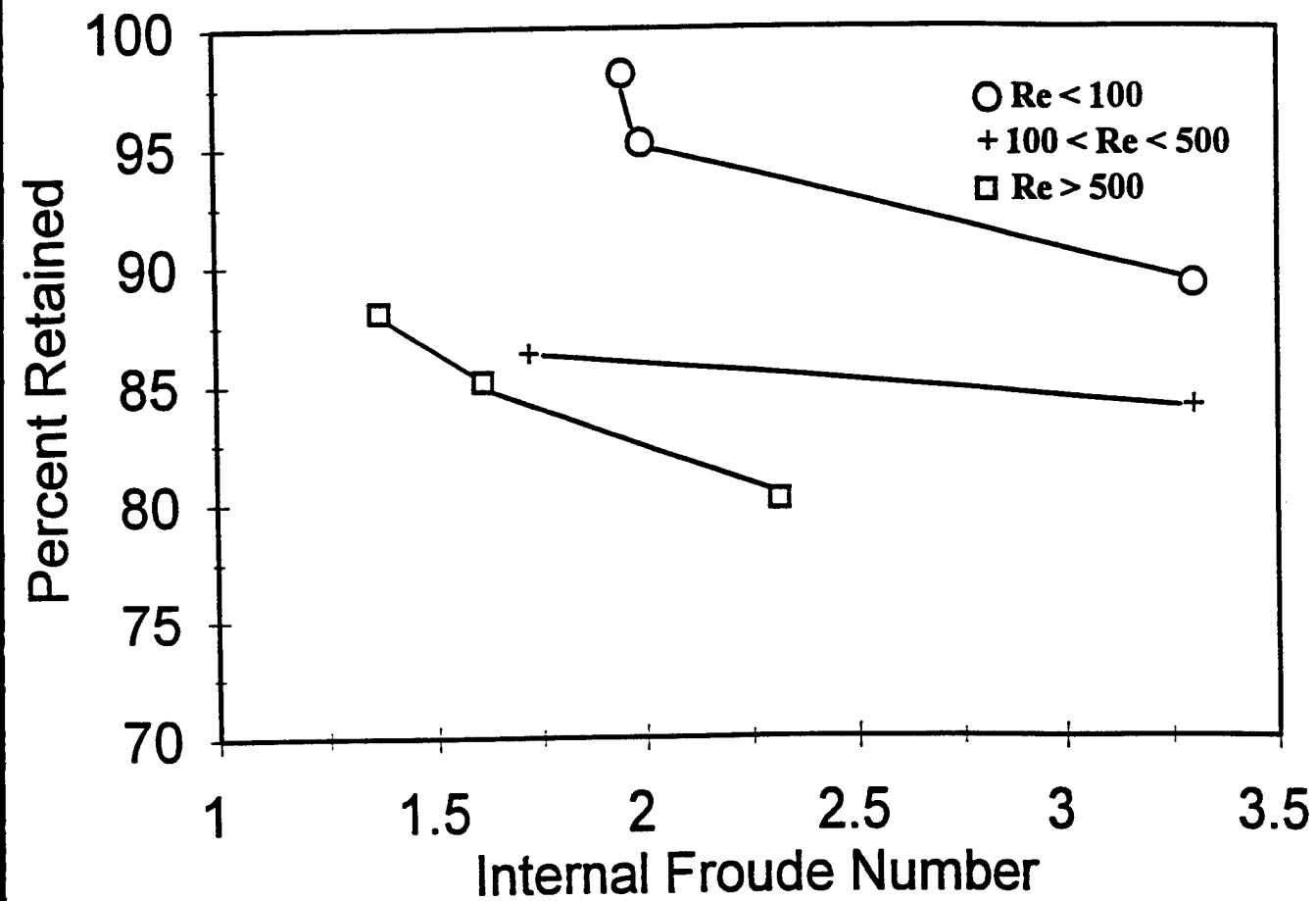


Fig. 5 Oil retention as a function of internal Froude number.

III. THREE-DIMENSIONAL DESIGN DEVELOPMENT

PURPOSE

Having experimentally determined the effectiveness of the submergence plane concept configured as shown in Fig. 3, the next step was to develop free-floating, 3-dimensional systems duplicating the proven 2-dimensional cross-section. This, in fact, is the main purpose of the Phase II effort. In the design process, concepts were generated, analyzed and tested in a series of steps building towards full scale prototypes. The design objective was full scale barriers capable of replacing standard oil boom in situations where failure would occur due to high speed currents.

In the design development, two generic working applications were envisioned for the end product. As illustrated in Fig. 6, in one instance the barrier might replace oil boom at the apex of a containment configuration, while in the other, the barrier system replaces standard oil boom at a critical section of a deflection configuration. Since it is easier and cheaper to use standard oil boom where it will function satisfactorily, standard oil boom would still be used where the configuration is nearly parallel to the current and/or where currents are spatially reduced in speed.

In the containment configuration, boom near the anchors is nearly parallel to the current, so standard oil boom will perform satisfactorily and should be used. Where the boom turns perpendicular to the flow and in the perpendicular apex portion, submergence plane barriers need to be employed. It will be important to be continually evacuating oil from the containment region of the apex barrier using a skimmer. Since the system concentrates oil in the upper part of the containment region, it should be possible to pump fluid that is nearly all oil.

In implementing deflection configurations in high current areas, there is often a critical section between the outer portion where the boom is parallel to the current and the inshore portion where current speed is low (and/or back eddying). This critical section would be a suitable application of the submergence plane technology. Here again, there should be continuous removal of the oil product by skimming the near-shore oil slick.

DEVELOPMENT METHODOLOGY

Because the construction and testing of prototypes is costly and time consuming, a systematic methodology of design development needed to be employed. In general, small scale physical models were considered first; then larger physical models and finally prototypes were built. Evaluation took place at each stage, and improvements were incorporated in the design for the next level.

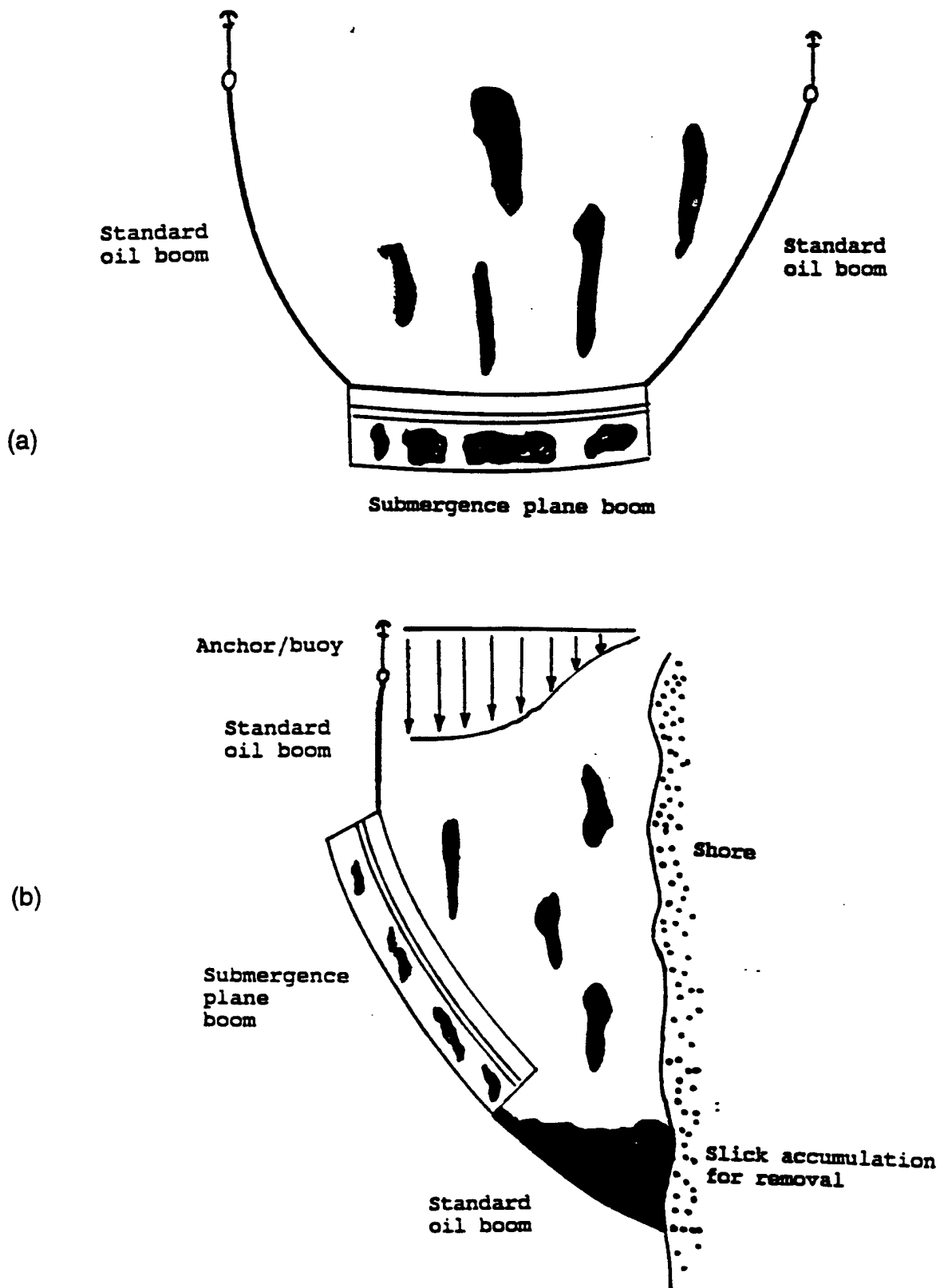


Fig. 6 Applications where submergence plane barriers are used to replace critical parts of standard oil booms. In (a) the barrier forms the apex of a containment configuration, and in (b) the barrier forms part of a deflection configuration where the normal component of current exceeds the critical value for leakage.

Initial screening of design concepts included how well it could be predicted to duplicate the desired 2-dimensional cross-section. Concepts with minimal components were favored. Designs were analyzed for adequate structural strength and stability to maintain shape. Naval architecture considerations included hydrostatic analysis, drag force estimation and factors causing changes in attitude (pitch orientation) with speed.

The main criterion considered during testing was replication of the proper cross-section. Particular attention was paid towards maintaining an effective submergence plane and gap opening with stable dimensions and angles. Other considerations were seakeeping (in field trials), ease of deployment, transportation logistics and manufacturing aspects.

Concepts evolved along two different design tracks - segmented, semi-rigid barriers and continuous, flexible systems. The segmented barriers were made up of linked modules having hard components. The shape of the unit was better controlled, but connection hardware and transportation logistics were of concern. The continuous, flexible systems were more like the standard boom they were to replace, but stable duplication of the design cross-section represented a significant design challenge.

Both design tracks were followed roughly in parallel. The shape-reproducing ability of the semi-rigid barrier, however, resulted in the first full scale system being of this segmented type. The development of segmented, semi-rigid barriers are described in the next chapter (Chapter IV), while continuous, flexible systems are treated in the one following (Chapter V).

IV. SEMI-RIGID SYSTEM

DESIGN RATIONALE

The semi-rigid barrier concept consists of a series of linked modules with each module being constructed of "hard" materials. This prototype development effort resulted in two such modules being designed, built and tested. Important intermediate steps were design analysis and the construction and testing of a 1/3 scale physical model.

Since each module was to be fabricated of rigid materials, duplication of the Fig. 3 cross-section would be straight-forward. The modules were designed to have these dimensions but also to have adjustable design parameters for testing purposes. Draft, submergence plane angle and gap opening could all be varied. The intent was to produce a system for multiple purposes including future design parameter studies in full scale experiments.

The beam of each full scale module was to be slightly less than 6 feet. Thus when attached, they would just fit into the UNH wave/tow tank. The 6 foot beam also allows easy over-the-road transport without special permits. The design life of the system needed only to be long enough for laboratory and field performance tests. Thus the system was considered expendable, and no attempt was made to incorporate durable materials.

Once this "design mission" was established, work began on designing and constructing a 1/3 scale physical model for laboratory testing. Then the final prototype design was completed and the two module system constructed. After preliminary tests in a tank, the full scale prototype was field tested in the Great Bay estuary.

ONE-THIRD SCALE MODEL

The first physical manifestation of the concept was a 1/3 scale physical model consisting of two 2 foot beam modules. In keeping with the multiple use design philosophy, the combined (4 foot wide) system could just fit into the newly widened recirculating flume should extensive testing prove valuable in the future.

The physical model was fabricated of sheet plastic attached to sealed wooden framing using stainless steel fastenings. The model was nearly neutrally buoyant, so only a small amount of structural foam was required to float the system at its design waterline.

Before tank testing, the system was subject to a series of strength experiments. The system was supported and loaded vertically at various points to identify weak modes which could lead to failure in seaways and/or during launching, towing and

recovery. The system possessed good longitudinal stiffness, fair transverse stiffness, but it was flexible when loaded and supported vertically along opposite diagonals in plan view. Cross bracing was incorporated to reduce this twisting deformation.

Tank testing included towing the model by its mooring lines in the deep engineering tank. There was a tendency for the submergence plane to tip the front up while accelerating and at high speed. This was corrected by raising the mooring lines' point of attachment and by distributing foam reserve buoyancy to the stern and bow to increase pitch stiffness.

A retention experiment was conducted using beads to represent the oil slick. This 1/3 scale test was, of course, much less scientifically meaningful than the previous full scale flume tests using oil, but we wanted to verify that the physical model worked in three dimensions as the cross-section models did in two dimensions. The beads' size and specific gravity (and, hence, rise velocity) matched droplets observed in testing the high viscosity oils with specific gravities greater than 0.9 listed in Table 1. At a Froude scaled velocity of 1 ½ knots, beads encountered by the submergence plane were satisfactorily captured in the containment region. Moreover, visually observed flow patterns were similar to the flume cross-section tests, and no new problems were observed in going to a free-floating, 3-dimensional system from the 2-dimensional, fixed flume model. Overall, the 1/3 scale model experiments were judged to be very successful, so further development of this design concept took place.

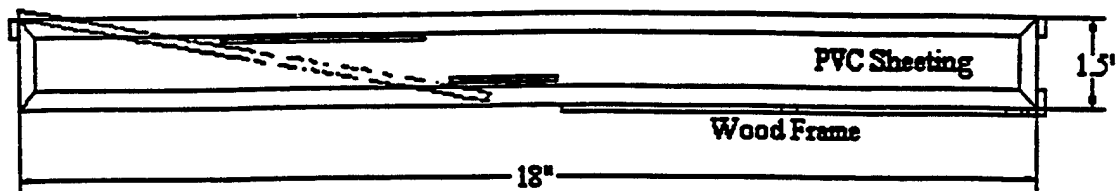
FINAL DESIGN AND CONSTRUCTION

Since the 1/3 scale physical model tests were favorable, the prototype design was based largely on the arrangement and construction of the model scaled up to full size. A schematic of a single module showing the major components is shown in Fig. 7.

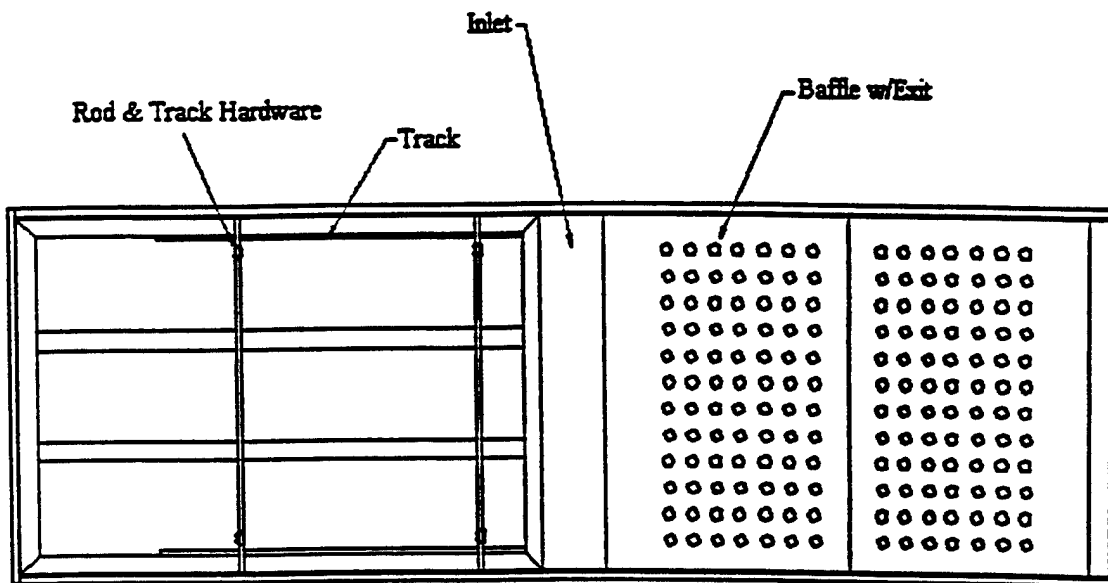
Materials were selected on the basis of strength, stiffness, weight and cost (not design life). The choice of 1/4 inch sheet PVC plastic for the skin and sealed spruce for the framing was also made with one-off construction in mind. The submergence plane was mounted using a track system so that it could be adjusted vertically, fore-and-aft and with a variable angle of attack. Details of the fixtures and hardware are provided by Heather et al. (1996).

Strength calculations were done for generic components and for bending and twisting of a module as a whole. The system weight and displacement (hydrostatics) were analyzed for a draft of 1 foot. Foam buoyancy (including reserve buoyancy) was concentrated near the bow and stern to improve pitch stiffness. Draft changes can be made (in future experiments) by simply shifting the foam buoyancy vertically.

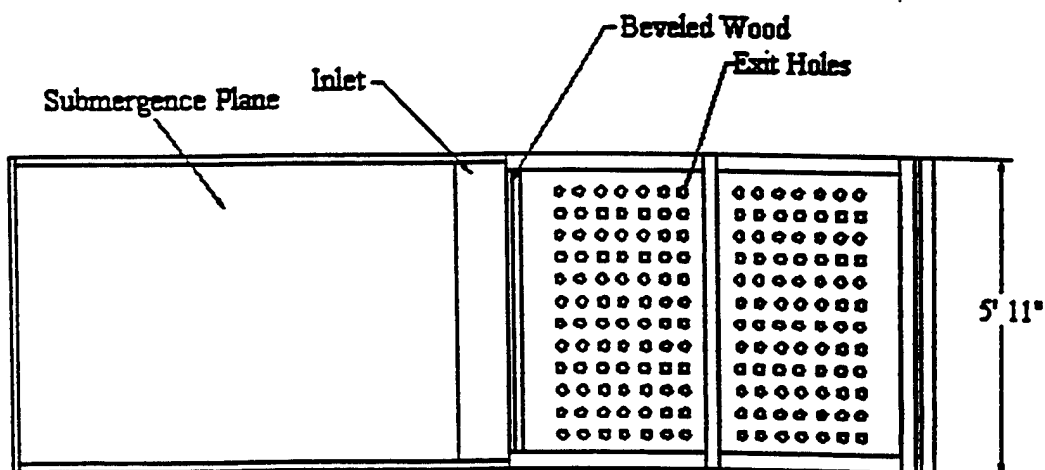
A photo of a completed module is shown in Fig. 8. Each module was placed into the deep engineering tank to verify buoyancy/draft considerations. The adjustable



Schematic side view of Prototype. Wood frame and PVC sheeting are labeled.



Schematic top view of Prototype. Major components are labeled.



Schematic bottom view of Prototype. Major components are labeled.

Fig. 7 Construction schematic of a segmented system module.

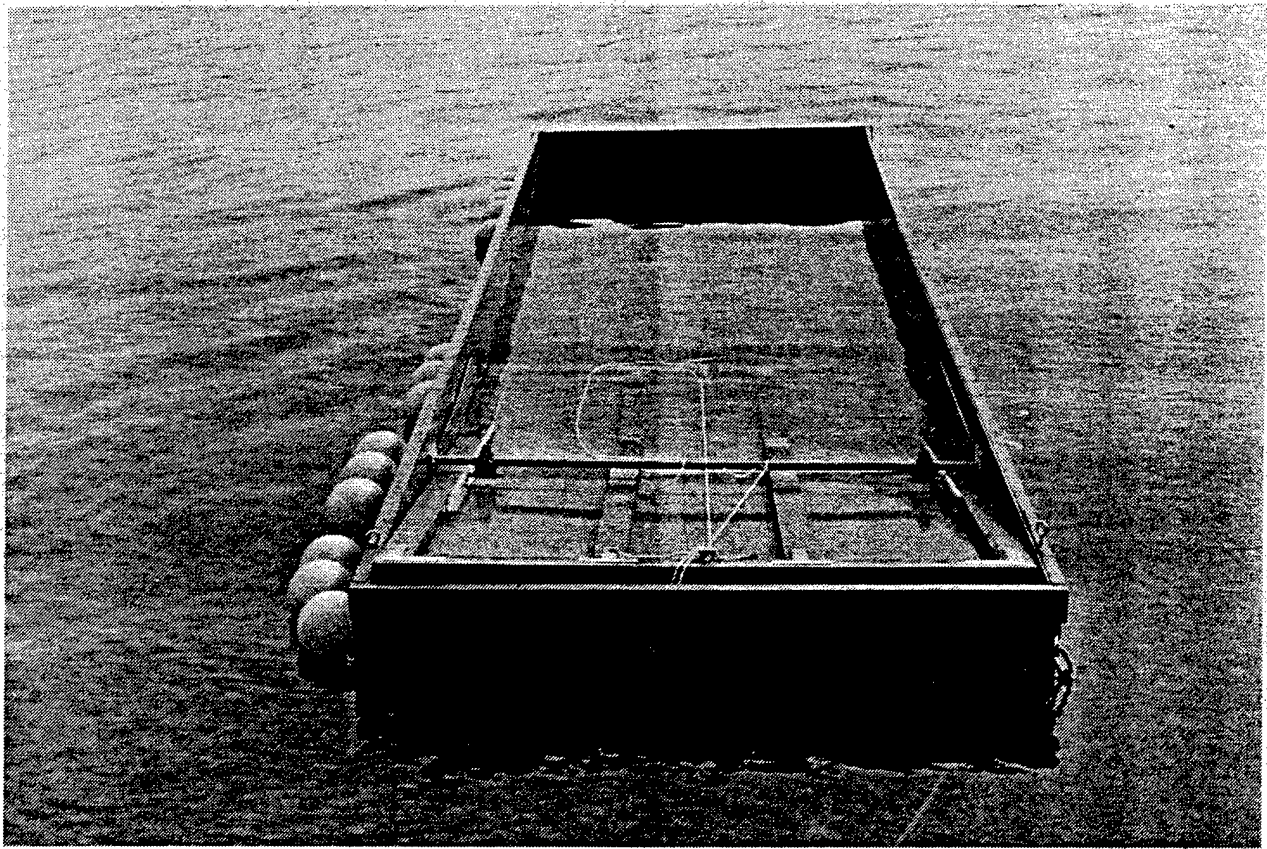


Fig. 8 A prototype module for a segmented system.

submergence plane was fixed at settings commensurate with the 2-dimensional (Fig. 3) submergence plane angle and gap dimensions.

INITIAL TESTING

A single module was launched in the Great Bay estuary on May 1, 1996 for initial field tests. The barrier was towed by a 20 foot workboat at 2 - 3 knots in a sweeping mode. Wind was 10 - 15 knots, and wave heights were on the order of ½ foot with occasional larger waves due to passing boat wakes. The towed barrier exhibited no control problems and maintained its shape and structural integrity. The system did not respond significantly to the small waves and gently contoured the larger boat wakes.

Retention tests were conducted using popcorn as an environmentally benign oil substitute. Popcorn is, of course, usually lighter (though with a variable specific gravity due to soakage) and consists of solid particles rather than droplets or continuous slicks. Retention tests using popcorn, however, are useful to verify proper flow processes and trajectories and to identify problem areas if any. We regard the ability to retain popcorn as a necessary condition for proper operation, so this test has been included in all our field experiments. (Real oil retention of the cross-section shape was, as discussed previously, evaluated successfully in the complementary flume experiments.)

Popcorn was deployed and intercepted by the barrier with nearly 100% recovery. Particle trajectories into and within the containment region were seen to duplicate trajectories of oil droplets in the 2-dimensional flume experiments.

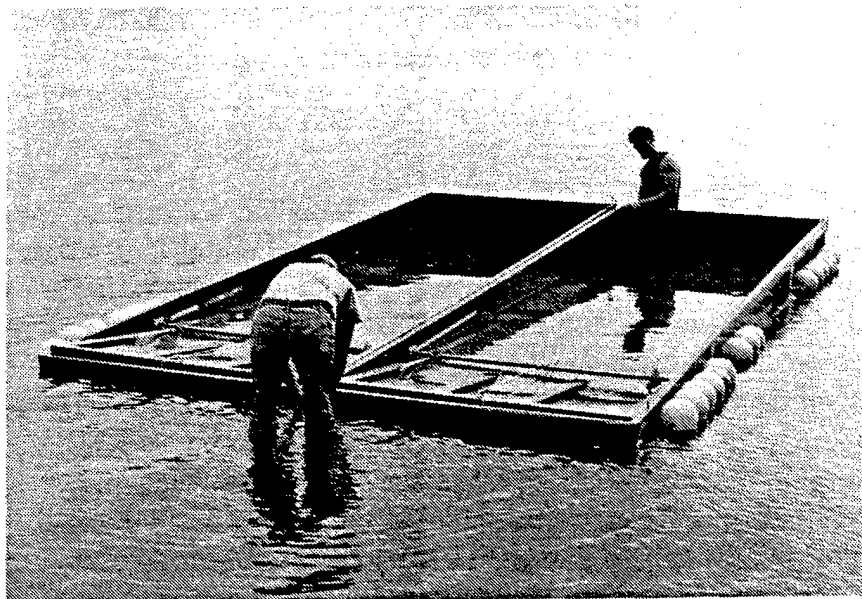
FIELD EXPERIMENT

The complete semi-rigid prototype barrier was tested on June 27, 1996 in the Great Bay estuary off Adams Point, NH. The semi-rigid barrier was used to form the apex portion of a complete containment system as shown in Fig. 6a. The two modules together constituted the apex with 100 feet of standard boom added each side. The 100 foot standard boom sections were angled to the current, and their up-current ends were attached to anchored mooring balls.

The objective was to test the practical aspects and logistics of using a semi-rigid barrier as part of a larger standard boom/rapid current barrier system. A second objective was to try controlling the angle of the standard boom using netting. The netting would be deployed in a horizontal plane below the water surface at the level of the bottom of the boom skirt. The netting was to be attached along the bottom of each skirt and be shaped so as to hold each side at a constant 30 degree angle to the current.

All components were transported to the staging area on Adams Point at high tide and assembled in the water at the shore. Fig. 9a shows the two modules being

(a)



(b)

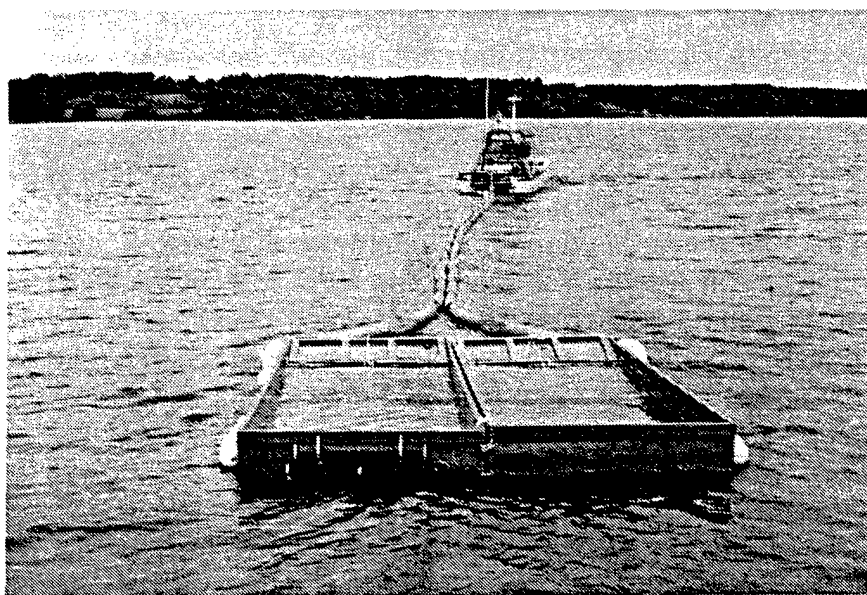


Fig. 9 A segmented barrier section consisting of 2 prototype modules. In (a) the modules are being connected, and in (b) containment boom and the segmented barrier are being towed to the moorings.

connected to each other. The standard boom (with netting in between) was then secured to the forward corners. The standard boom/netting was furled together for towing out to the pre-deployed, anchored mooring balls as shown in Fig. 9b. This method worked very well, and transport incurred very little drag and virtually no control problems. The up-current ends were clipped to the mooring balls, which were 112 feet apart, and the rest of the furling lashing cut. The overall system assumed the containment configuration as the ebb tide intensified.

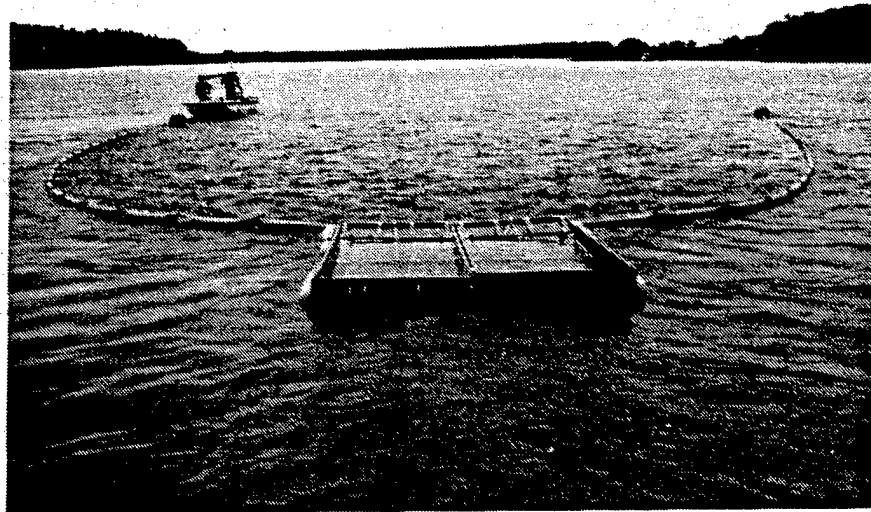
The opened containment configuration is shown in Fig. 10a, while a closeup of the apex barrier during a popcorn retention test is illustrated in Fig. 10b. At this time, the current was about 1 ½ knots, and there was a cross wind of about 10 knots.

The use of netting to maintain side boom shape was not as successful as anticipated, and it has since been recut. It should be noted, however, that the wide-angle camera lens has distorted the Fig. 10a shape to make it look worse than it actually is. There were no structural problems encountered, and the barrier itself maintained its designed shape.

Popcorn retention by the barrier was 100 % and was not affected by the small wave action. Particle trajectories were again similar to the desired oil droplet tracks seen in the flume experiments with the 2-dimensional cross-section. (The popcorn retention experiments were, of course, subject to the same limits of interpretation discussed in the previous section.)

Recovery was easily accomplished by detaching the up-current ends of the standard boom from the mooring balls, bringing them together behind the boat and towing the system to shore. Tow lines were then passed to a shore party that quickly recovered the system and loaded the components on trailers for transport.

(a)



(b)

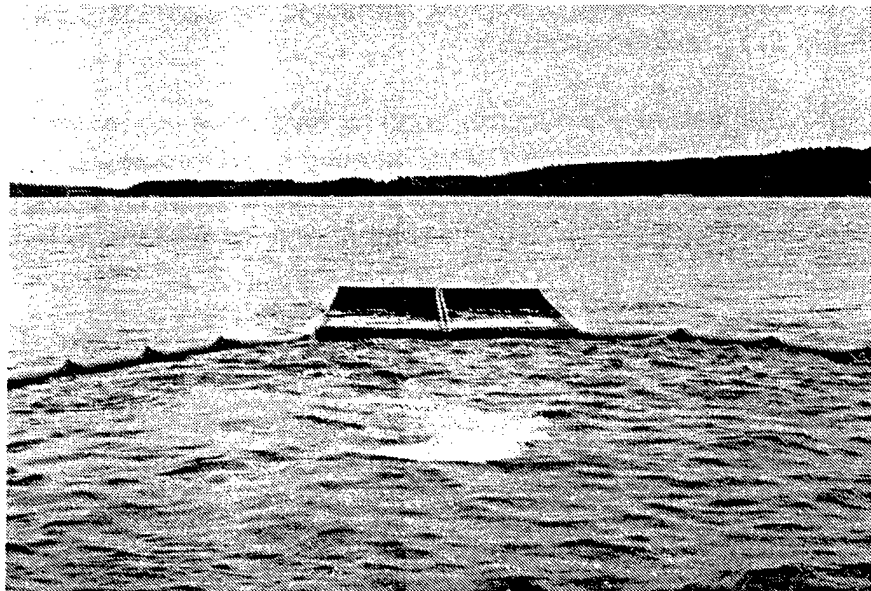


Fig. 10 Containment configuration with the 2 module segmented barrier forming the apex. In (a) the full containment configuration is shown, while in (b) the submergence plane apex is undergoing testing with popcorn.

V. FLEXIBLE SYSTEMS

SMALL SCALE MODELS

Development Rationale

The purpose of the flexible small scale physical model experiments was to initiate development and testing of design concepts which incorporate compliant construction. In contrast to the semi-rigid modules discussed in the previous chapter, flexibility was attained through the use of fabric and deformable foam for planar surfaces. As in standard oil boom, systems were continuous in the cross-channel direction and free-floating.

The developmental approach was to add flexibility to physical model designs in an orderly, gradual manner. Each model was designed to achieve the desired cross-section shape, then constructed and flume tested. The first model employed fabric for the largest planar surface - the horizontal baffle. Based on this experience, the next model was made having generally more flexibility but also incorporating necessary shape maintaining components.

The physical models developed here were tested solely for their shape rendering capability. At 1/12 of the scale used in the 2-dimensional oil retention tests, they were too small scale for experiments with oil. Since the purpose of these tests was to evaluate model shape, position and orientation while running at speed on the surface, Froude scaling was used. The primary physical model tests were run at the 2-dimensional oil retention test speed (1 ½ knots) Froude scaled which is 0.43 knots (= $(1/12)^{1/2}$ times 1.5). Of course while in the flume, visual observations were made at actual speeds ranging from still water to 1 knot (3 ½ knots at full scale).

Flexible Baffle Physical Model

The objective of this first flexible design was to introduce a stable, free-floating capability and to allow for flexibility in the horizontal bottom baffle which is the largest of the system components. As seen in the cross-section construction drawing, Fig. 11, flotation and ballast are positioned to maximize stability. The intention was to use the drag of the aft vertical barrier to keep the horizontal baffle taut and flat.

In the flume, the system floated at the designed waterline in still water and "towed" at the proper orientation at 0.43 knots (1 ½ knots full scale) as shown in the Fig. 12 photograph. The horizontal baffle, however, did not remain taut and billowed downward aft due to exit flow drag. It could be argued that this is acceptable since entrainment by current below the barrier is not likely to increase and the containment volume is in fact larger. Since the objective of this study was to duplicate the proven 2-

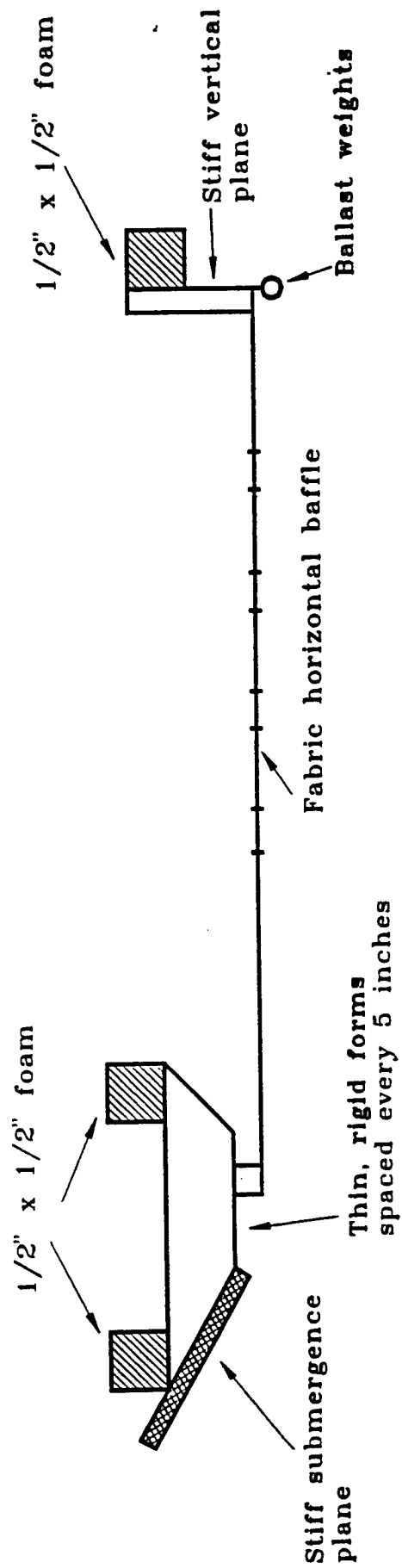


Fig. 11 Construction schematic of the flexible baffle 1/12 scale physical model.

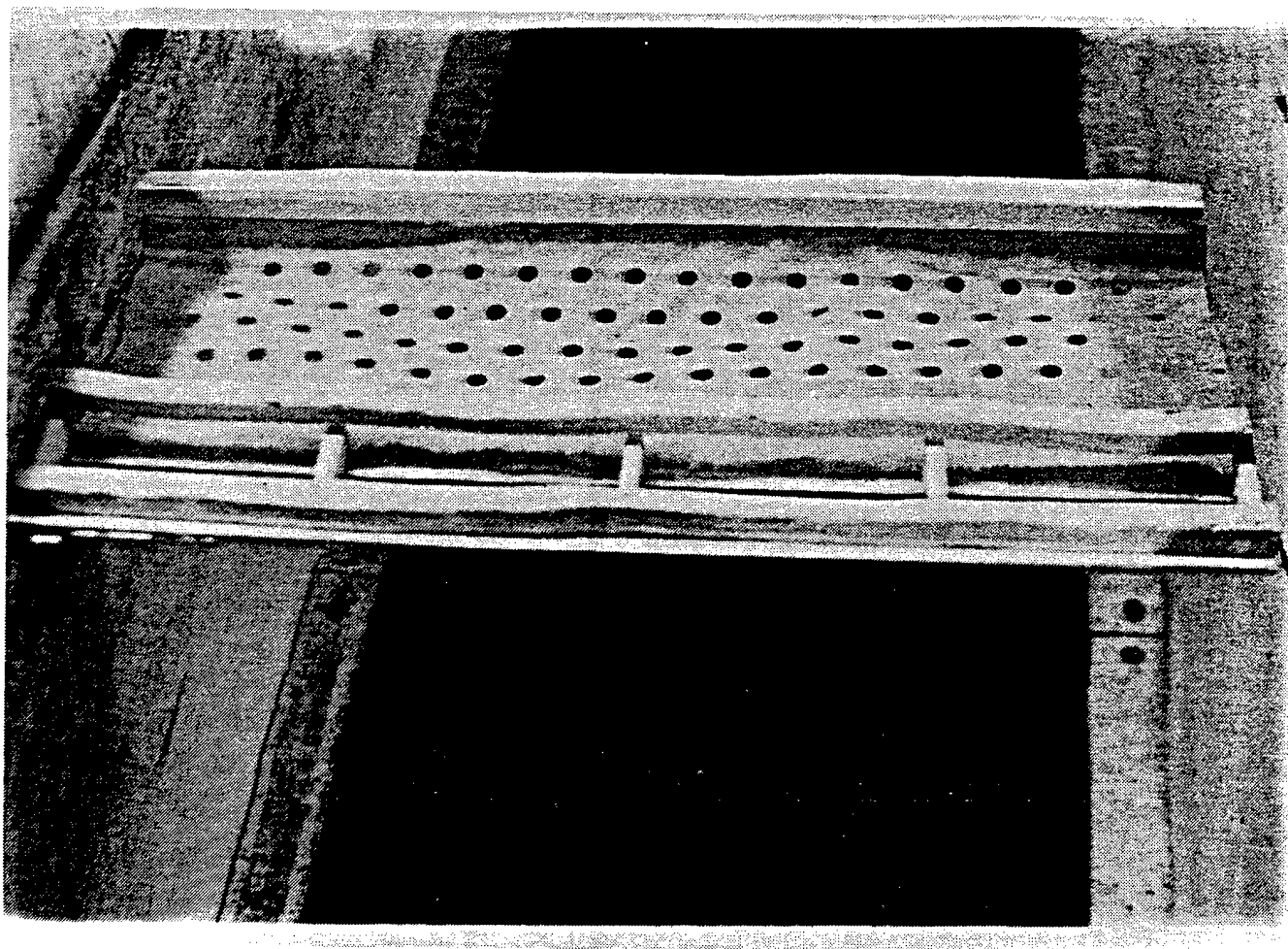


Fig. 12 Flexible baffle 1/12 scale model at 1½ knots (Froude scaled) in the flume.

dimensional cross-section shape, on the other hand, horizontal baffle tautness was addressed in the next 1/12 scale physical model design.

Though the main thrust of subsequent development was toward designs which had additional features expressly to maintain horizontal baffle tautness, one full scale system largely similar to the flexible horizontal baffle model was fabricated and tested in the tow tank. This system exhibited the same downward billowing of the baffle and general distortion of the containment region as seen at 1/12 scale.

Flexible Components Physical Model

In this model, flexibility is incorporated into the submergence plane and the trailing vertical plane (as well as the horizontal baffle). These are constructed of foam as shown in the Fig. 13 structural schematic. The model was designed to bend in plan view (in the cross-current direction), so it can assume the usual catenary curve associated with standard oil booms. To maintain tautness in the horizontal baffle, light weight longitudinal spars are used. They are spaced at regular intervals in the cross-current direction. Stability is achieved by placing the foam buoyancy sources at the leading and trailing edges.

In the flume, the system floated at the proper waterline in still water and maintained the design position and orientation when "towed". As seen in the Fig. 14 photograph, the desired cross-section shape as well as cross-current curvature were obtained. Since this flexible model had the proper shape, was continuous in the cross-current direction and possessed both dynamic and structural stability with a minimum of add-on features, it served as the basis for further flexible system development.

ONE-THIRD SCALE MODEL

In view of the desirable characteristics observed in testing the 1/12 scale flexible components physical model, a 1/3 scale model was designed, built and shape-tested primarily in the flume. Since the flume is 4 feet wide, the model was constrained to be slightly less than 4 feet in the cross-channel direction. The model should, therefore, be viewed as a representative section of a barrier long in the cross-current direction.

The model employed longitudinals to maintain cross-section shape as shown in the Fig. 15 schematic. To enhance stability, each longitudinal individually was ballasted low in the center and had buoyancy high at the fore and aft ends such that the member would float upright at the correct water level by itself. This was also done to increase anticipated ease of handling at the prototype level during deployment and recovery.

A further increase in flexibility was added at this stage by using fabric for the submergence plane. With this change, the whole system could be collapsed for out-of-water transport and storage. The strategy was to keep this taut by use of the system

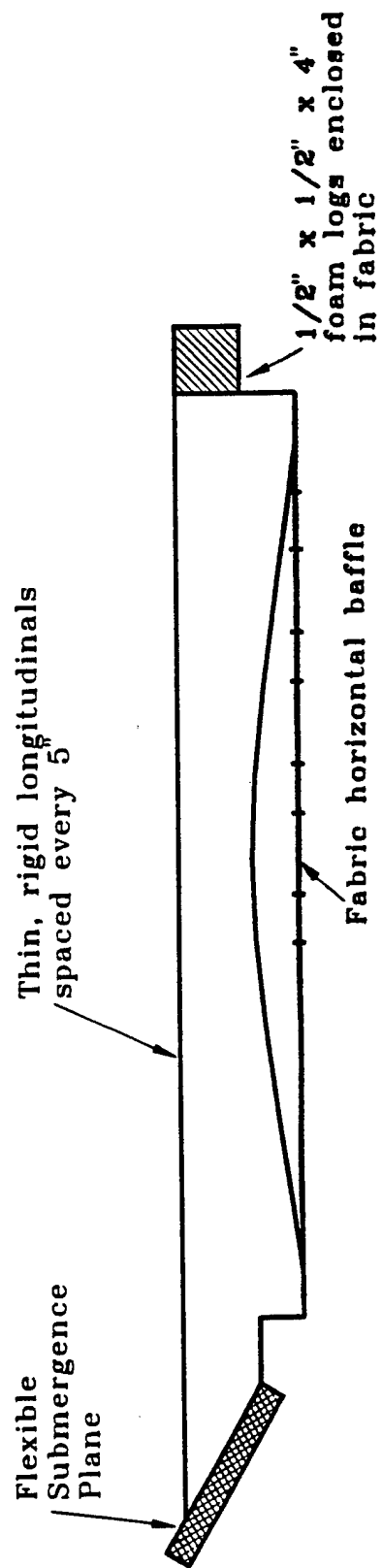


Fig. 13 Construction schematic of the flexible components 1/12 scale physical model.

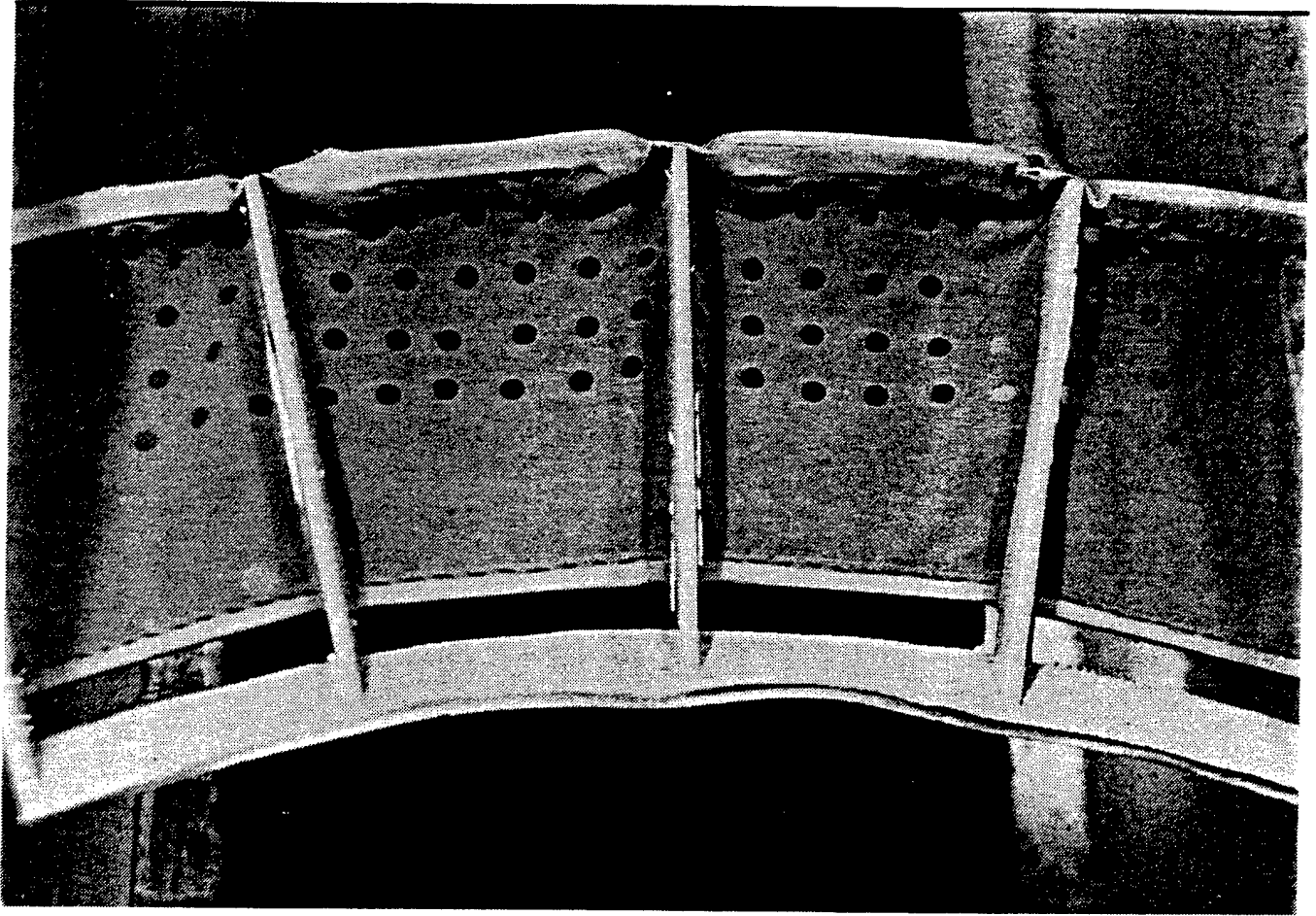


Fig. 14 Flexible components 1/12 scale physical model at 1½ knots
(Froude scaled) in the flume.

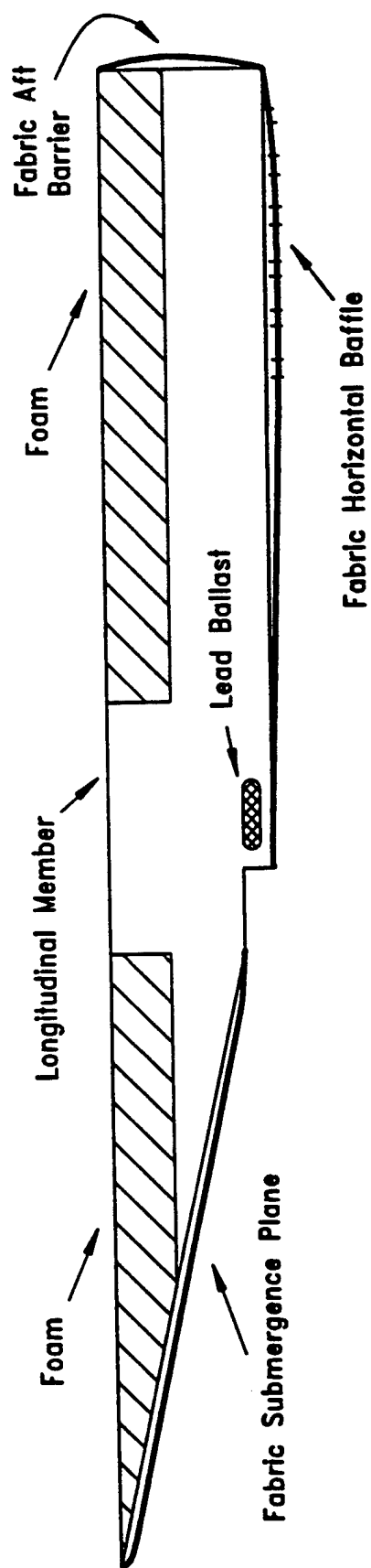


Fig. 15 Construction schematic of the flexible 1/3 scale physical model.

tension in the cross-current direction. In standard oil booms, this tension force is quite large in current, so it was employed in the barrier system for shape maintenance. A cable was also enclosed by a hem in the leading edge of the horizontal baffle and arranged to carry part of the along-barrier tension force. This is to keep the critical gap opening in its designed position.

The system was shape-tested in the flume, as shown in the Fig. 16 photograph, with generally good design cross-section form. The new submergence plane was nearly flat with a gentle upwards bowing between longitudinals. The leading edge of the horizontal baffle was also nearly straight with a slight downwards bowing between longitudinals due to the tendency of the fabric to be forced downwards by the exit flow. Thus the gap opening had a natural tendency to widen slightly which is highly preferable to a propensity to close down.

Problems encountered with this design consisted of a certain amount of fabric drooping above the waterline at the top of the submergence plane and the aft vertical barrier between longitudinals. Flexible foam inserts were deemed necessary at these points to provide some stiffness and reserve buoyancy to prevent slop-over. This change would be incorporated into the prototype design.

Overall, the shape characteristics were excellent for a fabric system (when properly tensioned), and structural, positioning and attitude stability were achieved. This concept, with the fabric freeboard control modification, was next used for the full scale flexible prototype.

FULL SCALE FLEXIBLE BARRIER

The full scale system design was based principally on the 1/3 scale model with important improvements in longitudinal member construction and reserve buoyancy. The cross-section shape was designed to effectively replicate the successful 2-dimensional flume cross-section. The draft, however, was increased to 1 foot to preserve a minimum draft when encountering wave troughs. The length in the cross-current direction was set at just under 12 feet so the system could be used in future tow tank experiments. Thus the system should be viewed as a representative section of a barrier much longer in the cross-current direction. Materials were chosen for ease of construction and cost rather than durability. An extended design life was not considered essential in this first generation, developmental prototype which would be subject only to controlled laboratory and field experiments.

As shown in the Fig. 17 schematic, the longitudinals are composed of a truss-like spruce frame as opposed to the solid construction used in the 1/3 scale model. At full scale, the improvement in longitudinal weight was significant. Since the main function of the intermediate longitudinals is to spread the fabric, structural loads are not great and desirable lightness can be achieved. Each longitudinal was designed to individually

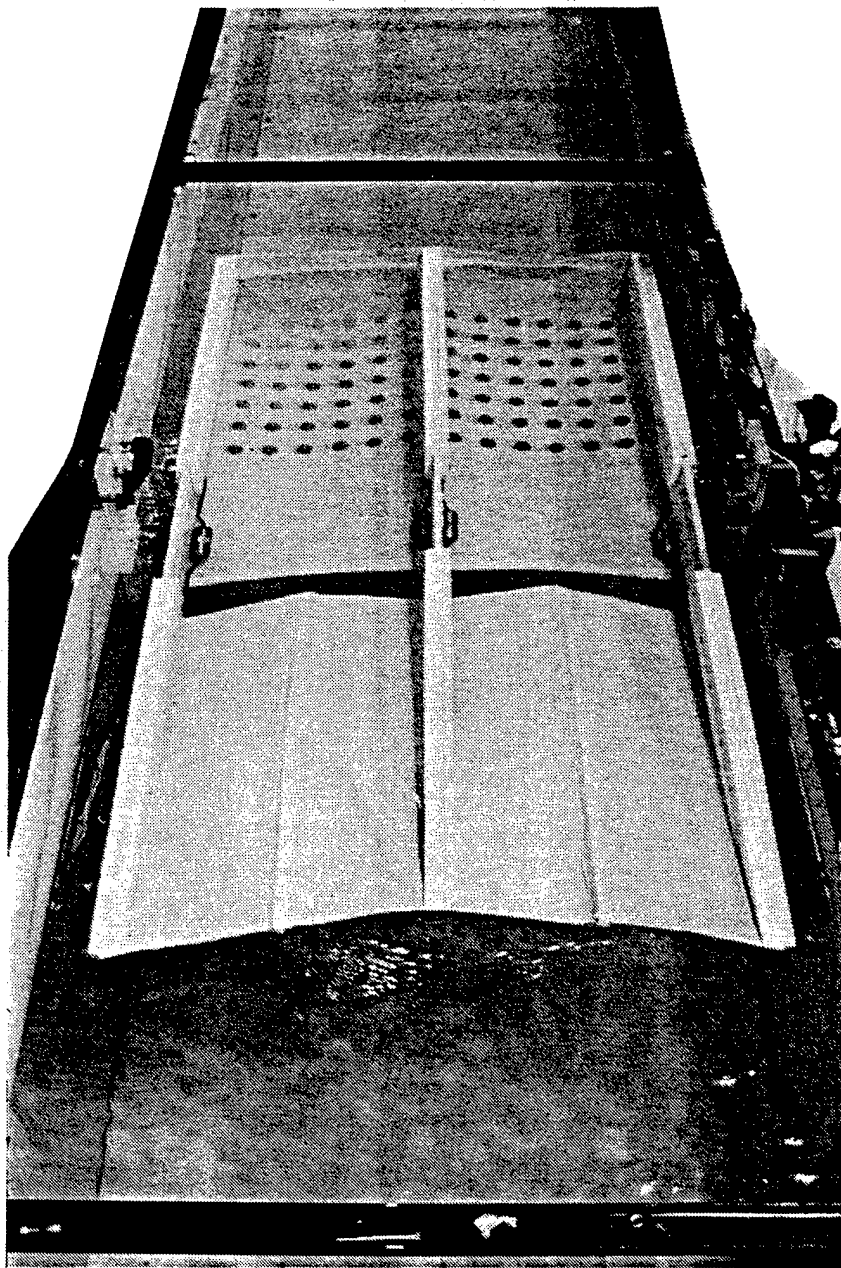


Fig. 16 Flexible 1/3 scale physical model in the flume.

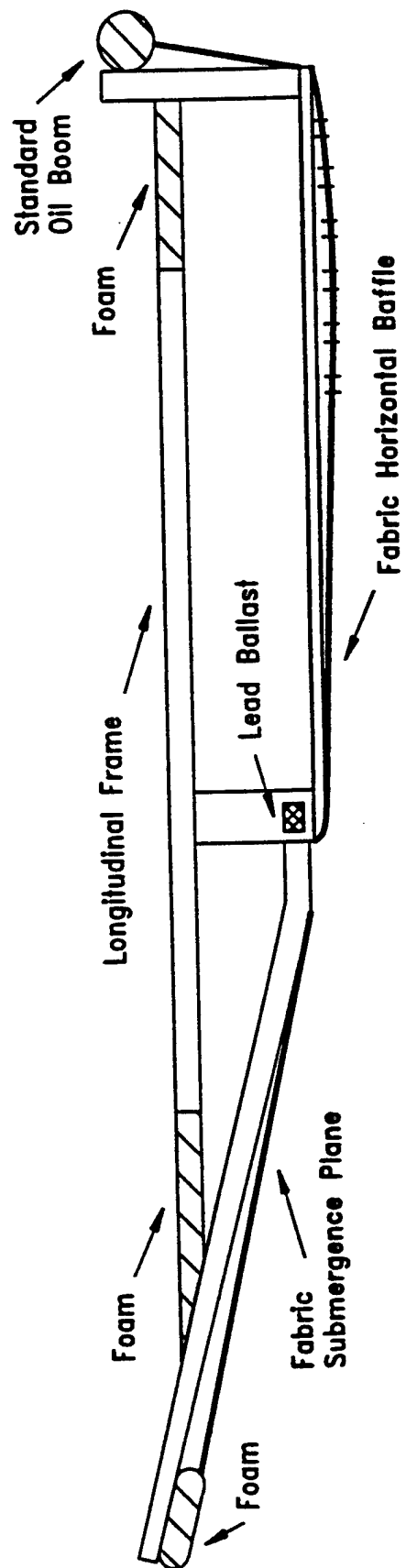


Fig. 17 Construction schematic of the full scale, flexible barrier prototype section.

float at the 1 foot waterline. This forces the whole system to float as intended and makes in-water assembly (and disassembly) much easier. Weights, submerged volume, foam buoyancy and ballasting were analyzed to check hydrostatic balance and hydrostatic stability in pitch and roll.

The submergence plane design was modified from the 1/3 scale version by including foam buoyancy across the top. The foam provides the reserve buoyancy needed to keep adequate freeboard at the bow particularly between longitudinals. The slab foam is inserted in pockets after assembly so that the system can still be collapsed for transport and storage. Though the foam itself is flexible, it does provide some needed stiffness to the upper leading surface of the submergence plane.

In this full scale design, the aft barrier consists of a section of standard oil boom. It is attached to the vertical ends of the longitudinals and the aft edge of the horizontal baffle. There was no attempt to make the horizontal baffle connection watertight since exit area is nearby and a little more may even be beneficial. The aft barrier is consequently modular and can be connected or removed at any time (even while deployed). The foam buoyancy built-in to the boom also provides the reserve buoyancy needed at the aft end for hydrodynamic stability.

The completed system was first tested hydrostatically and generally debugged in the deep tank. Preliminary tests included the assumption of operational shape when tensioned by the mooring lines and when towed gently by the mooring lines.

Field testing took place at Adams Point in the Great Bay estuary, NH on July 31, 1996 and August 1, 1996. The system was assembled on-site and deployed facing the current between two widely spaced finger floats. The deployed prototype section, stretched between mooring points, is shown in the Fig. 18 photograph. The floats provided secure mooring line attachment points and excellent viewing of the system. During the first day, the system was set up to face the ebb current which was weak (less than 1 knot). We returned the next day and deployed the system to face the flood tide which was stronger at that location (1 1/4 to 2 knots).

At maximum current, shape retention of the tensioned system was very good. The reserve buoyancy at the ends made a dramatic improvement in maintaining proper attitude and freeboard. As in the 1/3 scale model, the gap opened slightly and remained stable with no tendency to spontaneously close down. It was found that mooring line attachment is critical. The system must be tensioned, and (like the standard boom) the lines must be led off horizontally. There was some minor fabric billowing observed between the longitudinals, but this can be reduced by stronger fabric and more accurate cutting.

Retention characteristics were observed by spreading popcorn up-current of the system. This popcorn test was, of course, subject to the same limits of interpretation

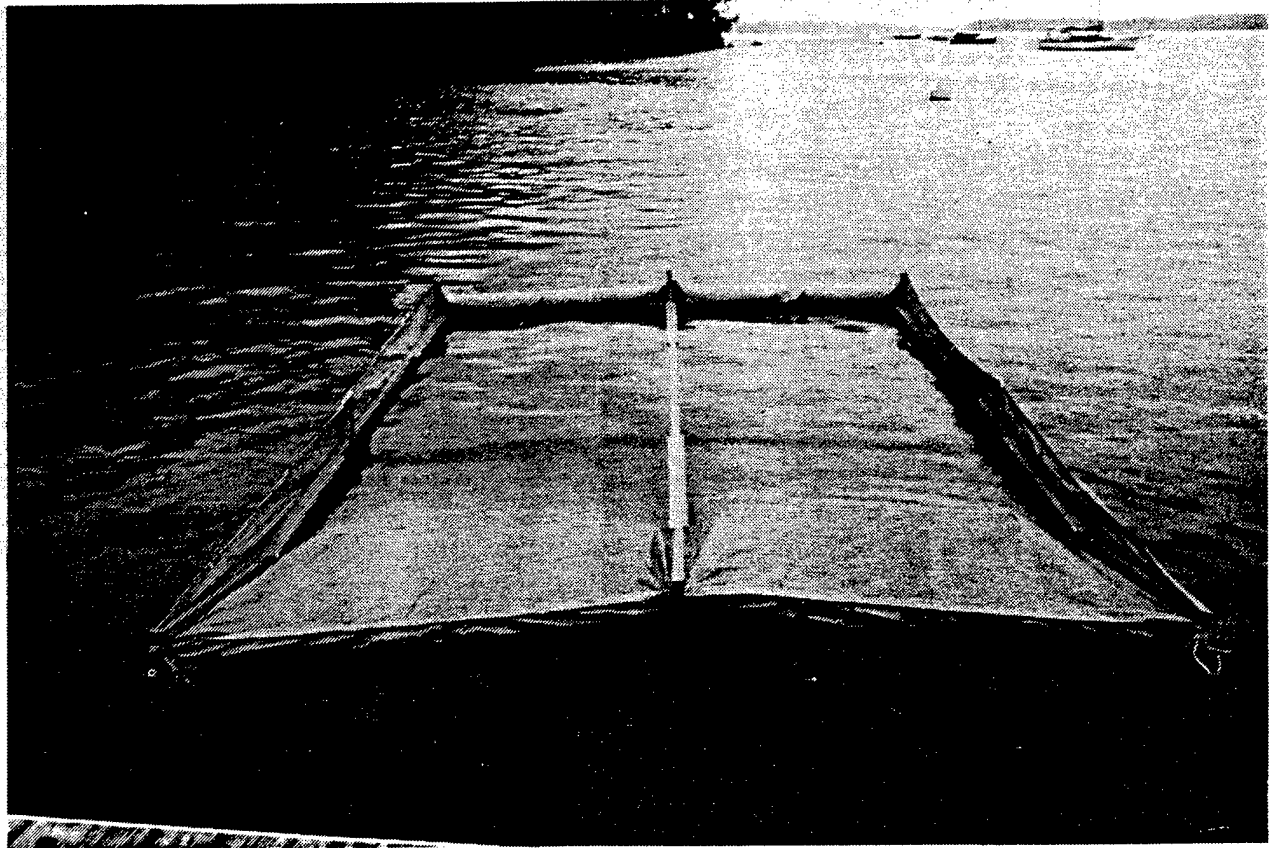


Fig. 18 Full scale flexible barrier prototype section off Adams Point, NH.

discussed in the previous chapter. Popcorn encountered by the submergence plane entered the containment region and was retained. Particle paths were again similar to oil droplet tracks seen in the flume experiments with the 2-dimensional cross-section. The system also captured broken fragments of eel grass which were prevalent at the test site during the experiment.

VI. DISCUSSION

The main goal of developing 3-dimensional, floating oil barriers having the oil-tested 2-dimensional cross-section was achieved. Physical models and full scale representative sections of segmented and continuously flexible prototypes were designed, analyzed and tested primarily for shape, stability and strength. Methods and logistics of using submergence plane systems at the critical apex position of a containment boom configuration were demonstrated.

Future development of submergence plane barriers should include continued experimentation with respect to gap control, draft and exit area. The full scale, 3-dimensional prototypes constructed in this study could be used in these laboratory studies. New full scale systems should be extended in the cross-channel direction for field use. This next generation development effort should culminate in a "standardized" OHMSETT full scale oil retention experiment. Practicality can then be enhanced by continuing the design effort to improve logistics, robustness and manufacturing.

REFERENCES

- Agrawal, R.K. and L.A. Hale (1974) "A New Criterion for Predicting Headwave Instability of an Oil Slick Retained by a Barrier", Proc. of the Offshore Technology Conf.
- Bianchi, R.A. and G. Henry (1973) "The Development and Demonstration of an Underwater Oil Harvester Technique", Report submitted to the EPA, EPA-R2-73-205.
- Cox, J.C., L.A. Schultz, R.P. Johnson and R.A. Shelsby (1980) "The Transport and Behavior of Oil Spilled In and Under Sea Ice", ARCTEC, Inc., Columbia, MD.
- Coyne, P.M. (1995) "Development of a Fast Current Oil Containment Barrier", M.S. Thesis, Ocean Engineering, UNH, Durham, NH.
- Delvigne, G.A.L. (1989) "Barrier Failure by Critical Accumulation of Viscous Oil", Proceedings of the 1989 Oil Spill Conference, American Petroleum Institute, Washington, DC, 143-148.
- Delvigne, G.A.L. (1984) "Laboratory Experiments on Oil Spill Protection of a Water Intake", in Oil in Freshwater, Vandermeulen and Hrudý (eds), Pergamon Press, Elmsford, New York, 446-458.
- Heather, S., W. DiProfio and D. Ryan (1996) "Swift Current Oil Boom Experiment", Ocean Projects Course Final Report, available through Sea Grant, UNH, Durham, NH 03824.
- Johnston, A.J., M.R. Fitzmaurice and R.G.M. Watt (1993) "Oil Spill Containment: Viscous Oils", in the Proceedings of the 1993 International Oil Spill Conference, American Petroleum Institute, Washington, DC, 89-94.
- Milgram, J.H. and R. Van Houghton (1978) "Mechanics of a Restrained Layer of Floating Oil above a Water Current", J. Hydronautics, Vol. 12, No. 3, 93 - 108.
- Swift, M.R., B. Celikkol and G. Savage (1990) "Diversion Booms in the Piscataqua River, NH", in Oil Spill Management and Legislative Implications, M.I. Spaulding and M. Reed (eds.) ASCE, New York, 528-540.
- Swift, M.R., B. Celikkol, C.E. Goodwin, R. Carrier, S.P. McDonald and J. Chadwick (1991) "Oil Spill Response Engineering and Planning", Final Report submitted to the NH Water Resources Research Center, UNH, Durham, NH

Swift, M.R., B. Celikkol, G. LeCompagnon and C.E. Goodwin (1992) "Diversion Booms in Current", Journal of Waterway, Port, Coastal and Ocean Engineering, Vol. 118, No. 6, 587-598.

Swift, M.R., B. Celikkol and P. Coyne (1995) "Development of a Rapid Current Containment Boom", Phase I report submitted to the U.S. Coast Guard, Volpe National Transportation Systems Center, 55 Broadway, Cambridge, MA.

Swift, M.R., P.M. Coyne, B. Celikkol and C.W. Doane (1996) "Oil Containment Performance of Submergence Plane Barriers", Journal of Marine Environmental Engineering, Vol. 3, 47-61.

Wicks, M., III (1969) "Fluid Dynamics of Floating Oil Containment by Mechanical Barriers in the Presence of Water Currents", Proceedings API/FWPCA Joint Conference on Prevention and Control of Oil Spills, 55-106.

